Modeling inelastic behavior of Al-rich Ti-Al alloys at ultra-high homologous temperature

DISSERTATION
zur Erlangung des akademischen Grades
Doktoringenieur
(Dr.-Ing.)

von M.Sc. Helal Chowdhury
geboren am 01.03.1983 in Feni, Bangladesch

genehmigt durch die Fakultät für Maschinenbau
der Otto-von-Guericke-Universität Magdeburg

Gutachter:
1. apl. Prof. Dr.-Ing. habil. Konstantin Naumenko
2. Prof. Dr.-Ing. habil. Manja Krüger

Datum der Einreichung am 30.11.2017
Promotionskolloquium am 13.04.2018

© docupoint Verlag || Otto-von-Guericke-Allee 14 || 39179 Barleben

ISBN 978-3-86912-145-1
Autor Helal Chowdhury
Titel Modeling inelastic behavior of Al-rich Ti-Al alloys at ultra-high homologous temperature
Layout Helal Chowdhury
Umschlag Marco Borchardt
Druck docupoint GmbH, 2018

Alle Rechte vorbehalten.
Kein Teil dieses Buches darf in irgendeiner Form (Druck, Fotokopie oder einem anderen Verfahren) ohne schriftliche Genehmigung der docupoint GmbH reproduziert oder unter Verwendung elektronischer Systeme, verarbeitet, vervielfältigt oder verbreitet werden.

Abstract

In this work, the Al-rich TiAl alloy family has been investigated in order to understand the microstructure-property relationship within the mean-field homogenization approach. This is the first study of Al-rich TiAl alloy family, combining both the material science and mechanics perspective. To understand the origin of different length-scales dependent macroscopic plastic anisotropy and asymmetry is one of the prime objective of this thesis. The appearance of one or more, stable or meta-stable, long-range ordering or long-period superstructure phases is one of the most important characteristics of this alloy family, which considerably changes microscopic deformation mechanisms and hence macroscopic mechanical properties. In this regard, the material science perspective of the Al-rich TiAl family has been reviewed in terms of phases, microstructure, morphology, deformation mechanisms etc. Then crystal viscoplasticity based modeling within finite strain and rotation framework has been applied to an exemplary intermetallic alloy Ti-61.8at.% Al from this family at ultra-high homologous temperature of approximately 0.73. After analyzing the plastic anisotropy of single crystal like alloy Ti-61.8at.% Al, the choice of the power-law type flow-rules at different conditions has been discussed in great detail. Why two or more internal-variable based flow-rule is more appropriate for complex microstructures has also been justified. The plastic anisotropy has been simulated for three different strain rates of 10^{-3}, 10^{-4} and 10^{-5} s^{-1}.

Determining critical stresses for different slip systems becomes a prerequisite in the modeling of plastic anisotropy. However, the task of finding individual critical resolved shear stress (CRSS) for every single slip-system, if not impossible, is formidable and a delicate one especially if the microstructure is very complex. In order to estimate CRSS values for all slip systems, a new iterative scheme has been proposed. A special version of this algorithm has been successfully applied. Related all material and model parameters have been determined. Finally, the crystal viscoplasticity model with the set of identified parameters and estimated CRSS has been used to predict high-temperature rate-dependent tension-compression asymmetry aiming a qualitative understanding. The commercial software package Abaqus Standard with its user-subroutine (UMAT) functionally in Fortran programming language has been used for all the finite element based simulations.

Some studies indicated that there are significant influences of long-range ordered superstructures in the Al-rich side of TiAl alloys, which is one of the most important characteristics of this family. This characteristic feature is emboldened by this study. In addition to the well known length-scales, i.e. grain scale, lamellar scale and dislocation density etc., the presence of long-period superstructural scale in the Al-rich side of TiAl alloys is also manifested by this study when the origin of the plastic anisotropy is investigated. The modeling approach and the parameter estimation technique can be extended to any other Al-rich alloys with long-period superstructures, which would ultimately assist in further possible alloy development.

Acknowledgement

First and foremost, I would like to express my earnest gratitude to my mentor Prof. Dr.-Ing. Konstantin Naumenko for his guidance, patience, and unreserved encouragement in sparking my interest into the world of micromechanics. He continuously helped to feel confident in this area, without which this work would not have been possible. I wish to take the opportunity of expressing my sincere respect and appreciation to Prof. Dr.-Ing. Holm Altenbach, who gave the complete freedom in working and helped to take some vital decision during the whole period. My deepest gratitude goes to Prof. Dr.-Ing. Manja Krüger for her special guidance in understanding material science perspective in general. As a beginner in material science, even a small discussion with her helped to enrich my understanding. Her efforts in managing experimental data were outstanding. From the modeling strategies, I feel honored to sincerely thank Prof. Dr.-Ing. Albrecht Bertram for his vital suggestions. Some fruitful discussions with him are worth ever-remembering.

I would also like to gratefully acknowledge the German Research Foundation (Deutsche Forschungsgemeinschaft - DFG) for their financial contribution through the graduate school GRK1554, and wish to express my sincere thankfulness to my colleagues and professors at the Graduiertenkolleg for their cooperation. I warmly thank two GRK members, Phillipp Thiem and Julia Becker, who took extra burden for me from the experimental side. Special thanks goes to Frau Madeleine Ruhbaum who continuously cooperated in every aspects during the last four years. Lively environment and diversified scientific discussions in the biannual workshops are worth remembering. Many thanks and gratefulness should go to all of my colleagues, previous and current, at the institute of mechanics including Andreas, Oksana, Ivan, Johanna, Marcus, Oliver, Barbara, Mykola, Sasha, Anna etc. They provided important information and advice, directly or indirectly, regarding various technical and nontechnical issues. Besides, Frau Schildt, Frau Spröte and Dr. Ringwelski deserve special thanks for their cooperation in administrative issues.

My heartfelt thanks go to two of my friends, Dr. Mokarram Hossain and Mamun Al-Siraj, for their cooperation in proof reading and in many other technical issues. I am absolutely grateful to my parents, siblings and relatives for their love, support and constant encouragement. Last, but not least, I thank my beloved wife Jannatul Nayeem for her understanding, love, and support all the way from the beginning. Munawwar, my son and my inspiration, brought new dimension in my life.

Magdeburg Helal Chowdhury

Contents

1 **Introduction and background** **13**
- 1.1 The increasing demand for high-temperature materials 13
- 1.2 Defects, dislocations in solids 14
  - 1.2.1 Preliminary remarks 14
  - 1.2.2 SSD vs. GND 15
  - 1.2.3 Deformation modes and dislocation mechanics 16
  - 1.2.4 Macroscopic effects of microscopic collective behaviors of dislocations 20
- 1.3 High-temperature deformation mechanisms 21
  - 1.3.1 Recovery and recrystallisation 21
  - 1.3.2 Grain coarsening or coarsening-dissolution 23
- 1.4 Bridging materials science and mechanics 23
- 1.5 Homogenization and scale separation 23
  - 1.5.1 Homogenization types 25
  - 1.5.2 Common mean-field approaches 27
  - 1.5.3 RVE and ergodicity 28
- 1.6 Plasticity modeling 30
  - 1.6.1 Plasticity types 30
  - 1.6.2 Modeling approaches 30
  - 1.6.3 State variables 30
  - 1.6.4 Phenomenological vs. physical modeling 31
  - 1.6.5 Classical crystal plasticity 32
  - 1.6.6 Dislocation density based CP 33
  - 1.6.7 Gradient and higher order CP 34
  - 1.6.8 Short-range vs. long-range interactions 34
  - 1.6.9 Internal stress and its origin 35
  - 1.6.10 Backstress and hardening variables 37
  - 1.6.11 Boundary condition 37
- 1.7 TiAl alloy system 38
- 1.8 Objectives of this thesis 41

2 **Al-rich Ti-Al alloy family** **45**

2.1 Phase diagram of Al-rich side . . . 45
2.2 Highly brittle Al-rich TiAl alloys . . . 45
2.3 Phases in Al-rich side . . . 46
2.4 Production routes . . . 48
2.5 Ordering and stability . . . 48
2.6 Lamellar alloys: Ti-rich vs. Al-rich with LPS . . . 50
2.7 Deformation mechanisms: Ti-rich vs. Al-rich lamellar TiAl . . . 51
2.8 Yield stress anomaly (YSA) . . . 54
2.9 Basic microstructural features of Ti-61.8at.%Al . . . 56
2.10 Deformation mechanisms of Ti-61.8at.%Al at high homologous temperature . . . 57
2.11 Experimental procedures and test data . . . 59

3 Micromechanical modeling approach **61**
3.1 Continuum framework for crystal plasticity . . . 61

4 Crystal viscoplasticity modeling: Choosing a power-law **65**
4.1 Introduction . . . 65
4.2 Choosing flow, hardening and recovery rules . . . 69
  4.2.1 Type-1 flow-rule . . . 69
  4.2.2 Type-2 flow-rule . . . 72
  4.2.3 Type-3 flow-rule . . . 74
  4.2.4 Type-4 flow-rule . . . 75
  4.2.5 Type-5 flow-rule . . . 75
4.3 Flow-rules and slip activities . . . 78

5 Numerical aspects **81**
5.1 Choosing RVE . . . 81
5.2 Numerical implementation . . . 83
5.3 Solver, matrix conditioning and mesh convergence . . . 85

6 CRSS estimation technique **87**
6.1 Introduction . . . 87
6.2 Critical resolved shear stresses . . . 90
  6.2.1 CRSS in Ti-rich TiAl . . . 90
  6.2.2 Preliminary remarks on CRSS in Al-rich TiAl . . . 90
  6.2.3 Constant CRSS assumption . . . 91
  6.2.4 Hard- and soft-modes based approach . . . 93
  6.2.5 Longitudinal-mixed-transverse modes based approach . . . 93
  6.2.6 Operative stress based approach . . . 94
6.3 Comparing four approaches . . . 100
6.4 A generalized iterative scheme for CRSS estimation . . . 101
6.5 The role of different hardening stresses . . . 103
6.6 Comments on the plastic anisotropy . . . 103

7 Parameter estimation 105
7.1 Components of the elasticity tensor . . . 105
7.2 Rate sensitivity parameter . . . 105
7.3 Latent hardening and interaction matrix . . . 107
  7.3.1 Self and latent based hardening phenomenology . . . 107
  7.3.2 On the origin of latent hardening description . . . 107
  7.3.3 Latent hardening experiments . . . 108
  7.3.4 Latent hardening practices . . . 109
  7.3.5 Latent hardening consideration in this study . . . 111

8 Model prediction: Tension-compression asymmetry 113
8.1 Introduction . . . 113
  8.1.1 Preliminary remarks . . . 113
  8.1.2 Origin of TCA . . . 114
  8.1.3 General observations on TCA . . . 114
  8.1.4 TCA reduction . . . 115
  8.1.5 Macroscopic modeling approach . . . 115
  8.1.6 Microscopic modeling approach . . . 116
  8.1.7 Modeling of Al-rich TiAl alloys . . . 117
8.2 TCA prediction in two lamellar directions . . . 118

9 Summary and outlook 123
9.1 Summary . . . 123
  9.1.1 Regarding microstructural and morphological impact on the mechanical properties 124
  9.1.2 Regarding CRSS estimation . . . 125
  9.1.3 Regarding material parameters . . . 125
  9.1.4 Regarding the model and power-law flow-rules . . . 125
9.2 Outlook . . . 126

Bibliography 129

Nomenclature

Abbreviations

APB	Anti-phase boundary	BC	Boundary condition
BCC	Body centered cubic	CP	Crystal plasticity
CPFEM	Crystal plasticity finite element method	CRSS	Critical resolved shear stress
DBC	Displacement boundary condition	FCC	Face centered cubic
FFT	Fast Fourier transform	GND	Geometrically necessary dislocation
HT	High-temperature	HCP	Hexagonal closed pack
LH	Latent hardening	LPS	Long-period superstructure
LPSO	Long-period stacking ordered	LPT	Low pressure turbine
LRIS	Long-range internal stress	LRO	Long-range ordering
OR	Orientation relationship	PBC	Periodic boundary condition
PST	Polysynthetically twinned	RVE	Representative volume element
SFE	Stacking fault energy	SSD	Statistically stored dislocation
SRO	Short-range ordering	SSRVE	Statistically similar RVE
TBC	Traction boundary condition	TCA	Tension-compression asymmetry
TiAl	Titanium Aluminide	UMAT	User material (subroutine)
WQ	Water quenched	YSA	Yield stress anomaly

Symbols

γ, α	Phases of TiAl alloys	r, h	Al-rich Phases of TiAl
d	Scale of heterogeneity	l	Scale of a RVE
$\mathbf{u}$	Displacement vector	$\mathbf{u}^{+}$, $\mathbf{u}^{-}$	Displacements of opposite nodes
$\mathbf{t}^{+}$, $\mathbf{t}^{-}$	Traction vectors of opposite nodes	$\partial\Omega$	Boundary of RVE
$\boldsymbol{F}$	Deformation gradient	$\boldsymbol{F}^{*}$	Elastic part of $\boldsymbol{F}$
$\boldsymbol{F}^{p}$	Plastic part of $\boldsymbol{F}$	$\boldsymbol{L}$	Velocity gradient
$\dot{\gamma}^{\alpha}$	Slip rate along the slip system α	α, β	Specific slip system
$\mathbf{s}^{\alpha}$	Direction of α-th slip system	$\mathbf{m}^{\alpha}$	Plane of α-th slip system
N	Total number of slip systems	$\boldsymbol{\mathcal{L}}$	Fourth order elasticity tensor
t	time	$\boldsymbol{\epsilon}$	Logarithmic Hencky strain tensor
$\boldsymbol{D}$	Symmetric part of $\boldsymbol{L}$	$\boldsymbol{W}$	Anti-symmetric part of $\boldsymbol{L}$
$\boldsymbol{D}^{*}$	Elastic part of $\boldsymbol{D}$	$\boldsymbol{D}^{p}$	Plastic part of $\boldsymbol{D}$
$\boldsymbol{W}^{*}$	Elastic part of $\boldsymbol{W}$	$\boldsymbol{W}^{p}$	Plastic part of $\boldsymbol{W}$
$\boldsymbol{\sigma}$	Cauchy stress	$\boldsymbol{\tau}$	Kirchoff stress

$\overset{\nabla *}{\boldsymbol{\sigma}}, \overset{\nabla}{\boldsymbol{\sigma}}$	Jaumann rate of the Cauchy stress	$\overset{\nabla *}{\boldsymbol{\tau}}, \overset{\nabla}{\boldsymbol{\tau}}$	Jaumann rate of the Kirchoff stress
τ^α	Resolved shear stress on the slip system α	J	jacobian
$\boldsymbol{\mu}^\alpha$	Symmetric part of the tensor $(\mathbf{s}^\alpha \otimes \mathbf{m}^\alpha)$	$\boldsymbol{\omega}^\alpha$	Anti-symmetric part of the tensor $(\mathbf{s}^\alpha \otimes \mathbf{m}^\alpha)$
X^α	Internal stress on the slip system α	g^α	Slip system strength along α
R^α	Internal resistance along α-th slip system	${R_0}^\alpha$	Initial CRSS of α-the slip system
K	Drag stress	n	Rate sensitivity parameter
$\mathbf{H}^{\alpha\beta}$	Hardening interaction matrix	$\dot{\gamma}_0$	Slip rate at the beginning
h_0	Hardening rate at the beginning	h_s	Hardening rate at the saturation point
τ_0	Shear stress at the beginning	τ_0	Shear stress at the saturation point
γ_t	cumulative shear strain of all slip systems	p	Latent hardening ratio
ν^α	cumulative shear strain of the slip system α	C	Internal stress estimate at a fixed temperature
b, Q, r	Isotropic hardening related model parameters	d, ϕ, δ	Kinematic hardening related parameters

Chapter 1

Introduction and background

1.1 The increasing demand for high-temperature materials

Since the beginning of the last century, the quest for high-temperature materials has been maintained a sharp rising trend driven by ever-increasing demands from different sophisticated and extreme engineering applications. Aero-engine components, leading edges-tips/nose-tips of the hypersonic vehicles and weapons as well as their propulsion system components are a few of such applications. With the constraint of cost and time, more effective alloy development, modeling and prediction of their thermo-mechanical responses etc. in extreme conditions (e.g. high stress, high speed and temperature) have become a high priority. So the development of an appropriate constitutive model for accurately simulating material responses, not only in the elastic range but also inelastic, is of particular importance. In order to achieve more realistic predictions of structural behaviors, an understanding of the elastic and thermal properties is often not sufficient. More precisely the consideration of plasticity, viscoplasticity or damage is often required [1]. Long term material behaviors such as creep analysis, thermo-mechanical fatigue life prediction etc. are also inevitable in the design of high-temperature materials. These are inherently related to the analysis of plasticity for any material. That is why the study of the inelastic stress-strain analysis under various loading conditions is inescapable for more accurate results. Metal forming is a good example of industrial applications where high plastic deformation potential with reasonable strength is expected [2].

Many high-temperature engineering-materials exhibit relaxation or creep behavior that can be regarded as rate-depended. This rate-dependency is correlated to the viscoplasticity of the material. In the study of viscoplasticity, creep can be considered as a special case of viscoplasticity without elastic domain. Most high-temperature materials are either single or polycrystalline in nature. They exhibit different material properties and often preferred directions are found [1]. This means that the instantaneous and time-dependent deformation of crystalline aggregates depends on the direction of the mechanical loads and geometrical constraints imposed. In practice, all crystalline materials are mechanically anisotropic, and many single crystals also reveal macroscopic anisotropy. This anisotropy consequently leads to the associated mechanical phenomena such as shape change, crystallographic texture, strength, strain hardening, deformation-induced surface-roughening and damage etc. that are also orientation dependent [3]. This loading-direction sensitivity or anisotropy originates from various sources. Some of them are the anisotropy of the elastic tensor, crystallographic texture due to the rotation of grains into preferred orientations, morphological pattern, and the orientation dependence of the activation of the crystallographic deformation mechanisms (e.g. dislocations, twins, martensitic transformations etc.) [3,4].

Most materials appear homogeneous from the structural point of view, observations however at other length-scales show a different picture. The underlying microstructure is usually a geometrically complex aggregate containing a variety of different heterogeneous micro-constituents [1]. It is well-known that the macroscopic behavior of a polycrystalline material is influenced by the size and morphology of the grains, the volume fraction of different phases, and subgrain processes [5]. Anisotropy and inhomogeneity are two inherent characteristics of most polycrystalline solids. So an understanding of the local mechanisms and the effects of microstructural changes can help to improve the quality of an alloy. For a comprehensive understanding of these characteristics, it is necessary to study systematically the material properties at least at three different length-scales: (i) the properties of the slip system at the microscale; (ii) the properties of the single crystal at the crystalline scale; and (iii) the overall properties of the polycrystals at the macroscale [6].

The family of high-temperature materials contains a few thousands of different materials. Among them, many a time intermetallic compounds are preferred for different elevated temperature conditions due to their superior properties. The improved weight to strength ratio of an alloy is often the driving factor for intermetallic group of materials [1]. The intermetallic materials often have high melting points, partly due to the strong bonding between unlike atoms, which is, in general, a mixture between metallic, ionic and covalent bonds to different extents. The presence of these strong bonds also results in high creep resistance. Another factor that contributes to the superior strength of intermetallics at elevated temperature is the high degree of long-range orders, consisting of large number of atoms per unit cell that drives slow diffusivity. The strong atomic bonds as well as the long-range order give rise to high Peierls stresses. On the other hand, one of the major disadvantages of these materials is brittleness which disturbingly limits their industrial application. Their viscoplastic/creep behaviors are more complicated than that of pure metals and disordered solid solution alloys due to their complex structures together with the varieties of chemical composition [7].

1.2 Defects, dislocations in solids

1.2.1 Preliminary remarks

Almost all real crystals contain defects, which means, deviations from the ideal crystal structure. Some of the well known defects are dislocations, disclinations, vacancies, misorientations, stacking faults etc. There are translational defects (e.g. dislocations), rotational defects (e.g. disclinations), and dilatational point-defects (e.g. lattice vacancies or interstitial atoms) [8]. Depending on the geometry, major crystal defects can be four types: point, line, surface, and volume defects. A defect concentrated about a single lattice point and involving only a few atoms is called a point defect; if it extends along a row of many atoms, it is called a line defect; and if it covers a whole plane of atoms, it is a planar defect [9]. Point defects represent vacancies and interstitial atoms. Line defects e.g. dislocations and disclinations, correspond to certain imperfections in the structure of a real crystal. Surface defects include grain boundaries, twins, internal phase boundaries, stacking faults etc. Voids and cavities are volume defects [10]. They can be either mobile or immobile in nature. Among them, the most important defect for inelastic deformation is the presence of dislocations, their motion, interaction, rearrangement, generation and annihilation. In crystalline materials, ideally, a dislocation is a line defect which represents permanent deviations of atoms from their original crystallographic periodicity [11]. In fact, dislocations are more complex geometric objects than that of merely a line; they appear in curves or loops and they are sources of significant stress field [12]. Linear dislocations reveal themselves indirectly through the electron microscope as edge and screw type. Many dislocations found in crystalline materials are probably neither pure edge or pure screw but mixed [13]. In micrographs of dislocation-structures, one can recognize individual dislocations and dislocation clusters. In order to understand their collective appearances, dislocation-cluster and dislocation-network type models are often used. Dislocation clusters are basically two types: (a) dipolar clusters, and (b) polar clusters. They differ in their origin, the dislocation arrangement and their role in the plastic deformation process [14]. The dipolar cluster of dislocations contains mostly dipole loops of dislocations, and multipoles. Their common characteristic feature is close-to-zero total Burgers vector. In other words, in a dipolar cluster the densities of + and - dislocations are nearly the same. Dipoles are partly annihilated and transformed by various mechanisms that are basic building elements of dislocation dipolar loops, arrays, etc. During observation, the short thicker objects of dislocations are often appeared in the form of dipolar loops, while the glide dislocations are thin lines. Pile-ups of opposite signs on parallel glide planes convert into dipolar arrays through simple glide and thus cannot persist beyond the initial part of the stress-strain curve [12]. Due to stress increase, dipoles tend to dissociate, and dislocations tend to re-mobilize when stress is reversed. It is also observed that dislocations tend to form clusters with regions of high density and regions of low density [14]. The voluminous dipolar loop clusters are known with different terms like tangles, braids, veins, dislocation patches and they serve storage facilities for leftovers of some other bunch of dislocations; what is realized in the initial stage of deformation. In the subsequent stages, the voluminous clusters rearrange itself into a flat arrangements called walls or incidental boundaries, which is served as annihilation centers for the leftovers and often as sources of fresh glide dislocations. Thus cell like structures are created inside a grain. The most commonly encountered type of heterogeneous dislocation distribution is the 3D cell structure this is usually developed under the condition of multiple slip. In dislocation cell structures, the overwhelming majority of dislocations are actually located in the dislocation cell walls which are frequently also referred to as sub-cell boundaries [15]. The density of clusters and their size increase with proceeding deformation. On the other hand, the polar clusters, mostly in a form of planar arrays, contain excess dislocations of one sign and form a network of boundaries between misoriented regions of the crystal lattice, they are called subgrain boundaries, misoriented cell boundaries etc. [14]. Often dislocations form a randomly distributed 3D network of dislocations where the detailed form of this network depends on both the internal (e.g. stacking fault energy) and external factors like applied mechanical and thermal loading. If the temperature of a creep test is high enough, this dislocation structure can rearrange gradually to form a cell structure or a subgrain structure. Both processes allow the material to minimize the overall energy by forming low energy boundaries [16].

1.2.2 SSD vs. GND

If one phase or precipitate deforms less than the other, or not at all, gradients of deformation form with a wavelength equal to the spacing between the phases or particles. Such alloys are plastically non-homogeneous, because the microstructure imposes gradients of plastic deformation. Dislocations are stored in them to accommodate the deformation gradients, and so allow compatible deformation of the two phases. Indeed, the resulting deformation incompatibility between hard and soft phases (e.g. inclusion and matrix) is accommodated by the development of so called geometrically-necessary dislocations (GND). We call them GND to distinguish them from the statistically-stored dislocations (SSD), which accumulate in pure crystals during straining and are responsible for the normal 3-stage hardening [17]. In addition to precipitates/phase boundaries, a large concentration of GNDs appear and pile up near the grain boundaries where the lattice mismatch is most pronounced [8].

There is a kind of energetic threshold for the dislocation nucleation. If the shear strain exceeds this threshold, the presence of the second type of dislocations is originated and stored due to the locally heterogeneous plastic shear strain. In other words, the heterogeneous deformation within a crystal, typically occurring between the crystal core and the grain boundaries, initiates the generation (either through nucleation or dislocation motion) of GND to maintain lattice compatibility [18]. In addition to preserving lattice compatibility, they give rise to inhomogeneous deformation (and, thus, stress) fields. The emergence of GNDs do not contribute to the plastic strain, but they are necessary to support the plastic part of the deformation as they form an (additional) obstacle to further dislocation flow. Their behaviors as obstacles to the motion of other SSDs facilitate the local inhomogeneous/incompatible deformation [19] and contribute to the length-scale-dependent system and additional work hardening of the material. As plastic deformation proceeds, dislocations multiply and eventually get stuck, which creates extra hurdles on mobile dislocations. As a result, their movement becomes progressively more difficult, and an ever higher applied stress is necessary to produce additional plastic deformation. This is the phenomenon of work-hardening [9]. Thus GNDs cause the slip resistance near the grain boundaries to increase [18], and influence the local hardening [2]. Increasing material hardening with decreasing (grain) size is experimentally observed for a large class of materials, which is commonly associated with the development of GNDs. Being particularly associated with interfaces and boundaries, GND accumulation leads to additional energy storage and kinematic-like hardening effects which exhibit a dependence on the size of the microstructure relative to the sample [5].

So two types of dislocations during the plastic deformation are available, SSD and GND. Statistically stored dislocations accumulate by a random trapping process. The SSD are assumed earlier to be responsible for isotropic hardening. These GNDs can be further divided into dislocations responsible for a macroscopically stress free curvature of the crystal lattice, and dislocations responsible for macroscopic residual stresses, both after the removal of external loads. Thus, GNDs obviously have to be taken into account when modeling of plasticity [8]. When the density of GNDs exceeds the SSD-density, the former one controls the stress-strain curve. They contribute to the hardening in two ways. First, geometrically necessary arrays in general have a long-range stress field, with wavelength equal to the particle spacing associated with them. There is evidence that this long-range stress field controls the hardening during the first 1 or 2% strain, but thereafter remains more or less constant. The rest of the stress-strain curve is then controlled by short-range interactions between moving dislocations, and the steadily increasing density of GNDs [17, 20].

1.2.3 Deformation modes and dislocation mechanics

In plastically deformed engineering materials, an enormous number of dislocations move in a collective fashion. They do not just travel carrying plastic deformation during their short active life, but they can also stop, interact, rearrange, multiply or generate, annihilate and tangle together. There are a number of distinguishable ways in which a polycrystal can be deformed and yet remain crystalline. Apart from the dislocation processes (motions and interactions like glide, climb, their combination, cross-slip, jogs etc.), twinning, diffusion, grain boundary sliding are also well-known. Unlike the others, twinning can supply only a limited amount of deformation [21]. The dislocation motion is controlled by several types of forces. Many of them are not well understood till today. Uncertainty in the understanding of controlling dislocation forces and dislocation arrangements make any reliable estimate of the critical value of the resolved shear stress (yield stress) and its change during deformation difficult [14]. Complexity of forces acting on dislocations and spontaneous arrangement of dislocations into patterns/ structures etc. make the change of the yield stress with plastic deformation a very complex problem.

The most important characteristic and the dominating dislocation process is the glide, which results in plastic slip. Depending on the dislocation structure, dislocation glide can lead to various types of slips: single slip, coplanar double slip, codirectional double slip (along two different planes), dependent coplanar and codirectional slip, multi slip, etc. [14]. In practice, dislocation-glide in these crystals is limited by the presence of obstacles to slip: impurities, solute, other dislocations or precipitates. Point obstacles act as a strengthening mechanism for dislocation glide, but do not always inhibit diffusional flow. Restricting dislocation motion leads to increasing hardness and strength. Strain hardening is just the enhancement in strength (and decrease of ductility). During plastic deformation dislocation density increases, the average distance between adjacent dislocations decreases. Because of dislocation–dislocation repulsive interactions, dislocation mobility becomes more restricted; thus, the metal becomes harder and stronger [22].

In the last decades, apart from the dislocation motions, the complex interactions among dislocations have been recognized as dominating microscopic characteristics, such as morphological, mechanical, and thermodynamic properties of engineering materials [23]. The plastic strain is directly related to the motion of dislocations, and hardening/softening of metals is attributed to the interaction of dislocations with each other and with surrounding crystal microstructure [10]. Depending on the length-scales, interactions can be of various types, e.g. dislocation-dislocations, slip-slip, slip-twin, grain-grain etc. The first type of interactions of dislocations includes cross-slip, climb, jogs, intersection and multiplication of dislocations. Interactions of dislocations are not limited to dislocations and obstacles, moreover there are interactions among dislocations themselves. Dislocation interactions can be broadly divided into short-range and long-ranged type. The interactions with solute atoms are short-ranged [24]. In most cases, short-range and long-range obstacles contribute simultaneously to the flow stress [13]. Some of the most important dislocation interaction features are pile-up, climb, cross-slip, diffusion and jog etc. Besides different boundary obstacles to dislocation flow, solute atom atmospheres can restrict the dislocation movement, resulting in the starvation of mobile dislocations, requiring thereby additional stress in order to unlock arrested dislocations. As a consequence of the repeated pinning and unpinning of mobile dislocations due to the presence of solute atoms, serrated flow often takes place [25].

Many metallic systems nowadays operate in a regime where evolving mechanical properties are not simply dependent on dislocation glide mechanisms. There are climb-assisted deformations and creep as well, which are known to contribute significantly at high-temperature in pure metals, solid solution

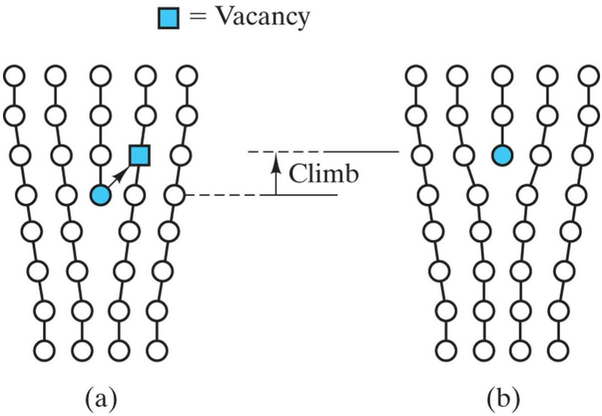

Figure 1.1: Mechanism of dislocation climb. [Courtesy: www.d.umn.edu]

and multi-phase alloys. Climb is an alternative and important mechanism of dislocation motion and hence deformation, fundamentally different from glide, which allows an edge dislocation to move out of its slip plane, or to move perpendicular to its slip plane. It is a diffusion-controlled (thermal activated) process and occurs more readily at elevated temperature where dislocations will more easily be able to move around the obstacles. Many hardened materials, for this reason, become exponentially weaker at higher temperatures. Generally climb reduces the plastic incompatibility between two phases (for two and multiphase alloys), which is certainly beneficial for the materials plasticity. So two constituents can deform more easily at elevated temperature. Macroscopically, it does not significantly contribute to the deformation, but an important mechanism in the recovery. This mechanism is non-conservative as it requires the diffusion of point defects through the crystal lattice. For dislocation climb to occur, vacancies have to be able to move through the crystal (Fig. 1.1). When a vacancy arrives at the site of dislocation arrest, it can cause the climb of dislocation out of its glide plane, after that the point defect is no longer in its way. Dislocation climb is therefore dependent from the velocity of vacancy diffusion. Depending on the creation or absorption of a vacancy, climb can be positive or negative. Climb occurs much more rapidly at high homologous temperatures, where the rate of self-diffusion is appreciable. The main role of climb is to provide a mechanism for dislocations to bypass microstructural barriers by changing slip planes, or to annihilation with a screw dislocation of opposite sign on a neighboring slip plane [26]. In other words, significant amounts of climb only occur at temperatures above a third of the melting temperature than at low temperatures owing to an increase in vacancy density and motion [4]. Up to now, climb has been considered as a recovery mechanism rather than as a plasticity mechanism [27]. However, there are few cases where climb has been shown to be the principal mode of plastic deformation. When a screw dislocation motion is disturbed by an obstacle, the slip temporary occurs on a cross-slip plane so that the dislocation avoids the precipitate [28]. So cross-slip is a change in the slip system of a dislocation. Glide of dislocations occurs along the slip planes whereas climb of edge dislocation is orthogonal to glide plane. Diffusion of vacancies alone can cause a deformation without any dislocations being involved, a process known as diffusion creep. In this process, grain boundaries are sources and sinks of vacancies [29]. At some temperatures usually below the homologous temperature of 0.7, the contribution of grain boundary diffusion is larger than that of self-diffusion through the grains. Thus diffusion of vacancies along grain boundaries can control the creep [30]. Climb and cross-slip permit dislocations to change slip planes and so promote annihilation of mutually attracting dislocations. The prevailing point of view is that cross-slip is a thermally controlled phenomenon manifesting a strong interaction with the lattice. Cross slip hardens the crystal by increasing the forest density [27]. Generally, dislocation annihilation can only happen if they meet exactly on the same slip plane [29]. This process can be thermally activated or athermal. The screw dipoles can be removed by cross-slip and the edge dipoles by climb [27]. The recovery mechanisms of climb and annihilation can slowly change the tangles into neat arrays and the rough cells into sub grains.

The atoms or vacancies that are required for climb are most easily added at kink-like features perpendicular to the glide plane that are called jogs. The basic sources of jogs can be two types. The first source type is the addition of atoms or vacancies to the dislocation line. A single atom or vacancy added to an edge dislocation effectively creates a pair of jogs. The second one is the intersection of dislocations. Often the climb of the jog segment is required. For these reasons jogs are almost always impediments to dislocation glide and they are often sessile segments that lock the dislocation locally [26]. Jogs are often very immobile compared to kinks, and require diffusion of crystallographic defects like vacancies or interstitial atoms to climb. They are not capable of glide along glide planes because the direction of motion is not on the plane itself, rather in the plane's normal direction. Climb proceeds by the nucleation and motion of jogs. Climb of short sections of dislocation lines result in the formation of jogs. They are steps (out of the slip plane) on a dislocation that move it from one atomic plane to another. At temperature where climb cannot occur the movement of screw dislocation is impeded by jogs [13].

Dislocations rearrangement and substructure formation are two important characteristics of collective dislocation behavior. The spatial distribution of dislocations evolves neither isotropically nor uniformly, rather they move along specific slip planes in preferred slip directions. They demonstrate an ability to organize and reorganize themselves in an ordered structures [31]. To a large extent, they are annihilated by mutual interactions leaving dislocation leftovers. Only few can escape to the surface, this characteristics is known by the term of surface relief. The leftovers are swept into high density regions mostly in a form of dislocation loops. This unique dislocation pattern represents a special case of so called dislocation substructure [14]. The key ingredient of dislocation substructure is spontaneous formation of dislocation arrangement. The substructures control plastic, creep, fatigue and fracture properties of ductile materials and depend on the chemical composition of the material, its processing, the thermal treatment and temperature-loading conditions [14].

One of the recent experimental-observation based dislocation-phenomena is dislocation source-burst or avalanche. Due to the external loading, a thermodynamic driving force is created which is probably the reason for the high generation of dislocations by the bursts of activated dislocation sources. This process results in an overproduction of dislocations. Only a small fraction of them is needed to carry plastic deformation, the rest are stored in the crystal [14, 32]. With rapid collective rearrangements of dislocations, it is found that they generate a slowly evolving configuration landscape. Comparatively a small fraction of the dislocations are involved in these rearrangements leading to an intermittent behavior of the net plastic response. This basic dynamic picture appears to be a generic feature in the deformation of many materials [33].

1.2.4 Macroscopic effects of microscopic collective behaviors of dislocations

It is widely accepted that dislocation is the most important microscopic carrier of plasticity [11]. Macroscopic plastic flow of metals is mainly due to the movement of mobile dislocations that move to accommodate the imposed macroscopic strain and interact with other dislocations and obstacles on their way. The macroscopic stress–strain curve is dominated by the competition between the multiplication, storage, rearrangement and annihilation of dislocations at the lower scale [34]. It is to be noted that this macroscopic hardening in crystalline materials results not only from the interaction between dislocations and obstacles, but also from interactions among dislocations themselves. Dislocation intersection mechanism, another kind of interaction, also contribute to the strain hardening process. The intersection of two dislocations produces a sharp break i.e. a few atom spacing in dislocation line. Besides, dislocation tangles and double cross-slip lead to the formation of macroscopic slip bands. Cross-slip involves a complex spatio-temporal developments in microstructure leading to hardening, dislocation pattern formation, and dynamic recovery. Cross slip of dislocations piled-up to obstacles can be a micromechanism of the dynamic recovery of kinematic hardening [35]. In a typical hot-working deformation at a given temperature and strain rate the collective dislocations glide, climb, multiply and combine into tangles. As a result, a rising amount of stress is required to maintain flow. As the density of the tangled dislocations goes up, the annihilation of the newly generated dislocations becomes more frequent. When the rates of annihilation and generation balance, the flow stress ceases to rise and deformation proceeds at a steady rate [36]. At the onset of plastic deformation more dislocations are generated than annihilated. The number of dislocations becomes higher with the increase of plastic strain, and there are more annihilations as well, until a stationary value of the dislocation density is reached. If we raise the working temperature, edge dislocations change their slip plane by the process of climb increasing the probability of annihilation. Thus dislocation density reduces. Annihilation speed is driven by the internal stress. The high internal stresses in small regions provide a driving force for recovery [37].

In the case of polycrystals, additionally, the presence of grain boundaries (GBs) significantly influence the macroscopic plastic deformation, where dislocations can pile up and also can be transmitted to adjacent grains across the grain boundary. This transmission process across GBs is influenced by both the orientation of the GBs and the orientation of the slip systems. It is clear that macroscopic strain hardening is influenced not only by trapping of mobile dislocations but also by other types of interactions e.g. the formation of jogs, locks, and different junctions, that lead to the increasing of the dislocation density. Some junctions start to form when the secondary slips are activated, which leads to the increase of effective stress [24]. In the absence of sufficient slip systems, phenomena like grain boundary sliding, cracking, or fracture etc. may occur to accommodate the deformation [38]. In addition to the dislocation and the diffusional creep, the grain boundary sliding is the important mechanism for poly-crystalline materials because of being weaker than the ordered crystalline structure. Furthermore, the formation of voids and micro-cracks on grain boundaries contributes to the sliding [39]. Dislocations pile-up at the obstacle or at the grain boundary and dislocation interactions are believed to be two major models for hardening of polycrystalline materials [18]. So far we have discussed that dislocations in the crystal can form loops,

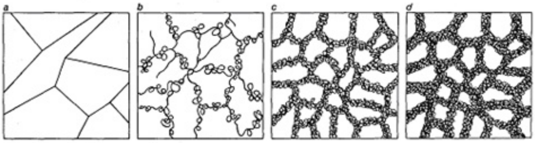

Figure 1.2: Substructure develops with the increasing of strain. (a) Before deformation, dislocations form a simple network. (b) At a light strain large cells are formed. (c) At somewhat more strain the cells reach their smallest size. (d) At further strain and thus further deformation, cell walls become much thicker. (Courtesy: [36])

can pile up on the grain boundaries and precipitate particles, and arrange themselves in various types of cells or substructures called dislocation networks or low energy dislocation structures, Fig. 1.2. These arrangements act as obstacles to the motion of other dislocations, thus providing an important mechanism of hardening. The point, surface and volume defects interact with dislocations and also play important role in hardening mechanisms [10]. All micromechanisms discussed so far including glide-plus-climb result in either hardening or recovery, so they can be related to the macroscopic recovery-hardening hypothesis. During the whole stages of deformation history, sometimes one is dominating over the remaining one, sometimes they are balanced by each other.

1.3 High-temperature deformation mechanisms

1.3.1 Recovery and recrystallisation

Some additional mechanisms are observed at higher temperature. When the deformation is done at high-temperature, as it is during the hot deformation or annealing and heat treatment, dislocations density is reduced by either of two mechanisms, recovery and recrystallization. Work hardening is counterbalanced by these two mechanisms of recrystallization and recovery. An understanding of the hot-working i.e. high strain-rates and high-temperatures, requires an appreciation of both dynamic recovery and recrystallization processes [7].

During the time of annealing, the temperature is generally high enough to permit climb, migrate and interact, both with one another and with free surfaces [26]. At high-temperature, some of the dislocations are annihilated; rest are gathered/rearranged into stable, an energetically more favorable planar configurations, such as low-angle grain boundaries (called subgrain boundaries), to reduce stored energy [12, 29, 40]. This process is knows as recovery. It entails a gradual decrease in the number of dislocations and a rearrangement of the remaining ones into orderly arrays. The dynamically recovered structure is quite stable [30]. The recovery is an important restoration/repair mechanism against work hardening, that is thermally activated process and inescapable at high-temperature. The most believed mechanism of recovery is the mutual dislocation annihilation in planar-glide which is thermally activated and facilitated by climb stresses and is the coarsening of the cell structure. Recovery can take place by climb for edges or cross-slip for screws. The screw dipoles can be removed by cross-slip and the edge dipoles by climb. During recovery, the dislocations rearrange themselves into configurations of lower energy and form low angle boundaries [41]. The stored internal strain energy is relieved during recovery by the virtue of dislocation motion (in the absence of an externally applied stress), as a result of enhanced atomic diffusion at the elevated temperature. Thus dislocation density decreases and dislocations assume low-energy configurations [22]. The boundaries are very resistant to recovery processes [27]. Since recovery decreases the dislocation density, the work hardening rate decreases with the stress [26]. In a dislocation network model, creep strain occurs when a dislocation link breaks away from the network and glides on an active slip system, before eventually being absorbed or arrested by other dislocations in the network. In recovery, longer links grow at the expense of smaller ones in a process akin to grain growth. The dislocation network coarsens through dislocation climb [7]. It has been suggested that smaller dislocation networks are unstable and grow rapidly by diffusion at high-temperatures under the action of their line tension [16].

Recovery can be either static or dynamic type. Generally the recovery that occurs after processing at high-temperature is termed static. It is controlled by solute drag and by dislocation annihilation. During static recovery, (1) dislocations migrate, annihilate and form more stable configurations, and (2) solute atoms preferably diffuse into dense dislocation substructures to relax their strong interactions with dislocations (that were mobile during deformation) [40]. Processes of dynamic recovery, caused mainly by large-scale cross-slip and climb of groups of dislocations, lead to a continuous decrease of the work hardening rate [27]. The term dynamic recovery is characterized by a decreasing hardening rate, strongly dependent on temperature and strain rate, generally used for stage III processes. Dynamic recovery also results in the re-arrangement of dislocations to form high dislocation density regions (e.g., dislocation walls) and low dislocation density regions (e.g., dislocation channels) [40]. These types of structures are mainly due to self-organization or patterning of dislocations with formation of high dislocation density and low dislocation density regions, also regarded as domains of high and low plastic slip accumulation [42]. The collective observations suggest that dynamic recovery is an essential component of the creep process and hence dominating, while static recovery may be of greater importance at higher temperature processing [27].

The recrystallization process is the formation of a new grain structure in a deformed material by the formation and migration of grain boundaries driven by the stored energy of deformation [43]. Recrystallization during deformation (dynamic recrystallization) is often observed at relatively high strain rates. So, a complete discussion of elevated temperature creep and plasticity is expected to include this restoration mechanism. The dynamic recovery is not the exclusive restoration mechanism, since dynamic recrystallization in pure metals (e.g. Al) has been confirmed. This mechanism becomes an additional restoration mechanism that can preclude a constant flow stress (for a constant strain-rate) or a genuine mechanical steady state. The increase in dislocation density causes a portion of the work done to be retained as stored energy of deformation. The stored energy is released during subsequent processes of recovery and recrystallization. During recrystallization, strain-free nuclei with high angle grain boundaries form and grow, leading to further decrease in stored energy [41]. If the dislocation density is high enough, and the material is heated to a temperature above its recrystallization temperature, then new, defect-free grains nucleate and grow at the expense of the old, producing a microstructure that is relatively free of dislocations [26]. At high-temperature, the kinetics of deformation are highly temperature and rate-dependent and the internal structure of a metal evolves, producing strain-hardening, dynamic recovery, and in many instances dynamic recrystallization [44].

1.3.2 Grain coarsening or coarsening-dissolution

During deformation, energy is stored in the material mainly in the form of dislocations. This energy is released by the three main processes, those of recovery, recrystallization, and grain coarsening. Grain coarsening can be defined as processes involving the migration of grain boundaries when the driving force for migration is solely the reduction of the grain boundary area itself. It is the growth of the mean grain size driven by the reduction in grain boundary area [43]. Experimental observations on uniaxially loaded single or polycrystals have shown that dislocations tend to organize themselves in a heterogeneous structure from the very early stages of deformation [7]. It is to be noted that the hardening-recovery based hypothesis can be generalized by hardening-softening, where the components of softening are recovery, recrystallization, grain coarsening, coarsening-dissolution. The phase transformation can also happen at high-temperature which abruptly hardens or softens the material.

1.4 Bridging materials science and mechanics

Hencky in 1932 rightly pointed out that the behavior of metals in the inelastic states cannot be explained by theories which do not assume a microstructure. This statement very succinctly emphasizes the necessity and challenges for modeling the constitutive response of materials by accounting microstructure [45]. The effective mechanical behavior of metals and alloys is influenced by the inherent microstructure and mechanisms therein. Microstructure can be controlled by engineering processes. Different strengthening mechanisms (e.g. work hardening, precipitate, and grain boundary strengthening) can alter the strength of a material in a predictive, quantitative manner and are readily linked to the deformation mechanisms. This quantification strongly depends on the characteristic length-scale of a particular microstructure, for example, grain or precipitate size, volume fraction, twin boundary spacing, or dislocation density. The development of novel material systems with radically superior properties will be achieved through architectural control at the appropriate microstructural scales [46]. To have a better control of the macroscopic properties driven by proper microstructural design, it is necessary to concentrate on the micromechanics of materials. Microstructural mechanics lies at the junction between structural mechanics and material sciences. One of the core objectives of micromechanics is to understand microstructure driven macroscopic properties relationship. By doing so, different length-scale dependent phenomena of heterogeneous materials can be studied, for example, local deformation mechanisms at different scales of heterogeneities, local damage process etc. Despite the fact that there exist many elementary geometrical types of dislocations in crystals (e.g. jogs, loops, dipoles etc), it is possible to establish a fundamental relationship between macroscopic plasticity effects and the properties of dislocations. Like any other physical process, plastic deformation can be best understood by considering and properly analyzing the underlying mechanisms responsible for it [31].

1.5 Homogenization and scale separation

Almost all materials in nature possess some heterogeneities (e.g. heterogeneous microstructure) at certain length-scale [47], for which material behaviors are motivated by more than one length-scale dependent

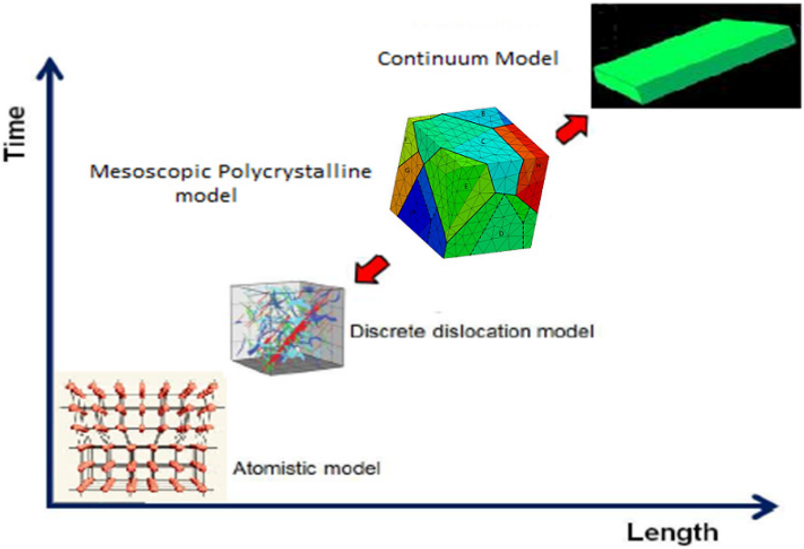

Figure 1.3: Scale dependent different mechanics

phenomena. Plastic deformation is a such type of multiscale phenomenon, where the mechanisms and governing equations at different length-scales e.g. microscale, mesoscale, and macroscale are strongly interrelated with each other [14]. Major practices in different scale dependent mechanics is shown in Fig. 1.3. Plastic deformation and its possible combination with other loading (e.g. thermal, irradiation, etc.) generally induce various types of dislocation microstructure evolution at different length-scales, which eventually result in a spatially heterogeneous deformation field [42]. However, in the literature of continuum micromechanics, the nomenclature with respect to micro or macro is far from a universal definition [48]. Often a specific length-scale can be related to more than one subscale. For example, microscale is generally associated with the scale of heterogeneities of micrometer scale that can be originated from more than one subscale. Thus the grain size of a polycrystalline material can be equally treated as a basic or secondary length-scale [49]. So, in order to include microscale dependent effects in a macroscopic model, a complete scale separation is necessary. In micromechanics, the physical interpretation of the characteristic length of a slip system is the average spacing between the stacked pile-ups of dislocations, which evolves with plastic deformation. The initial characteristic length for a well-annealed crystal can be agreed by the average spacing between the Frank-Read sources. In the later stages, the characteristic length is expected to be the cross-slip distance. The characteristic length has significant effect on hardening. The length of the Burger's vector, the most fundamental quantity characterizing the plastic deformation, is believed to be the intrinsic material length-scale of a crystalline material.

The central aim of continuum micromechanics is the bridging of length-scales. One aspect of this length-scale bridging is studying the structure–property relationships of inhomogeneous materials [48] and estimating the effective macroscopic properties of a heterogeneous material from the response of its underlying micro-structure thereby allowing the substitution of the heterogeneous material with an equivalent homogeneous one. It can also be interpreted as describing the behavior of a material that is inhomogeneous at some lower length-scale but homogeneous reference material at some higher length-scale, which is sometimes referred to as the homogeneous equivalent medium (HEM). The behavior at some larger length-scale is actually estimated or bounded by using information from a smaller length-scale. Usually, starting from a microscopic heterogeneous description of a problem, we seek a macroscopic or effective description. One important goal of the mechanics of heterogeneous materials is to derive their effective properties from the knowledge of suitable constitutive laws and spatial distribution of their components. Homogenization methods have been developed for this purpose. Homogenization is also known as upscaling or coarse-graining. A homogenization method can be termed as the rigorous version of averaging, which extracts effective parameters from disordered or heterogeneous media. Although homogenization has first been developed for periodic structures, it turns out that homogenization can be applied to any kind of disordered media, and is not restricted to the periodic case [50]. Since homogenization links the phase arrangement at the microscale to the macroscopic behavior, it provides microstructure–property relationships. These methods provide an effective way to model the mechanical behavior of heterogeneous materials [45]. In a first order homogenization, variables at the smaller length-scale influence the behavior at the larger length-scale only via their volume averages. On the other hand, gradient of the fields at the larger length-scale are not significant at the smaller length-scale, where these fields are considered to be locally constant and can be described in terms of uniform fields [48]. On the other hand, in contrast to homogenization, the local responses at the smaller length-scale can be deduced from the loading conditions and histories on the larger length-scale. This approach can be termed as 'zooming in' on the local fields in an inhomogeneous material [48]. The inverse description of homogenization estimating microscopic behavior, starting from the knowledge of macroscopic quantities is called localization, also referred as down-scaling or fine graining.

1.5.1 Homogenization types

Mathematical theory of homogeneous can be of various types , e.g. stochastic theory of homogenization, variational theory of homogenization etc. [50]. In micromechanics, homogenization techniques are commonly classified into two general categories of analytical homogenization and computational homogenization [47]. Although analytical homogenization methods give useful information and are computationally favorable, it is generally not suitable for complex geometries where the shape, size, distribution pattern and volume fraction of the inclusions greatly influence the final characteristic of the materials and the physically non-linear phenomena like plasticity or creep. Computational homogenization is one of these powerful approaches that has been established in the past two decades, even till now it is used systematically for the assessment of structure–property relations [51]. A common example of structure–property relations is to evaluate the stress-strain relationship at each quadrature point of the macro-scale through solving the associated boundary value problem at the microscale [47]. The quality of the solution obtained through a computational homogenization method especially for nonlinear behavior of a material entirely depends on the well-characterization of the microstructure e.g. on the quality of the description of materials, phases and interfaces at the microscale. The scale transitions are commonly complemented by two averaging equations: (1) volume averaging of quantities like deformation or stress;

(2) the Hill-Mandel macro-homogeneity condition, which essentially reflects volume averaging of the virtual work [52]. For macro-homogeneity, the conditions can be written for small strain case as follows:

$$<\boldsymbol{\sigma}:\dot{\boldsymbol{\epsilon}}> = <\boldsymbol{\sigma}> : <\dot{\boldsymbol{\epsilon}}> \tag{1.1}$$

$$<\boldsymbol{\sigma}> = \frac{1}{V}\int_V \boldsymbol{\sigma}(x)dV \tag{1.2}$$

$$<\boldsymbol{\epsilon}> = \frac{1}{V}\int_V \boldsymbol{\epsilon}(x)dV \tag{1.3}$$

Where $<\boldsymbol{\sigma}>$ and $<\boldsymbol{\epsilon}>$ are averaged or effective stress and strain fields, whereas $\boldsymbol{\sigma}$ and $\boldsymbol{\epsilon}$ stand for micro-stress and strain fields. If there is more than one phase, then Eqs. (1.2) and (1.3) can be written as:

$$<\boldsymbol{\sigma}> = \sum_p f^p <\boldsymbol{\sigma}>^p \tag{1.4}$$

$$<\boldsymbol{\epsilon}> = \sum_p f^p <\boldsymbol{\epsilon}>^p \tag{1.5}$$

where

$$<\boldsymbol{\sigma}>^p = \frac{1}{V^p}\int_{V^p} \boldsymbol{\sigma}(x)dV^p \tag{1.6}$$

$$<\boldsymbol{\epsilon}>^p = \frac{1}{V^p}\int_{V^p} \boldsymbol{\epsilon}(x)dV^p \tag{1.7}$$

Here f^p stands for volume fraction and the superscript p is to indicate corresponding phase. When micro-stress and strain fields are separated into a mean and a fluctuating part, i.e.

$$\boldsymbol{\sigma}(x) = <\boldsymbol{\sigma}> + \tilde{\boldsymbol{\sigma}}(x) \tag{1.8}$$

$$\boldsymbol{\epsilon}(x) = <\boldsymbol{\epsilon}> + \tilde{\boldsymbol{\epsilon}}(x) \tag{1.9}$$

the Hill condition implies

$$<\tilde{\boldsymbol{\sigma}}(x) \cdot \tilde{\boldsymbol{\epsilon}}(x)> = 0 \tag{1.10}$$

Two main classes exist in computational homogenization, they are mean-field and full-field homogenization approaches. The first one considers the microstructure of a material from statistical information and only average information about the fields can be determined. In such mean-field approaches the microstructure can be considered as a system of an inclusion that is embedded in a matrix [53]. The most important representatives of mean-field approach are effective field and effective medium approximations [48]. Unlike full-field approaches, only partial information about the microstructure is needed. This approach was originally proposed for matrix-inclusion based materials. In the model based on inclusion problems, volume fractions of the phases and statistical information on the distribution are required. The mean-field approach usually gives a coarse estimate for highly heterogeneous materials. To obtain a suitable estimate for nonlinear behaviors, more realistic field distribution is expected [54]. The phase geometry enters these models via statistical descriptions such as volume fractions, phase topology, etc.

In contrast to the mean-field methods, full-field approaches, on the other hand, need a complete or more realistic description of the microstructure and can then provide a more realistic representation of the stress and strain states [54]. Since the microstructure is completely resolved and phase interactions are accounted for, the most accurate and realistic one certainly is the full-field homogenization. With realistic states of stress and strain in each grain, this approach also can takes care of the accompanied gradients, an accurate description of the grain morphology, an improved quantitative description of the texture, and a reasonable representation of the interactions between the considered constituents (i.e., grains, phases, etc.). On the local scale, the full-field method allows us to resolve the heterogeneity of stress and strain within particular grains and across the grains [55]. The main drawback of this approach is the enormous computational effort which is still not compatible with industrial needs even though the computational power is developing rapidly. Considerably less computational resources are needed when applying mean-field approaches [45]. To remedy the high computational challenge in the full-field simulation problems, Fast Fourier Transform (FFT) based methods can be applied, which ensures much less computational times [53].

An alternative set of mean-field approaches for polycrystalline materials is the grain cluster model. They represent an intermediate approach between the mean-field and full-field schemes. They reduce the high computational cost of the latter by restricting the degrees of freedom to a small number of regions with (typically) homogeneous strain inside each region. Those areas can be grains or phases, thus extending the mean-field approaches by taking into account direct neighbor–neighbor interactions among the constituents of a polycrystalline and potentially also multiphase aggregate [53].

1.5.2 Common mean-field approaches

Multi-scale originated plastic deformation may lead to bulk deformation behavior of metals that is substantially different from that predicted by simple forms of polycrystal plasticity [56]. Based on the assumptions of local interactions between the constituent grains, comparatively simpler models can be separated [57]. Sachs and Taylor models, although simpler in nature neglecting local interactions, pioneered the development of polycrystal plasticity by proposing two simple approaches. The Sachs model, which is known as the lower bound model, assumes that each grain in the polycrystalline aggregate is under a uniform stress, equal to the macroscopic stress. The Taylor model, on the other hand, known as the upper bound model, assumes that all grains must accommodate the same plastic strain, equal to the macroscopically imposed strain. Taylor model of polycrystal deformation presupposes that, in the case of plasticity, the upper bound is much closer to the true solution than the lower bound [58]. In these models, the actual heterogeneities that occur during deformation within a grain are neglected. It is well known that the Taylor assumption is reasonable for materials that exhibit a mildly anisotropic plastic response that is, comprised of crystals with many slip systems of comparable strength. However, using Taylor model in other situations usually leads to prediction of excessively high stresses, incorrect texture evolutions, or both [59]. In short, Sachs and Taylor-type models neglect either stress or strain variations from grain to grain, respectively, in the polycrystalline aggregate. Another popular homogenizing method is the self-consistent approach, originally proposed by Kröner in 1958. The self-consistent models assume that each grain is an ellipsoidal inclusion embedded in an infinite homogeneous equivalent medium, thus account for grain morphology through the inclusion formalism. Often this model neglects plastic interactions between the inclusion and the surrounding matrix because the matrix is assumed to be elastic. The plastic interactions can also be taken into account in an incremental self-consistent model to simulate polycrystalline deformations. A rough comparison among this three common approaches can be seen in Fig. 1.4.

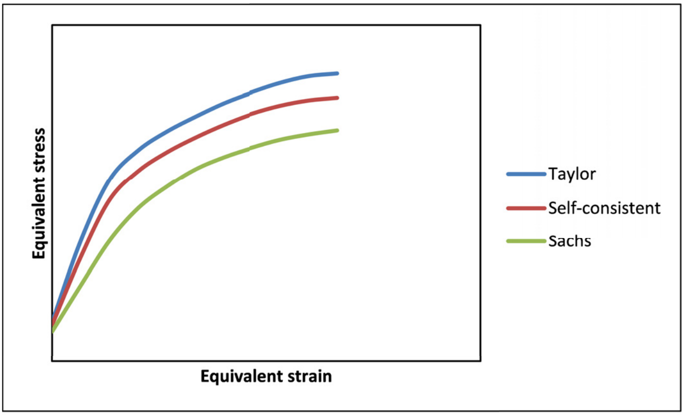

Figure 1.4: A rough comparison of three common mean-field estimates, Taylor vs. Sachs vs. Self-consistent

1.5.3 RVE and ergodicity

As mentioned earlier, when aiming to describe the overall realistic constitutive behavior of heterogeneous materials, it is necessary to not only account for the constitutive behavior of the constituent phases but also for their arrangement and shapes. However, the micro-geometries of real inhomogeneous materials are at least to some extent random and, in the majority of cases of practical relevance, their detailed phase arrangements are highly complex. Due to the enormous efforts of measuring and digitizing real 3-D microstructures, it is required to generate equivalent microstructures reproducing the important microstructural characteristics as accurately as possible [45]. Although modern image processing and mesh generation software nowadays offer increasing capabilities, truly realistic models are difficult to create and to solve [10]. An exact description of the microstructure based on purely experimental characterization is unlikely to be successful. The key idea is to replace the real microstructure by an artificial, geometrically simplified one with similar statistical properties [1]. The notion of representative volume element (RVE) is introduced in this regard as a statistical concept. A RVE should be a random volume element and should contain all possible heterogeneous elements. In fact, a RVE is a random distribution of microheterogeneities; when it applies for periodic structure then it becomes a unit cell. It is usually regarded as a volume of heterogeneous material that is sufficiently large to be statistically representative of the material, i.e., to effectively include a sampling of all microstructural heterogeneities that occur. Totally structured and totally random microheterogeneity can be viewed as extreme cases which provide limit that are useful for practical applications. [60]. Mathematically this means that when examining a microstructure, the local properties are distributed according to a spatially constant probability density. In particular, the same statistical distribution of the properties is found at any position. For statistically homogeneous materials all individual regions contained in a single random realization (of infinite size) of the material are statistically similar. For such materials it is sensible to propose an ergodicity hypothesis [1]. Since exact expressions for micro stress and strain fields cannot be given even with reasonable effort, approximations have to be introduced that are typically based on the ergodic

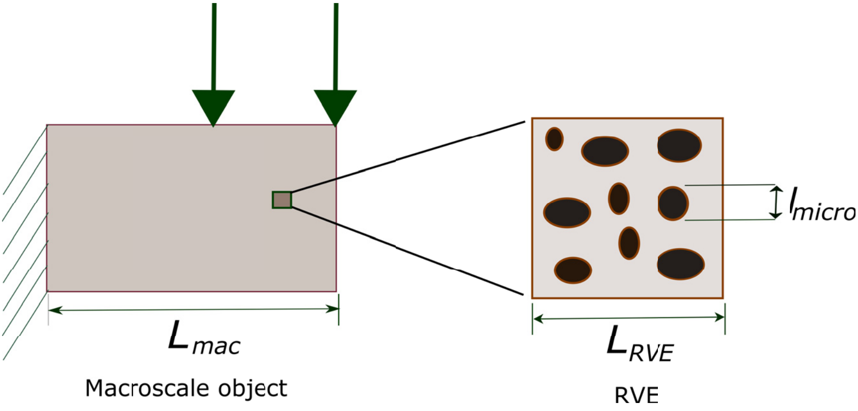

Figure 1.5: Approximate size of an RVE

hypothesis, i.e., the heterogeneous material is assumed to be statistically homogeneous [48]. The ergodicity hypothesis states that averaging a mechanical field at a fixed point over the ensemble is equivalent to averaging the same field over the volume of only one realization among the ensembles, if the volume of the sample is infinitely large [45]. As mentioned earlier, if real microstructures are considered, high computational costs arise from the complex morphology of the microstructure. Statistically similar RVEs (SSRVEs) can be used as an alternative, which are constructed to possess similar statistical properties as the real microstructure but are defined by a lower level of complexity [61]. Then the field variables such as stress and strain are also statistically homogeneous in the similar RVE [62].

The proper choice of a RVE largely determines the accuracy of the modelling of a heterogeneous material. It must however remain small enough to be considered as a volume element of continuum mechanics. If an RVE is extended to all directions then the collective body would be considered as a replacement of the real material. It is to be noted that, the size of a RVE depends on the investigated morphological or physical property. For the same microstructure, the RVE size can differ if different properties are under consideration. Hill first introduced a RVE at each material point of the macroscopic specimen, the size of which at the same time needs to be sufficiently large to be representative for the microstructure of the specimen and sufficiently small compared to the overall size of the specimen. In other words, as shown in Fig. 1.5, conditions on the size of a RVE are:

1. Sufficiently small compared to the typical macroscale dimension of the structural component, $L_{\text{RVE}} \ll L_{\text{mac}}$,

2. Sufficiently large compared to the typical subscale dimension of micro-constituents, e.g. grains, $l_{\text{mic}} \ll L_{\text{RVE}}$. When two above criteria are fulfilled, the mechanical behavior of the RVE is assumed to represent the conditions of the entire specimen. Using such a RVE, the effective macroscopic mechanical fields of stresses and strains are defined as volume averages of the fluctuating micro fields [45], as shown in Eqs. (1.2)-(1.7).

According to Hill, the macroscopic strain energy and the volume average of microscopic strain energy should be equivalent. the central point to the homogenization method is the Hill–Mandel condition that enforces incremental energy equivalence between the microscale and the macro-scale. The boundary conditions of the micro-problem are chosen such that the Hill–Mandel condition is a priori satisfied [47]. Hill-Mandel macrohomogeneity condition or the energy equivalence condition states that the strain energy density of the micro-fields equals the strain energy density of the macro-fields, making the microscopic and macroscopic descriptions energetically equivalent. In other words, the fluctuations of the micro-fields do not contribute to the macroscopic strain energy [48].

1.6 Plasticity modeling

1.6.1 Plasticity types

In general, most inelastic solids are rate-dependent. In spite of that, rate-independent plasticity theories have been developed in the past to represent an idealization of rate-dependent plasticity with limited applicability [60, 63]. If the deformation rate consists of an elastic and an inelastic constituent throughout the entire deformation history, then the theory can be termed as fully rate-dependent plasticity. In these theories there is no yield surface. On the other hand, if a clear yield surface is considered within which the response is elastic and no plastic deformation inside the yield surface; response may be elastic-viscoplastic on the yield surface where the plastic flow is rate-dependent, then the theories can be called rate-dependent viscoplasticity or simply viscoplasticity. Often loading and unloading are considered in a viscoplastic model [60].

1.6.2 Modeling approaches

The plastic response of metals is determined by the collective dynamics of dislocations, rather than by the dynamics of individual dislocations. In general, major underlying mechanisms of macroscopic plastic deformation phenomena (like stress-strain, creep, fatigue, hardening, recovery and many others) are transport, interaction, generation, annihilation, storage, lock formation and rearrangement of dislocations [34, 64]. Macroscopic deformation of crystalline materials can be attributed to the microscale mechanisms of crystals [65]. The dislocation microstructures resulting from such dynamics are intrinsically heterogeneous and highly complex that make the understanding of mechanical properties a puzzling problem. Therefore, the development of effective models for studying the multi-scale originated roots of macroscopic behaviors is a challenge in materials science and engineering. The complexity of deformation response across multi-length and multi-time scales makes the modeling of material behavior challenging. In spite of that, there are various modeling techniques available in the literature based on whether the principle of locality is considered or not. Crystal plasticity (CP) theories has been favored by many researchers since forty years. The understanding of the plasticity of crystals across various length and time scales is important for developing accurate and effective materials models. Some of the generalized higher order plasticity theories are micromorphic, micropolar, gradient based etc.

1.6.3 State variables

It is well-known that the physical processes defining a behavior are too complicated to be represented in terms of actual physical quantities. On the other hand, it is assumed that there is sufficient knowledge of the physical processes in order to understand adequately the main mechanisms controlling the behavior. Therefore some variables (structure parameters) corresponding to the dominant physical procedures and their evolution equations are attempted to be developed, so that the behavior of these variables simulates the behavior of the physical processes under the same conditions [66]. These variables are called state-variables, or internal variables, or hidden variables, as they cannot be directly determined by measuring the stresses and strains, but only indirectly by comparing the stress-response after different deformation processes [67]. In plasticity, most theories are based on the incorporation of internal state variables where plastic deformation depends on the continuously changing internal states. Internal variables of state are mathematical constructs that are considered in conjunction with the second law of thermodynamics [68]. The instantaneous response of a material is determined by its current state which is produced by the entire past history of deformation and it is assumed that the current state is representable by a small number of internal variables with their evolution equations usually with the rate form [44]. To explain some complex deformation features of metal forming (like temperature dependent softening, strain localization and microstructure evolution, etc.), material models are expected to be developed with the microstructural state variables [34]. Based on how state variables evolve, models can be classified into phenomenological and physically based.

1.6.4 Phenomenological vs. physical modeling

In a broader sense, physics-based models address microstructures and associated thermodynamic non-equilibrium mechanisms and processes at different length and time scales. In micromechanics, physically based material models are those where internal variables are directly linked to the physical processes. In other words, these are models where knowledge about the underlying physical process, dislocation processes etc, are used to formulate the constitutive equations [10]. This type of models have been remarkably successful in providing a qualitative understanding of specific materials behavior, but it is often difficult to generalize them for a class of technical materials [9, 16, 66]. Along with major mechanisms, the collected information support the view that the dislocation velocity is affected by various other processes involving lattice friction, jog dragging, impurity interactions, and many others. Quantitative assessment of the respective contribution of such mechanisms is difficult for several reasons. There is rather limited information on the temperature dependence of each individual mechanism and the rules of their superposition [13]. As a result, instead of physically based modeling, often we rely on phenomenological modeling. Phenomenological models can catch the essential phenomena dominating the deformation based on the underlying physics of the deformation coupled to microstructure evolution. These models reach their limits when smaller scales are considered [69] and the grain size effect is not usually reflected by such models. Another limitation of phenomenological models is that they are not fully capable of predicting properties of the material far from the validated experimental data [34]. To improve their predictive power, instead of pure phenomenology, a common tendency of developing more physics based phenomenology is often observed. The combination of physics and phenomenology in modeling is sometimes called physical-phenomenological approach. In this types of models, physical processes are considered somewhat implicitly, constitutive equations are constructed based on the knowledge about the physical process causing the deformation. Although constitutive equations of this type are laid out as phenomenological, they are based to some extent on physical considerations and experimental observation [10].

1.6.5 Classical crystal plasticity

The CP is a powerful approach for micro-mechanical modeling that can be used both at microscopic and macroscopic scales. These techniques are capable of treating a wide range of mechanical problems in materials science and engineering including slip, twinning, grain boundary shear etc. When formulated in conjunction with an appropriate homogenization scheme, the CP finite element method is also suited to predict various macroscopic mechanical behaviors that are necessary for material and process engineering [70]. Although CP has been used for long time as a mean-field approaches, efficient full-field approaches based on CP have also been applied to analyze the actual micromechanical fields that develop inside the grains of polycrystals [71]. Furthermore, the CP with FEM solver, commonly known as CPFEM, can take into account the local interactions between each grain and their neighbors by satisfying the equilibrium and compatibility conditions. It is commonly agreed that the CPFEM provides better predictions compared to the other homogenization models because it accounts for both stress equilibrium and strain compatibility. These theories can also be applied to predict the plastic anisotropy of polycrystalline materials by accounting the fundamental mechanisms of plastic deformation [57]. There is a strong industrial need to develop effective materials models based on CP in order to accurately describe and predict the material behavior, for example metal forming. Good models of this kind can enable fast and high quality productions in material development and production phases, can predict better life, and can asses the materials in services.

Classical crystal plasticity is based on a number of hypotheses. First, in spite of the presence of dislocations and defects, a crystal consists of a regular crystal lattice, which remains existent even under arbitrarily large deformations. Second, distortion of the lattice is effectively elastic, in which the stresses are related to the deformations of the lattice alone. Third, there exist crystallographic slip systems consisting of slip planes and slip directions (Fig. 1.6-1.7), along with the crystal deforms by simple shears and inelastic deformations take place. Forth, slip in a slip system can be activated only, when the shear stress in it reaches a critical value, called critical resolved shear stress. Fifth, the initial critical resolved shear stress can be considered as a material constant, and it changes as a functional of the entire slip history of the crystal. Finally, the elasticity is unaffected by slip and the lattice geometry is unaltered during the shears [72, 73]. One important point about the conventional theory of CP is that they only accounts for effects of the history of crystallographic slip based on SSD, not based on GND [74].

The basic state variable in classical CP is the internal resistance that is related to the material internal microstructure and has been identified as the intrinsic resistance to dislocation motion, thereby the creep/plastic deformation, provided by different obstacles [75]. It is assumed that the material internal state can manifest itself mainly by the change in the material internal resistance. The internal resistance is expressed in terms of the critical resolved shear strength (CRSS) of a slip system in the crystal plasticity framework [76]. This variable is deformation-history-dependent and represented as a function depending on the accumulated slip. Internal resistance originates mainly from three contributions: (i) dislocation to dislocation interaction, which is a function of both dislocation density and arrangement; (ii) dislocation interaction with solute elements; and (iii) dislocation interaction with second phase particles/precipitates [16]. Internal resistance is a reflection of the material internal microstructure that resists plastic deformation. It is due to a friction stress needed to move dislocations through the lattice and to pass short-range obstacles/interactions. Thermal vibrations usually assist the stress to overcome these

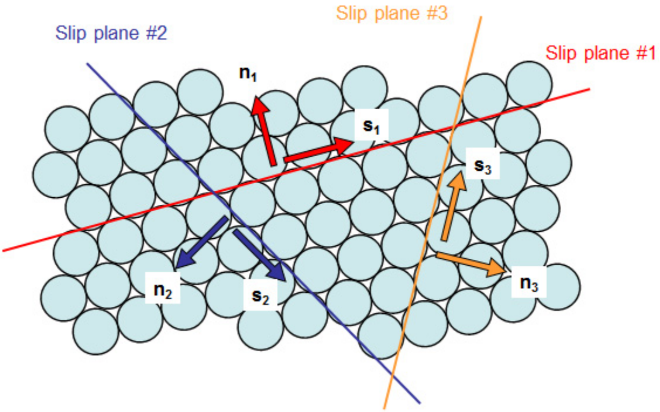

Figure 1.6: Possible slip planes (n) and directions (s) with atomic arrangement, (Courtesy: continuummechanics.org).

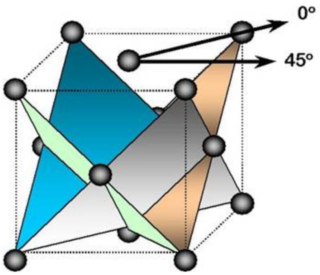

Figure 1.7: Possible slip planes in a face centered cubic type crystals, (Courtesy: clothingbuzz.blogspot.de).

obstacles [10]. The role of climb in this kind of theories has been addressed in a purely phenomenological manner, where the respective internal variable incorporates the contribution of climb. These classical CP models are not capable of capturing macroscopic size-dependent effects and do not contain intrinsic length-scales. Later, extended crystal plasticity theories have been developed in order to overcome this drawback [5].

1.6.6 Dislocation density based CP

Due to some limitations of phenomenological modeling, a number of physically based micromechanical models, i.e. based on dislocation densities and their arrangements, have been developed. This type of physically based constitutive equations are formulated on the concept of internal variables, that describe the material state and its history in terms of microstructural parameters. In the case of plasticity the most relevant microstructural state variable is the dislocation density as the dislocations are the carriers of plastic deformation [3, 4, 53]. Dislocation density based crystal plasticity theories basically fall within two broad categories. The first group relies on the heterogeneous dislocation substructure associated with subgrain boundaries. The second category relies on more uniform dislocation network (not associated with dislocation heterogeneities such as cells or subgrain walls) [7]. The simple model of this kind is based on an one-variable model in term of the average dislocation density. One of the great advantages of this type models is that the number of adjustable parameters is very less [77], though it ignores the heterogeneous nature of the dislocation substructures. Roters et al. [78] proposed a novel three-variable based model to describe the work hardening of metals and alloys. This model primarily takes into account three types of dislocations, i.e. mobile dislocation density, immobile dislocation densities in cell wall and cell interior. It is to be noted that motion of mobile dislocations carries the plastic strain while immobile dislocations contribute to the plastic hardening [10]. A set of evolution laws is derived for each type of dislocations accommodating the generation, annihilation, storage, locks and dipoles formation of dislocations [34]. This model is also extended by dividing each dislocation category into edge and screw dislocation. In some models grain boundary effects are also included by considering (i) GBs are transparent to dislocations, and (ii) interfaces are perfect obstacles that do not allow dislocation penetration events [3]. Even after harnessing of such physical processes, these models cannot reliably explain the size effect. A solution to this difficulty is proposed to introduce additional hardening variables incorporating an intrinsic length-scale. One of the most important such variables is the dislocation density tensor (also called density of geometrically necessary dislocations) [79]. The measure of the net dislocation density is a continuum description of both glide and geometrically-necessary dislocations [80]. In general, the overall hardening is influenced by the superposition of contributions from both SSD and GND [81]. For a full description of the microstructure, more parameters are required like grain size and shape, second phase fractions, and precipitate morphology etc. [3, 4].

1.6.7 Gradient and higher order CP

The inability of earlier models to predict size-dependent effects has motivated the use of higher-order gradient theories to model material behavior at the microscale. The physically motivated strain gradient theories have been based on the introduction of GNDs and their dislocation mechanics [82] and thus render the model size sensitive [83]. Such theories open the door of a new era of studying various behaviors in different scales, including intra-grain mechanics, grain-scale mechanics or inter-grain/grain-cluster mechanics, interfaces mechanics, thin film mechanics, grain boundary mechanics, grain interaction, grain size effects, diffusion mechanisms, martensite mechanics, phase transformation, shape memory mechanics, texture stability, in-grain texture formation, anisotropy, forming, deep drawing, process modeling, surface roughening, non-local formulations, superplasticity, extrusion, recrystallization, nano-indentation, micro-bending, fatigue, cyclic loading, void growth, multiphase mechanics, damage initiation, the prediction of local lattice curvatures, etc and may more [3].

1.6.8 Short-range vs. long-range interactions

The interactions of dislocations and thus stress fields in crystals can be either short-range, such as with individual dislocations, or long-range internal stress (LRIS) which refer to the variation in stress field that occurs over longer length-scales, such as the microstructure (often micrometer-range) [30]. The first kind includes dislocation-dislocation interactions that produce small pile ups, dislocation tangles, different locks and junctions like Lomer–Cottrell sessile dislocation junctions, interactions with other defects, e.g. solute atoms. On the other hand, long-range interactions arise due to inhomogeneous plastic deformation with microstructural heterogeneities of materials on different scales, i.e. grain/sub-grains boundaries, cell blocks, and families of dislocation walls/channels [84, 85]. Few decades ago, long-range internal stresses in deformed metals had been associated primarily with the existence of dislocation pile-ups. Short-range is expected to be saturated quickly while long-range one is expected to be saturated more slowly [86].

1.6.9 Internal stress and its origin

It is well known that the internal state of a material manifests itself at the microscale in many ways; but two that affect deformation rate are (i) a change in the material internal resistance and (ii) the presence of internal stress [75]. The former one is discussed earlier. There is a very important issue within the creep community regarding the later one is the presence of internal (or back) stress which has been suggested for plastic deformation in general, including cyclic deformation, monotonic deformation, the Bauschinger effect, springback in metal forming, etc. [30]. The internal stress is generally explained for polycrystals as a natural consequence of the strain incompatibility between grains which deform differently due to their specific orientations and/or the formation of cell/sub-grain structures [87]. This stress is also important for the evolution of the microstructure during thermo-mechanical treatments, as recovery and recrystallization are triggered by stress heterogeneities in the deformed state. As supported by electron microscope observations, the most important sources of the internal stresses are constraint stresses arising from misfitting interfaces, the lack of independent slip systems in the majority phases, and the elasto-plastic co-deformation of the different alloy constituents [88] as well as the heterogeneity of plastic deformation at the microscale leading to formation of inelastic-hard and inelastic-soft regions [89, 90]. It generally refers to the deviation of these local stresses from the applied stress. The presence of heterogeneities justifies the introduction of backstress concept. These heterogeneities could arise from the heterogeneous microstructure perspective, from the dislocation configuration model, and even from the heterogeneous SSD and GND distribution [7, 28, 91]. Internal stress fields in crystals can be either short-range (with individual dislocations), or long-range (variations in stress that occur over longer length-scales) [92]. The internal stress also arises due to long-range interactions is also known as long-range internal stress. Most of the time, the both terms are used interchangeably. The long-range dislocation–dislocation, dislocation–boundary interactions, GND–GND and GND–free surface interactions etc. are responsible for LRIS [58]. Long-range internal stresses (LRIS) associated with heterogeneous dislocation substructures causing heterogeneous stresses have also been widely embraced for monotonic deformation including elevated-temperature creep deformation process. In some context, the internal stress has been demonstrated to be equivalent to the residual stress as it helps maintaining of internal equilibrium within a stress-free body [76]. Based on the interactions of GND with slip systems, some authors formulated the backstress as self-internal and full-internal backstress. Hence, some formulations of backstress are exclusively based on the concept of GND density (that accommodate lattice incompatibilities) and its gradient [49, 58, 93]. For a lamellar material, the dislocations are concentrated in the matrix channels. As the precipitates are not always plastically deformed, the local strain is very heterogeneous on a microscale [28]. For this kind of material, back-stresses may come from the lamellar microstructures due to the trapping of dislocation segments at the lamellar interfaces, which leads to bowing of dislocations between interfaces [7]. At the beginning, it is interpreted that an internal back-stress is generated during deformation because of short-range interactions as mobile dislocations are piled-up at strong obstacles, like grain boundaries or precipitates [9]. Classical example of a heterogeneous dislocation distribution, namely pile-ups of primary dislocations, were considered as the sources of the long-range internal stresses [15]. Later, this concepts of internal stress caused by only dislocation pile-ups and short-interactions was heavily disputed [27]. The dislocation pile-ups also introduce some degree of long-range stress field which can exert a local back stress, i.e. LRISs are also interpreted as due to the dislocation pile-ups. This backstress assists the reversed motion of dislocations [94]. Recent experimental work has shown that the internal stress prevails also in crystals containing dislocation wall or cell structures which has so far been considered as energetically favorable dislocation patterns of negligible stress [15]. Heterogeneous microstructures and long-range interactions of dislocation substructures are the major sources of this stress. In the absence of dislocation pile-ups, interface dislocations maintain compatibility and give rise to LRIS [95]. Considering the all arguments it can be said that the internal stress has length-scale dependent consequences i.e. the presence of collective dislocations over different length-scales [24, 58], which arise due to inhomogeneous plastic deformation between microstructural heterogeneities of materials on different scales, e.g., grains, subgrains, cell blocks, and families of dislocation walls/channels [10, 24]. It is an athermal stress contribution and is derived through physical arguments [5, 84]. McDowell [96] divided the origin of backstress into five length-scales. (i) inelastic bowing of dislocations in cells or channels (10-100 nm), (ii) differential flow within crystals due to coherent or semi-coherent precipitates or particles (10–500 nm), (iii) interactions of heterogeneous dislocation distribution with scale on the order of the mean free path for dislocation glide (100–1000 nm), (iv) energy of dislocation arrays with net Burgers vector in confined volumes like pile-ups at grain or phase boundaries, and (v) differential flow among a set of grains with orientation distribution (10–500 mm). Hu et al. [76] describe the origin of residual stress from three different length-scales. These are equivalent to macroscopic specimen size, mesoscopic and microscopic. The mesoscale residual stress is a result of strain incompatibility between grains, created by the orientation dependent elastic and plastic anisotropy. The micro origin is associated with mismatch between the soft matrix and hard precipitates or dislocation cell walls, also known as composite effect. Internal stress appears as additional resolved shear stresses in the crystallographic viscoplastic constitutive law for individual slip systems.

For a polycrystalline alloy, internal stress can be divided into inter- and intra-granular type. Inhomogeneous plastic deformation is inherently present between grains, this grain-to-grain inhomogeneous plastic deformation or strain incompatibility is responsible for inter-granular back stress. This inter-granular backstress evolves first with dislocation distribution, and then with grain fragmentation. In a cluster of grains, intergranular back stress increases with the number of dislocation pile-ups which are present close to grain boundaries to accommodate the plastic strain incompatibilities between grains. In other words, intergranular back stress relates to differences in the numbers of dislocations close to grain boundaries and within the grains. After further loading, the strong activity of secondary slip results in higher numbers of dislocations inside grains, i.e., dislocations are distributed more homogeneously over grains, relieving the intergranular back stress. Once interior dislocations become abundant, dislocations start strongly rearranging to form dislocation high/low density regions and seek to form their most stable configuration. This process of rearrangement on the one hand contributes to further relief of the intergranular back stress, but on the other hand raises the intragranular back stress on a smaller scale due to the formation of dislocation high/low density regions (e.g., walls and channels) [84]. According to some results, the relative magnitude of the intra-granular backstress initially seems to increase with the applied strain level and finally both the relative intra- and inter-granular backstresses seem to stabilize [97]. When the stabilized condition of dislocation microstructures is established, the requirement of material continuity is totally fulfilled both at the intergranular and intragranular scales, leading to the saturation values of these back stresses.

1.6.10 Backstress and hardening variables

In plasticity theories, the most complex part is the modeling of hardening. The trapping of mobile dislocations with other mobile and immobile dislocations, formation of jogs, locks, and sessile junctions, etc. are the major causes of hardening. In a broader sense, it originates from the short and long-range interactions of dislocations. However, it is not clear to what extent these processes occur, and how these should be incorporated into the evolution of the hardening variables (or internal variables) of a crystal plasticity model at each material point. In most classical studies, one internal variables based CP constitutive modeling is common, however, one internal variable combining hardening-softening modeling is not very common [98]. The most common approach at the macroscale modeling is to consider two hardening variables, i.e. isotropic and kinematic. Similarly in crystal plasticity, often equivalent two variables are incorporated for each slip system considering the two types of interactions. This allocation of short-range and long-range and consequent hardening variables seems to offer more accurate description of the hardening behavior [86]. The concept of isotropic and kinematic hardening were originated from the expansion and movement of yield surfaces. Macroscopically, the isotropic hardening variable corresponds to the width of the elastic domain and expands the yield surface uniformly while the kinematic one moves the surface without changing size [99]. In practice, these are idealization, the real scenario is combined isotropic-kinematic [60]. Both yield and drag can be included in isotropic hardening variable. The former one is directly related to the increase of dislocation densities, whereas the later one is associated with the rapid changes in the dislocation structure. It is also explained that the equivalent backstress variable is related to the formation of GND and its gradient [24, 100]. According to Estrin [101], it is related to the density of less mobile (forest) dislocations. Usually both variables are treated as coupled in evolution equations whose various terms account for major dislocation reactions involved [101].

1.6.11 Boundary condition

It is agreed that the Hill–Mandel consistency condition is an essential part of homogenization methods. This condition is fulfilled via imposing three types of boundary conditions; they are displacement boundary conditions (DBC), periodic boundary conditions (PBC) or traction boundary conditions (TBC), collectively referred to as canonical boundary conditions [47]. Homogeneous traction boundary conditions give a softer effective material response, while the displacement boundary conditions overestimate the stresses. The respective BCs can be presented by the following equations:
Traction boundary condition

$$\boldsymbol{t} = \boldsymbol{\sigma} \cdot \tilde{\boldsymbol{n}} \quad \text{on} \quad \partial\Omega \tag{1.11}$$

Displacement boundary condition

$$\boldsymbol{u} = \boldsymbol{H} \cdot \boldsymbol{x_0} \quad \text{on} \quad \partial\Omega \tag{1.12}$$

Periodic boundary conditions

$$\boldsymbol{u}^{+} - \boldsymbol{u}^{-} = \boldsymbol{H} \cdot (\boldsymbol{x}_{\mathbf{0}}^{+} - \boldsymbol{x}_{\mathbf{0}}^{-}) \tag{1.13}$$

$$\boldsymbol{t}^{+} + \boldsymbol{t}^{-} = 0 \quad \text{on} \quad \partial\Omega \tag{1.14}$$

Here, $\boldsymbol{t}$ stands for traction, $\boldsymbol{n}$ is for normal vector, $\boldsymbol{u}$ is the displacement, $\boldsymbol{H}$ is some sort of average strain measure and $+$, $-$ denote two opposite nodes. The symbol $\partial\Omega$ as usually indicates the boundary surfaces. It is widely accepted that for a finite size of the RVE, the effective behavior obtained from the PBC is bounded by DBC from above and TBC from below. In other words, PBC, the most versatile one, is a compromise between the homogeneous TBC and linear DBC in the sense that they distribute the constraints that are needed to complete the boundary value problem equally [102]. A related case comparing the three BCs is shown in Fig. 1.8. Hence, PBC has become the most popular and commonly used boundary condition in homogenization problems. Although PBC is a natural choice for the heterogeneous body which exhibits a periodic structure, but later it is proved that for general heterogeneous materials also, PBC with relatively small unit cell size provide reasonable estimates of the effective properties, even if the medium does not have actual geometrical periodicity [103]. Thus a faster convergence in terms of the RVE size is achieved compared to linear displacement boundary conditions [104]. It is well-known that PBC provides the most precise results only for periodic micro-structures and also good but not necessarily for micro-structures with random distributions of inclusions [47]. This means that the PBC provides the more reasonable estimates among the class of possible boundary conditions for statistical homogeneous or non-periodic media [52, 62]. It is also to be noted that, for highly random and heterogeneous media, it is not always guaranteed that the PBC would be the most accurate one and would be bounded by DBC and TBC [47]. In a RVE, the spatial periodicity conditions follow from the compatibility demands with respect to the opposite edges. This also enforces two adjacent RVEs to show identical deformations without overlapping or separation. This compatibility of two opposite boundaries implies two points. First, the shape of both boundaries is and remains identical, and second, the stresses acting on those boundaries are opposite in sign. This second condition states that the stress field is continuous when passing from one cell to the next one [105]. It is worth mentioning that, for large RVE containing a large number of heterogeneity, if the ratio d/l is small i.e. the size of RVE is sufficiently large, then boundary condition type is unimportant, where d is the size of heterogeneity, l is the size of RVE. If the ratio is closer to 1 in local plasticity theory then the BC important [106]. Thus, with increasing the size of the RVE, the effect of boundary condition is reduced.

1.7 TiAl alloy system

The generation of Ti-rich TiAl-based intermetallic alloys represent an important class of high-temperature structural materials providing a unique set of physical and mechanical properties that can lead to substantial rewards in various sophisticated engineering applications like aircraft engines, industrial gas turbines and automotive industry [107–109]. For example, This alloy system represents a major advance in propulsion efficiency, realizing a 20% reduction in fuel consumption, a 50% reduction in noise, and an 80% reduction in NOx emissions compared with prior engines in its class [110]. The GEnx(TM) engine is the first commercial aircraft engine that is flying with titanium aluminide alloys in its low-pressure turbine (LPT) blades, Fig. 1.9. The most successful of the automotive applications has been the development of TiAl

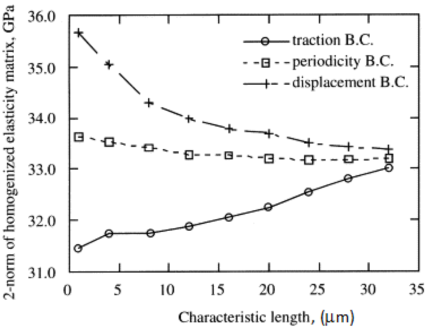

Figure 1.8: A case of convergence trend for homogenized elasticity with respect to the three boundary conditions, TBC, PBC and DBC [62].

turbochargers in 1998. In the last decades, it has replaced many contemporary metals and alloys till 800°C. A recent version of polysynthetically twinned (PST) single crystals like lamellar intermetallic Ti-45Al-8Nb has been proposed to be used till 900°C [111]. Beyond aero-engine, gas turbine, etc., the growing application has also been extended to petroleum, medical, and defense industries [112,113]. Since 1970s, this alloy system has been widely recognized as a possible basis for novel lightweight materials for high-temperature applications [114]. Experts are convinced that the alloy system has immense potential that could revolutionize the world of aviation. According to some experts, titanium aluminides are the only promising alternatives in areas where heavy nickel alloys still prevail [115, 116]. As compared to some other metals and alloys, the potentiality of the TiAl family can be shown by the Fig. 1.10. These alloys exhibit impressive material properties such as high specific yield strength and stiffness, good oxidation and ignition resistance combined with good creep properties at high-temperatures, fracture toughness, corrosive resistance, low density, high thermal capability, and biocompatibility, etc. [109, 112, 113]. Sufficient strength at high-temperature and ductility at ambient temperature are crucial issues for those lightweight alloys. Low ductility of TiAl alloys has long been considered an obstacle to its production and use [115]. In order to increase the high-temperature capabilities of γ-TiAl-based alloys, current alloy development programs are focused on Nb and C contents as ternary element [117] . Higher temperature capability have been developed containing higher levels of Nb and Mo. The ternary additions serve to improve properties such as increasing the room temperature ductility, improving high-temperature properties, or refining the grain size. Brittleness was reduced by adjusting the material composition, and manufacturing processes and the design were tailored to suit the material properties.

The development of TiAl based alloys began about 1970. The composition of engineering γ-TiAl based alloys generally consists of 45-51 at.% Al with 1-10 at.% ternary additions. They consist predominantly of the γ-TiAl phase with a reasonable amount of α_2-Ti_3Al phase. Earliest major work on γ-TiAl alloy development was initiated in 1975-1983 by the U.S. Air Force Materials Laboratory, recommended Ti-48Al-1V-(0.1C) as the best alloy composition based on ductility and creep resistance. Second major development phase was 1986-1991, again initiated by the Air Force and performed by General Electric, identified a second generation of alloys, Ti-48Al-2(Cr or Mn)-2Nb with improved ductility, strength,

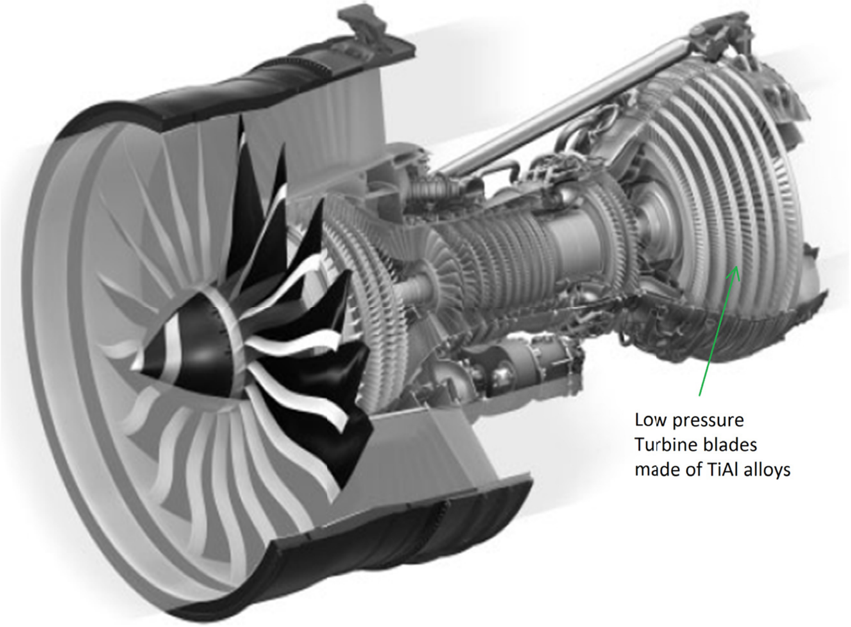

Figure 1.9: One of the most important applications of TiAl alloys is in the rear side (low pressure turbine blades) of aerospace engine. (Courtesy: GEnx Aero Engine [118])

and oxidation resistance. One of the largest TiAl programs in the last two decades was the IMPRESS Project, which was coordinated by the European Space Agency (ESA). The objective of the project was to understand the strategic link between the material processing, the structure, and the final properties of new intermetallic alloys, such as TiAl, that has many different applications ranging from aerospace components to power generation systems [110]. Different generations of this alloy system has been proposed as:
First generation, Al: 45-51%, 1-10% other ternary elements
Second generation, Al: 45-48%, Nb/Ta/W/Mo: 2-5%, Cr/Mn/V: 1-3%, Si/B/C: <1%
Third generation, Al: 42-46%, Cr/Mn/Nb: 0-10%, W/Mo/Hf/Zr: 0-3%, B/C: 0-1%, Rare earth elements: 0–0.5%

It is to be noted that the highly successful and potential alloys from this family are processed in lamellar structure as it is a key morphology. Three relevant length-scales have been proposed for lamellar TiAl alloy: the colony size, the gamma domain size parallel to the interface and the lamellar spacing [114]. The class of Ti-rich lamellar alloys (γ-TiAl+α_2-Ti_3Al) are already in many industrial applications fulfilling strength and ductility requirements at high-temperature. Based on its higher aluminum content, Al-rich $TiAl_2$ phase is expected to have a lower density and better oxidation resistance than TiAl and α_2-Ti_3Al, potentially making it a very attractive elevated temperature alloy constituent [119]. The Al-rich Ti–Al alloys with Al-contents exceeding 54at.%Al are of special interest, because they are expected to form protective Al_2O_3 scales instead of titanium oxides [120]. In short, due to better oxidation resistance,

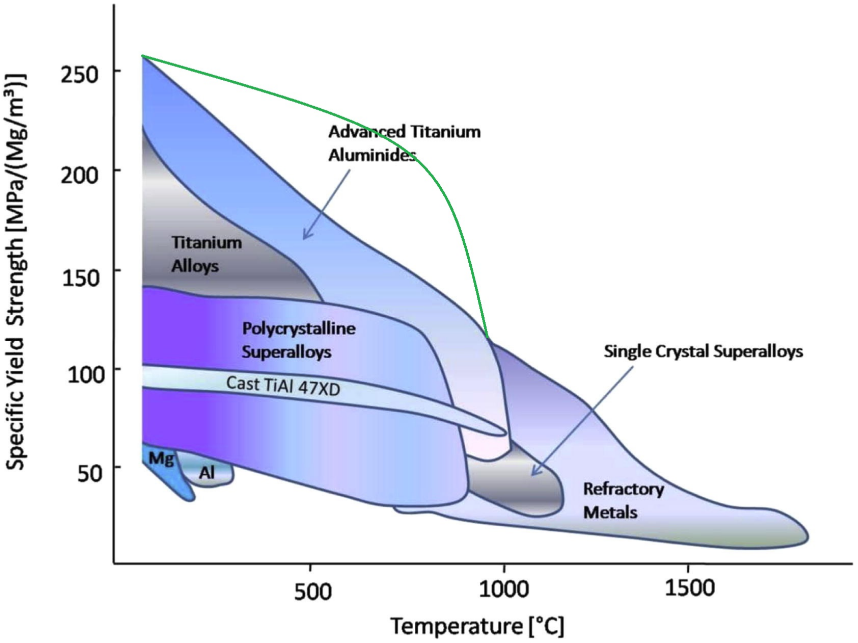

Figure 1.10: Specific yield strength comparison among TiAl family and some other contemporary materials. The Green line shows the future potential of this alloy system. (Courtesy: [109])

20% lower density and higher (till 1050°C) operating temperature possibility of Al-rich Ti-Al alloys over Ti-rich side, they have recently become a focus of interest [107, 121, 122].

1.8 Objectives of this thesis

Understanding different inelastic behaviors e.g. plasticity, plastic anisotropy, and tension-compression asymmetry of high-temperature material is an integral part of modern engineering problems. In spite of having a huge number of studies on Ti-rich side, the literature on the Al-rich part is very limited. This Al-rich family of alloys is especially important to understand the combined effect of the lamellar morphology and long-period superstructure (LPS). Directionally solidified such lamellar material is expected to be highly anisotropic due to the presence of LPS and preferred orientations of the lamellar colonies as like PST TiAl [123]. In the context of Al-rich TiAl alloys, rate-dependent asymmetric phenomena of such alloys is especially important at high homologous temperature because of the appearance of one or more long-period superstructures and subsequent activation of various deformation modes. To understand the combined effect of the lamellar morphology and long-period superstructure is also of great interest. However, the modeling approach of this alloy systems has not been attempted yet. Therefore, this study is focused on this Al-rich side of the TiAl alloys. To the best of authors' knowledge, micromechanical modeling endeavor of Al-rich family has not been attempted so far. This study fills the gap of modeling by addressing a specific lamellar single crystal like Al-rich Ti-61.8at.%Al intermetallic where material microstructure is highly complex with long-period superstructures. This is the first micromechanical modeling project combining the rate-dependent anisotropic and asymmetric phenomena at high homologous temperature. Determining critical stresses for different slip systems becomes one of the most important parts, in fact a prerequisite, in modeling of plastic anisotropy. However, the task of finding individual critical resolved shear stress (CRSS) for every single slip system, if not impossible, is formidable and a delicate one especially if the microstructure is very complex. Slip family based, mechanism based and morphology based (e.g. phase interface) slip systems classification and hence determining CRSS consistent with experimental measurements are often used in crystal plasticity, that are not adequate for this type high-temperature complex alloys.

As a part of the comprehensive micromechanical modeling approach, first, this study reviews the current status of intermetallic Al-rich TiAl family as a whole, based on the available literature. From the material science perspective, different issues have been highlighted including phases, microstructures, deformation mechanism, mechanical properties etc. Then micromechanical, more specifically, crystal viscoplasticity modeling of an exemplary lamellar alloy from this family has been presented. The model has been tested and validated with two sets of experimental data taken from two lamellar/loading orientations, each set contains stress-strain behavior for three different strain rates. The compressive test data at ultra-high homologous temperature of 1050°C have been utilized. The commercial software package Abaqus Standard has been used for the simulation of all related models that have been implemented through its user-subroutine (UMAT) functionally in Fortran programming language. Necessary material parameters have also been identified and their justification is also discussed. From a variety of options in identifying modeling parameters, which set of flow-rule dependent parameters is meaningful is discussed here. Different related numerical aspects including slip activities are also outlined. Modeling strategies for any alloy belongs to the family of Al-rich TiAl have also been discussed. A possible comparison with Ti-rich side, where applicable, is also presented. The choice of the internal variables in CP power-laws depending on the microstructural complexity and subsequent deformation mechanisms especially at high homologous temperature has been discussed in great detail. Moreover, a generalized hardening-recovery based evolution equation has also been proposed. A novel iterative algorithm for estimating individual critical stresses for all slip systems has been developed. This scheme can be applied for various sets of anisotropic and asymmetric data. Conventional approaches related to CRSS estimation are also compared with the proposed one. At the end, based on the most reasonable set of identified material parameters, the model has been used for qualitative prediction of the evolution of rate-dependent tension-compression asymmetry. One central objective of this study is to understand the Al-rich TiAl based alloys as a whole and establish a microstructure-properties relationship through a suitable homogenization scheme, which would potentially assist in further alloy development to allow an assessment in terms of their potential for possible applications.

This thesis has been organized with nine chapters. Apart from the introduction and background in the chapter-1, a comprehensive review has been presented in the second chapter. Finite strain and finite rotation based continuum framework, crystal plasticity modeling with detail of flow-rule and numerical aspects have been demonstrated in chapter 2-5. The next three chapters (6-8) describe the iterative scheme of CRSS estimation along with simulation results, parameter estimation and model prediction of tension-compression-asymmetry along with the investigation of its probable origin at different length-scales. At the end concluding remarks and possible outlook have been presented.

Chapter 2

Al-rich Ti-Al alloy family

2.1 Phase diagram of Al-rich side

Due to the formation of some metastable phases, the phase equilibria in the Al-rich side of The Ti-Al system are rather complex [122]. This phase diagram was not settled even some years ago and there were many uncertain states. Therefor, all phase equilibria above 50at.% Al were given as dotted lines in the relevant binary phase diagram. The most controversial area of Ti-Al binary phase diagram ranges between 55 and 77 at.% Al, and 900 to 1450°C [124]. Hence, efforts to the development of appropriate alloys have been hindered substantially because no settled phase diagram of the Al-rich part [120]. One of the recent binary phase diagram is shown in Fig. 2.1. Some other unsettled phase diagrams can be found in [120, 125].

2.2 Highly brittle Al-rich TiAl alloys

Generally Al-rich phases in the TiAl alloy family make the alloy brittle and hard, so the increasing of CRSS in different slip systems is expected with the increase of Al content. Kad and Fraser [126] reported that the Ti-rich γ-TiAl alloys are significantly ductile at high-temperature because of no Al-rich brittle phases. Depending on the amount of deviation from the stoichiometry, TiAl compounds exhibit brittleness with the increasing of Al concentration. In Ti-62.5at.%Al, plate like r-$TiAl_2$ type precipitate in the γ matrix interrupt the motions of dislocations and retards the improvement in ductility below 1200°C [127]. Fujiwara et al. [128] mentioned that the cause of brittleness might be the partial dislocation 1/6<112], which is a constituent of the <011] type superlattice dislocation. The refractory elements like Nb can improve tensile ductility as well as creep resistance of the Ti-Al alloys [129]. Besides the beneficial effect of lamellar microstructures in improving mechanical properties, the fracture toughness, elevated temperature strength and oxidation resistance are further enhanced by the addition of Nb [129]. Considering Ti-62.5at.%Al alloys containing Al_5Ti_3 precipitates in the $L1_0$ matrix, Appel and Oehring reported that the strong hardening is mainly caused by the anti-phase boundaries that provide additional resistance to subsequent glide processes. This indicates that some dislocations in TiAl are permanently locked during the high-temperature deformation [118].

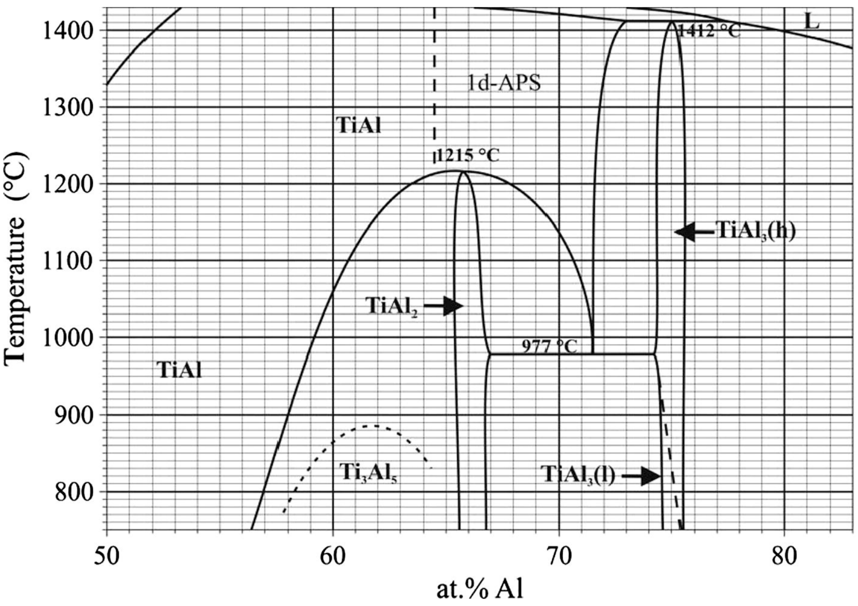

Figure 2.1: Stability ranges of different phases in the Al-rich part of the Ti-Al system [122]

2.3 Phases in Al-rich side

Three different stable phases are possible in multiphase Ti-Al alloy system, these are γ-TiAl, α_2-Ti$_3$Al and r-TiAl$_2$ [120]. With melting point of 1463°C, γ-TiAl (L1$_0$-type) has a wide solubility range from the near stoichiometry to the Al-rich side [130, 131]. In the near stoichiometric Ti-rich side, alloys mostly consist of two phases, γ-TiAl and α_2-Ti$_3$Al. The γ-phase consists of face centered tetragonal (with c/a=1.02) lattice and the α_2-phase has hexagonal closed pack (HCP) crystal structures. Due to the tetragonal structure of γ-TiAl phase, the atomic arrangement is not perfectly coherent and hence ledges and misfit dislocations accommodate the lattice mismatch and reduce the elastic stresses in the lamellar plates [114]. Beyond stoichiometric composition especially from 54at.%Al content, depending on the Al content and annealing condition, one or more phases mostly with γ-matrix phase are emerged [132]. Along with stable γ-TiAl matrix phase, other precipitate phases are mostly metastable with long-range order of L1$_0$-type structure. Among them, Al$_5$Tl$_3$ and h-Al$_2$Ti are widely observed metastable phases. Two superstructure phases, Al$_5$Tl$_3$ and h-Al$_2$Ti, are frequently observed in as-cast and low-temperature-annealed Al-rich TiAl alloys [133]. The Al$_5$Tl$_3$ phase rapidly dissolves above 900°C and h-Al$_2$Ti remains as metastable phase at least up to 1200°C. Annealing of Ti-58.0at.%Al below 800°C results in an island like Al$_5$Tl$_3$ phase developed in the host L1$_0$ phase, which in turn completely dissolves by annealing at higher temperature [130, 134], and ultimately transforms fully into h-Al$_2$Ti with the increasing of Al concentration (at least till Ti-62.5at.%Al) [135]. In general, precipitates of Al$_2$Ti, alone or with other phases, are found in the composition range of 56-75 at.%Al. This r-Al$_2$Ti superstructure phase has an approximate melting point of 1215°C [119, 131]. Mostly, it has been found to be stable below 1150°C.

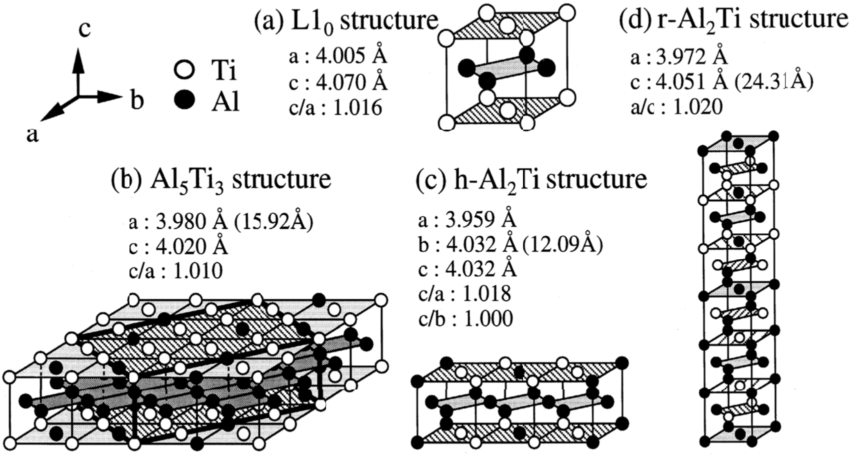

Figure 2.2: Crystal structures with lattice parameters for different phases appearing in the Al-rich TiAl alloys. (a) L1$_0$ structure, (b) Al_5Tl_3 superstructure, (c) h-$TiAl_2$ superstructure, (d) r-$TiAl_2$ superstructure. The figure is taken from [130].

When the Al composition is higher than 60at.%, this phase is appeared with significant volume fractions maintaining semi-coherence to the L1$_0$ matrix, sometimes with Al_5Ti_3 superstructure. The density of the r-$TiAl_2$ phase is 3.53-3.54 g/cc, lower than γ-TiAl and α_2-Ti_3Al [119]. In Ti-62.5 at.% Al alloys, annealed at temperatures below 1200°C, the r-$TiAl_2$ phase is finally formed as an equilibrium phase, but the ordering of Al_5Ti_3 and subsequently h-$TiAl_2$ often proceeds prior to the precipitation of r-$TiAl_2$ [132]. A recent study on the phases and their evolution for 59.4 to 60.4at.%Al contents depending on the processing and annealing condition can be found in Palm et al. [122].

All of the three superstructure phases consist of face centered ordered structures of γ-TiAl. The h-$TiAl_2$ phase is similar to threefold face centered structure while r-phase is six fold and Al_5Tl_3 superstructure is equivalent to sixteen face centered lattice units. These long-period superstructures have different lattice periodicity, e.g. four-fold periodicity along the a- and b-axes in the Al_5Tl_3 superstructure; three-fold periodicity along the b- axis in the h-$TiAl_2$; and six-fold periodicity along the c-axis in the r-$TiAl_2$ [130], as shown in Fig. 2.2. In the h-$TiAl_2$ and r-$TiAl_2$ superstructures, the periodicities of Al layers are different. There is consistent indication that the superstructure phases formed in the Al-rich γ-TiAl often exhibit fine microstructures with short-range order (SRO), anti-phase domain boundaries, and so on in certain ranges of Al concentrations and temperatures [133, 136, 137]. This is one of the most characteristic features of the long-period ordering phenomena in Al-rich TiAl [138]. For both 62.5 and 60at.%Al alloys, Al_5Ti_3 SRO structures are found in Ti-rich (002) layers of the L1$_0$ ordered γ-TiAl matrix along with long-range order (LRO) phase up to about 800°C. At higher temperature, SRO state becomes unstable in the course of the phase transformation from the Al_5Ti_3 to the h-$TiAl_2$ phase [134]. In spite of a number of studies, structural details and formation processes of the fine microstructures are still controversial in many cases, owing to insufficient experimental information at the atomic scale [138].

2.4 Production routes

The major challenges for the implementation of TiAl alloys are low ductility and processing. A range of processing routes has been explored including casting, extrusion, and forging. Powder metallurgy and additive manufacturing routes have also been explored. In principle, casting offers the most cost-effective route for the production of complex shapes, since it is a well-established process. Extrusion and forging have been used to produce compressor blades for engine testing. There has been significant interest in centrifugal casting of TiAl, and hence, both horizontal and vertical forms of centrifugal casting have also been explored [110]. The stability of a long-period superstructure remarkably decreased in rapidly solidified process and the constituent phase may changes from one to another, however, rapid solidification is effective to examine the subsequent ordering process during heat treatment [130]. Benci et al. [119] and Nakano et al. [139] reported that powder-processed r-TiAl$_2$ shows superior strength to TiAl polycrystals below 900°C. The yield strength of powder processed r-TiAl$_2$ at 400°C is approximately 1000 MPa, decreasing to about 500 MPa at 800°C, almost six times greater than the yield strength of cast TiAl$_2$ over this same temperature range [119].

2.5 Ordering and stability

So far we know, the r-Al$_2$Ti is stable at about 58 to 62.5at.%Al in the temperature range between 700°C and 1200°C [120, 122, 125, 133]. The volume fraction of the constituent r-TiAl$_2$ phase depends on the alloy composition and annealing temperature, and decreases with increasing Ti content and increasing temperature. The compositions ranging from Ti-54.7at.%Al to Ti-62.5at.%Al annealed at 1200°C, the Al$_5$Ti$_3$ long-period superstructure is embedded in the host L1$_0$ matrix, then transformed gradually into h-TiAl$_2$ with the increasing Al concentration, and finally, there is a complete transformation into h-TiAl$_2$ for Ti-62.5at.%Al alloy [135]. Since the periodicity of Al layers in the r-TiAl$_2$ phase is different from that in the L1$_0$ structure (the Al$_5$Ti$_3$ and h-TiAl$_2$ phases have stacking periodicity analogous to that in the L1$_0$), a complex diffusion process is necessary for the nucleation and growth in the phase transformation to r-TiAl$_2$ phase [130]. Therefore, the Al$_5$Ti$_3$ and h-TiAl$_2$ phases appear prior to the formation of the final equilibrium r-TiAl$_2$ phase. At first the Al$_5$Ti$_3$ phase formed rapidly and then the metastable h-TiAl$_2$ phase appeared prior to that of the r-TiAl$_2$ phase [130], which has been confirmed in Ti-60at.%Al and Ti-62.5at.%Al during annealing below 800°C.

Further ordering under long-period superstructures may occur in the Al-rich region depending on the Al composition and heat treatment [135]. Annealing of Ti-58at.%Al at 1000°C for 1 h, only the r-Al$_2$Ti phase is remained in the L1$_0$ matrix. In Ti-62.5at.%Al alloy, Al$_5$Ti$_3$ were obtained with the matrix phase by the floating zone method and subsequent heat treatment at 750°C for 48h [140]. If the intermetallic alloys containing Al of 56, 58 and 60 at.% are aged at 700°C, the TiAl phase decomposes into the two-phase state of Ti$_3$Al$_5$ and TiAl [141]. Moreover, annealing at 930°C results a nice lamellar morphology of the γ and r phases [130], as shown in Fig. 2.3. Single-phase single crystal of only Al$_5$Ti$_3$ phase can also be generated over a wide temperature and time range of annealing although the anti-phase boundaries (APB) based on the Al$_5$Ti$_3$-type ordering exist [132]. First annealing of Ti-62.5at.%Al at 1200°C and then at 750°C for 48h results in Al$_5$Ti$_3$ single-phase single crystals [135].

More interestingly, one or more phases (e.g. Al$_5$Ti$_3$) can be completely eliminated by the choice of a set of suitable heat treatment parameters. From Ti-60at.%Al and Ti-62.5at.%Al crystals containing Al$_5$Ti$_3$

Figure 2.3: Electron micrographs of Ti-62.5at.%Al alloy annealed at 930°C, taken from [130]

and r-$TiAl_2$ phases embedded in the γ-TiAl matrix, the plate like r-$TiAl_2$ phase can be eliminated by annealing for 1 h at 1100 and 1200°C, respectively [134]. The r-$TiAl_2$ is only found to be stable in Ti-62.5at.% Al if the alloy is annealed at temperatures below 1200°C [132]. The Al_5Ti_3 superstructural spots start disappearing and the h-$TiAl_2$ spots become dominant after 800°C [132]. In short, the Ti-62.5at%Al alloy exhibits a clear annealing temperature dependence of the long-period superstructure phases: an Al_5Ti_3 ordered state below 800°C, Al_5Ti_3 with SRO state and h-$TiAl_2$ or r-$TiAl_2$ till 1200°C, and an h-$TiAl_2$ ordered state above 1200°C [132, 138, 142, 143]. More detail about different SRO states and the SRO-LRO transition in Ti-62.5at.%Al can be found in [143, 144].

As reported earlier, the plate-like r-$TiAl_2$ phase in as-grown Ti-62.5at.% Al single crystals were easily annihilated by annealing at 1200°C for 1 h, while small h-$TiAl_2$ particles were homogeneously distributed in the $L1_0$ matrix. Subsequent annealing at temperatures between 500 and 900°C for 1 h did not produce r-$TiAl_2$ yet, although both r-$TiAl_2$ and $L1_0$ are known to be stable phases in this annealing temperature range [132]. Metastable nature of the h-$TiAl_2$ phase is observed at various annealing temperatures below 1200°C [132]. So, in general, the r-$TiAl_2$ and h-$TiAl_2$ phases are believed to be final stable structures in the temperature range below and above 1200°C, respectively, but some preceding phases appear prior to the ordering of the final superstructure [132]. The precipitation of h-$TiAl_2$ can be accelerated by increasing annealing temperature. Annealing time is also a very important factor in the stability of superstructures. For instance, annealing at 900°C for 1 h, the h-$TiAl_2$ phase is formed with lamellar morphology along with the matrix phase whereas further annealing may introduce r-$TiAl_2$ into this crystals [132]. Single crystals of Ti-54.7at.%Al, Ti-56.0at.%Al, Ti-58.0at.%Al, Ti-60.0at.%Al and Ti-62.5at.%Al produced by different annealing temperatures and times along with a comparative study can be found in [135]. An overview of different alloy phases with appeared LPS in Al-rich region has been documented according to Al concentration and heat treatment in [120, 131, 133]. Further works on the appeared phases are [125] and [122] with special emphasize on Ti-62at.%Al and Ti-60at.%Al. In spite of a number of experimental studies in the Al-rich side, the stability and ordering mechanism of the LPSs are sometimes controversial [145, 146]. There are many uncertain points remaining and their actual influence in deformation mechanisms is still not fully understood. As mentioned earlier, the most controversial area of Ti-Al binary phase diagram ranges between 55 and 77 at.% Al, and 900 to 1450°C [124]. The TiAl-$TiAl_2$ region with Al contents from 56 to 65 at.%Al is still not resolved satisfactorily [120]. Some other unresolved issues are the precise morphological stability of the microstructure, the dynamics of the microstructural changes, the stability and the ordering mechanisms, and accurate precipitation processes etc. [145–147]. This may be due to the fact that the long-period ordering is quite sensitive to the Al concentration and annealing conditions [148].

2.6 Lamellar alloys: Ti-rich vs. Al-rich with LPS

Gamma-TiAl based Ti-rich alloys derive their superior creep properties from their lamellar γ-TiAl + α_2-Ti_3Al microstructures. It is worth to mention that the lamellar structure is a key morphology for many complex engineering materials [149]. Such a lamellar structure is expected to have a significant influence on the deformation behavior [128]. This kind of microstructures generally exhibit improved ductility, fracture toughness and creep resistance in comparison to their monolithic constituents [150, 151]. Lamellar strengthening sometimes might be more influential than grain size strengthening [114]. Current activities to improve the properties of γ-TiAl based alloys mainly focus on improving strength and creep resistance at high-temperatures and a better oxidation behavior [120], for which Al-rich alloys deserve special attention. For a lamellar alloy, there are mainly four components of shear stress, from which one or more are responsible for yield and plastic anisotropy depending on the microstructural and morphological combination. These four components are: 1) lattice resistance of the material or Peierls stress which depends on the lattice type and lattice plane, 2) stress to operate dislocation sources or the Frank Read stress, 3) stress required to transmit dislocations through interfaces or the Hall-Petch stress, and 4) internal stress generated by lattice mismatches in the lamellar interfaces. Even though deformation modes along the lamellar plane is easy or soft-mode, and across the lamellae is hard, these stresses have very different effects on soft- and hard-modes of deformation and account for some of the plastic anisotropy. For the complex hardening mechanism of individual slip system, the effect of the Hall-Petch stress is believed to be dominant [152].

From the rough range of 58-65 at.%Al content, there is a possibility of generating lamellar structure with stable γ and r phases. Further interest is on alloys with about 62at.%Al due to the possibility of generating lamellar and stable phases of γ-TiAl + r-$TiAl_2$ microstructures (like in Fig. 2.3), which may enhance the prospects of possible alloy developments as Ti-rich side. There is a number of studies on the choice of the heat treatment parameters for which lamellar alloys with stable phases can be generated. A summary of some of the available studies on phases and morphology appeared in alloys with 58, 60, 62, 64%Al contents for different heat treatment parameters can be found in [120, 133]. Braun and Ellner [131] investigated some alloys with 60-64at.%Al contents and showed that the lamellar structure can be generated by the choice of the annealing temperature ranging from 800-1100°C. With the increase of Al-content, higher annealing temperature might be necessary. An elaborated summary on this issue can be found in [120]. Another detailed study on the formation of lamellar structures can be found in [125], where phases, microstructures, lamellar spacing, lamellar coarsening, and related heat treatment parameters etc. are also discussed. Special emphasize is given on 62%Al content, which shows that 950C/200h/WQ are the most favorable parameters for generating coarse and fully lamellar alloy of γ-TiAl

+ r-$TiAl_2$ phases where supersaturation with Al is apparently a prerequisite for the formation of such lamellar structure [122].

As mentioned earlier, over a wide solubility range in off-stoichiometric Al-rich region, long-period superstructures appear depending on the Al concentration and annealing conditions e.g. temperature and time [145, 146]. They plays an important role in operative deformation modes and configuration of dislocations in Al-rich TiAl, depending on the Al concentration. Plastic deformation behavior and activated slip systems in Al-rich TiAl crystals are closely related to the formation of mentioned superstructures such as Al_5Ti_3, h-Al_2Ti and r-Al_2Ti [132, 140]. Anomalous strengthening and slip-plane transition for the 1/2<110] ordinary dislocations at temperatures around the peak stress in the yield stress-temperature curve are also thought to be influenced by the Al_5Ti_3-type ordering in Ti-62.5 at.% Al [132]. Fourfold ordinary dislocations, for example, often move as a group in the Al_5Ti_3 superstructure embedded in the $L1_0$ matrix. Many studies have concluded that dislocation motion in Al-rich TiAl is strongly influenced by the appearance of some long-period superstructures [145].

2.7 Deformation mechanisms: Ti-rich vs. Al-rich lamellar TiAl

The deformation modes of TiAl based alloys strongly depend on their microstructure, alloy composition (e.g. Al concentration), orientation, impurity content of interstitial atoms and deformation temperature [117, 153]. It is now well established that the fundamental deformation mechanisms of Ti-rich γ-TiAl+α_2-Ti_3Al based alloys consist of ordinary slip $\frac{1}{2}$ <110]{111}, superdislocation slip <101]{111} as well as twin systems $\frac{1}{6}$ <112]{111} [128, 136, 154, 155]. Often $\frac{1}{2}$ <112]{111} type superdislocation slip is also observed [117, 155]. Under most conditions deformation occurs along the {111} planes by the glide of ordinary dislocations with the Burgers vector 1/2<110] and superdislocations with <101] and 1/2 <112]. Below the peak temperature, ordinary slips are dominantly operative for most loading orientations. As the γ-phase is considerably weaker than the α_2-phase, mostly it is assumed that the plastic deformation parallel to the interface is controlled by the softer γ-TiAl phase, while deformation component normal to these boundaries is dominated by the harder α_2-Ti_3Al phase [117, 150]. Although some authors previously considered ordinary dislocation slips and twinning are predominant than superlattice dislocations, later investigation shows that superdislocations are significant and there is clear evidence that superdislocations are kinematically necessary for plastic deformation [156].

On the other hand, excess Al atoms in the Al-rich alloys may replace some Ti atoms on the (001) plane and form different ordered structures. As a result we observe three long-period superstructures of r-Al_2Ti, h-Al_2Ti and Al_5Ti_3 and they are based on the face centered lattice. Such periodic ordering contributes to the deformation modes of these alloys. The work of Nakano et al. [140] is a good example in this regard. They found that the CRSS for {111}1/2<110] ordinary slip family is quite lower in Al_5Ti_3 single-phase single crystals than that in other Al-rich TiAl crystals composed of Al_5Ti_3 precipitates and the $L1_0$ matrix [140]. Analyzing Al_5Ti_3 single phase single crystals, they further reported that, almost all dislocations exists as a group of four dislocation segments with the same sign of 1/2<110] Burgers vector. Three APBs are created between the 1/2<110] dislocations, thus the group motion of four ordinary dislocations is most favorable for suppressing the effect of APBs, resulting in a stress drop in Al_5Ti_3 single-phase single crystals. In contrast, superlattice dislocations did not move as a group and glided independently in that single-phase single crystals [140]. So it is clear that the plastic deformation behavior and activated slip systems in Al-rich TiAl crystals are closely related to formation of the respective superstructures [132]. Fundamental deformation features of the Al-rich alloys compared to the Ti-rich side can be divided into the following points.

- Firstly, twinning is suppressed for most alloys and the dislocation motion is strongly influenced by the appearance of LPS in Al-rich TiAl alloys [157, 158]. However, Inui et al. [159] observed twinning in Ti-56at.%Al alloys in the temperature range 800-1000°C.

- Secondly, in contrast to the ordinary slips in Ti-rich alloys, superlattice dislocations are mostly operative below the peak temperature in the Al-rich side. Analyzing Ti-54.5at.%Al, Jiao et al. [160] noted that a major part of the slip occurs via the <0l1] superdislocations in the temperature range below the peak. On the other hand, {111}<101] superlattice slip is found to be a dominant system in Ti-54.7at.%Al and 58.0at.%Al single crystals at all the tested temperatures up to 900°C [140]. Nakano et al. [153] reported that the <101] superlattice dislocations were more often observed than other slip systems. Higher mobility of these dislocations than that of 1/2<110] ordinary dislocations has been confirmed by analyzing many compounds in the composition range 52-60at.%Al. They further explained that the CRSS for the ordinary dislocations rises sharply with increasing Al concentration, while the superlattice dislocations showed no strong sensitivity to the composition. Therefore, ordinary dislocations were dominantly operative in Ti-Al alloys with near-stoichiometric composition, while the motion of superlattice dislocations controlled the plastic behavior of Al-rich Ti-Al. In Ti-52.6at.%Al, the predominant deformation modes change from the ordinary slips to superslips due to the emergence of superstructure [145, 157]. In some Al-rich TiAl single crystal, 1/2<112] type superdislocations are also found to be mainly active at 800°C [161]. One important point is that the superdislocations with 1/2<112] have been observed to dissociate to form faulted dipoles during low-temperature deformation and this dissociation contributes to the strong hardening rate, while at a higher deformation temperature (T = 750°C or more) these dislocations disappear [162]. However, Nakano et al. [139, 158] documented that the 1/2<110] ordinary dislocations are always operative in the $L1_0$ structure like in Ti-rich side. Moreover, they glide on the {111} planes independently in the matrix phase and as a pair in the superstructures of r-Al_2Ti and h-Al_2 in Ti-62.5at.%Al. According to them, ordinary dislocations glide individually although slight threefold grouping is also encountered with the periodicity of h-Al_2Ti [135, 158]. The ordinary slips are operative and independent of the tested temperature and crystal orientation, is also reported in [140]

- Thirdly, ordinary dislocations are suppressed by the LPS. Nakano et al. [130] found that the motion of 1/2<110] ordinary dislocations was suppressed by the development of the Al_5Ti_3-type ordering with increasing Al composition. Nakano et al. [140] also found that the existence of the $L1_0$ matrix with the Al_5Ti_3 phase is closely related to strengthening for the ordinary slip, because the strengthening of ordinary slips was not observed with Al_5Ti_3 single phase single crystals with similar compositions. So it is evident that the plastic deformation behavior and operative slip system in Al-rich off-stoichiometric TiAl crystals are very sensitive to formation of the long-period superstructures such as Al_5Ti_3, h-Al_2Ti and r-Al_2Ti [140]. Nakano et al. [158] concluded that with the addition of Al, <101] slip becomes gradually favored at the expense of $\frac{1}{2}$ <110] ordinary slip as the energy of APBs engendered in Al_5Ti_3 by ordinary dislocations is higher than those created by <101] superlattice dislocations. Because the isolated dislocations created extra APBs behind the dislocations, the pronounced frequency of APB formation must have contributed to the rapid increase in the CRSS till the peak temperature for $\frac{1}{2}$ <110] ordinary slip relative to <101] slip [145]. So the relative motion of ordinary dislocations is difficult compared to superlattice dislocations at lower temperature. At some very low temperature, e.g. -77°C, ordinary dislocation has not been observed in alloys with 56%Al content [163]. Considering $Ti_{50}Al_{50}$ to $Ti_{42}Al_{58}$ alloys, for instance, the critical shear stresses resolved on ordinary and superslips increase by a factor of 4 and 1.5, respectively [136]. Which means extra strengthening is achieved by increasing Al, and mainly ordinary slips gets harder. Studying Ti-62.5.%Al, it is concluded that the CRSS of 1/2<110] ordinary system increases with the growth of h-Al_2Ti and with the increasing of Al concentration and annealing time. The CRSS for the same system further increases with the further formation of superstructures within the $L1_0$ matrix. Like Al_5Ti_3 and h-Al_2Ti phases, the r-Al_2Ti precipitate suppresses the motion of $\frac{1}{2}$ <110] ordinary dislocations resulting in significant strengthening [127].

- Fourthly, transition of slip plane from {111} to {110} and (001). Nakano et al. [139] and Jiao et al. [164] reported that a transition of predominance in slip plane from {111} to (001) occurs near and above the peak temperature around 800°C due to the anisotropy of anti-phase boundary (APB) energies on {111} and (001) in the r-Al_2Ti and Al_5Ti_3 phases created by $\frac{1}{2}$ <110] ordinary dislocations [139, 160]. Hayashi et al. [157] further reported that, with the presence of the Al_5Ti_3 superstructure, the transition of slip plane for 1/2<110] ordinary dislocations from {111} to {110} and/or {001} occurred at and above the peak temperature.

- Fifthly, the existence of the regular misfit dislocation network at the interfaces. As long as the lamellar phases in the matrix are very fine, the misfit dislocations were hardly observed in the interlamellar boundaries. Regular misfit dislocations are increased with the coarsening of the lamellae [125] due to discontinuous grain boundary migration as well as continuously by fault migration [122]. Fully coarsened lamellar microstructures contain misfit dislocation networks at the interfaces with orthogonal burger vectors, which results activation of the slip systems along the interface plane [125, 165]. Semi-coherent boundaries containing misfit boundary dislocations are also formed at the interface of the r-Al_2Ti /$L1_0$. This also suggests that strengthening is achieved by the r-Al_2Ti [139].

- Sixth and finally, complex deformation modes at and after the peak temperature. Inui et al. [159] investigated Ti-56at.%Al alloys from -200 to 1100°C for seven different loading orientations. Till 700°C, it is found that the superlattice slips are operative for six orientations, while ordinary slips are operative only for a single case. At 800°C, super slips are replaced by twinning for one orientation, other loading cases are same as before. At 900°C, ordinary slips are replaced by superslips for another loading case, rest are same as the case of 800°C. The operative systems, so far, all belong to the {111} planes. Surprisingly at 1000°C, in addition to {111} planes, ordinary and superslips are found to be operative for some orientations along {110} and (001) planes. The summary is presented in Fig. 2.4.

So it can be summarized that, above the peak temperature, 1/2<110] slip, twinning and 1/2<112] superlattice slip can be considered to be operative depending on the alloy composition and orientation. Ordinary slip 1/2<110] occurs not only along the {111} planes but also on (001) and {1l0} planes for

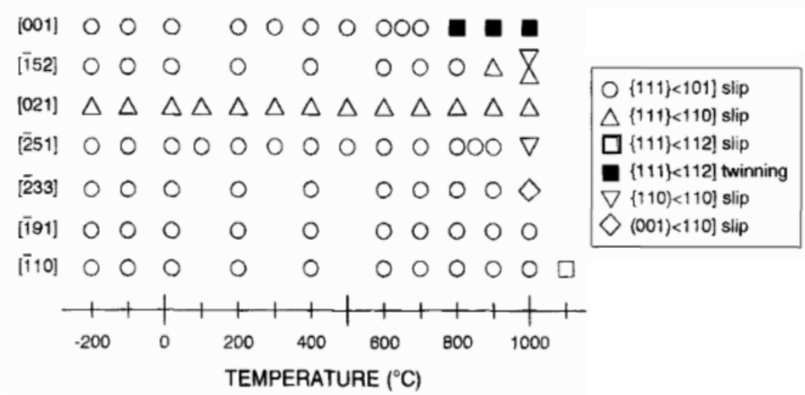

Figure 2.4: Summary of the deformation modes for the seven different orientations investigated in wide temperature range from -200 to 1100°C. Different deformation modes are indicated by different symbols. (Courtesy: [159]).

some orientations [159]. In general, the ordinary slips are active only in a limited range of orientations below the peak temperature [166].

2.8 Yield stress anomaly (YSA)

Anomalous yielding is a very important issue that has been reported in many papers and is not clearly understood for the TiAl alloy family. The slip systems operating in Al-rich γ-TiAl exhibit a pronounced anomalous increase of the critical stress with temperature, specifically near and after the peak temperature. In this regard, Inui et al. [159] is one of the finest contributions in understanding YSA for Al-rich TiAl alloys. Investigating the Ti-56at.%Al alloys with seven different loading orientations, Inui et al. [159] reported that the yield stress varies with temperature in three stages, Fig. 2.5. Firstly at low temperatures, it decreases rapidly with increasing temperature followed by a plateau region up to about 600°C. Secondly, then the yield stress increases anomalously with increasing temperature and reaches a peak at 700-1000°C, depending on crystal orientation. Thirdly, above the peak, it again decreases rapidly with increasing temperature. As mentioned earlier, in the first two stages, the major deformation mode is either ordinary or <101] superlattice slip depending on the crystal orientation. The CRSS for ordinary slip is considerably larger than that of <101] superlattice slip. The third stage is the highest-temperature stage where 1/2<110] slip, twinning and 1/2<112] superlattice slip are identified to be operative. Slip along 1/2<110] occurs not only on {111} but also on (001) and {110}, depending on the orientations [159]. Similar trend has also been observed in alloys with 58-62.5at.%Al, showing the peak of anomaly at 800°C [139]. The microscale yield, or CRSS, is also observed to be anomalous in the same range of YSA. Both the ordinary and <101] superlattice slips exhibit an anomalous increase in the critical resolved shear stress (CRSS). However, the extent of the anomaly associated with the ordinary slip is much smaller than that for the superlattice dislocation slip [159]. Jiao et al. [160] made the similar conclusion mentioning that the observed anomaly in the yield stress reflects mainly an anomaly for <0ll]{111} slip. According

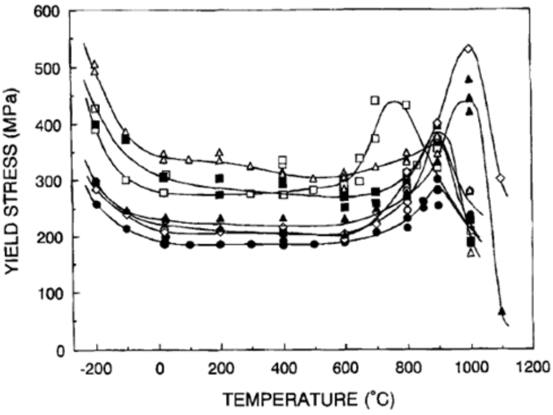

Figure 2.5: Yield stress anomaly against temperature for seven different orientations. (Courtesy: [159]).

to Feng and Whang [155], both the 1/2<110]{111} and <101]{111} slips are two dominant slip systems responsible for the plastic deformation and anomalous hardening in this material, and their presence strongly depends on temperature and applied stress direction. In Al_5Ti_3 single phase single crystals, superlattice slips do not exhibit an anomalous stress peak with Al concentration and thus anomalous strengthening does not appear in that alloys [140]. Interesting to note that the anomaly is not limited to the macroscopic yielding and microscopic CRSS, but also observed in the lattice parameters. Nakano et al. [130] investigated three Al-rich alloys (Ti-58at.%Al, Ti-60at.%Al, Ti-62.5at.%Al) with different annealing temperatures where it is observed that the ratio of the lattice parameters c/a has an anomalous trend of sudden decrease and increasing in the temperature range of 700-900°C. Some other works on the yield stress anomaly in Al-rich side are [164, 167–169]. Analyzing Ti-56at.%Al, Feng and Whang stated that the softening occurs in the third stage with increasing temperature after 900°C, which could mean the decoupling of the anomalous hardening mechanism occurs in the final stage [155].

Two other explanations of YSA in the Al-rich side can be found in the literature. These are the jog formation by cross slip of ordinary dislocations and dislocation lock/unlock by the LPS or minor phases. In Ti-54.5at.%Al single crystals, Jiao et al. [164] observed that the Al-rich γ-TiAl alloys show yield stress anomaly (YSA) between 600-900°C depending on the alloy composition, texture and grain size. With the increasing temperature, due to increasing amounts of larger jogs formation onto {110) planes by cross-slip of ordinary dislocations in gliding on the {111} primary planes is thought to be the cause of the YSA [155, 164]. Hayashi et al. [157] also pointed a similar explanation. The said that the cross slipping of some ordinary dislocation from {111} to {110) and/or (001) planes at elevated temperatures might lead to anomalous strengthening. In the case of the <101]{111} superdislocation glide systems, Appel and Oehring [118] noted that the yield stress anomaly can be attributed to the formation of thermally stable dislocation locks. They further reported that the anomalous yielding and hardening of the 1/2<110]{111} ordinary glide system is probably caused by the formation of an ordered superstructure e.g. Al_5Ti_3 phase. These results provide good supporting evidence that the yield stress

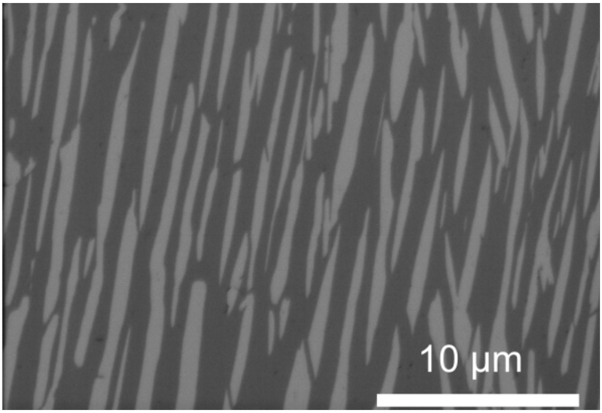

Figure 2.6: Micrograph of nearly lamellar morphology of Ti-61.8at.%Al single crystal like alloy [151], as processed by FIB (Focused Ion Beam), r-plates: bright, and γ-phase: dark.

anomaly can be strongly affected by minor phases present in Al-rich alloys [118]. The yield stress of Ti-62.5at.%Al was approximately twice as large as that of Ti-58at.%Al at and below 1100°C where the r-Al_2Ti precipitates still remained in Ti-62.5at.%Al. This suggests that the anomalous strengthening is achieved by the r-Al_2Ti precipitates [139].

2.9 Basic microstructural features of Ti-61.8at.%Al

In this section, we are going to concentrate on a specific complex alloy with lamellar morphology and LPS. As mentioned earlier, Al-rich TiAl with nearly 62at.%Al is especially important due to the possibility of generating lamellar γ-TiAl + r-Al_2Ti microstructures. Palm et al. [122] reported that after heat treatment at 950°C for 200 h Ti-62at.%Al showed a fully lamellar microstructure of γ-TiAl + r-Al_2Ti where supersaturation with Al is apparently a prerequisite for the formation of such lamellar structure. With the same heat treatment parameters, the as-cast alloy with 62%at.Al contains some metastable phases, for example, numerous h-Al_2Ti and spot of Al_5Ti_3 in some areas. Since Al_5Ti_3 is unstable after 800°C, some spots of this phase disappear after short time annealing and others transforms into the γ-phase. On the other hand h-Al_2Ti transforms (probably by discontinuous dissolution) into equilibrium r-phase after similar heat treatment of 950°C/200h [125]. Here we have chosen a single crystal like an exemplary Al-rich binary intermetallic compound Ti-61.8at.%Al, which consists of lamellar phases of γ-TiAl matrix phase and r-Al_2Ti lamella, Fig. 2.6. As mentioned earlier, the γ-phase has face centered tetragonal (with c/a=1.02) crystal structure and the r-phase is so called superstructure that is actually an ordered sixfold structure of γ-phase together along [001] as shown in Fig. 2.7. It is a general agreement that the r-phase will only display the structure of six fold face centered structure of $TiAl_2$ at around 1000°C [170]. Since our working temperature is 1050°C, according to Sturm [151], this specific alloy with nearly 62at.%Al contains discontinuous lamellar stable phases of γ-TiAl + r-Al_2Ti. The chemical analysis of this alloy is presented in Table 2.1. Volume fraction (γ/r) in the lamellar state is nearly 1.1:1. The volume fraction of r phase depends on the annealing temperature and decreases with the increase of temperature. A

Table 2.1: Compositions of different elements in Ti-61.8at.%Al

Ti	Al	Fe	C	H	O	N
37.0 at.%	61.8 at.%	238 ppm	69 ppm	206 ppm	608 ppm	125 ppm

summary of Ti-62.5%Al on the volume fraction with different annealing temperature can be found in Nakano et al. [137]. Focused ion beam (FIB) processed investigation shows that the average width of a r-Al_2Ti lamella in most regions is about 0.6±0.2 μm while the inter-lamellar spacing is about 1±0.3 μm. Annealed below 1200°C, this alloy maintains the orientation relationship (OR): $[001]_\gamma \parallel [001]_\mathrm{r}$ and $<100]_\gamma \parallel <100]_\mathrm{r}$. At the lamellar boundary, interface planes are parallel, e.g. the γ/r interfaces are basically formed by the (001) planes of both phases [133] maintaining $(001)_\gamma \parallel (001)_\mathrm{r}$.

Due to the ordered superstructure one would expect that the translation vectors (Burgers vectors) are very large in the r-phase. Thus, dislocation glide or climb could be confined to the γ-phase for some specific orientations. Observations also show that the OR is independent of annealing procedures and can approximately be regarded as cubic-to-cubic relationship [151, 170]. Like Ti-rich side, γ-matrix phase is comparatively softer at room temperature.

Furthermore, the investigation revealed that a network of regular misfit dislocations exists at the γ/r inter lamellar boundary interfaces [151], resulting in significant slips on (001) planes above the peak temperature of 800°C [137, 157] with two types of $\frac{1}{2}<110]$ dislocations [125]. Here the dislocations type along the plane (001) is $\frac{1}{2}<110]$. The notations {hkl} and <hkl> generally indicate a set of slip planes and directions, respectively, while (hkl) and [hkl] indicate one specific plane and direction, respectively. A mixed notation <hkl] indicates a subset from the family of symmetric directions without changing the third index. For example, here the line directions of the two types of dislocations denoted by $\frac{1}{2}<110]$ are $\frac{1}{2}[110]$ and $\frac{1}{2}[1\bar{1}0]$. Both types of dislocations are near-edge dislocations along the (001) interface plane, and the interfacial misfit of approximately 0.6% may exist between γ/r planes [125].

The r-Al_2Ti precipitates suppress the motion of $\frac{1}{2}<110]$ ordinary dislocations at lower temperature regimes resulting in significant strengthening [127]. Semi-coherent boundaries containing boundary dislocations are formed at the interface of the r-Al_2Ti /$L1_0$. This also suggests that strengthening is achieved by the r-Al_2Ti [139].

2.10 Deformation mechanisms of Ti-61.8at.%Al at high homologous temperature

As documented in many papers, $\{111\}\frac{1}{2}\langle 110]$ slip was dominant at temperatures below the peak, while there are some reports stating that slip predominance might change to (001) plane above the peak temperature. Similar behavior is also observed in Ti-62.5at.%Al and Ti-58.0at.%Al. Slight slip traces on (001) were observed in Ti-62.5at.%A1 even below the peak temperature. The dislocations in the r-Al_2Ti precipitate are aligned on a straight line parallel to $\frac{1}{2}[110]$ with a screw character [139]. It should be noted that in the case of large scale glide, even at high-temperatures, slip planes {111} are significant [118], these planes cannot be neglected as we have seen in Fig. 2.4. Experimental evidence for slip of ordinary dislocations on (001) plane was also obtained at elevated temperatures for other Al-rich TiAl alloys with nearly similar compositions, what is unique for high-temperature deformation of Al-rich TiAl alloys including Ti-61.8at.%Al. Since superdislocation slips are kinematically necessary and most of the times

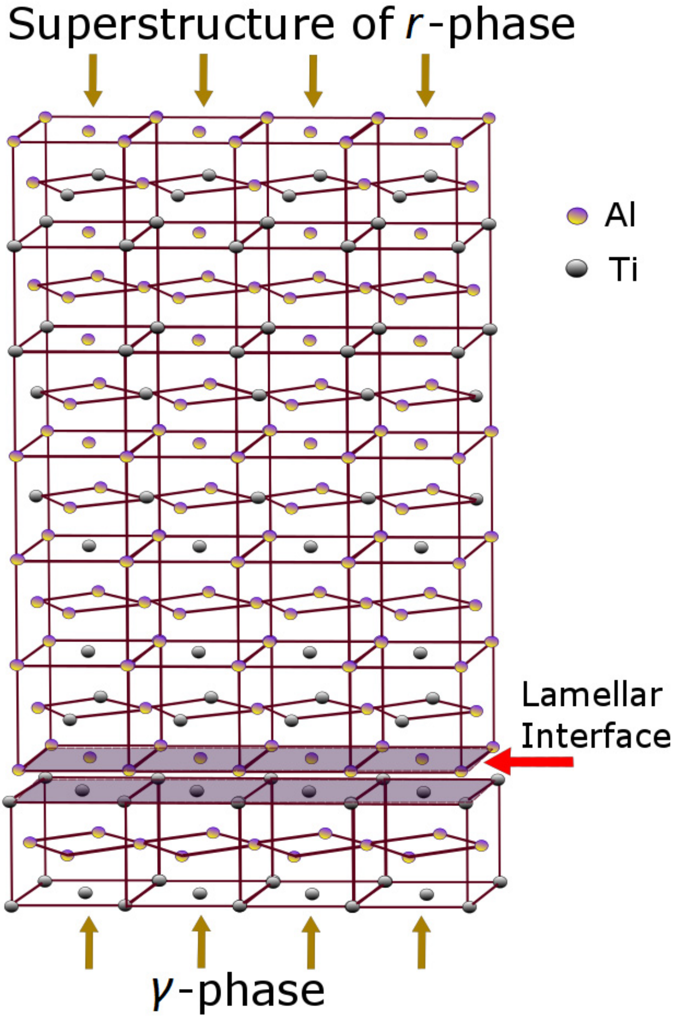
Superstructure of r-phase
Al
Ti
Lamellar Interface
γ-phase

Figure 2.7: Crystal structures of the γ-TiAl phase (bottom) with FCC lattice, the r-$TiAl_2$ phase (top) with FCC long-range order, and their schematic periodic arrangement, and interface in between

they are experimentally observed for alloys with similar compositions, here we will consider all twelve systems from the octahedral family. Analyzing deformation mechanisms of similar Al-rich lamellar alloys (Ti-61.8at.%Al, Ti-62at.%Al and Ti-62.5at.%Al) we considered both families, e.g. {111} and (001), are active at elevated temperature. This alloy does not contain any superstructure other than r-Al$_2$Ti and there is no experimental evidence that {110} plane is active for this specific material above the peak temperature. Slip systems parallel to the interface are commonly agreed to be operative. To account indirect lamellar interface effects, considering slip planes perpendicular to the interface are also important, so we will consider all six systems from the cubic family. In total we will consider all 18 slip systems from the both families. Besides in a rate-dependent formulation, all slip systems potentially can be active for stress above the threshold even though only a few slip systems accommodate most of the deformation [171–173]. After all, considering few non active systems in rate-dependent case does not make a significant change in the overall results.

Particularly in the case of Ti-61.8at.%Al alloy, the dislocation glide is obvious and the climb is inescapable as the working temperature is greater than 0.7_{m}. Not only deformation of the γ phase is supported by the climb of ordinary dislocations but also these factors make the co-deformation of the two phases easier and ensure strain continuity, as instructed for lamellar TiAl alloys [118]. For this reason, the strength difference between the two phases which is significant at room temperature becomes less at that high-temperature. Moreover, the detailed deformation mechanisms specifically for this alloy is not well-known, for example which locks and dislocation processes are dominating. Phase transformation is unlikely for the concerned alloy because of the stability of two phase at the working temperature. Recrystallization cannot take place as the alloy is single crystal like. It is not experimentally confirmed that whether the phase coarsening and dissolution is present. If present then their relative contribution in deformation process are not known. How influential is the static recovery effect is also not assessed. Irrespective of the presence of some unknown mechanisms, the macroscopic collective behavior is expected to be reflected by hardening and recovery mechanism. This hardening-recovery treatment of dislocation-based hardening has been well-established in the literature where Armstrong and Frederick in 1966 first established the evolution of dislocation density in a hardening-recovery format [174]. So the choice of the model for this alloy is based on the phenomenology of hardening/recovery. Other deformation mechanisms such as grain boundary sliding and twinning etc. are not applicable for this single crystals.

2.11 Experimental procedures and test data

For the preparation of test samples, at first, polycrystalline ingots of Al$_{62}$Ti$_{38}$ alloy (ϕ=6.5 mm and L=90 mm) have been produced by centrifugal casting process. Then subsequent annealing at 950°C/200h and water quenching have been applied. Directional solidification using a laser zone melting process has been applied to produce single crystal like specimen of Ti-61.8at.%Al with nearly lamellar morphology of γ-TiAl + r-TiAl$_2$ phases, as shown in Fig. 2.6. Compression tests at 1050°C have been applied on the specimens of $5.5\times3.1\times$ 3.5 mm^3 size with three different strain rates (10^{-3} s^{-1}, 10^{-4} s^{-1} and 10^{-5} s^{-1}).

Two sets of experimental data related to rate-dependent anisotropy of the concerned alloy are available. we have deformation responses for three different strain rates for two lamellar orientations. The first set is about true stress vs. plastic strain for three different strain rates of 10^{-3} s^{-1}, 10^{-4} s^{-1} and 10^{-5} s^{-1} when compression axis is perpendicular to the lamellar axis. In other set, we have only the peak stresses

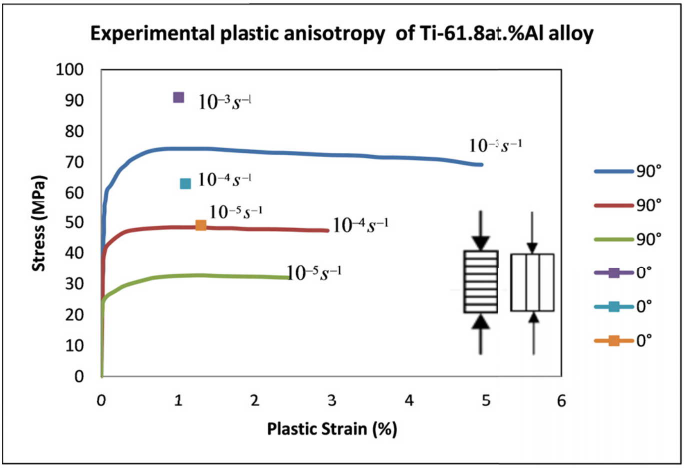

Figure 2.8: Experimental stress vs plastic strain data for three different strain rates at 1050°C [151]. Three curves are taken when $\phi = 90°$ and three peak stress points are taken at $\phi = 0°$. The specimen size was $3.1 \times 3.8 \times 5.5$ mm^3

i.e. the maximum stresses at the end of first stage of deformation for three above strain rates when both compression and lamellar axes are parallel. Both sets were taken from the work of Sturm (2010) [151]. For convenience, lets say, $\phi = 90°$ orientation, when the compression axis is perpendicular to the lamellar direction; and $\phi = 0°$ orientation, when the lamellar axis is parallel to the loading direction. If we look at the experimental data (true stress vs true strain in Fig. 2.8) we can see there is strain hardening and there is significant recovery of hardening in the next stage due to climb assisted deformation with possible other softening effects. Unlike complete deformation behavior at $\phi = 90°$, we have three peak stress points only when $\phi = 0°$. Because the second set of data at $\phi = 0°$ was taken for estimating rate sensitivity parameter for which peak stresses at different rates are enough. From Fig. 2.8, We can also see that $\phi = 0°$ lamellar orientation exhibits higher stress than that of $\phi = 90°$, which is in contrast with Ti-rich intermetallic of PST (polysynthetically twinned) crystals.

Chapter 3

Micromechanical modeling approach

3.1 Continuum framework for crystal plasticity

In this section we will summarize the continuum framework based on finite strain and finite rotation. Tensors are presented with bold and italic characters, vectors and matrices are bold and upright, and non-bold symbols are scalars. For better comprehensibility, index notation has been thoroughly avoided. It is well known that the geometric basis of the continuum slip theory of finite crystal plasticity is a multiplicative decomposition of the local deformation gradient ($\boldsymbol{F}$) into a plastic part, solely due to crystalline slip on given crystallographic planes ($\boldsymbol{F}^p$), and a remaining part ($\boldsymbol{F}^*$), say elastic part. Elastic distortion as well as rigid-body rotations (lattice rotation) are both contained in $\boldsymbol{F}^*$ which maps the intermediate configuration to the current configuration [175]. According to isoclinic assumption, the plastic deformation is assumed here to take place first, followed by the elastic deformation, as shown in Fig. 3.1. This framework is a summary following Asaro and Rice [176] and Asaro [177]. The deformation gradient, $\boldsymbol{F}$, is as usually decomposed as:

$$\boldsymbol{F} = \boldsymbol{F}^* \cdot \boldsymbol{F}^p, \tag{3.1}$$

Since the plastic deformation is taken to be volume preserving, so the incompressibility condition,

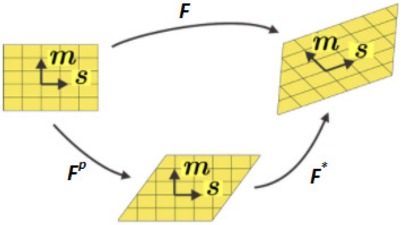

Figure 3.1: Kinematic decomposition of deformation gradient in crystal plasticity showing a slip system. Courtesy: www.mm.ethz.ch

det$\boldsymbol{F}^p = 1$ holds. The fundamental geometric ansatz of the continuum CP theory is to macroscopically describe the plastic deformation as shearing of given crystallographic slip systems, as shown in Eq. (3.2). This macroscopic picture is micromechanically motivated by the movement of dislocations through an idealized crystal lattice [178]. The velocity gradient follows the standard expression as:

$$\boldsymbol{L} = \dot{\boldsymbol{F}}^{*}\cdot \boldsymbol{F}^{*-1} + \boldsymbol{F}^{*}\cdot (\dot{\boldsymbol{F}}^{p}\cdot \boldsymbol{F}^{p-1})\cdot \boldsymbol{F}^{*-1} = \dot{\boldsymbol{F}}^{*}\cdot \boldsymbol{F}^{*-1} + \sum_{\alpha=1}^{N} \dot{\gamma}^{\alpha}(\mathbf{s}^{\alpha} \otimes \mathbf{m}^{\alpha}) \tag{3.2}$$

where $\dot{\gamma}^{\alpha}$ is the slipping rate along the slip system α, N is the total number of slip systems, and the vectors $\mathbf{s}^{\alpha}$ and $\mathbf{m}^{\alpha}$ define the slip direction and the normal to the slip plane in the deformed configuration, respectively. It is to be noted that $\mathbf{s}^{\alpha}$ and $\mathbf{m}^{\alpha}$ are not necessarily unit vectors, but at the initial configuration, $\mathbf{s_0}^{\alpha}$ and $\mathbf{m_0}^{\alpha}$, they are unit and orthogonal. So it is obvious that $\mathbf{s}^{\alpha} = \boldsymbol{F}^{*}\cdot \mathbf{s_0}^{\alpha}$. To maintain orthogonality in the deformed state it is necessary to define $\mathbf{m}^{\alpha} = \mathbf{m_0}^{\alpha}\cdot \boldsymbol{F}^{*-1}$ so that $\mathbf{m_0}^{\alpha}\cdot \mathbf{s_0}^{\alpha} = \mathbf{m}^{\alpha}\cdot \mathbf{s}^{\alpha} = 0$. The velocity gradient $\boldsymbol{L}$ can also be decomposed as:

$$\boldsymbol{L} = \boldsymbol{D} + \boldsymbol{W} = (\boldsymbol{D}^{*} + \boldsymbol{W}^{*}) + (\boldsymbol{D}^{p} + \boldsymbol{W}^{p}) \tag{3.3}$$

where $\boldsymbol{D}$ and $\boldsymbol{W}$ are, the symmetric and antisymmetric part of $\boldsymbol{L}$, expressing the rate of stretching and the spinning (rate of rotation), respectively.

$$\boldsymbol{D} = \frac{1}{2}(\boldsymbol{L} + \boldsymbol{L}^{t}) \tag{3.4}$$

$$\boldsymbol{W} = \frac{1}{2}(\boldsymbol{L} - \boldsymbol{L}^{t}) \tag{3.5}$$

A constitutive law can be expressed as the relationship between $\boldsymbol{D}^{*}$ and $\overset{\nabla *}{\boldsymbol{\sigma}}$, as given in Eq. (3.6), where $\boldsymbol{D}^{*}$ is the elastic part of the symmetric rate of stretching and $\overset{\nabla *}{\boldsymbol{\sigma}}$ is the Jaumann rate of the Cauchy stress with respect to lattice spin ($\boldsymbol{W}^{*}$). In other words, $\overset{\nabla *}{\boldsymbol{\sigma}}$ is the corotational stress rate of the Cauchy stress formed on axes that spin with the lattice [177].

$$\overset{\nabla *}{\boldsymbol{\tau}} = \boldsymbol{\mathcal{L}}\colon \boldsymbol{D}^{*} - \boldsymbol{W}^{*}\cdot \boldsymbol{\tau} + \boldsymbol{\tau}\cdot \boldsymbol{W}^{*} \simeq \boldsymbol{\mathcal{L}}\colon \boldsymbol{D}^{*} = \boldsymbol{\mathcal{L}}\colon (\boldsymbol{D} - \boldsymbol{D}^{p}) = \overset{\nabla *}{\boldsymbol{\sigma}} + \boldsymbol{\sigma}(\boldsymbol{I}\colon \boldsymbol{D}^{*}) \tag{3.6}$$

In Eq. (3.6), $-\boldsymbol{W}^{*}\cdot \boldsymbol{\tau} + \boldsymbol{\tau}\cdot \boldsymbol{W}^{*}$ is often neglected comparing with $\boldsymbol{\mathcal{L}}\colon \boldsymbol{D}^{*}$, $\boldsymbol{I}$ is the second-order unit tensor, $\boldsymbol{\mathcal{L}}$ is the fourth-order elastic stiffness tensor and $\overset{\nabla *}{\boldsymbol{\tau}}$ is the Jaumann rate of the Kirchhoff stress formed on axes that spin with the lattice [177]. The last part of the equation, i.e. the relation between $\boldsymbol{D}^{*}$ and $\overset{\nabla *}{\boldsymbol{\sigma}}$ is followed by Hill and Rice [72]. The objective stress rate $\overset{\nabla *}{\boldsymbol{\sigma}}$, or the Jaumann stress rate of the Cauchy stress tensor based on the rotation of the crystal lattice or lattice spin $\boldsymbol{W}^{*}$ can be expressed as:

$$\overset{\nabla *}{\boldsymbol{\sigma}} = \dot{\boldsymbol{\sigma}} - \boldsymbol{W}^{*}\cdot \boldsymbol{\sigma} + \boldsymbol{\sigma}\cdot \boldsymbol{W}^{*} \tag{3.7}$$

We also can write Jaumann rate with respect the rotation of the material or based on the continuum spin as:

$$\overset{\nabla}{\boldsymbol{\sigma}} = \dot{\boldsymbol{\sigma}} - \boldsymbol{W}\cdot \boldsymbol{\sigma} + \boldsymbol{\sigma}\cdot \boldsymbol{W} \tag{3.8}$$

When there is no relative rotation of the material and lattice or only elastic deformation then $\overset{\nabla *}{\boldsymbol{\sigma}} = \overset{\nabla}{\boldsymbol{\sigma}}$. From Eqs. (3.7) and (3.8) we can correlate both objective stress rate or Jaumann rates of the Cauchy stresses as:

$$\overset{\nabla *}{\boldsymbol{\sigma}} = \overset{\nabla}{\boldsymbol{\sigma}} + (\boldsymbol{W} - \boldsymbol{W}^{*})\cdot \boldsymbol{\sigma} - \boldsymbol{\sigma}\cdot (\boldsymbol{W} - \boldsymbol{W}^{*}) \tag{3.9}$$

Now let split the symmetric and antisymmetric part of the tensor $(\mathbf{s}^{\alpha} \otimes \mathbf{m}^{\alpha})$ as $\boldsymbol{\mu}^{\alpha}$ and $\boldsymbol{\omega}^{\alpha}$.

$$\boldsymbol{\mu}^{\alpha} = \frac{1}{2}(\mathbf{s}^{\alpha} \otimes \mathbf{m}^{\alpha} + \mathbf{m}^{\alpha} \otimes \mathbf{s}^{\alpha}) \tag{3.10}$$

$$\boldsymbol{\omega}^{\alpha} = \frac{1}{2}(\mathbf{s}^{\alpha} \otimes \mathbf{m}^{\alpha} - \mathbf{m}^{\alpha} \otimes \mathbf{s}^{\alpha}) \tag{3.11}$$

So we can write:

$$\boldsymbol{W} - \boldsymbol{W}^{*} = \boldsymbol{W}^{p} = \sum_{\alpha=1}^{N} \boldsymbol{\omega}^{\alpha} \dot{\gamma}^{\alpha} \tag{3.12}$$

$$\boldsymbol{D} - \boldsymbol{D}^{*} = \boldsymbol{D}^{p} = \sum_{\alpha=1}^{N} \boldsymbol{\mu}^{\alpha} \dot{\gamma}^{\alpha} \tag{3.13}$$

Using Eqs. (3.9) and (3.12) we can write:

$$\overset{\triangledown *}{\boldsymbol{\sigma}} = \overset{\triangledown}{\boldsymbol{\sigma}} + \sum_{\alpha=1}^{N} \boldsymbol{\omega}^{\alpha} \dot{\gamma}^{\alpha} \cdot \boldsymbol{\sigma} - \boldsymbol{\sigma} \cdot \sum_{\alpha=1}^{N} \boldsymbol{\omega}^{\alpha} \dot{\gamma}^{\alpha} \tag{3.14}$$

Hence,

$$\overset{\triangledown}{\boldsymbol{\sigma}} = \boldsymbol{\mathcal{L}} \colon \boldsymbol{D} - \boldsymbol{\sigma}(\boldsymbol{I} \colon \boldsymbol{D}) - \sum_{\alpha=1}^{N} \left[\boldsymbol{\mathcal{L}} \colon \boldsymbol{\mu}^{\alpha} + \boldsymbol{\omega}^{\alpha} \cdot \boldsymbol{\sigma} - \boldsymbol{\sigma} \cdot \boldsymbol{\omega}^{\alpha} - \boldsymbol{\sigma}(\boldsymbol{I} \colon \boldsymbol{\mu}^{\alpha})\right] \dot{\gamma}^{\alpha} \tag{3.15}$$

Following the above procedure, the expression for $\overset{\triangledown *}{\boldsymbol{\tau}}$ and $\overset{\triangledown}{\boldsymbol{\tau}}$ can be deduced. In this regard, Asaro (1980) [177] can be consulted as well. In Eq. (3.15), $\overset{\triangledown}{\boldsymbol{\sigma}}$ is the Jaumann stress rate of the Cauchy stress tensor based on the rotation rate of the crystal lattice. Therein the operator $\colon$ as usually indicates the double inner dot product or double contraction. Following the expression of the plastic rate of working $\tau \colon \boldsymbol{D}^{p} = \sum_{\alpha=1}^{N} \tau \colon \boldsymbol{\mu}^{\alpha} \dot{\gamma}^{\alpha}$ the resolved shear stress τ^{α} can be identified in terms of Kirchhoff stress $\boldsymbol{\tau}$ as follows:

$$\begin{aligned} \tau^{\alpha} &= \mathbf{s}^{\alpha} \cdot \boldsymbol{\tau} \cdot \mathbf{m}^{\alpha} = \mathbf{m}^{\alpha} \cdot \boldsymbol{\tau} \cdot \mathbf{s}^{\alpha} = \mathbf{m}^{\alpha} \cdot J\boldsymbol{\sigma} \cdot \mathbf{s}^{\alpha} = \mathrm{sym}(\mathbf{s}^{\alpha} \otimes \mathbf{m}^{\alpha}) \colon J\boldsymbol{\sigma} \\ &= \boldsymbol{\mu}^{\alpha} \colon J\boldsymbol{\sigma} = \boldsymbol{\tau} \colon \boldsymbol{\mu}^{\alpha} \end{aligned} \tag{3.16}$$

For small elastic strains, it is to be noted that the volumetric change resulting from the elastic stretch of crystal is usually very small. Therefore, the assumption that $J \approx 1$ (i.e. tr$\boldsymbol{L} \approx 1$) is generally justified and no distinction between the Kirchhoff and Cauchy stresses is needed in practical or engineering computations [179]. So for small elastic strains formulation it is often taken as $\tau^{\alpha} = \boldsymbol{\sigma} \colon \boldsymbol{\mu}$ [28].

There are various possibilities of defining the rate formulations, e.g. $\dot{\mathbf{m}}^{\alpha}$ and $\dot{\mathbf{s}}^{\alpha}$, depending on how we consider orthogonal system $\mathbf{m}^{\alpha}$ and $\mathbf{s}^{\alpha}$ behaves with the slip plane in the deformed state. Several possibilities are discussed in the work of Asaro and Rice (1977) [176]. Similarly different considerations for defining $\dot{\tau}^{\alpha}$ is also discussed in detail in the work of Asaro (1983), though differences in the various choices for the $\dot{\tau}^{\alpha}$'s are of the order of the elastic strain rates and are thus usually negligible [177]. Here we consider the case where the vector $\mathbf{s}^{\alpha}$ convects with the slip plane so that its lengths changes in accordance with the deformation of the lattice-slip plane and $\mathbf{m}^{\alpha}$ also changes its length but remains normal to the deformed slip plane. The interesting part of this version is, along with Eq. (3.16) it maintains the normality precisely in work conjugate variables. As given in [177], the rate formulations are:

$$\dot{\mathbf{s}}^{\alpha} = (\boldsymbol{D}^{*} + \boldsymbol{W}^{*}) \cdot \mathbf{s}^{\alpha}, \qquad \dot{\mathbf{m}}^{\alpha} = -\mathbf{m}^{\alpha} \cdot (\boldsymbol{D}^{*} + \boldsymbol{W}^{*}) + \mathbf{m}^{\alpha}(\boldsymbol{I} \colon \boldsymbol{D}^{*}) \tag{3.17}$$

Hence the rate form of the resolved shear stress will be:

$$\dot{\tau}^{\alpha} = \mathbf{m}^{\alpha}\cdot \left[\overset{\triangledown *}{\boldsymbol{\sigma}} + \boldsymbol{\sigma}(\boldsymbol{I}\colon \boldsymbol{D}^{*}) - \boldsymbol{D}^{*}\cdot \boldsymbol{\sigma} + \boldsymbol{\sigma}\cdot \boldsymbol{D}^{*} \right] \cdot \mathbf{s}^{\alpha} \tag{3.18}$$

With Eqs. (3.15) and (3.16), Eq. (3.18) can be put in the following form, as shown by Peirce et al. [180] for rate-dependent formulation as:

$$\dot{\tau}^{\alpha} = \left\{ \sum_{\alpha=1}^{N} (\boldsymbol{\mathcal{L}}\colon \boldsymbol{\mu}^{\alpha} + \boldsymbol{\omega}^{\alpha}\cdot \boldsymbol{\sigma} - \boldsymbol{\sigma}\cdot \boldsymbol{\omega}^{\alpha}) \right\} \boldsymbol{:} \boldsymbol{D}^{*} \tag{3.19}$$

Chapter 4

Crystal viscoplasticity modeling: Choosing a power-law

4.1 Introduction

Flow-rule is the starting point in analysis of plastic deformation phenomena. In a plastic flow-rule, we generally deal with the relation of measurable variables (strain rate, temperature) and associated variable (stress) along with one or more internal variables. In contrast to phenomenological internal variables, first two types (i.e. measurable and associated) can be termed as external variables [181]. Similar to other phenomenological modeling approaches in mechanics, classical plasticity modeling including crystal plasticity is based on the incorporation of one or more internal state variables which are, in general, functional of the histories of the external ones. Plastic deformation depends on the loading history and on the continuously changing internal states that are considered representable by one of more internal variables. How many internal variables should be considered and how to deal with the phenomena of hardening i.e. how to accommodate hardening in the internal variables is a crucial issue in developing a proper flow-rule. Depending on the microstructural and morphological complexity and the related deformation mechanisms associated with, the number of internal variables can be one or more. In micromechanical modeling especially in crystal plasticity, earlier models considered flow-rule with one internal variable where hardening phenomena was accommodated as interactions of different slip systems. Accordingly, it was divided into self and latent based phenomena. On the other hand, there are a number of modeling approaches that consider slip system level backstress as an additional internal variable. In such cases, most micromechanical processes (e.g long-range internal stress) related to the hardening interactions (latent hardening) is included in the evolution of backstress. So this type of models include separate terms for the evolution of backstress and self-latent hardening. In some other models, latent hardening is completely avoided. There are two more issues that are involved in choosing a flow-rule. Firstly, the type of flow-rule e.g whether the flow-rule is power-law type or hyperbolic-sine, exponential or mixed type. Secondly, the arrangement of the ratio of plastic driving force to the flow resistance. Whatever the variety in the above issues, one of the most important part of these flow-rules is the ratio of the plastic driving force to the flow resistance, or dimensionless stress quantity, which directs the internal slip mechanisms and activities during inelastic deformation. Specific choice of the definition leads to a unique number of consequences. Some authors recently considered this ratio both in the temperature dependent term and in the remaining term with power exponent, such flow-rules can be found in dislocation density based crystal plasticity modeling [93, 182]. The foremost point is, how to define effective stress in the dimensionless quantity, which is to be considered as the driving force for the plastic deformation and how to define the yield, drag, or flow resistance along a slip system.

All flow-rules can be roughly associated with different stress levels.

- Firstly, moderate stress level.
  Engineering applications dominate this regime where power-law usually works fine. For example, power-law creep has been used in Cui et al. [183] and Alfredsson et al. [184] for steel, in Vose et al. [185] and Yang et al. [186] for Cu, in Naumenko and Gariboldi [187] for Al, and in Staroselsky and Cassenti [188] for a single crystal superalloy, etc. Because of smaller effort in identification of material constants and simplicity in the structural analysis power-laws are popular [189]. To accommodate power-law with primary and tertiary creep often additional internal state variables along with damage variable are included [190].

- Secondly, low and moderate stress.
  At low stress, generally a transition to diffusion type creep occurs (Harper-Dorn Creep) where power exponent decreases and power-law becomes linear [189]. Many engineering structural analyses belong to these regimes. Sometimes a sum of linear (diffusion type) and power-law functions is applied to accommodate deformations with both low and moderate stress levels [189, 190]. When the power-law is extrapolated from moderate to low stress regime, a significant underestimation of the creep rate for the low stress values may result [183,189]. That is why sometimes hyperbolic-sine function without power exponent is used [191]. Similar laws can also be found in [192] and [193].

- Third and finally, moderate and high stress.
  Generally breakdown of power-law is observed at high stress. Sometimes a transition from climb dominated to glide dominated plastic flow might result power-law breakdown [44]. As a consequence, flow-rule with hyperbolic-sine is preferred when there is a breakdown of power-law or a transition from power-law to power-law-breakdown regime [30] i.e. medium to high stress regimes. Hyperbolic-sine flow-rule can be either Garofalo type [194] which is usually good for hot working analysis and the power exponent is outside the hyperbolic-sine function, or Miller Type [195] i.e. the two power exponents in both inside and outside of the hyperbolic-sine function. With two power exponents of inside and outside of hyperbolic-sine function, Miller [195] considered it as a generalized flow-rule for monotonic, cyclic and creep deformation. Flow-rule with power of hyperbolic-sine function has also been used in Becker [196] for texture evolution in channel die compression, in Chen and Feng [197] for cyclic viscoplasticity, in Zhang [198] for hot deformation of Ni alloy GH4698, in Längler et al. [199] for thermo-mechanical loading dependent deformation etc. Chen and Feng [197] also reported that the hyperbolic-sine function can capture additional non-linearity in the relationship between the viscous-stress and the inelastic strain rate. Some studies, [200–202] for example, considered the power-law with hyperbolic-sine function as a possible general case, which reduced to a power relation at lower stresses and to an exponential relation at high stress levels. Hence it describes well the flow stress dependence of strain rate for the entire stress/strain rate regime in hot working applications. Barrett et al. [203] claimed that the hyperbolic-sine flow-rule facilitates the identification of strain-rate-independent material

parameters at high-temperature. To model the complete stress regime of a typical power plant component single power-law exponent is not sufficient. The use of a hyperbolic-sine material model can overcome this drawback and allows for reliable interpolation and extrapolation beyond a limited range of experimental data [204]. Kowalewski et al. [205] noted that the hyperbolic-sine function is the best one to describe the strain rate and rupture behavior, while according to Dyson and McLean [191] it is advantageous in damage evaluation as well. They [191, 206] also argued that for particle or precipitation-strengthened alloys, a kinetic creep equation based upon either an empirical or a theoretical power-law is inadequate, alternative functional hyperbolic-sine form can explain the differences in a polycrystalline and directionally-solidified alloy. Dyson and Osgerby also proposed that climb and glide occur as a parallel, rather than a sequential process, where the creep strain can be associated with a hyperbolic-sine dependence on the applied stress [207]. For the jogs on screw dislocations (jogs are of edge character) driven creep where they move by climb (emission/absorption of point defects or interstitials), Barrett and Nix found the a hyperbolic-sine dependence [208]. When both climb and glide are modeled and that the collective behavior of dislocations, which is not amenable to simple analytical treatment, contributes to the power-law dependence [209]. Forward and backward thermal activation of vacancies might cause the hyperbolic-sine dependence of the strain rate on the stress [44]. Furthermore, apart from hyperbolic-sine, sometimes flow-rule with power exponent inside an exponential function can also be found e.g. in [210] for two phase single crystal deformation.

In plastic/creep deformation, there are usually three stages or regimes of behavior, where each regime can be fit (over a range of stress) by a power-law [211]. There are mechanism based stage dependent flow-rules as well. A pure power relation of strain rate and stress is often used to characterize steady creep (stage II where hardening is balanced by the dynamic recovery) of metal and alloy at temperature above $0.3T_m$ in the stress range of one or two digits, below a certain stress level. Experimental data show that power-law can be applied for one to two order of stress, four to eight order of strain rate [212]. So, if we want to model all three regions with a power-law then a little compromise in at least one stage is not unexpected. Each power-law type flow-rule generally takes a term of stress or dimensionless stress like quantity with a power exponent. In these flow-rules, temperature dependency is often accommodated by a separate multiplicative Arrhenius type function, even sometimes this function is considered with a power exponent, like temperature dependent drag variable in the power-law [213] type flow-rule. In spite of various flow-rules, power-law is the most widely used one in engineering calculations both at low and high-temperatures because of its effectiveness in simulating steady state creep. They have retained a pre-eminent position in both the metallurgical and mechanics literature [191]. Irrespective of the scale whether it is micro or macro, whether the flow-rule is phenomenological or mechanism based [214], the application of the power-law type flow-rule is abound in the literature especially at high homologous temperature and moderate to low stress conditions [215]. Specifically in crystal plasticity, power-law remains as the central one, and hence, our focus is limited to the power-law flow-rules of crystal plasticity. Moreover, it is believed that power-laws are founded on the basis of physical processes. Based on the driving force and flow resistance definitions there are three types of flow-rules, mostly used for isothermal case, generally found in the literature for classical crystal plasticity, as shown in Eqs. (4.1)-(4.3). See for example [216–219], among others. These commonly used flow-rules are purely phenomenological. The numerators (effective or operative stress) inside the rate sensitivity exponent n in all three equations represent the driving force, while the denominators represent some sort of slip resistance. In this work we will try to highlight different aspects based on the choice of the flow-rule with the possibility of accommodating climb driven recovery at high-temperature.

$$\dot{\gamma}^{\alpha} = \dot{\gamma}_0 \left| \frac{\tau^{\alpha}}{g^{\alpha}} \right|^n \operatorname{sgn}(\tau^{\alpha}) \tag{4.1}$$

$$\dot{\gamma}^{\alpha} = \left| \dot{\gamma}_0 \frac{\tau^{\alpha} - X^{\alpha}}{g^{\alpha}} \right|^n \operatorname{sgn}(\tau^{\alpha} - X^{\alpha}) \tag{4.2}$$

$$\dot{\gamma}^{\alpha} = \left\langle \frac{|\tau^{\alpha} - X^{\alpha}| - R^{\alpha}}{K} \right\rangle^n \operatorname{sgn}(\tau^{\alpha} - X^{\alpha}) \tag{4.3}$$

Here $\dot{\gamma}^{\alpha}$ indicates the slip rate of the slip system α, τ^{α} is the shear stress, X^{α} is the backstress or the internal stress of the same slip system. The threshold stress g^{α} and R^{α} both can be considered as a component of friction that evolves with slip [96]. In Eq. (4.3), K is the temperature dependent drag while g in Eqs. (4.1)-(4.2), and X and R in Eqs. (4.2)-(4.3) are phenomenological internal variables. The internal variable R or g can be considered for the critical resolved shear stress (CRSS) evolution. Inclusion of backstress in the model by strain hardening and dynamic recovery is simple and physically sound [35]. Moreover, it allows us to distinguish a tensile and a compressive yield strength. This flow-rule should be considered as an extension to the micro-level of macroscopic model including isotropic and nonlinear kinematic hardening [28]. K and n are two material coefficients characterizing the viscous effect of a hardened material. Macaulay brackets $< y >$ indicate the following:

$$< y > = \begin{cases} y, & y \geq 0 \\ 0, & y < 0 \end{cases} \tag{4.4}$$

Due to the microstructural and morphological complexity, the plastic behavior of a single crystal material is inherently anisotropic [70]. More and more complex materials (e.g. intermetallic compounds) are currently of growing interest at high-temperature applications. So sophisticated microstructures nowadays are becoming heterogeneous and complex. Therefore, for a good micromechanical model with superior prediction capability, more microscale phenomena should be considered. In particular, non-Schmid effect, the internal activities in constitutive modeling like interplay between secondary slips and hardening, experimental evidence based slip activities modeling, and correct attribution of material parameters etc. Details of slip interactions are essential in understanding the overall hardening of single crystals. Secondary slips are not only the key to fundamental hardening behaviors, they are also the key to coarse slip band formation and, to a lesser extent, the details of macroscopic shear band formation [220]. The accuracy of the model predictions depends on the characterization of hardening of instantaneous active and inactive slip systems [221]. With few exceptions, nuances of many microscale phenomena have not been analyzed sufficiently. Acute details of slip interactions, which have been commonly neglected in most analyses, are essential in understanding overall hardening of single crystals. Until these issues are resolved in crystalline analysis, the understanding ability to predict deformation behaviors is certain to be limited. Moreover, rate-dependent and temperature dependent anisotropic phenomena are becoming more important. That is why, this work is concerned with the prediction power of the most commonly used approaches in crystal plasticity at very high homologous temperature by analyzing a highly rate sensitive alloy with complex microstructure and morphology and highlights model dependent behaviors particularly slip activities, secondary slip activation, and material parameters etc.

4.2 Choosing flow, hardening and recovery rules

Power-law creep can be regarded as a competition between recovery and work hardening. When a balance is achieved between the rates of these two processes, the material exhibits steady-state creep as shown in [222] for TiAl alloys. Our case is for high homologous temperature ($\approx 0.75T_\mathrm{m}$) with three different strain rate controlled experimental database where stress is observed to be moderate. In such case generally power-law works fine, although for a wide range of advanced functions of stress may be required [223]. As mentioned in the introduction, the choice of the power-law type flow-rule and their corresponding evolution equations depends on the number of internal variables and the assumptions that are made for their evolution. The most fundamental internal variable among them is the CRSS or internal resistance for a slip system. In the earlier works, the evolution of the CRSS was assumed to be dependent mainly on the the consideration of hardening and its interaction. An evolving self and latent based phenomena was frequently used with different expressions of evolution equations in the form of an interaction matrix. Considering a combined hardening-recovery process, we will apply three above flow-rules (4.1-4.3) and will examine which flow-rule can reproduce experimental data with meaningful set of modeling parameters. In addition, we will also examine two more flow-rules based on the phenomena of self and latent hardening in order to check how the most widely used flow-rules behave for this alloy at high homologous temperature. So, considering our alloy condition and all the issues discussed in Sect. 4.1, we can divide the power-law type flow-rules in crystal plasticity into five categories.

4.2.1 Type-1 flow-rule

The fundamental aspect of slip theories is to describe macroscopic plastic deformation as shearing of some given crystallographic slip systems. This macroscopic picture is micromechanically motivated by kinetic relations for dislocation motion through an idealized crystal lattice. An idealized single crystal behavior is based on the early work of Taylor [224] where plastic deformation is assumed to arise solely from slip in certain directions on specific crystallographic planes, and these process occurs when the resolved shear stress (Schmid stress), τ is on one or more of this slip systems reaches a critical value τ_0 (Schmid law) that is determined by the current dislocation density and substructure. Although the Schmid law is a good starting point, the micromechanics of slip on the other hand, suggests that deviation from the Schmid law is inherent at the onset of the dislocation slip itself, regardless of how Kirchoff stress is related to the lattice elasticity. As plastic deformation proceeds the critical yield stresses associated with the slip system can change, usually to raise the yield stresses so that the crystal hardens [225]. Taylor hardening assumed an equal increment of flow stress on all active and latent slip systems for any set of shear increments on the active systems that leading to isotropic behavior of the material [226]. Afterwards, this law has been improved to account dislocation cross-slip, climb, and other micromechanical processes [177]. Thus, instead of Taylor type hardening, many researchers developed modified hardening laws for different materials. Several modifications of hardening laws are often discussed in the literature, a few of them are [180, 226, 227] and [228]. Two popular models of work hardening are dislocation pile ups and forest or secondary dislocations [221, 229]. In general, work hardening is a consequence of the fact that some fraction of the mobile dislocations that produce the strain do not exit through the surface, are not absorbed in grain boundaries, and do not annihilate each other, but are stored in the crystals or react with other dislocations to form new obstacles to continue slip [230]. Depending on the microstructure, when we assume the Schmid stress as the driving force for plastic deformation, slip system yield and drag g as the flow resistance, and hardening is in the form of (self-latent) interaction, then Hutchinson type flow-rule [212], as given in Eq. (4.1), is a good choice. In this case g is the only internal variable. One important aspect of this type flow-rule for cubic crystals is that the CRSS, the initial slip resistance, is independent of the orientation and there is no tension-compression asymmetry. In fact, CRSS depends both upon the orientation of the loading axis as well as the sense of the load; i.e. tension or compression [220]. If the deformation behavior contains several stages including rapid hardening and if there exist different junctions/locks then Bassani-Wu type [228] hardening evolution equation can be chosen. In such case, hardening evolution equations would be as follows.

$$\dot{g}^\alpha = \sum_{\beta=1}^{n} \mathsf{H}^{\alpha\beta} |\dot{\gamma}^\beta| \tag{4.5}$$

$$\mathsf{H}^{\alpha\alpha} = (h_0 - h_s)\,\mathrm{sech}^2\left(\frac{h_0 \gamma_t}{\tau_s - \tau_0}\right) + h_s \tag{4.6}$$

$$\mathsf{H}^{\alpha\beta} = p\mathsf{H}^{\alpha\alpha}, \quad (\alpha \neq \beta), \tag{4.7}$$

$$\gamma_t = \sum_\alpha \int_0^t |\dot{\gamma}^\alpha| dt \tag{4.8}$$

Here γ_t is the cumulative shear strain of all the slip systems. The overall hardening $\mathsf{H}^{\alpha\beta}$ is divided into self ($\mathsf{H}^{\alpha\alpha}$) and latent ($\mathsf{H}^{\alpha\beta}, \alpha \neq \beta$) type phenomena, where self is for active and latent refers to the hardening interaction of the active and inactive slip systems, together $\mathsf{H}^{\alpha\beta}$ represents the hardening evolution. Instantaneous hardening coefficients of $\mathsf{H}^{\alpha\beta}$ depend on the previous deformation history [225]. Two material parameters h_0 and h_s indicate the hardening rate at the beginning and at the saturation point, respectively, while other two parameters τ_s and τ_0 stand for the corresponding stress level, and p is the ratio of latent to self hardening. Worth to mention that the terms for rapid hardening stage (or parabolic hardening, the final stage of hardening where the hardening rate is very high) is not included in Eq. (4.6). The originally proposed hardening equation for three stages of deformation including the rapid one looks like the following equation.

$$\mathsf{H}^{\alpha\alpha} = \{(h_0 - h_s)\,\mathrm{sech}^2\left(\frac{h_0 \gamma_t}{\tau_s - \tau_0}\right) + h_s\}\{1 + \sum_{\beta\neq\alpha} f^{\alpha\beta}\,\tanh(\frac{\gamma^\beta}{\gamma_0})\} \tag{4.9}$$

The additional part in Eq. (4.9) is associated with cross hardening what is usually happens in a complex microstructure, responsible for different locks and junctions like sessile, glissile etc., γ_0 is the amount of slip after which the interaction between slip systems reaches the peak strength. The interaction constant $f^{\alpha\beta}$ represents the magnitude of the strength of a particular interaction. In FCC type single crystals there could be five distinct slip interactions [231] e.g. coplanar interactions, non-coplanar interactions etc. will be discussed in detail in the next section. For some materials, the following equation was used for latent hardening evolution instead of Eq. (4.7).

$$\mathsf{H}^{\alpha\beta} = p(\mathsf{H}^{\alpha\alpha} + \mathsf{H}^{\beta\beta}),\ (\beta \neq \alpha) \tag{4.10}$$

The advantage of this type hardening model is the ability to measure hardening parameters from experimental data except p. The accuracy of these predictions depends on the precise characterization of the hardening of instantaneous active and inactive slip systems [221], which is not easy for materials with

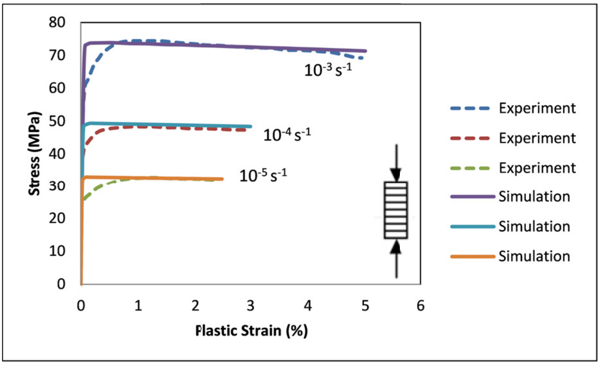

Figure 4.1: Experimental plasticity curves taken from [151] and simulation results for type-1 flow-rule. lamellar and compression axes are perpendicular.

Table 4.1: Identified material parameters for type-1 flow-rule

Parameters	Name	Values
Rate-dependence	Rate sensitivity, n Initial slip rate, $\dot{\gamma}_0$ (1/s)	5.7 0.000007
Isotropic hardening	Initial CRSS, τ_0(MPa) Saturation stress, τ_s(MPa) Initial hardening rate, h_0 Latent hardening ratio, p	15 40 -5.0 1.4

complex microstructures. In essence, this hardening law assumes that hardening is mainly controlled by the competition of storage and annihilation of statistically stored dislocations and its derivation implicitly assumes an average interaction among dislocations gliding on different slip systems and there is nothing about geometrically necessary dislocations.

In our case, deformation is driven by both glide and climb, which is experimentally observed. In spite of that, the purpose of using this glide driven flow-rule is to examine how well the model behaves with the experimental data and how significant is the recovery, and whether this recovery is negligible in high-temperature and moderate stress regime. Experimental single crystal plasticity (true stress vs true strain) curves and simulation results with the flow-rule in Eq. (4.1) and with above evolution equations (4.5-4.8) are shown in Fig. 4.1. Identified material parameters are given in Table 4.1.

Results show that, the above set of flow-rule and hardening law cannot simulate the deformation behavior correctly, especially the hardening stage (first stage) deviates significantly. Although it covers rate-dependency in the hardening/recovery stage, however, the rate sensitivity parameter n is little higher and it cannot reasonably reproduce overall experimental behaviors. Additionally, we need to consider latent hardening coefficient as 1.4 and negative initial hardening rate which is not so meaningful. The point here is, if we cannot choose a proper flow-rule consistent with proper deformation mechanisms then some material parameters might be beyond the meaningful explanation or overestimated.

4.2.2 Type-2 flow-rule

There has been a widespread acceptance in the creep community about the phenomenological idea that creep deformation is not driven by the applied stress, rather by an effective stress, which is the driving force for material deformation. Sometimes this stress is seen as the difference between the applied stress and the so called internal stress, or backstress, often considered to be representative of the material internal state [9, 16]. Thus the effective stress is not simply related to the resolved shear stress (RSS), but stress components which do not contribute to the RSS on active slip systems can contribute to the effective stress [196]. For complex materials, instead of using purely Schmid stress as driving force, incorporating phenomenological slip system level backstress, sometimes termed as resolved backstress, is more meaningful. In crystals in which a heterogeneous dislocation distribution develops during deformation, substantial long-range internal stresses arise unavoidably as a natural consequence of the compatibility requirements in the strain. Deformation results for Cu single crystals, loaded monotonically, demonstrate that small long-range internal stresses are present in cell interiors. This LRIS varies substantially from cell to cell as 0 % to 50 % of the applied stress [92]. The most commonly encountered type of heterogeneous dislocation distribution is the three dimensional cell structure which develops under conditions of multiple slip. As discussed in Sect. 1.6.9, it is suggested that the boundary (e.g. phase boundary) is a source for internal stresses. With the accumulation at the boundary (e.g., a pile-up at the boundary), a backstress is created. So the lattice mismatch/incompatibility can be considered as a source of internal stress for this specific alloy, because GNDs are necessary to accommodate lattice incompatibilities [58]. Geometrically necessary dislocations may form at the interfaces that could assist the backstress. So from GND perspective, internal stresses should exist even under homogeneous loading, because of the additional long-range GND-surface interactions [58]. The presence of micro-level heterogeneities in the microstructure like the formation of inelastic-hard and inelastic-soft regions also justifies the introduction of the internal stress variable. In short, in our alloy, interface dislocations, the presence of long-period superstructures and the strain incompatibility between two phases hence the presence of GND can be considered as potential sources of internal stress.

So let us consider effective stress $\tau - X$ as the driving force, as given in Eq. (4.2). The Evolution of slip system level internal stress or backstress X is adopted from [28] as given below.

$$X^{\alpha} = C^{\alpha} a^{\alpha}, \tag{4.11}$$

$$\dot{a}^{\alpha} = \phi\left(\nu^{\alpha}\right)\dot{\gamma}^{\alpha} - \left|\dot{\gamma}^{\alpha}\right| d^{\alpha} a^{\alpha}, \tag{4.12}$$

$$\phi\left(\nu^{\alpha}\right) = \phi_0 + (1-\phi_0)e^{-\delta\nu^{\alpha}} \tag{4.13}$$

Here ν^{α} is the cumulative shear strain of the slip system α.

$$\nu^{\alpha} = \int_0^t \left|\dot{\gamma}^{\alpha}\right| \mathrm{d}t \tag{4.14}$$

In Eq. (4.11), C is the temperature dependent internal stress of the slip system α, in other words, the internal stress estimate at a fixed operating temperature. The variable a governs the evolution of internal stress and its rate form is based on the one dimensional Armstrong-Frederick [232] type nonlinear kinematic hardening rule. In many cases especially in small strains, the Armstrong–Frederick model for kinematic hardening elasto-plasticity is widely accepted as appropriate for the simulation of the most characteristic phenomena of the hardening behavior of metals [233]. Activation of a slip system depends

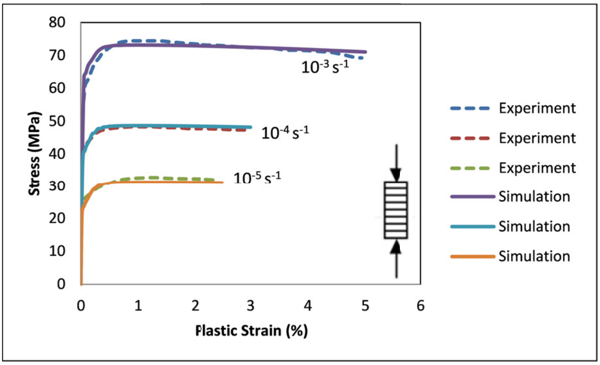

Figure 4.2: Experiment plasticity curves vs. simulation results for type-2 flow-rule. lamellar and compression axes are perpendicular.

Table 4.2: Identified material parameters for type-2 flow-rule

Parameters	Name	Values
Rate-dependence	Rate sensitivity, n Drag Stress, $K(\mathrm{MPa})$	6.93 0.11
Isotropic hardening	Initial CRSS, $\tau_0(\mathrm{MPa})$ Saturation stress, $\tau_s(\mathrm{MPa})$ Initial hardening rate, h_0	11 20 -5.0
Kinematic hardening	Internal stress, $C(\mathrm{MPa})$ Recovery parameter, d Parameters for flow accumulation function, ϕ_0 and δ	2850 50 0.24 and 580

not only on the orientation but also on the deformation history, which contributes to the hardening [234]. So the evolution of the backstress X^α depends not only on the shear rate but also on the deformation history function $\phi\left(\nu^\alpha\right)$. This function $\phi\left(\nu^\alpha\right)$ is responsible for the deformation history effects and it depends on the plastic flow accumulation ν^α with two related parameters ϕ_0 and δ as given in Eq. (4.13). In Eqs. (4.12) and (4.13), d is related to the recovery of the internal stress in a hardening-recovery based evolution equation, d>0 ensures nonlinear internal stress evolution. The the two parameters ϕ_0 and δ related to the flow accumulation function $\phi(\nu^\alpha)$ ensure a reasonable approximation of the slip level kinematic hardening variable. With the increasing of plastic flow, the function $\phi\left(\nu^\alpha\right)$ acts as a coupling between the internal stress and internal resistance. This coupling function $\phi\left(\nu^\alpha\right)$ also helps to avoid under or overestimation of the strain hardening part. Many a time, e.g. monotonic loading case, this coupling function is not necessary. Like internal resistance evolution, the first term in the right side of Eq. (4.12) represents strain hardening and the second part stands for dynamic recovery effects.

Simulation results, Fig. 4.2, show that this type of flow-rule can accommodate experimental behavior but still it needs some unreasonable negative value of h_0 as shown in Table 4.2. The rate sensitivity parameter n is quite high.

4.2.3 Type-3 flow-rule

In the flow-rule of type-1 and 2, internal variable for flow resistance and yield g accommodates the evolution of self and latent hardening. In our case, deformation is driven by both glide and climb, which is experimentally observed. So it is assumed that glide driven self and latent based hardening phenomena will not be sufficient to accommodate our experimental data. Instead of individual mechanism based modeling, here it is assumed that the microscopic picture of glide, cross-slip and climb can be effectively represented by the slip-system-level hardening and recovery. This phenomenological approach has been accommodated in the evolution equation of the respective internal variable. From now on, we will consider hardening-recovery based formulation for the evolution of CRSS, i.e. yield and drag. For a set of meaningful material parameters, hardening-recovery driven evolution equations are necessary. So it is reasonable to consider the recovery terms in the internal variables of the flow-rule. So we are adopting Eq. (4.15), a modified version of Eq. (4.1), which takes a modified generalized evolution equation for the internal variable R related to CRSS evolution combining the slip-system-level hardening and recovery effects. The modified flow-rule of Eq. (4.1) would look like Eq. (4.15). The corresponding evolution equations for the internal resistance or CRSS evolution would look like as follows.

$$\dot{\gamma}^{\alpha} = \left| \frac{\tau^{\alpha}}{K R^{\alpha}} \right|^{n} \operatorname{sgn}(\tau^{\alpha}), \tag{4.15}$$

$$R^{\alpha} = R_0^{\alpha} + \sum_{\beta} \mathsf{H}^{\alpha\beta}(1 + b^{\beta}) q^{\beta}, \tag{4.16}$$

$$\dot{q}^{\alpha} = |\dot{\gamma}^{\alpha}| \left(1 - b^{\alpha} q^{\alpha}\right) \tag{4.17}$$

Here K can be considered as temperature dependent drag, R is responsible for CRSS evolution. For any slip system α, R^{α} starts with initial CRSS, R_0 and its evolution is governed by the variable q along with the choice of the material parameters b and hardening interaction (cross hardening) matrix $\mathsf{H}^{\alpha\beta}$. Here q is the governing variable combined with hardening and recovery terms and b associated with the recovery of hardening. $\mathsf{H}^{\alpha\beta}$ can be considered with constant values as the hardening evolution is considered with an additional variable X. If we consider no recovery during deformation e.g. $b = 0$, then the evolution equation would be purely glide driven. In that case, Eq. (4.16) would be similar to Eq. (4.5) if we use Eqs. (4.6)-(4.10) for the evolution of $\mathsf{H}^{\alpha\beta}$. Simulations have been attempted with both sets of equations. Along with the governing isotropic state variable q, the internal variable R^{α} represents slip system level equivalence of isotropic hardening/softening effects. Results with Eqs. (4.15)-(4.17) have been shown in Fig. 4.3, which shows that, the above set of flow-rule and hardening law cannot simulate the deformation behavior correctly, and the primary hardening stage deviates significantly with overestimation. Although it covers rate-dependency in the hardening/recovery stage, it cannot reasonably reproduce overall experimental behavior. In spite of the rate sensitivity parameter $n = 5.8$ is in the range of 3-6, it is expected to be even lower considering very high homologous temperature. Related model parameters are presented in Table 4.3. In our observation, one internal variable based flow-rule with most available hardening law at such high-temperature results overestimation in the hardening stage followed by a flat curve. Not considering recovery term in such case could lead to meaningless value of one or more modeling parameters. If we cannot choose a proper flow-rule consistent with proper deformation mechanisms then some material parameters might be beyond the meaningful explanation. Although another version of hardening/dynamic recovery based evolution equation of R can also be found in [235], it is also not expected to be successful because of only one internal variable.

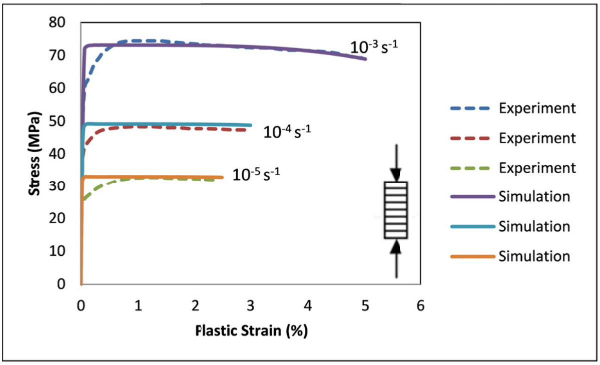

Figure 4.3: Experiment plasticity data at 1050°C for three different strain rates vs. simulation results using type-3 flow-rule, lamellar and compression axes are perpendicular.

Table 4.3: Identified model parameters for type-3 flow-rule

Parameters	Name	Values
Rate-dependence	Rate sensitivity, n	5.8
	Drag Stress, $K(\mathrm{MPa})$	9.7
Hardening + Recovery	Initial CRSS, $r(\mathrm{MPa})$	12
	Recovery parameter, b	9

4.2.4 Type-4 flow-rule

If we want to consider two internal variables X and R with accommodating hardening and recovery, then the flow-rule of Eq. (4.2) will be similar to the following, Eq. (4.18). Evolution equations of X and R will remain the same as given in Sects. 4.2.2 and 4.2.3.

$$\dot{\gamma}^{\alpha} = \left| \frac{\tau^{\alpha} - X^{\alpha}}{K R^{\alpha}} \right|^{n} \operatorname{sgn}(\tau^{\alpha} - X^{\alpha}) \tag{4.18}$$

Simulation results with the flow-rule of Eq. (4.18) and corresponding evolution equations are shown in Fig. 4.4, which indicate that the fitting with experimental data is reasonably good with hardening and recovery, but the rate sensitivity exponent n seems a higher value of 8.12, Table 4.4. At high homologous temperature and moderate to low stress range, comparatively lower value of n is expected as documented by Padmanabhan et al. [215]. Experimental curves presented in Fig. 4.4 are taken when lamellar axis and compression axis are perpendicular, say at $\phi = 90°$. With the above model and with identified parameter set in Table 4.4, we tried to validate the model with another set of data. Figure 4.5 shows that this modeling parameter set highly overestimate the available experimental peak stress points that are also taken from other compression tests when both axes (lamellar and compression) are parallel, say at $\phi = 0°$. The higher value of the rate sensitivity exponent could be the reason of overestimation.

4.2.5 Type-5 flow-rule

Now we will consider the third type flow-rule with two internal variables. Regarding plastic slip, following [28, 213], we took the viscoplastic driving force for a slip system as the difference of shear

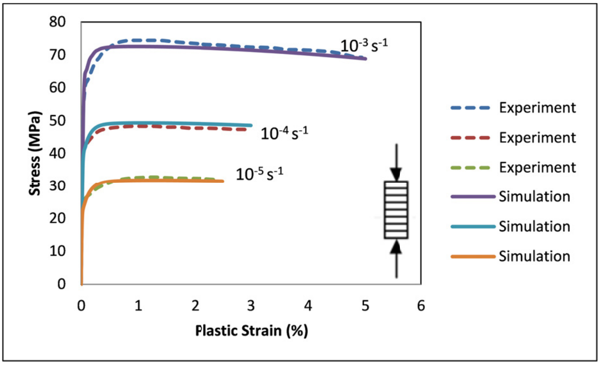

Figure 4.4: Experiment plasticity data at 1050°C for three different strain rates vs. simulation results using type-4 flow-rule, lamellar and compression axes are perpendicular.

Table 4.4: Identified model parameters for type-4 flow-rule

Parameters	Name	Values
Rate-dependence	Rate sensitivity, n Drag stress, $K(\mathrm{MPa})$	8.12 7.83
Isotropic hardening	Initial CRSS, $R_0(\mathrm{MPa})$ Recovery parameter, b	12 2.4
Kinematic hardening	Internal stress, $C(\mathrm{MPa})$ Recovery parameter, d Parameters for flow accumulation function, ϕ_0 and δ	3500 45 0.24 and 600

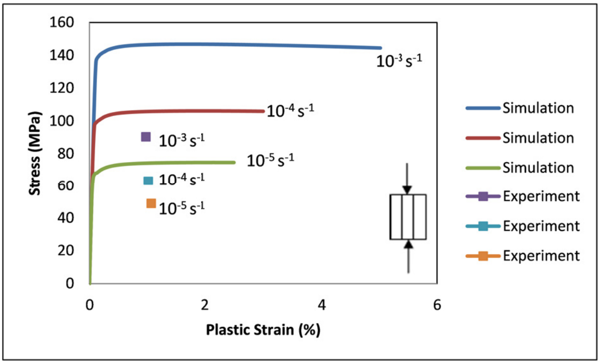

Figure 4.5: Experimental three peak stress points at 1050°C for three different strain rates vs. simulation results using type-4 flow-rule, lamellar and compression axes are parallel.

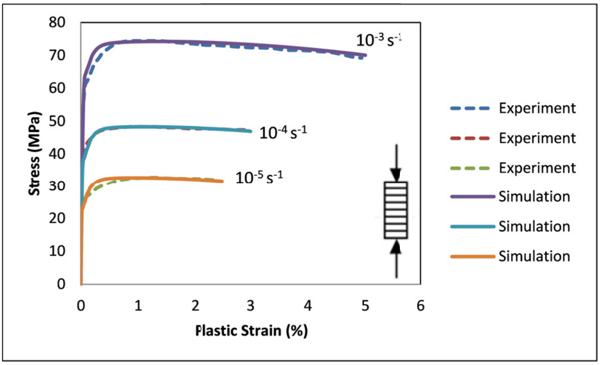

Figure 4.6: Experiment plasticity data at 1050°C for three different strain rates vs. simulation results using type-5 flow-rule, lamellar and compression axes are perpendicular.

stress and all hardening stresses as given in Eq. (4.19).

$$\dot{\gamma}^\alpha = \left\langle \frac{|\tau^\alpha - X^\alpha| - R^\alpha}{K} \right\rangle^n \operatorname{sgn}(\tau^\alpha - X^\alpha) \tag{4.19}$$

As described in the earlier cases, K, X^α and R^α bear the usual meaning. The variable R^α can be compared to the viscoplastic friction resistance or to the radius of the elastic domain in a 1D stress space for a specific slip system. The fact is, kinematic hardening type variable allows us to distinguish a tensile and a compressive yield strength.

In essence, type-5 flow-rule i.e. Eq. (4.19) is similar to type-4, with a rearrangement in the dimensionless stress quantity. The term $|\tau - X| - R$ can be considered as operative stress. Evolution equations for the two internal variables will be the same as given earlier in Eqs. (4.11)-(4.14) and (4.16)-(4.17) where both variables contain the term for strain hardening and dynamic recovery. It is to be noted that the thermodynamic consistency is generally ensured by the this type models for any (positive) values of the material/model parameters [236]. Simulation results, Fig. 4.6, show that this type flow-rule is by far the better one in terms of both reproducing experimental behavior and reasonable material parameters as given in Table 4.5. The type-5 model along with parameter set given in Table 4.5 can well reproduce the anisotropic data i.e. the both compression data sets for $\phi = 90°$ and $\phi = 0°$ orientations. Results for the later case are shown in Fig. 4.7. In order to avoid many material parameters, we considered same values for both phases. From the crystal plasticity constitutive modeling perspective, the overall plastic behavior in the first stage is dominated by the kinematic hardening part while the both isotropic and kinematic hardening contribute to the next stage. In the following subsections we will discuss all related material constants and identified parameters. Following [28], [99] and [213] and based on simulation results it can be opined that two internal variables may be effectively used as a first approximation to model the strain hardening or softening characteristics, dynamic recovery and strain rate sensitivity etc. A two internal variables based model corresponds in spirit to the isotropic and kinematic hardening assumption of the classical rate-independent plasticity theory [44].

Table 4.5: Identified model parameters for type-5 flow-rule

Parameters	Name	Values
Rate-dependence	Rate sensitivity, n Drag Stress, $K(\mathrm{MPa})$	4.5 122
Isotropic hardening	Initial CRSS, $R_0(\mathrm{MPa})$ Recovery parameter, b	14 8
Kinematic hardening	Internal stress, $C(\mathrm{MPa})$ Recovery parameter, d Parameters for flow accumulation function, ϕ_0 and δ	3500 45 0.24 and 600

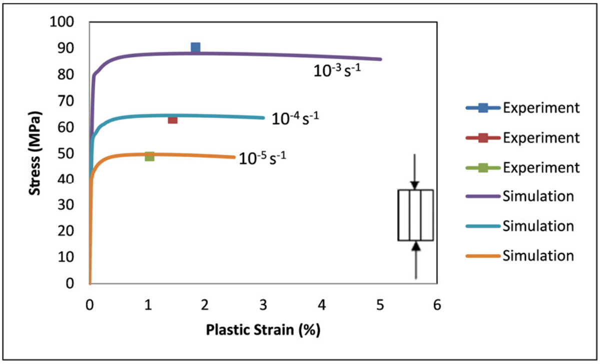

Figure 4.7: Experimental three peak stress points at 1050°C for three different strain rates vs. simulation results using type-5 flow-rule, lamellar and compression axes are parallel.

4.3 Flow-rules and slip activities

The introduction of the concept of different stages of work hardening was certainly a milestone in the developing understanding of work hardening mechanisms [37]. Stage I, or primary creep, is associated with easy glide when the material experiences hardening through changes in the dislocation substructure. Then stage II, or secondary, or steady-state creep, is observed. Finally stage III is resulted to the rapid or parabolic hardening, which might lead to cracking, fracture in pure and class M type alloys [30]. Generally fewer slip systems are activated during stage I deformation, and stage II hardening is associated with secondary slip activation. For example, let us assume that only two slip systems may become active, primary system denoted by 1 and the secondary system denoted by 2. So during stage I, only system 1 is activated and during stage II both systems 1 and 2 are activated. In stage II, hardening is balanced by dynamic recovery. As mentioned earlier, this stage is particularly important as large strains can accumulate during steady-state at low, constant, stresses leading to failure. According to forest dislocation theory, this secondary slip for the flow stress is that the dislocations produced are mostly 'forest' dislocations with respect to the primary slip system. The term forest refers to the concept that the flow stress on a given slip plane is determined by the short-range interaction of mobile dislocations on the slip planes with those dislocations that intersects the slip planes. Thus under multiple-slip condition, secondary dislocations or slips are the key to understanding the complex hardening behavior. Considering all stages of hardening

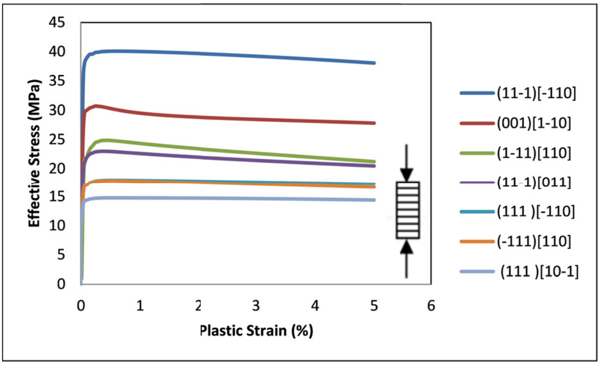

Figure 4.8: Active slip systems for type-2 flow-rules at $\phi = 90°$

including stage III, slip systems can be divided into four categories based on the slip activities. These are primary, conjugate (secondary), cross-glide and critical systems. Rapid increase of flow stress in stage II depends on the deformation history and cross-slip interactions. Amount of secondary slips increases continuously during stage II and III deformation [221]. The presence of stage III sometimes limits the extent of stage II and may eliminate it as a separate stage, especially at high-temperatures and for materials of high SFE [37]. Stage III is believed to be driven by the development of the cross-slip mechanism [237] and is characterized by a specific, strong dependence on temperature and strain rate, which is applicable in both single and polycrystalline alloys.

Slip system activities are mainly driven by the choice of the effective stress. In our case, we did not observe secondary slip activation at any point of the deformation and, conversely, no deactivation of a slip system after being active once. In type-1 and 3 type flow-rule as described in Sects. 4.2.1 and 4.2.3, if the absolute value of the resolved shear stress is greater or equal to CRSS then the system would be active. We found 6 slip systems are active for the first case and the systems are in symmetric pairs. Among them, four are from the octahedral and two from the cubic family. Active system pairs are: 1. (11-1)[-110], (1-11)[110], 2. (001)[1-10], (001)[110], and 3. (1-11)[10-1], (11-1)[101]. Resolved shear stresses on both systems of a pair are almost identical. Similar behavior of slip as a pair was observed for a Ni-based single crystal superalloy [27].

On the other hand, in type-4 and 5 as discussed in Sects. 4.2.4-4.2.5, since the effective stress (plastic driving force) definition is different from the previous case we see a shuffle in slip system activities. Symmetry pair is broken here and the number of active systems increases to seven. Among them first three are common, rest are different than the previous case. Interestingly, for this case, six from seven are from octahedral family. Additional active systems are: 4. (11-1)[011], 5. (111)[-110], 6. (-111)[110], and 7. (111)[10-1]. As an example, active systems based on the positive operative stress is presented in Fig. 4.9.

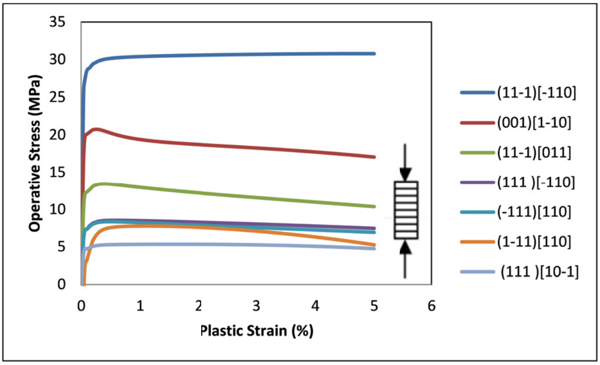

Figure 4.9: Active slip systems for type-4, 5 flow-rules at $\phi = 90°$

Chapter 5

Numerical aspects

5.1 Choosing RVE

We have seen in the first chapter that a RVE should be statistically representative of heterogeneities. For the alloy under consideration, lamellar phases are not continuous, thickness is not uniform, lamellar spacing is not also constant. According to mean-field homogenization, we can take an idealized RVE, which can be with various geometrical consideration. As long as the volume fraction of the individual phases, their mean width, mean spacing and the RVE-size etc. are rightly chosen, then according to the concept of statistically similar RVE, we can choose phases with complete lamellae as shown in Fig. 5.1. In other words, although the microstructure is not perfectly lamellar, RVE can idealized with lamellar structures and with nearly similar lamellar thicknesses. Since the microstructure is non-periodic, we considered sufficiently large RVE (thirteen lamellae) in order to ensure that its size is sufficiently large than that of lamellar scale heterogeneity. Figure 5.1 shows the RVE when loaded perpendicular to the lamellae. The RVE is meshed with 16250 eight node solid elements C3D8, i.e. eight-noded, isoparametric, three dimensional brick elements with trilinear interpolation functions. The loading and the boundary surfaces are also shown. Generally the objective of studying single crystals is to understand the grain level mechanics of polycrystalline alloys. Since Ti-61.8at.%Al is a single crystal alloy, we have simplified two basic aspects of mean-field homogenization. Firstly, for 90° orientation, we have applied three different strain rates (i.e. 10^{-3} s^{-1}, 10^{-4} s^{-1} and 10^{-5} s^{-1}) perpendicular to the one side of the Z-planes, and displacement boundary condition to the opposite side i.e. $U_z = 0$, as shown in Fig. 5.1. No restriction has been applied to the other four sides of the RVE. Similarly, for 0° orientation, same strain rate and boundary condition have been applied perpendicular to two X-planes, Fig. 5.2. Secondly, the overall stress has been computed based on the element centroidal average of the stress component σ_{33}. In the computing of the overall stress, we do not expect a significant difference between the volumetric average and the centroidal one, since the volumes of different elements are nearly the same.

It is discussed in the first chapter that, a larger sized RVE is important for non periodic microstructure. Two relevant microscales, or scale of heterogeneity, for this analysis is the size of slip and lamellae, the mesoscale here is the size of the RVE. In this mean-field simulation the main microscale is the average spacing of dislocation sources, where the most fundamental scale is the size of the Burgers vector. The lamellar scale is a secondary scale. For a particular material, Terada et al. [62] showed that if the characteristic length, the size of the RVE with respect to the size of the scale of heterogeneity, is more

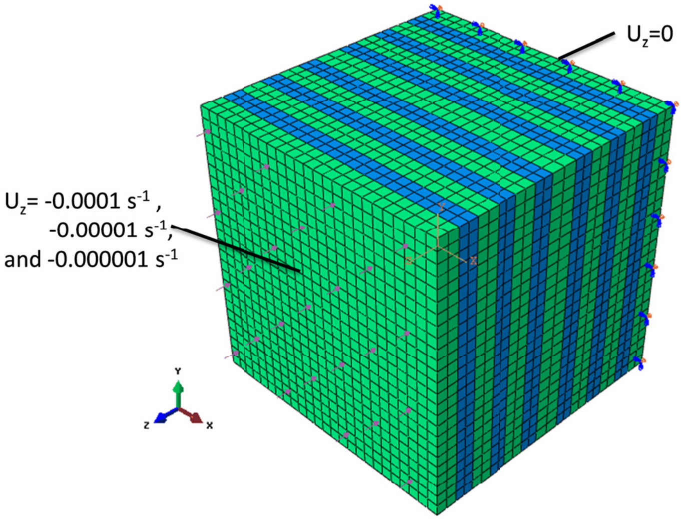
$U_z=0$
$U_z= -0.0001\ s^{-1}$,
$-0.00001\ s^{-1}$,
and $-0.000001\ s^{-1}$
Y
Z
X

Figure 5.1: Meshed RVE, schematically showing load and boundary surfaces along Z-axis, loading and lamellar axes are at 90°, γ-phase: green, r-phase: blue

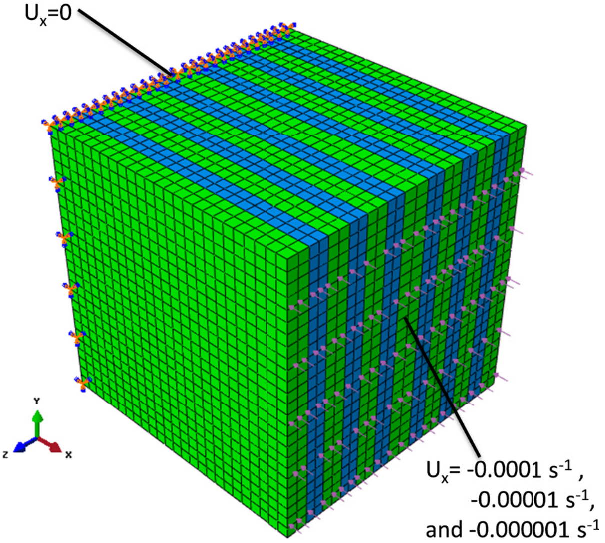
$U_x=0$
$U_x= -0.0001\ s^{-1}$,
$-0.00001\ s^{-1}$,
and $-0.000001\ s^{-1}$
Y
Z
X

Figure 5.2: Meshed RVE, schematically showing load and boundary surfaces along X-axis, loading and lamellar axes are at 0°, γ-phase: green, r-phase: blue

than 35 then TBC, DBC or PBC do not make a significant difference. The RVE of Fig. 5.1 is extremely large in terms of the primary microscale and even much larger as compared to the secondary scale. So in terms of the primary microscale the choice of the BC is insignificant.

5.2 Numerical implementation

Employing a linear interpolation within $\triangle t$ and following the generalized Euler time integration scheme we can write the increment of shear strain as:

$$\triangle\gamma^{\alpha} = \triangle t\left[(1-\theta)\dot{\gamma}_{t}^{\alpha} + \theta\dot{\gamma}_{t+\triangle t}^{\alpha}\right] \tag{5.1}$$

Where $\triangle\gamma^{\alpha}$ is the increment of slip along the system α within the time period $\triangle t$. Slip rates at the beginning and at the end of the time step are denoted by $\dot{\gamma}_{t}^{\alpha}$ and $\dot{\gamma}_{t+\triangle t}^{\alpha}$. Here a choice of 0.5 to 1 for θ is recommended, whereas $\theta = 0$ corresponds the simple Euler scheme. Since the slipping rate $\dot{\gamma}^{\alpha}$ is in general a function of the resolved shear stress, τ^{α}, and of the internal variables, X^{α} and R^{α} or g^{α}, Taylor expansion of the slipping rate gives:

$$\dot{\gamma}_{t+\triangle t}^{\alpha} = \dot{\gamma}_{t}^{\alpha} + \frac{\partial\dot{\gamma}^{\alpha}}{\partial\tau^{\alpha}}\triangle\tau^{\alpha} + \frac{\partial\dot{\gamma}^{\alpha}}{\partial g^{\alpha}}\triangle g^{\alpha} \tag{5.2}$$

$$\dot{\gamma}_{t+\triangle t}^{\alpha} = \dot{\gamma}_{t}^{\alpha} + \frac{\partial\dot{\gamma}^{\alpha}}{\partial\tau^{\alpha}}\triangle\tau^{\alpha} + \frac{\partial\dot{\gamma}^{\alpha}}{\partial X^{\alpha}}\triangle X^{\alpha} + \frac{\partial\dot{\gamma}^{\alpha}}{\partial R^{\alpha}}\triangle R^{\alpha} \tag{5.3}$$

where $\triangle\tau^{\alpha}$, $\triangle X^{\alpha}$ and $\triangle R^{\alpha}$ or $\triangle g^{\alpha}$ are the increments of resolved shear stress, backstress and isotropic hardening stress, respectively, in the slip system α within the time increment $\triangle t$. The Eq. (5.2) for one internal variable and Eq. (5.3) for two. Combining Eqs. (5.1)-(5.2) and (5.1)-(5.3), we obtain:

$$\triangle\gamma^{\alpha} = \triangle t\left[\dot{\gamma}_{t}^{\alpha} + \theta\frac{\partial\dot{\gamma}^{\alpha}}{\partial\tau^{\alpha}}\triangle\tau^{\alpha} + \theta\frac{\partial\dot{\gamma}^{\alpha}}{\partial g^{\alpha}}\triangle g^{\alpha}\right] \tag{5.4}$$

$$\triangle\gamma^{\alpha} = \triangle t\left[\dot{\gamma}_{t}^{\alpha} + \theta\frac{\partial\dot{\gamma}^{\alpha}}{\partial\tau^{\alpha}}\triangle\tau^{\alpha} + \theta\frac{\partial\dot{\gamma}^{\alpha}}{\partial X^{\alpha}}\triangle X^{\alpha} + \theta\frac{\partial\dot{\gamma}^{\alpha}}{\partial R^{\alpha}}\triangle R^{\alpha}\right] \tag{5.5}$$

For numerical implementation we need the expressions for $\triangle\boldsymbol{\sigma}$, $\triangle\tau^{\alpha}$, $\triangle X^{\alpha}$ and $\triangle R^{\alpha}$ etc. Considering $\triangle\boldsymbol{\sigma} = \overset{\triangledown}{\boldsymbol{\sigma}}\,\triangle t$ and $\triangle\tau^{\alpha} = \dot{\tau}^{\alpha}\triangle t$, and using Eqs. (3.14) and (3.18) we can write increment of the Cauchy stress and increment of the resolved shear stress by the following equations:

$$\triangle\boldsymbol{\sigma} = \boldsymbol{\mathcal{L}}\colon\triangle\boldsymbol{\epsilon} - \boldsymbol{\sigma}(\boldsymbol{I}\colon\triangle\boldsymbol{\epsilon}) - \sum_{\alpha=1}^{N}\left[\boldsymbol{\mathcal{L}}\colon\boldsymbol{\mu}^{\alpha} + \boldsymbol{\omega}^{\alpha}\cdot\boldsymbol{\sigma} - \boldsymbol{\sigma}\cdot\boldsymbol{\omega}^{\alpha} - \boldsymbol{\sigma}(\boldsymbol{I}\colon\boldsymbol{\mu}^{\alpha})\right]\triangle\gamma^{\alpha} \tag{5.6}$$

$$\triangle\tau^{\alpha} = \left[\boldsymbol{\mathcal{L}}\colon\boldsymbol{\mu}^{\alpha} + \boldsymbol{\omega}^{\alpha}\cdot\boldsymbol{\sigma} - \boldsymbol{\sigma}\cdot\boldsymbol{\omega}^{\alpha}\right]\colon\left[\triangle\boldsymbol{\epsilon} - \sum_{\beta=1}^{N}\boldsymbol{\mu}^{\beta}\triangle\gamma^{\beta}\right] \tag{5.7}$$

Increment of internal variables can be derived as:

$$\triangle X^{\alpha} = \frac{C^{\alpha}\delta(1-\phi_{0})e^{-\delta\nu^{\alpha}}}{\delta - d^{\alpha}\mathrm{sgn}(\dot{\gamma}_{t})}\triangle\gamma^{\alpha} \tag{5.8}$$

$$\triangle R^{\alpha} = \sum_{\beta=1}^{N}\mathbf{H}^{\alpha\beta}Q^{\beta}b^{\beta}e^{-b^{\beta}|\gamma^{\beta}|}\triangle\gamma^{\beta} \tag{5.9}$$

$$\triangle g^{\alpha} = \sum_{\beta=1}^{N}\mathbf{H}^{\alpha\beta}\triangle\gamma^{\beta} \tag{5.10}$$

To obtain $\boldsymbol{\mu}^{\alpha}$ and $\boldsymbol{\omega}^{\alpha}$ at the current state it is necessary to know $\dot{s}^{\alpha}$ and $\dot{m}^{\alpha}$, for which we need to compute $\triangle s^{\alpha}$ and $\triangle m^{\alpha}$. Thus we can fully characterize the lattice deformation and rotation by the reciprocal vectors $\dot{s}^{\alpha}$ and $\dot{m}^{\alpha}$ in the deformed configuration. Necessary expression $\triangle s^{\alpha}$ and $\triangle m^{\alpha}$ can be given as:

$$\triangle s^{\alpha} = \left\{ \triangle \boldsymbol{\epsilon} + \boldsymbol{W} \triangle t - \sum_{\beta} \left[\boldsymbol{\mu}^{\beta} + \boldsymbol{\omega}^{\beta} \right] \triangle \gamma^{\beta} \right\} \boldsymbol{\cdot} s^{\alpha} \tag{5.11}$$

$$\triangle m^{\alpha} = -m^{\alpha} \boldsymbol{\cdot} \left\{ \triangle \boldsymbol{\epsilon} + \boldsymbol{W} \triangle t - \sum_{\beta} \left[\boldsymbol{\mu}^{\beta} + \boldsymbol{\omega}^{\beta} \right] \triangle \gamma^{\beta} \right\} + m^{\alpha} \boldsymbol{\cdot} \left(\boldsymbol{I} \boldsymbol{:} (\triangle \boldsymbol{\epsilon} - \sum_{\beta} \boldsymbol{\mu}^{\beta} \triangle \gamma^{\beta}) \right) \tag{5.12}$$

If we put the relevant expression for $\triangle \boldsymbol{\sigma} = \overset{\triangledown}{\boldsymbol{\sigma}} \triangle t$, $\triangle \tau^{\alpha} = \dot{\tau}^{\alpha} \triangle t$, $\triangle \tau^{\alpha}$, $\triangle X^{\alpha}$ and $\triangle R^{\alpha}$ in the incremental formulation of Eqs. (5.4) and (5.5), depending on the type of flow-rule we will end up with different forms. For example, if we consider the evolution of g as given in Sects. 4.2.1, we will get the following form. For the sake of brevity we write $\boldsymbol{P}^{\alpha} = \boldsymbol{\mathcal{L}} \boldsymbol{:} \boldsymbol{\mu}^{\alpha} + \boldsymbol{\omega}^{\alpha} \boldsymbol{\cdot} \boldsymbol{\sigma} - \boldsymbol{\sigma} \boldsymbol{\cdot} \boldsymbol{\omega}^{\alpha}$.

$$\sum_{\beta=1}^{N} \left\{ \boldsymbol{\delta}^{\alpha\beta} + \theta \triangle t \frac{\partial \dot{\gamma}^{\alpha}}{\partial \tau^{\alpha}} (\boldsymbol{P}^{\alpha} \boldsymbol{:} \boldsymbol{\mu}^{\beta}) - \theta \triangle t \frac{\partial \dot{\gamma}^{\alpha}}{\partial g^{\alpha}} \mathsf{H}^{\alpha\beta} \mathrm{sgn}(\dot{\gamma_t}^{\beta}) \right\} \triangle \gamma^{\beta} = \dot{\gamma_t}^{\alpha} \triangle t + \theta \triangle t \frac{\partial \dot{\gamma}^{\alpha}}{\partial \tau^{\alpha}} (\boldsymbol{P}^{\alpha} \boldsymbol{:} \triangle \boldsymbol{\epsilon}) \tag{5.13}$$

On the other hand, if we consider the evolution of X and R as given in Sects. 4.2.2 and 4.2.3 along with the flow-rule in Sect. 4.2.5, we will get the following form.

$$\begin{aligned} &\sum_{\beta=1}^{N} \left\{ \boldsymbol{\delta}^{\alpha\beta} + \theta \triangle t \frac{\partial \dot{\gamma}^{\alpha}}{\partial \tau^{\alpha}} (\boldsymbol{P}^{\alpha} \boldsymbol{:} \boldsymbol{\mu}^{\beta}) - \theta \triangle t \frac{\partial \dot{\gamma}^{\alpha}}{\partial X^{\alpha}} \frac{C^{\alpha} \delta (1 - \phi_0) e^{-\delta \nu^{\alpha}}}{[\delta - d^{\alpha} \mathrm{sgn}(\dot{\gamma_t})]} \right\} \triangle \gamma^{\beta} \\ &- \sum_{\beta=1}^{N} \left\{ \theta \triangle t \frac{\partial \dot{\gamma}^{\alpha}}{\partial R^{\alpha}} \mathsf{H}^{\alpha\beta} Q^{\beta} b^{\beta} e^{-b^{\beta} |\gamma^{\beta}|} \right\} \triangle \gamma^{\beta} = \dot{\gamma_t}^{\alpha} \triangle t + \theta \triangle t \frac{\partial \dot{\gamma}^{\alpha}}{\partial \tau^{\alpha}} (\boldsymbol{P}^{\alpha} \boldsymbol{:} \triangle \boldsymbol{\epsilon}) \end{aligned} \tag{5.14}$$

Where $\boldsymbol{\delta}^{\alpha\beta}$ is the Kronecker delta. The above equation represents a linear system of equations where $\triangle \gamma^{\beta}$'s are the only unknown variables. Instead of being a linear system, Eq. (5.14) would be a nonlinear system if we do not consider Taylor's linear expression of Eqs. (5.2) and (5.3). Depending on the number of variables, lets say $\dot{\gamma}^{\alpha} = f^{\alpha}(\tau^{\alpha}, g^{\alpha})$, or, $\dot{\gamma}^{\alpha} = f^{\alpha}(\tau^{\alpha}, X^{\alpha}, R^{\alpha})$. Then at $t + \triangle t$, the shear rate for the slip system α can be written:

$$\dot{\gamma}^{\alpha}_{t+\triangle t} = f^{\alpha}(\tau_t{}^{\alpha} + \triangle \tau^{\alpha}, g_t{}^{\alpha} + \triangle g^{\alpha}) \tag{5.15}$$

$$\dot{\gamma}^{\alpha}_{t+\triangle t} = f^{\alpha}(\tau_t{}^{\alpha} + \triangle \tau^{\alpha}, X_t{}^{\alpha} + \triangle X^{\alpha}, R_t{}^{\alpha} + \triangle R^{\alpha}) \tag{5.16}$$

Then the general expression of Eq. (5.1) would be like below.

$$\triangle \gamma^{\alpha} - \triangle t (1 - \theta) \dot{\gamma}^{\alpha}_t - \triangle t \theta \dot{\gamma}^{\alpha}_0 f^{\alpha}(\tau_t{}^{\alpha} + \triangle \tau^{\alpha}, g_t{}^{\alpha} + \triangle g^{\alpha}) = 0 \tag{5.17}$$

$$\triangle \gamma^{\alpha} - \triangle t (1 - \theta) \dot{\gamma}^{\alpha}_t - \triangle t \theta \dot{\gamma}^{\alpha}_0 f^{\alpha}(\tau_t{}^{\alpha} + \triangle \tau^{\alpha}, X_t{}^{\alpha} + \triangle X^{\alpha}, R_t{}^{\alpha} + \triangle R^{\alpha}) = 0 \tag{5.18}$$

These equations, (5.17) and (5.18), are nonlinear systems of equations that can be solved by Newton-Rhapson iterative method, while linear solution of Eq. (5.13) or (5.14) can be used as an initial guess [231]. Generating a lamellar representative volume element (RVE) with $10 \times 10 \times 10$ μm^3 as shown in Fig. 5.1, all these necessary formulas have been implemented in the UMAT (user material) subroutine from the commercial finite element software package Abaqus Standard. With the presented incremental formulation technique, this framework has been implemented with UMAT functionality.

5.3 Solver, matrix conditioning and mesh convergence

All of the computations in this work are based on the implicit numerical scheme with structured meshing of almost equal sized 3D brick elements. The direct solver, LU decomposition method has been used for solving all linear system of equations, both for the linear incremental scheme (generalized Euler) and for the linearization of nonlinear Newton's solver. In most cases, Newton's solution procedure for the non-linear system in finite element formulation exhibits second order convergence. The prediction has been started with the increment of slip. All CP constitutive equations have been implemented in the user subroutine (UMAT) functionality of Abaqus Standard. The UMAT is being called several times during the time of computations, in every cycle of external load increments, every cycle of equilibrium iterations, in every element, in every integration point of an element [10]. The main tasks in the UMAT are, updating stress state from the prescribed deformations, updating material states i.e. state variables, and the computation of the material Jacobian or tangent stiffness matrix [238]. Implicit scheme generally guarantees the convergence whereas very small time step is necessary for explicit scheme as convergence is not guaranteed always [70]. In an implicit analysis, like in ABAQUS standard, the finite element momentum balance or equilibrium equations are solved implicitly.

The performance of finite element computations depends strongly on the quality of the meshing, polynomial degree and the efficiency of the solver for the linear systems resulting from the discretization of partial differential equation [239]. Thus poorly shaped elements (e.g. severely unstructured meshing, different volumes for 3D elements) can give ill-conditioned matrices, which tend to slow down or even prevent the convergence of iterative solvers. Precise and explicit descriptions of the relations between the mesh geometry and the spectral condition numbers are naturally helpful to the understanding of the whole finite element solution process. With the increasing of polynomial degree, the eigenvalue spectrum of the resulting finite element matrices will also grow, that causes the condition number of the matrix to grow as well. Sometimes, this growth could be exponential which would be the worst case scenario of matrix conditioning [240]. The first order tri-linear brick element is advantageous considering the efficiency and convergence of the computation.

In nonlinear mechanics, a common approach of computing a nonlinear quantity is usually followed by a predictor-corrector scheme. A related quantity (e.g. stress, strain, deformation gradient) is predicted then the subsequent prediction is updated by Newton-Raphson solver and, thus the residual error is minimized [70]. Since slip rate is highly nonlinear, the calculation of slip rate by predicting stress does not easily converge. Conversely, the calculation of stress from slip rate is comfortable for convergence. In this work, the prediction has been started always from the increment of slip for all slip systems.

When we try to understand the effect of mesh size, we find that some components of stress are mesh size and time step sensitive, however if we concentrate on the homogenized value we find very little differences, specifically in the order of less than one percent. In general, the more the heterogeneity and complexity in the microstructure, the more the mesh sensitivity in the local level. If so, more refined mesh is necessary in the polycrystal level.

Chapter 6

CRSS estimation technique

6.1 Introduction

The ease of slip or twinning on a slip/twin system is usually quantified by critical resolved shear stress (CRSS). In order to calculate local yield limits, the critical resolved shear stress of these systems must be known at the temperature and strain rate under consideration. Characterizing slip systems for their proper CRSS values is one of the most important parts in crystal plasticity modeling of anisotropic responses. Initial critical resolved shear stresses for different slip systems, or at least for different planes, and elastic constants are the set of input parameters that are necessary to start a crystal plasticity simulation, especially modeling of anisotropy. Initial CRSS is the most important quantity in crystal plasticity modeling and simulation. A small change in this value will result in a nearly different set of model parameters especially two main flow-rule parameters. Generally precise values of critical stresses according to the experimental observation improve the predictive power of the model. However they are generally anisotropic i.e. orientation dependent [154, 158, 241–243], and depend both upon the orientation of the loading axis as well as the sense of the load; i.e., tension or compression [220]. Researchers have investigated these values for different alloys under various conditions, both experimentally and computationally. However, there is no consensus on these values [244], particularly as they change as a function of alloy content and testing conditions.

There is often contradictory opinion about the ease of activation in different microstructures. Hexagonal closed packed (HCP) materials is an ideal example of such controversies. Accordingly to Li et al. [245], prismatic slip is easier to activate than other deformation modes, and then basal slip and finally pyramidal systems, i.e. $\text{CRSS}_{\text{prismatic}}<\text{CRSS}_{\text{basal}}<\text{CRSS}_{\text{pyramidal}}$. This order is supported by various experiments, for example, on α_2-Ti_3Al single crystals [156], and on magnesium [246]. However, HerreraSolaz et al. [247] reported that it is generally accepted as $\text{CRSS}_{\text{basal}}<\text{CRSS}_{\text{prismatic}}<\text{CRSS}_{\text{pyramidal}}$. Li et al. [245] also presented the case of Ti-6Al-4V alloy with such contradiction. They also described that the first view is supported by majority of the researchers even at high-temperatures. Temperature also plays a role in the relative activation of basal and prismatic slip systems. A summary of experimental CRSS and simulation based estimation is documented in Li et al. [245] for single crystalline and polycrystalline Ti and Ti alloys. Hutchinson and Barnett [248] explained the issue in a more generalized way. They reported that the basal slip is the easiest in magnesium and zinc while prismatic planes are the softest in titanium and zirconium. In magnesium, prismatic slip operates at CRSS values that are nearly two orders of magnitude greater than for basal slip, but intrinsically harder prismatic glide becomes more favored relative to basal glide as the dislocation density rises, which means basal slip has been hardened and prismatic slip softened [248].

Experimental measurement is done on single-crystal specimens where a unique slip system is activated. But, it is almost impossible to determine these values precisely for all slip systems using conventional uniaxial tests. One potential reason is that, it might be impossible to initiate slip on a system if the CRSS is much lower on other systems. Moreover, many structural materials are polycrystalline and/or multiphase and often are not available in single-crystal form, making traditional approaches difficult. Analyzing Mg bicrystals, Uranagase and Matsumoto (2016) [249] mentioned that both CRSS and deformation modes depend on the misorientation angle between the grains and the loading direction. In polycrystals, it is not possible to directly find values of CRSS, although approximate values can be obtained for very strongly textured alloys [245, 248]. One important alternative is nano-indentation of grains within a polycrystal combined with crystal plasticity finite-element simulations that has been used to quantitatively determine the CRSS for different slip systems [245], which is known to require higher order continuum theories.

Apart from the experimental efforts, there are few other computational approaches available depending on the complexity of the microstructures, which take experimental measurements as a basis. For high symmetry face centered cubic materials, if the grain morphology is not complex then, generally, the slip system deformation resistances are considered not too different from each other and for these materials it is possible to make an assumption that the slip resistances have approximately the same value for all the slip systems, see for example [250]. In fact the application of this type of simplistic approach is limited to specific deformation behavior with non complex microstructures. To overcome this limitation, categorizing slip systems as 'hard-mode'and 'soft-mode', see for example [117, 150, 248], played an important role in modeling different mechanical behaviors of some lamellar alloys. Considering symmetric slip planes as one family and setting a fixed CRSS for all systems in that family is a well known approach, see for example [241] and [156] for hexagonal closed packed (HCP) materials. We often see the classification of octahedral and cubic families for FCC (face centered cubic) materials, where the octahedral one is treated as the primary group [251]. For BCC (body centered cubic) materials, families are $\{110\}\langle 111\rangle$, $\{112\}<111>$, and $\{123\}<111>$; consisting of 12, 12 and 24 slip systems, respectively. Here the notation $\{110\}$ denotes the set of all equivalent planes by the symmetry of the BCC lattice. Similarly, $<111>$ denotes the set of all directions that are equivalent by the symmetry. Basal, prismatic and pyramidal are three well known families in HCP materials [252]. Apart from the hard-soft or family based classifications, Lebensohn et al. [123] proposed morphology based (e.g. lamellar interface) slip grouping for multiphase lamellar TiAl alloys. The idea is, dislocation piles up at the phase boundary that create additional resistance for plastic slip, thus slip systems that are transverse to the lamellar interface will have higher CRSS than that of longitudinal systems. Slip systems that are neither parallel nor perpendicular to the interface, termed as mixed group, will have a CRSS in between. This morphology based approach can be considered as an extension of the previously proposed hard-soft systems.

Anisotropy of inelastic behavior, or in a more broad sense, the dependence of inelastic behavior on the kind of loading and direction are common for many high-temperature materials [223]. A preferred orientation of crystal planes and directions is developed with the increase of strain. Thus an initially isotropic material may become anisotropic in respect of many properties. In the last decades, there has been a huge attention from the research community regarding anisotropic and asymmetric phenomena, whereas in recent times, strain rate and temperature dependence anisotropic phenomena are getting more attentions. Some of the recent works that include rate-dependent and/or temperature dependent anisotropic investigations are: Huh et al. [253] for high-strength steel, Meredith and Khan [254] for ultra fine grained Ti, Khan and Liu (2012) [255] and Khan and Yu (2012) [256] for temperature and strain rate-dependent anisotropy of Ti-6Al-4V, Nixon et al. [257] for α-titanium, Naumenko and Gariboldi [187] and Gariboldi et al. [258] for aluminum alloys, and many more.

Important features of plastic anisotropy and asymmetry can be related to the different length-scales, like grain/subgrain scale, phase/lamellar scale, crystal lattice scale, dislocations and atomic scales etc. Privileged crystallographic orientation or texture development can be associated with grain scale. Similarly many other origins of anisotropy like defects inclusions-cavities in metals and multiphase alloys, directionality distribution of a particular phase, anisotropy of individual grains etc., can be related to at least one scale dependent phenomena. In order to understand different macroscopic behaviors including the plastic anisotropy and asymmetry in Ti-Al alloys, it is necessary to understand their origins at the lower length-scales. Regular misfit dislocations along the lamellar interfaces, formation of faulted dipoles of superdislocations, changes in deformation modes due to the appearance of some superstructures, domination of climb at high-temperature, etc. for the Al-rich TiAl family are few of them at the smaller scales. Various macroscopic behaviors of this family, like anomalous yielding and hardening, recovery, increasing brittleness with the increase of Al-content, etc. are also deserved to be investigated in order to understand the inelastic phenomena. A detailed knowledge of the fine structure of dislocations is essential in analyzing the origin of the various deformation features. This knowledge is in turn instrumental to the understanding of the mechanisms responsible for the anomalous behavior, plastic anisotropy and tension compression asymmetry, etc. [259]. In general, it is believed that the plastic behavior in Al-rich TiAl alloys depended on the formation of superstructural phases and the activated slip systems varied [130].

Ti-rich lamellar alloys exhibit a significant plastic anisotropy whether they are polysynthetically twinned (PST) or polycrystalline intermetallics [128, 260]. Anisotropy of Ti-rich side alloys is highly pronounced irrespective of whether it is at room temperature [156, 261] or at high-temperature [262]. It is agreed that the maximum yield stress occurs when the lamellar direction is perpendicular to the compression axis, stress is minimum when both axes are approximately at $\phi = 45^\circ$, and stress is in between at $\phi = 0^\circ$ orientation [128, 260]. It is proposed that loading at 45°with lamellar axis resulted in the activation of soft longitudinal deformation modes, where both the slip plane and the slip direction were parallel to the interfaces, probably as a result of the lack of interaction with the lamellar interfaces, and therefore, little interaction of dislocations with lamellar interfaces is expected. At 0°loading, deformation was mainly carried by harder mixed deformation, although the lamellar interfaces seemed to be relatively transparent to slip transfer, which indicates that the lamellar interfaces are relatively transparent to mixed deformation modes. On the contrary, 90°loading represented the hardest direction and deformation was accommodated by the activation of transverse deformation modes, confined to individual lamellae, together with longitudinal modes that were activated due to their softer nature. Those systems are expected to display the larger interaction with lamellar interfaces, since only isolated transversal twins could be found in individual lamella, that did not propagate across lamellar interfaces [263]. This anisotropic deformation behavior depends strongly on the angle between the lamellar and compression axes rather than on the crystallographic orientation of the compression axis. This kind of anisotropy of TiAl single crystals is associated with the difference in the deformation mode e.g. shear deformation modes are different depending on the angle ϕ. The plastic anisotropy of the two-phase lamellar alloys of PST crystal is mainly a morphological anisotropy. This kind of anisotropy of TiAl single crystals is associated with the difference in the deformation mode e.g. shear deformation modes are different depending on ϕ. A significant portion of the anisotropy is coming from to the asymmetric core spreading of the $\langle 101]$ superdislocations that occur in the $L1_0$ structure of gamma-TiAl. The coupling of partial dislocations by different planar faults (that are specific for the $L1_0$ structure) makes the resistance to slip and cross-slip of the $\langle 101]$ superdislocation sensitive to its direction of motion. Both slip and twinning are active in such Ti-rich alloys.

Even though the anisotropy and asymmetry in Ti-rich side have been investigated reasonably for single-crystal and polycrystalline alloys, the lamellar orientation dependence of plastic anisotropy in Al-rich side, either theoretically or experimentally, is not well documented. This directionally solidified lamellar material is expected to be highly anisotropic due to the preferred orientations of lamellar colonies as like PST Ti-rich TiAl [123]. By modeling rate-dependent anisotropy of this alloy, we will focus on the CRSS estimation techniques along with proposing a novel approach consistent with conventional approaches and observed experimental issues.

6.2 Critical resolved shear stresses

6.2.1 CRSS in Ti-rich TiAl

Shear deformation parallel to the lamellar interfaces is considered to be easier (the soft-mode) than that normal to the interfaces (the hard-mode) [150]. The relative difficulty of these harder slip modes compared to the softer ones plays an important role in determining textures, strength and ductility [248]. Considering Ti-rich TiAl, Grujicic and Batchu [150] proposed half of the slip systems belongs to the softer group and half to the harder group based on interface effect. Kad et al. [264] reported that the soft- and hard-modes are controlled by the domain size and width of the lamellae, respectively. Lebensohn et al. [123] extended this harder-softer version to more elegant morphology based characterization. The idea of this approach is, there are few planes and directions that are parallel to the lamellar interface while some are (nearly) transverse, and rest are mixed. When the lamellae are at $\phi = 90°$ with the loading axis, the deformation is carried out mainly by systems of the transverse type which should have high critical stresses while parallel systems should have low CRSS and mixed type systems are expected to be in between. This means, due to lamellar boundary, the basic assumption for such case has been proposed as $R_0^{\mathrm{T}} < R_0^{\mathrm{M}} < R_0^{\mathrm{L}}$, where R_0 denotes CRSS and superscripts L, M, T stand for longitudinal, mixed and transverse systems, respectively. This morphology-based or phase interface based classification, originally introduced to address anisotropy of lamellar PST Ti-rich TiAl alloys, is able to capture the main effect of the morphology on the simplified 2-lamellae structure of PST crystals [123].

6.2.2 Preliminary remarks on CRSS in Al-rich TiAl

There are some experimental works that have been performed on γ-TiAl single crystals, most of them with an aluminum concentration of 54% or 56%. In two-phase lamellar alloys, the estimation of the CRSS of γ-phase is complicated by the lamellar morphology [156] whereas long-period superstructures add additional complexity. Nevertheless, the general agreement is that, crystals containing $L1_0$ phase beyond 54 at.%Al, the CRSS for $\frac{1}{2}\langle 110]\{111\}$ ordinary slip is higher than that for $\langle 101]\{111\}$ superlattice slips [158, 265].

An increase in Al concentration makes TiAl harder and the difference increases suggesting that ordinary dislocations become relatively less mobile than $\langle 101]$ dislocations [153, 158, 159, 265]. So below the peak temperature, superlattice dislocations control the plastic slip behaviors of Al-rich TiAl [153]. Since the energy of the anti-phase boundary (APB) created by the ordinary dislocations was higher than that created by the superlattice dislocations, the motion of the ordinary dislocations was effectively interrupted by the APB, resulting the activation of the superlattice dislocations, and a loss of ductility in Al-rich TiAl. The formation of superstructures in the $L1_0$ matrix was responsible for change in deformation mode and low ductility in Al-rich TiAl [153]. The difference in CRSS between these two slip systems (ordinary and super) become pronounced with the development of the Al_5Ti_3 long-period superstructure. The frequency of $\langle 101]$ dislocation decomposition into a $1/2\langle 110]$ and a $1/2\langle 112]$ dislocation decreases abruptly with the development of Al_5Ti_3. A reduced mobility of ordinary dislocations may be at the origin of this behavior [158]. Nakano et al. [140] showed that, at 500°C, the CRSS of {111}<101] increases linearly with increasing Al concentration, while the CRSS of {111}<110] was lower at the beginning then increases rapidly till 58at.% then starts falling sharply and goes below the line of superdislocation slip. Inui et al., [159] and Nakano et al. [153] reported that, at temperatures below 600°C, the CRSS for $\frac{1}{2}\langle 110]$ ordinary slip is considerably higher than those for $\langle 101]$ superlattice slip. The ratio of the CRSS is 1.5-2.0 at room temperature. However, after 900°C the trend reverse, approx after 1050°C superslips are no longer active in Ti-56%at.Al [159]. A contradictory case also can be seen in [259], where they proposed, it is reasonable to assess that <011]{111} and <112]{111} exhibit the smallest and highest CRSSs respectively, with that of <110]{111} located in between. At room temperature, the ratio of the maximum to minimum CRSS can be 2 to 5 or even more. But at high-temperature, CRSS values for different planes become very closer. At T>900°C, orientation dependence of CRSS and difference among ordinary systems becomes very less [155, 166], but significant differences might be observed even at high-temperature with complex superstructures. Interestingly, the CRSS value is found to be independent of deformation orientation below room temperature at -77 °C, while a strong orientation dependence of the CRSS values is clearly observed for all different orientations between 400°C and 800°C [155].

6.2.3 Constant CRSS assumption

Depending on the simplicity of the microstructures, the simplest approach is to consider a constant value of CRSS for all systems. For high symmetry face centered cubic materials, if the single crystal morphology is not complex, it is possible to make an assumption that the slip resistances take approximately the same value for all the slip systems [155,260]. Besides, at very high-temperature, not much differences of critical stresses among slip systems are expected. For isotropic material this assumption is expected to be fine. For our case, CRSS are roughly estimated for high-temperature, extrapolated from lower temperature experimental data from similar alloys, which was estimated in the range of 10 to 40 MPa. Then we applied constant value based approach for two experimental data set, i.e. $R_0^{\mathrm{O}} = R_0^{\mathrm{S}}$ for both families, where superscripts O and S stand for ordinary and superslips, respectively. A fixed CRSS can reproduce one set of experimental data only, e.g. either for $\phi = 90°$ or $\phi = 0°$, highly under or overestimating the other set. We found that two different values, i.e. 14 MPa and 24.4 MPa, can successfully reproduce two plasticity data sets separately. This means we estimated a constant CRSS of 14 MPa for all slip systems for which the deformation responses at $\phi = 90°$ can be simulated. Similarly we found 24.4 MPa for simulating deformation responses at $\phi = 0°$. Simulating experimental data in two directions, our best approximation

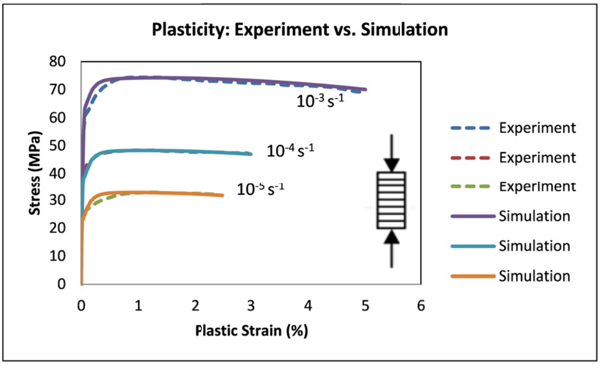

Figure 6.1: True stress-plastic strain curves for three different strain rates at $\phi = 90°$: experiment vs. simulation with constant CRSS.

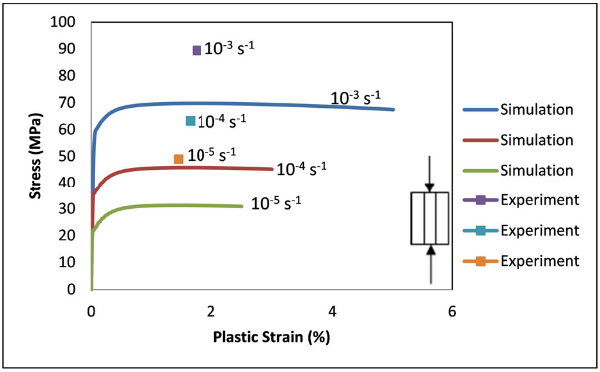

Figure 6.2: True stress-plastic strain curves for three different strain rates at $\phi = 0°$: experiment vs. simulation with constant CRSS.

is in the range of 14 to 25 MPa, more precisely, we expect that the CRSS values would be in the range of 14 - 24.4 MPa. It is to be noted that using a constant CRSS for all systems might be a very simplistic approach considering the complex morphology and long-period superstructures. Furthermore, A small deviation is not unexpected for the first stage of deformation because the rate sensitivity parameter is often little different for different stages of deformation behavior. Another objective of this simulation is to check the amount of deviation in a particular experimental behavior when simulating the other loading responses successfully. One set of simulation results are shown in Figs. 6.1 and 6.2, where we see that this assumption of fixed CRSS highly underestimates three experimental peak stress points once we fix a constant CRSS for $\phi = 90°$ orientation.

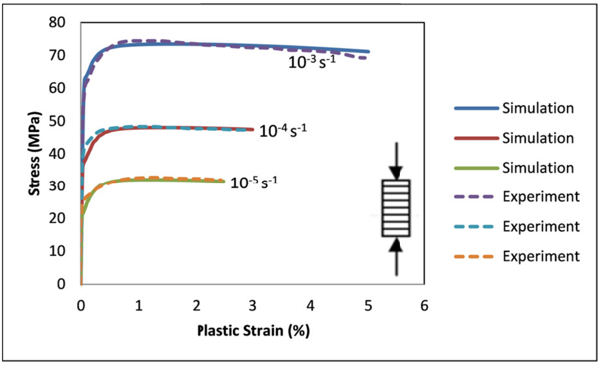

Figure 6.3: Rate-dependent plasticity at $\phi = 90°$: experiment vs. simulation with hard-soft based CRSS configuration.

6.2.4 Hard- and soft-modes based approach

If we closely observe any slip plane in the octahedral family we could see that two systems are different than the third one. In many cases this two systems move as a pair. There are plenty of experimental observation on that, which is mostly known as mechanism-based systems. In FCC materials, we often divide slip systems into ordinary and superlattice dislocation slips. The earlier version of this idea was hard-mode and soft-mode based classification. Depending on the complexity of the microstructure, sometimes the ordinary systems are observed to be hard and superslips are soft, and vice versa. Regarding Al-rich TiAl family, there are some experimental works that explicitly mentioned that the ordinary systems, whether they are on $\{111\}$ or (001) plane, are more mobile and thus CRSS of these systems are relatively low when operating temperature exceeds the peak [159]. Based on this finding, we considered six $\frac{1}{2}$<110] ordinary systems as soft and other 12 systems are hard expecting an improved results, i.e. $R_0^{\mathrm{O}} < R_0^{\mathrm{S}}$. After several simulations we found that, using CRSS of 24.5 MPa for hard-modes and 14 MPa for soft-modes can simulate the first data set (i.e. for $\phi = 90°$) only. We did not observe significant improvement in simulating the second set, as shown in Figs. 6.3 and 6.4. The later figure also shows an interesting point that this hard and soft based approach predicts similar deformation behavior for both loading directions.

6.2.5 Longitudinal-mixed-transverse modes based approach

At the lamellar or phase length-scale, anisotropy arises from the differences in deformation resistance of different slip systems within the same phase, while in microscopic or grain length-scale, it is related to inter- and intra-phases differences in the deformation resistances [150]. Necessary kinematic coupling between the two phases can be incorporated by requiring that slip parallel to the lamellar interfaces is dominated by the softer phase, while slip normal to these interfaces is taken to be controlled by the harder phase. In a lamellar alloy, one would expect that the lamellar boundary is a potential barrier to dislocation movement and hence shear deformation parallel to the lamellar interfaces is considerably easier (the soft-mode) than that normal to the interfaces (the hard-mode) [150]. In the previous subsection 6.3.4, hard-soft classification was based on various experimental evidences, whereas, the current harder-softer

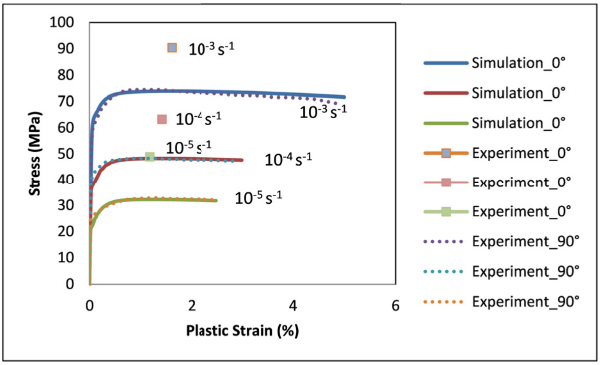

Figure 6.4: Rate-dependent plasticity at $\phi = 0°$: experiment vs. simulation with hard-soft based CRSS configuration, dotted lines are included to show that this approach predict almost isotropic deformation behavior.

grouping is related to the phase interface. Considering Ti-rich TiAl, Grujicic and Batchu [150] proposed half of the slip systems belongs to the easier group and half to the harder group based on the presence of interface. In fact, this interface based version is a rearrangement of the early idea of easy (ordinary) and hard (superdislocation) slip [266]. Due to lamellar structure, this approach is expected to be a better choice for our case in characterizing CRSS.

For our lamellar alloy, since the interface is parallel to (001) plane, we found all six ordinary systems are longitudinal to the interface. Rest of the two planes from the cubic family are perpendicular to the interface, for which, we considered them (4 systems) as transverse type. Finally, rest eight superslips from the octahedral family have been considered as mixed type. We used CRSS of 14, 20 and 24.5 MPa for longitudinal, mixed and transverse systems, respectively. The classification based on hard-soft as described in Sect. 6.2.4 and Longitudinal-Mixed-Transverse (or interface based) are summarized in Table 6.1 with estimated CRSS. Like the previous case, simulation results with this interface based classification, shown in Figs. 6.5 and 6.6, can reproduce one set only, and again highly underestimate the other set. This approach of CRSS characterization works good only for the first experimental data set, but did not work when we try to validate the model with second data set. Since CRSS estimation according to longitudinal-mixed-transverse type classification does not work in our case, it indirectly indicates that the interface effect is not the dominating case here. Alternately, if we simulate the deformation behavior at $\phi = 0°$, then the predicted results for $\phi = 90°$ are expected to highly overestimate the experimental data. So we applied a novel approach of CRSS characterization based on the domination of different slip systems.

6.2.6 Operative stress based approach

Since the lamellar morphology based approach cannot reproduce our available anisotropic responses, it means that the interface effect might not be the dominating case here. An increase in Al concentration makes TiAl harder with the appearance of some superstructures. As γ-phase is little weaker than the r-phase at high-temperature, it is expected that r-phase with LPS also plays an important role to the overall

Table 6.1: Hard-Soft and Longitudinal-Mixed-Transverse based Slip system classification

Slip Systems	Hard-Soft	Interface based Type and Value		Comment
1. (111)[0-11]	Soft	Mixed	20 MPa	Nothing parallel or perpendicular
2. (111)[10-1]	Soft	Mixed	20 MPa	Nothing parallel or perpendicular
3. (111)[-110]	Hard	Longitudinal	14 MPa	Parallel direction
4. (-111)[101]	Soft	Mixed	20 MPa	Nothing parallel or perpendicular
5. (-111)[110]	Hard	Longitudinal	14 MPa	Parallel direction
6. (-111)[0-11]	Soft	Mixed	20 MPa	Nothing parallel or perpendicular
7. (1-11)[011]	Soft	Mixed	20 MPa	Nothing parallel or perpendicular
8. (1-11)[110]	Hard	Longitudinal	14 MPa	Parallel direction
9. (1-11)[10-1]	Soft	Mixed	20 MPa	Nothing parallel or perpendicular
10. (11-1)[011]	Soft	Mixed	20 MPa	Nothing parallel or perpendicular
11. (11-1)[101]	Soft	Mixed	20 MPa	Nothing parallel or perpendicular
12. (11-1)[-110]	Hard	Longitudinal	14 MPa	Parallel direction
13. (001)[110]	Hard	Longitudinal	14 MPa	Parallel direction
14. (001)[1-10]	Hard	Longitudinal	14 MPa	Parallel direction
15. (010)[101]	Soft	Transverse	24.5 MPa	Perpendicular plane
16. (010)[10-1]	Soft	Transverse	24.5 MPa	Perpendicular plane
17. (100)[011]	Soft	Transverse	24.5 MPa	Perpendicular plane
18. (100)[01-1]	Soft	Transverse	24.5 MPa	Perpendicular plane

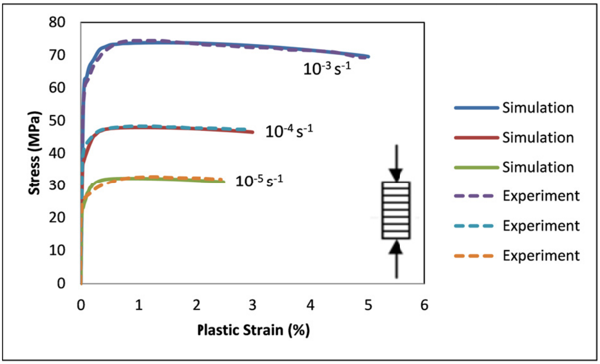

Figure 6.5: Rate-dependent plasticity for $\phi = 90^\circ$: experiment vs. simulation with longitudinal-mixed-transverse type CRSS configuration.

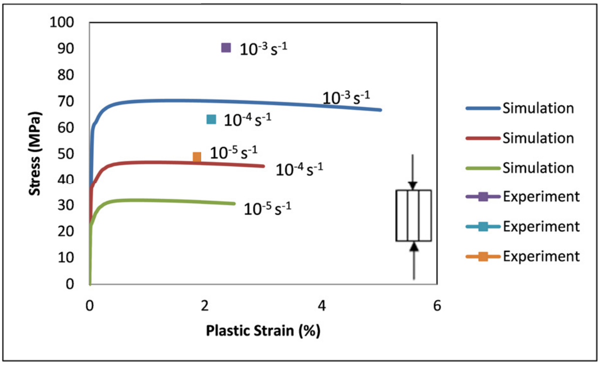

Figure 6.6: Rate-dependent plasticity for $\phi = 0°$: experiment vs. simulation with longitudinal-mixed-transverse type CRSS configuration.

deformation process. We further assume that some systems in the softer gamma phase will dominate the plastic slip when $\phi = 90°$ and some other systems will dictate when $\phi = 0°$ that is controlled by the harder r-TiAl phase. Usually few systems will dominate the plastic slip when $\phi = 90°$ and some other systems will dictate when $\phi = 0°$. Only a few slip systems dominate the overall deformation behavior for particular loading responses [171–173]. For a particular orientation, how and which systems are directly dictated by r-phase with LPS is not clearly understood. From the two experimental data sets of Fig. 2.8, we see that the $\phi = 0°$ orientation is harder than that of $\phi = 90°$ for all strain rates, which implies that slip along some slip systems are directly suppressed by LPS in the former case. Besides r-lamellae are discontinuous, slip can occur across the gap at $\phi = 90°$ loading orientation which makes the deformation process softer. Deformation is carried out by softer γ-phase, where LPS contributes to alloy strengthening. On the other hand at $\phi = 0°$ orientation, the harder r-phase absorbs external loading first, then it is transmitted to softer phase as well. The transmission of dislocations through the interface is harder at $\phi = 0°$ loading. It is agreed that, below the peak temperature, motions of the ordinary type dislocations are suppressed by LPS resulting in additional resistance [127, 158, 265]. At $\phi = 0°$ lamellar orientation, we are assuming that some ordinary systems remain harder at high-temperature as well due to the presence of LPS. This additional resistance is also manifested by comparing peak stresses in the two experimental data-sets. So it is assumed that the harder r-phase with LPS dictates the loading-lamellar orientation of $\phi = 0°$ more than that of $\phi = 90°$.

To identify those unique ordinary systems and to estimate CRSS, we have adopted a different approach. In this approach, the general idea is based on the operative stress domination for a particular loading response. Usually some slip systems are favored for one orientation while other systems are favored for another orientation, which is showed by Nakano et al. [153] and Inui et al. [159]. The most dominant system in a particular loading direction controls the major part of the plastic deformation. Slip system exerting the most resistance is the most dominant one. According to the formulation of Sect. 4.2.5, a slip system is considered to be active when the operative stress $|\tau - X| - R$ on that system is positive. Based on this, we computed individual overall operative stress of all slip systems both in perpendicular and parallel directions.

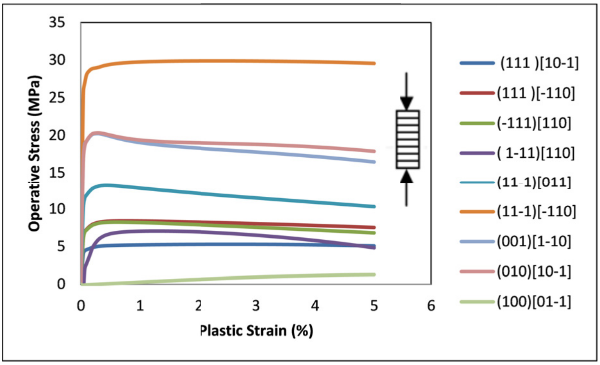

Figure 6.7: Operative stresses for $\phi = 90°$ lamellar setting

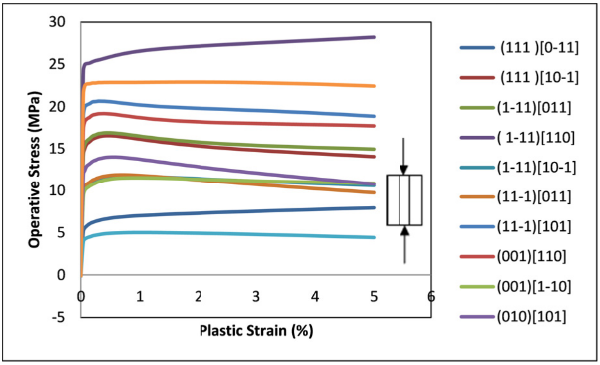

Figure 6.8: Operative stresses for $\phi = 0°$ lamellar setting

Since all superslips have higher CRSS than ordinary group, it can be assumed that the reason of underestimating experimental data at $\phi = 0°$ is that the CRSS of some ordinary systems are underestimated. That is why, we are assuming that those systems lie in the ordinary group where CRSS is underestimated. Shear along those dominating systems are expected to control plastic deformation at $\phi = 0°$. Operative stress for all slip systems are presented in Figs. 6.7 and 6.8. After investigating individual operative stress for each ordinary system in both lamellar orientations we found that three ordinary systems out of six remain harder than other. These major contributing ordinary slip systems are $(1\bar{1}1)\frac{1}{2}[110]$, $(001)\frac{1}{2}[110]$ and $(001)\frac{1}{2}[1\bar{1}0]$. For $\phi = 90°$ orientation, dominating role of the system $(001)\frac{1}{2}[1\bar{1}0]$ can be observed from the Fig. 6.7. Similarly other two systems are dominating at $\phi = 0°$ orientation, Fig. 6.8. To be consistent with the experimental observation, we are considering all twelve superslip systems from both families with higher CRSS, and three ordinary systems with lower CRSS and rest three uniquely dominating systems are in between, i.e. $R_0^{\mathrm{O}} < R_0^{\mathrm{OH}} < R_0^{\mathrm{S}}$, where OH stands for ordinary harder systems.

Table 6.2: Approximated CRSS values (in MPa) comparing three approaches

Slip System	Hard-soft based	Morphology based	Proposed approach
1.(111)[0-11]	24.5	20	24.5
2.(111)[10-1]	24.5	20	24.5
3.(111)[-110]	14	14	14
4.(-111)[101]	24.5	20	24.5
5.(-111)[110]	14	14	14
6.(-111)[0-11]	24.5	20	24.5
7.(1-11)[011]	24.5	20	24.5
8.(1-11)[110]	**14**	**14**	**23**
9.(1-11)[10-1]	24.5	20	24.5
10.(11-1)[011]	24.5	20	24.5
11.(11-1)[101]	24.5	20	24.5
12.(11-1)[-110]	14	14	14
13.(001)[110]	**14**	**14**	**24.5**
14.(001)[1-10]	**14**	**14**	**18.3**
15.(010)[101]	24.5	24.5	24.5
16.(010)[10-1]	24.5	24.5	24.5
17.(100)[011]	24.5	24.5	24.5
18.(100)[01-1]	24.5	24.5	24.5

To approximate a reasonable value for a R_0^{OH} along a slip system α, we adopted the following formula:

$$R_0^{\mathrm{OH},\alpha} = \frac{R_0^{\mathrm{O}}\bar{\tau}_{\mathrm{T}}^{\alpha} + R_0^{\mathrm{S}}\bar{\tau}_{\mathrm{L}}^{\alpha}}{\bar{\tau}_{\mathrm{T}}^{\alpha} + \bar{\tau}_{\mathrm{L}}^{\alpha}} \tag{6.1}$$

where R_0^{O} and R_0^{S} are CRSS for ordinary and superlattice systems, respectively. $\bar{\tau}_{\mathrm{L}}^{\alpha}$ and $\bar{\tau}_{\mathrm{T}}^{\alpha}$ denote averaged operative shear stresses on the slip system α for the loading in longitudinal ($\phi = 0°$) and transverse ($\phi = 90°$) directions, respectively. In essence, these three dominating systems took a weighted average CRSS based on both directional operative stresses. Since we are not differentiating individual CRSS in different loading directions, so we need to take a weighted averaged, which is approximated by Eq. (6.1). For example, considering slip system $(001)\frac{1}{2}[1\bar{1}0]$, we can find from Figs. 6.7 and 6.8, $\bar{\tau}_{\mathrm{T}} = 16.5$ MPa and $\bar{\tau}_{\mathrm{L}} = 10.9$ MPa. So approximate CRSS for this system would be $\frac{14\times16.5+24.5\times10.9}{16.5+10.9} \approx 18.2$ MPa. Similarly, we found 23 and 24.5 MPa for two other systems. To have a comparative view, all approximated values of CRSS including hard-soft and lamellar morphology based approaches are summarized in Table 6.2. For better visibility in the tabular form, index $\bar{1}$ is written as -1. From the table, we can see that CRSS ratio varies from 1.3 to 1.8 which is also consistent with experimental finding. Simulation results, illustrated in Figs. 6.9 and 6.10, show that with the last set of Table 6.2 can successfully reproduce rate-dependent plastic anisotropy in both lamellar orientations. In short, all ordinary systems are harder below the peak temperature, and all superlattice dislocation slips are harder beyond the peak. Accordingly, all twelve superslip systems from the both family are harder with the highest CRSS , three ordinary systems softer with the lowest CRSS beyond the peak temperature. In our case, we found additionally three special ordinary systems with comparatively higher CRSS above the peak temperature. This means, $R_0^{\mathrm{O}} < R_0^{\mathrm{OH}} < R_0^{\mathrm{S}}$, where superscripts O, S and OH denote ordinary, super and harder ordinary systems, respectively. The presence of LPS might be a potential reason, that can suppress shear along these three systems. It is to be noted that these three systems are not the major contributor when loading at

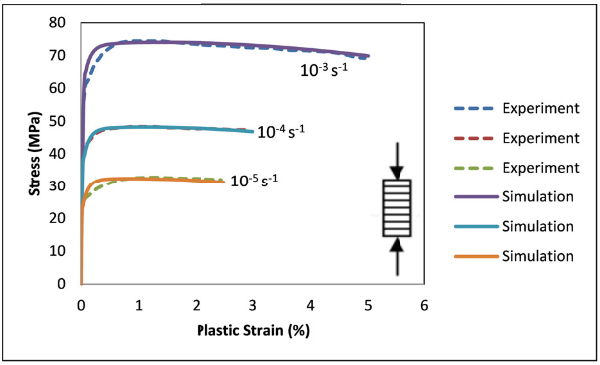

Figure 6.9: Rate-dependent plasticity when the compression and lamellar axes are at $\phi = 90°$: experiment vs. simulation with the proposed approach.

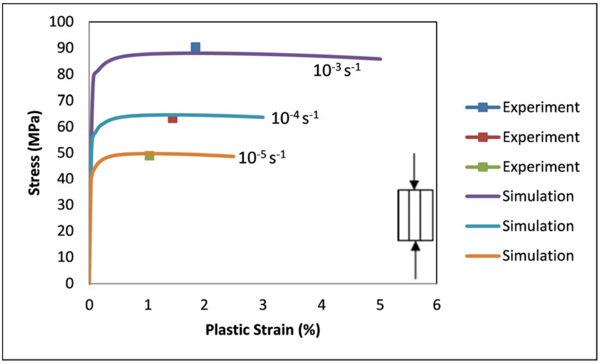

Figure 6.10: Rate-dependent plasticity when the compression and lamellar axes are at $\phi = 0°$: experiment vs. simulation with the proposed approach.

$\phi = 90°$. Since peak stresses are higher at $\phi = 0°$ for all three rates, it is clear that the harder r-phase with LPS has more influence to the loading responses at $\phi = 0°$ than that of $\phi = 90°$. In other words, the loading responses at $\phi = 90°$ are more influenced by the softer γ-phase, while responses $\phi = 0°$ by the harder r-phase with LPS. In Ti-rich side, lamellar interface plays major role, while in Al-rich side, phase lamellar boundary alone is not playing the dominating role, rather slip systems in the harder phase with long-period superstructure adds additional role in the overall anisotropic plastic deformation. Availability of experimental data in many loading direction will certainly refine the estimation process. The estimation of CRSS in dominating systems is expected to be more reliable that that of less active or inactive systems. Nevertheless, we believe the approach can be applied for many directional deformation behaviors and possibly for tension-compression asymmetry as well.

To have a better reflection of harder phase r-Al$_2$Ti and softer γ-TiAl, we can also apply a distinction in CRSS between the two phases. Since we did not have any experimental data about the differences at

Table 6.3: Used CRSS for both phases

Slip System	CRSS for γ-phase	CRSS for r-phase
1.(111)[0-11]	22.5	26.5
2.(111)[10-1]	20	24
3.(111)[-110]	12.5	16.5
4.(-111)[101]	12.5	16.5
5.(-111)[110]	12.5	16.5
6.(-111)[0-11]	12.5	16.5
7.(1-11)[011]	22.5	26.5
8.(1-11)[110]	20.8	24.8
9.(1-11)[10-1]	22.5	26.5
10.(11-1)[011]	17.3	21.3
11.(11-1)[101]	22.5	26.5
12.(11-1)[-110]	12.5	16.5
13.(001)[110]	22.5	26.5
14.(001)[1-10]	16.3	20.3
15.(010)[101]	22.5	26.5
16.(010)[10-1]	14.5	18.5
17.(100)[011]	22.5	26.5
18.(100)[01-1]	12.5	16.5

such high-temperature, we took a rough estimate of differences as presented in Table 6.3. It should be noted, whether we use the values of CRSS from the last column of Table 6.2 or from the set of Table 6.3, we do not find significant differences in results shown in Figs. 6.9 and 6.10.

6.3 Comparing four approaches

To see the degree of accuracy it is better to compare all four approaches. Fig. 6.11 presents deformation behaviors for $\phi = 0°$ lamellar orientation and for the strain rate of 10^{-3} s^{-1}, comparing results based on all CRSS estimation methods. It shows that the other three techniques of slip system classification highly underestimate the results in parallel lamellar direction. Conversely, we can say that if we simulate experimental data-points correctly at $\phi = 0°$ then the predicted results at $\phi = 90°$ would overestimate the experimental curves. Phase interface due to lamellar morphology is not the only contributor, rather long-period superstructures in the harder phase also dictate the overall anisotropic plastic deformation. As a result mechanism and morphology based approaches were not successful. Our method is so flexible that we could apply it in a generalized way, as described in the next section. The strength of our approach is, it can be accommodated for many set of mechanical behaviors and for materials with very complex microstructures. We also believe it can be applied for twin system classification as well. Still the modeling approach as usually cannot distinguish among primary and conjugate systems. Although higher value of CRSS or less mobility of ordinary systems, as experimentally observed, is not directly reflected in the final set of weighted average CRSS values, but they are intrinsically considered in each individual direction. As mentioned earlier we do not have any experimental data about the difference between the two CRSS of the two families, nor any idea about CRSSs of individual slip system in a family. Asymmetry and anisotropy are expected to be a little bit higher with different values of CRSS.

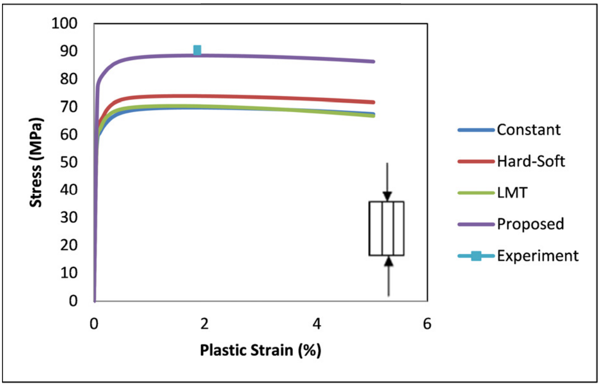

Figure 6.11: Comparison of four approaches, LMT: longitudinal-mixed-transverse.

6.4 A generalized iterative scheme for CRSS estimation

Instead of considering lamellar morphology and LPS effect separately, operative stress based CRSS estimation technique considers the combined effect of both the morphology and the superstructures. The root idea is the individual slip domination based on the operative stress. Once the most dominating system is known then whether we use constant CRSS for all systems or morphology based three different values (longitudinal-mixed-transverse based) the overall results will not make a big difference. The technique, described in Sect. 6.2.6, has been applied for only two sets of anisotropic data. In fact the approach can be presented as a special case of a generalized iterative scheme. In other words, we can generalize this technique in an iterative scheme for many set of anisotropic responses. The idea will remain the same, i.e. operative stress based directional domination of individual slip system. The task is to quantify the degree of dominance of all slip systems for all possible anisotropic loading responses, then to make a weighted average. The slip system exerting the most resistance is the most dominant one.

Let us consider that we know the number of active slip systems N, we have M anisotropic experimental data sets, and we know the necessary material parameters. Now we can represent the idea in five steps as follows.

- Step-1: Find a constant CRSS for all systems, based on the the simulation of a particular loading responses. Then do the same for all sets of anisotropic data. Let's say the identified values are R_{01}, R_{02}, R_{03} .... R_{0M} for M anisotropic responses. Considering N slip systems and M data sets, we can write the initial estimate of CRSS for all slip systems as:

$$\begin{array}{cccc}
R_{11} = R_{01}, & R_{12} = R_{02}, & \ldots\ldots & R_{1M} = R_{0M} \\
R_{21} = R_{01}, & R_{22} = R_{02}, & \ldots\ldots & R_{2M} = R_{0M} \\
\ldots & \ldots & \ldots\ldots & \ldots \\
\ldots & \ldots & \ldots\ldots & \ldots \\
R_{N1} = R_{01}, & R_{N2} = R_{02}, & \ldots\ldots & R_{NM} = R_{0M}
\end{array}$$

- Step-2: Compute average operative stress for each slip system individually for every experimental data set. Doing so we will have $N \times M$ average operative stresses. We can write all these values in an array as:

  $$\begin{array}{cccc} \tau_{11} & \tau_{12} & ...... & \tau_{1M} \\ \tau_{21} & \tau_{22} & ...... & \tau_{2M} \\ ... & ... & ...... & ... \\ ... & ... & ...... & ... \\ \tau_{N1} & \tau_{N2} & ...... & \tau_{NM} \end{array}$$

  where the first index indicates the slip system number and the second one stands for the number of anisotropic data sets.

- Step-3: Calculate the CRSS for all slip system using the following formula. For Nth slip system, it will look like:

  $$R_0^{\mathrm{N}} = \frac{R_{N1} \times \tau_{N1} + R_{N2} \times \tau_{N2} + ... + R_{NM} \times \tau_{NM}}{\tau_{N1} + \tau_{N2} + ... + \tau_{NM}} \qquad (6.2)$$

  Thus we have the second set of estimated CRSS for all slip systems as R_0^1, R_0^2 ..... R_0^{N}. This set of CRSS would under or overestimate experimental data sets. So we need to adjust the second set of estimated CRSS for individual data sets.

- Step-4: Let N^{th} slip system is dominant for the first set of experimental data, then put $R_{N1} = R_0^{\mathrm{N}} + r_1$, where r_1 is a real number, so that the the first set of experimental behavior can be simulated. In the same way, repeat this procedure for all data sets M. Again, for each set of M, compute average operative stresses $\tau_{11}, \tau_{12}, ...\tau_{NM}$.

- Step-5: Go to step-3 and continue the loop until a single set of CRSS can successfully reproduce all experimental anisotropic data sets.

According to this approach, the most dominant system should take a reasonable estimate of CRSS, other systems will be assigned with relative to the most dominant system. The whole algorithm is based on the relative activity of different slip systems or weights of operative stresses with respect to a particular loading responses. For a particular loading, some slip systems from N might be inactive or nearly inactive. In that cases, CRSS values can be put a minimum one, as zero CRSS is not meaningful. If fact, using this approach will severely underestimate the CRSS values of the less or non active systems against a particular loading responses. The interesting point is that, whether we use a fixed CRSS for all systems or a set of relative values with respect to the operative stresses, we get almost similar results with very little deviation, as long as the most dominant system takes the same value. So underestimated CRSS can be refined by dealing with mechanical responses from many loading directions. If the number of responses are very few, then the estimation of CRSS in dominating systems is expected to be more reliable than that of less active or inactive systems. One of the major advantages of this technique is the flexibility in modeling, i.e. this technique can choose a set of CRSS for which arbitrary plastic anisotropy can be simulated.

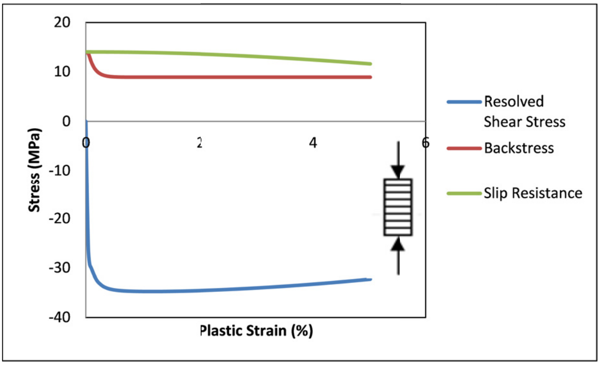

Figure 6.12: Comparing slip system level three different stresses, two hardening stresses with resolved shear stress along the most active system (11-1)$\frac{1}{2}$[-110] when $\phi = 90°$.

6.5 The role of different hardening stresses

From the previous discussion, we have seen that only few slip systems control the plastic deformation. We found that a very few slip systems from each family is dominating. The slip system level contribution of two hardening, isotropic and kinematic, has been shown in Figs. 6.12-6.13 for the most active slip systems, (11-1)[-110] and (001)[1-10], at $\phi = 90°$ and $\phi = 0°$ loading, respectively. For better comparison, resolved shear stresses of the two slip systems are also included. Two figures indicate that the contribution of kinematic hardening is quite significant and it might be more or equally important as isotropic hardening. The internal resistance varies almost linearly throughout the deformation while kinematic part (backstress) is nonlinear. As we can see from Fig. 6.12, there would be an overestimation of the operative stress without considering the backstress. The figure also indicates that the overall plastic behavior in the first stage is more influenced by the kinematic hardening part while the both isotropic and kinematic hardening govern the next stage. These results for superalloy also suggest that the hardening is much more kinematic than isotropic [28].

6.6 Comments on the plastic anisotropy

With the set of constitutive equations mentioned earlier along with a fixed set of materials and model parameters we can successfully simulate the rate-dependent plastic anisotropic behaviors both at $\phi = 90°$ and $\phi = 0°$ orientations. Results are illustrated in Figs. 6.9 and 6.10. During plastic deformation, microstructure evolves at different scales depending on the material, loading path, loading rate and the boundary conditions. These microstructures manifest themselves as plastic anisotropy upon strain path changes [42].

For this specific case of partial lamellar morphology, it seems Hall-Patch stress is the dominating factor of plastic deformation. The overall stress responses are higher at $\phi = 0°$ than that of at $\phi = 90°$. This is because, some dislocations can easily pass across the gap of two discontinuous r-lamellae at

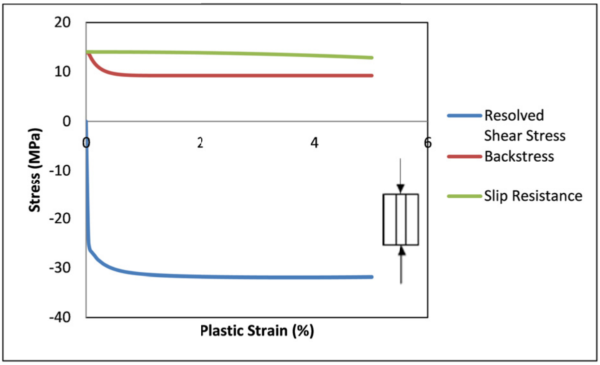

Figure 6.13: Comparing slip system level three different stresses, two hardening stresses with resolved shear stress along the most active system (1-11)$\frac{1}{2}$[110] when $\phi = 0°$.

$\phi = 90°$, which is comparatively difficult at $\phi = 0°$ loading orientation. From the crystal plasticity constitutive modeling perspective, we observed that the overall plastic behavior in the first stage is dominated by the kinematic hardening part while the both isotropic and kinematic hardening governs the next stage. So on can say the plastic deformation behavior of off-stoichiometric Al-rich TiAl alloys generally depends strongly on the morphology, size and condition of the superstructures [138, 140]. At the crystal structure length-scale, anisotropy arises from the differences in deformation resistance of different slip systems within the same phase, while in microscopic length-scale, it is related to large differences in the deformation resistances within each phase and to the differences in deformation resistances of the two phases [150]. Hard-modes are influenced by the harder α_2 phase, and hard-modes are limited due to one tenth volume fraction of the harder phase in Ti-rich TiAl alloys [150].

Chapter 7

Parameter estimation

In this chapter we will try to understand which material and model parameters are playing big role in the simulation process and whether different flow-rules fitting experimental data lead to the similar values of the similar material parameters, and at the end, which flow-rule leads to a more meaningful parameter set.

7.1 Components of the elasticity tensor

Generally a small differences in the independent constants of the elasticity tensor cause a negligible variation in the overall results. The Elastic constants of γ and r-phases, individually or in intermetallic condition, are not readily available at high-temperature regimes. Tanaka [267] experimentally measured elastic constants of γ-phase for Ti-56at.%Al alloy up to 300K, while He et al. [268] measured at 750K and extrapolated till 1273K. These are summarized in Yoo and Fu [269]. Based on these experimental and approximated calculation, we extrapolated these values at 1050°C. On the other hand, for r-TiAl$_2$ phase we only have these constants at room temperature [270]. Following the similar pattern regarding temperature dependence, we have approximated values of elastic constants for r-phase at 1050°C. A small change in these constant does not make a reasonable difference in the results. Both data sets are summarized in Table 7.1. According to the Voigt notation system, the symmetric fourth-order elasticity tensor (L_{ijkl}) can be reduced to a 6×6 matrix (C_{ij}). For an orthotropic material there will be only 9 independent components in the elasticity tensor. For our case, $C_{11} = C_{22}$, $C_{23} = C_{13}$, and $C_{55} = C_{44}$. So there will be only six independent components.

7.2 Rate sensitivity parameter

Rate sensitivity parameter n is generally a function of stress, strain rate, and temperature. The temperature dependence is proposed as less strongly [212]. In spite of that it can be taken as a constant for engineering calculations over a range of these three variables. Padmanabhan et al. [215] showed that n is not

Table 7.1: Extrapolated elastic stiffness constants (in GPa) of γ and r phases at 1050°C

Phase	C_{11}	C_{12}	C_{23}	C_{33}	C_{44}	C_{66}
γ-TiAl	150	76	76	153	82	64
r-TiAl$_2$	162	73	60	182	60	80

Table 7.2: Identified material parameters

Parameters	Name	Values
Rate-dependence	Rate Sensitivity, n	4.5
	Drag Stress, $K(\mathrm{MPa})$	122
Isotropic Hardening	Initial CRSS, $R_0(\mathrm{MPa})$	14
	Recovery Parameter, b	9
Kinematic Hardening	Internal Stress, $C(\mathrm{MPa})$	3500
	Recovery Parameter, d	45
	Parameters for Flow Accumulation Function, ϕ_0 and δ	0.24 and 600

independent of temperature as assumed in many cases and generally decreases with temperature. With increasing homologous temperature, n is expected to be less. Critical dependence of n on temperature has been repeated in Dyson and McLean [191]. This parameter varies depending on the mechanisms, n is believed to be 1 for diffusional creep, 2-4 for grain boundary sliding controlled creep, also 1-2 for climb controlled, more than 5 for glide controlled creep. Based on the stress level, Bower [211] mentioned that at low stresses n=1 to 2.5; at intermediate stresses n=2.5 to 7, and at high stress n increases rapidly and can exceed 10-20, depending on the material, type of alloying and processing conditions. Similar view has been supported in Padmanabhan et al. [215]. In creep deformation of single-phase $\mathrm{Ti_3Al}$, n is separated into two stress exponent regimes. The stress exponent had a value in between 4.3 and 5.0 for stresses above 138 MPa, and between 2.3 and 2.5 for stresses below 138 MPa [222]. For rate-dependent case, Hutchinson (1976) [212] reported that n usually falls in between 3 to 8 for metals. Recently Chen et al. [16] mentioned that it can be taken as a constant over a range of temperature, stress, and strain-rate, and falls within the range of 3 to 7 observed in pure metals and Class M alloys. This range has been conveniently termed five power. As claimed by Kassner and Perez-Prado [30], if the deformation mechanism is associated with dislocation climb then the exponent is relatively 5 over a range of temperature and strain rates until the temperature decreases below roughly $0.5 - 0.6T_\mathrm{m}$.

For our alloy at 1050°C, Sturm [151] has approximated this value nearly 5.5 using log-log graph of strain rate and stress. So we started our analysis with this value of 5.5, however, simulation results with this value of n do not agree with the experimental data sets. As a result, keeping minimum contributions of the two internal variables we identified the value of n as 4.5 and viscous drag constant K as 122 MPa. Afterwards, we adjusted other seven parameters for slip system level isotropic and kinematic hardening (Table 7.2). Quantification of two internal variables in a more generalized way is possible with calibrating experimental data both for monotonic and cyclic loading.

From our results we see that n is in the acceptable range for type-5 flow-rule. As discussed above, lower value of n from the above range is more meaningful, to be precise, approximately 5 of less. Since our case is at moderate to lower moderate stress range and the working temperature is well above $0.7T_\mathrm{m}$, the identified value of n indicates that the deformation is dislocation climb-controlled as it is widely believed [271]. It also means that we cannot use the set of identified parameters to predict very high strain rate controlled tests far beyond our experimental cases. Because n generally increases with the higher strain rate. Another power-law parameter is K or $\dot{\gamma}_0$, which influence the experimental behavior together with n as it is dependent on n [215] and they are fitted against the experimental data.

If the creep processes i.e. glide and climb are sequential then the slower one is expected to be the rate controlling. Generally climb velocity is slower. On the other hand, if the processes are in parallel, then the faster one will be the rate controlling. Depending on the value of n as 4.5, it probably can be assumed that the processes are parallel, the climb velocity is faster and rate controlling, as indicated by Sturm et al. [121, 151]. For climb controlled dislocation creep, Weertman model predicts power-law stress exponent, $n = 4.5$.

7.3 Latent hardening and interaction matrix

7.3.1 Self and latent based hardening phenomenology

The classical crystal plasticity theories are founded on the ground that the hardening on a particular slip system and its corresponding work-hardening rate will depend on the slip activity on both this slip system and all others as well. The exact form of this dependence is defined by the phenomenology of self/latent hardening description or slip interactions in the form of a hardening matrix or the interaction matrix [234]. This self and latent based hardening interaction is widely used. In a slip driven deformation process, self hardening is related to slip accumulation due to dislocation pile up, while all other causes of hardening are explained in the literature as latent hardening (LH). If the latent hardening equals self-hardening, an isotropic response is expected in that case [272]. The stronger the interaction between primary and secondary slip systems, the higher the resulting value of the LHR, for very strong interactions, caution must be exercised in interpreting the results [273]. The interaction matrix could be diagonally dominant or off-diagonally dominant [228, 274]. The self hardening evolution is considered as a function of the cumulative slip of the respective slip system or all slip systems. The latent hardening is taken as a fraction of self hardening, sometimes more than self hardening, sometimes less. If the softening effect (e.g. dynamic recovery) exists in the deformation mechanisms then that effect is also considered in the evolution of the self hardening. Cross hardening or hardening interaction, sometimes used instead of latent hardening, arises when the activity in one slip system suppresses the activities in all other slip systems at the same point [275]. The most controversial part of this phenomenology of self-latent based hardening is the latent hardening ratio, p. According to earlier literature, the ratio of latent to self hardening has a sharp increasing trend from 1 to a value of 1.4 in the earlier stage of primary slip before decreasing to a saturation value higher than unity [276]. In crystal plasticity modeling, it is often considered an average value in the range of 1.2 to 1.4 [277] at the beginning of plastic deformation. The earliest review on this phenomena suggests nearly unity for coplanar systems, and it should be in the range of 1-1.4 for non-coplanar slip systems [177, 278] especially for materials with a very low stacking fault energy.

7.3.2 On the origin of latent hardening description

Various explanations on the origin of latent hardening evolution can be found in the literature. There are several dislocation models that are based on different interactions. However, there is not general agreement on this issue. In a crystalline materials some of the interactions are pile-up model, forest dislocation model, dislocation tangles model etc. Some other models are dislocation-impurity, dislocation-solute atoms, primary-primary, and primary-forest, dislocation–substructure interactions etc. [220]. At lower temperature, LH is believed to be due to lack of mobile dislocations in the latent system to maintain applied strain rate, while at high-temperature it is due to either interaction between glide and forest dislocations or the lack of mobile dislocations in the latent system or both. Mobile dislocations increase rapidly with temperature, thus lack of mobile dislocation becomes highly important for latent systems at lower temperature only. The consequence is, this mechanism predicts a rather isotropic LH. However, there are also a several attempts to understand anisotropic LH based on anisotropic interactions and densities, when LH is in the increasing trend [279].

Nakada and Keh [229] also interpreted the causes of LH interactions between dislocation-impurity, primary-primary and primary-forest dislocations) are associated with long-range internal stress (LRIS). This means latent hardening is associated with long-range internal stresses and with the lack of mobile dislocations in the latent system at lower temperature [229]. Similar explanation is given by [280], where it is said that the LH is associated with the long-range elastic interaction of the intersecting dislocations and the formation of junctions. Both processes generate obstacle structures with long-range stress fields, which limit the slip path of the gliding dislocations. The overcoming of the obstacle structures results in an athermal contribution to latent hardening. They concluded that in such case LH must be equal to or less than self hardening and LH ratio due to LRIS would be half. In some recent works, for example [281], only marginal contribution form LH is considered motivated from dislocation dynamics. Khadyko et al. [234] showed a similar trend in his work. At higher temperature, dislocations become more and more mobile for which recovery process gets stronger. On the other hand, there is often more than one mechanism active during the deformation of a metal or alloy. If we do not consider any important mechanism in the constitutive model then the hardening caused by the missing mechanism is inherently attributed to the latent hardening. Thus a portion of latent hardening is largely responsible for missing mechanisms. In dislocation density based modeling, some part of LH is related to the evolution of geometrically necessary dislocations [74], which is adopted by backstress or kinematic hardening variable in phenomenological modeling. Thus LH is also linked to slip system level backstress evolution.

7.3.3 Latent hardening experiments

Usually latent hardening tests were mostly conducted by single slip deformation measuring flow stress in a single active system making all other systems latent. Experimental investigations using strain-path changes was considered at the beginning to estimate the latent hardening contribution. In the early stages of experiments and modeling, the most practices considered this ratio is more than 1. This result was highly debated especially when larger dependency of hardening is attributed to the latent hardening [5, 234]. Latent hardening tests on silver, silver-gold alloy, aluminium, iron all have indicated a stronger latent hardening on the coplanar and/or the intersecting systems, however Franciosi et al. [279] mentioned that most of the forest systems have higher LH values than coplanar ones. There is further contradiction about the values of LH ratio being greater than one. If LH is based on the dislocation-impurity interactions then it should be equal to self hardening considering uniform distribution of impurity, if it is based on the dislocation-forest interactions then it is expected to be in the range of 1.4-2.2 [229]. Wu et al. [221] mentioned that the enhanced hardening arising from secondary slips during stage II deformation (forest hardening) and the activation of secondary slips indicate that the hardening of an active (primary) system is greater than that of an inactive latent system. For Cadmium and Zinc crystals, LH was found to be less than unity. They also described that the initial rapid hardening associated with activation of a previously latent system is caused by slip interaction and, therefore, should be interpreted as active (self) hardening. Furthermore, experimental procedure for estimating latent hardening was also criticized. Because the estimates of the initial yield stress based on back extrapolation in the secondary test of the latent hardening experiment ignore the details of initial hardening, and a latent hardening model established on such an estimate cannot predict the transition from straining stage I to II of a single-crystal stress-strain curve [282]. A short summary of different experimental methods of LH and inconsistencies in results is available in [234]. Wu et al. [221] concluded that the total hardening on any truly latent/secondary system is lower than the total active hardening on the primary system, at least before the activation of the secondary slips. When aluminum crystals tested separately for primary single slip and for primary-conjugate double slip, it was found that the LH ratio is higher for single slip than double slip condition [226, 228]. That means high latent hardening will tend to give slip on as few systems as possible [14, 278].

7.3.4 Latent hardening practices

There are more than one practices regarding the consideration of the hardening interaction matrix, $\mathsf{H}^{\alpha\beta}$, in the phenomenological modeling of crystal plasticity. If the flow-rule is one internal variable based, the traditional approach is to consider the total hardening into the evolution of that internal variable. In such cases, the major contributor in the evolution of yield and drag or CRSS is the hardening interaction matrix. The second approach of considering this ratio is less than 1, usually in the range of 0.1 to 0.5. When more than one internal variables are considered in the flow-rule, some additional deformation mechanisms are expected to be included in the evolution of the later internal variables. Thus only a minor fraction of latent hardening is important to successfully mimic the mechanical behaviors of a material. So in the interaction matrix $\mathsf{H}^{\alpha\beta}$, diagonal components are 1 and off-diagonal components depend on the material. For uniqueness of the solution especially in rate-independent crystal plasticity, a positive definite hardening matrix is expected, so off-diagonal components should be positive [283]. The third approach is to excluding the contribution of latent hardening, which is seen in the evolution equations of physical process based internal variables. Few recent works on this type of practice are [284–288].

The first type of practices is not limited to a single value of this ratio. Instead of using an averaged value of latent hardening, many researcher attempted to understand this quantity from the physical processes. Hence more than one components based latent hardening ratio has been proposed. The more complex is the microstructure, the more independent components in the nonsymmetric LH matrix are expected. Bertin et al. [289] considered 19 independent values for the interaction matrix in simulating HCP Mg. It is also proposed that the systems in which dislocations can form sessile and glissile junctions with the primary ones display the highest and the second highest latent hardening, respectively [282]. The most common and complex latent hardening models utilize the 6 independent components based interaction matrix corresponding to 6 types of the dislocation interactions [228, 234, 290–292]. First of them is g_0, which is associated with the interaction between the dislocations belonging to the same slip system, or self-hardening. The second coefficient g_1 describes the interactions between the coplanar dislocations (slip systems with parallel slip planes). The coplanar interaction is assumed to be the weakest of all. The third one is g_2, responsible for Hirth lock, the interaction of the dislocations on the pairs of the slip systems with normal slip directions. This interaction is also weak compared to the other interaction types. The next component is g_3 which defines the strength of the interaction between the dislocations gliding on the slip systems with collinear slip directions. In such cases, cross-slip of planes with respect

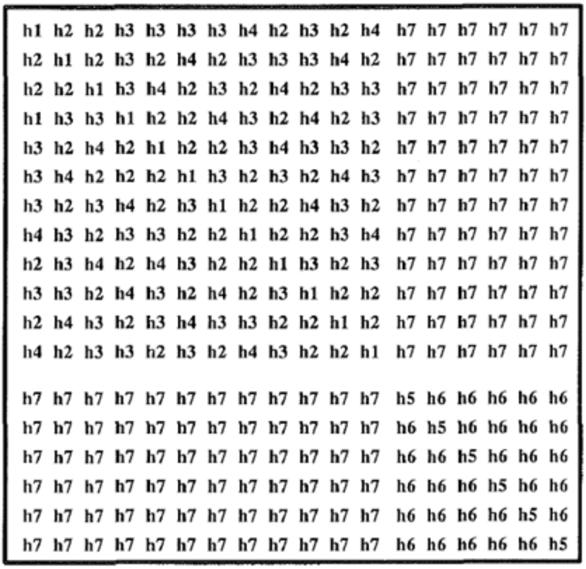

h1	h2	h2	h3	h3	h3	h3	h4	h2	h3	h2	h4	h7	h7	h7	h7	h7	h7
h2	h1	h2	h3	h2	h4	h2	h3	h3	h3	h4	h2	h7	h7	h7	h7	h7	h7
h2	h2	h1	h3	h4	h2	h3	h2	h4	h2	h3	h3	h7	h7	h7	h7	h7	h7
h1	h3	h3	h1	h2	h2	h4	h3	h2	h4	h2	h3	h7	h7	h7	h7	h7	h7
h3	h2	h4	h2	h1	h2	h2	h3	h4	h3	h3	h2	h7	h7	h7	h7	h7	h7
h3	h4	h2	h2	h2	h1	h3	h2	h3	h2	h4	h3	h7	h7	h7	h7	h7	h7
h3	h2	h3	h4	h2	h3	h1	h2	h2	h4	h3	h2	h7	h7	h7	h7	h7	h7
h4	h3	h2	h3	h3	h2	h2	h1	h2	h2	h3	h4	h7	h7	h7	h7	h7	h7
h2	h3	h4	h2	h4	h3	h2	h2	h1	h3	h2	h3	h7	h7	h7	h7	h7	h7
h3	h3	h2	h4	h3	h2	h4	h2	h3	h1	h2	h2	h7	h7	h7	h7	h7	h7
h2	h4	h3	h2	h3	h4	h3	h3	h2	h2	h1	h2	h7	h7	h7	h7	h7	h7
h4	h2	h3	h3	h2	h3	h2	h4	h3	h2	h2	h1	h7	h7	h7	h7	h7	h7
h7	h7	h7	h7	h7	h7	h7	h7	h7	h7	h7	h7	h5	h6	h6	h6	h6	h6
h7	h7	h7	h7	h7	h7	h7	h7	h7	h7	h7	h7	h6	h5	h6	h6	h6	h6
h7	h7	h7	h7	h7	h7	h7	h7	h7	h7	h7	h7	h6	h6	h5	h6	h6	h6
h7	h7	h7	h7	h7	h7	h7	h7	h7	h7	h7	h7	h6	h6	h6	h5	h6	h6
h7	h7	h7	h7	h7	h7	h7	h7	h7	h7	h7	h7	h6	h6	h6	h6	h5	h6
h7	h7	h7	h7	h7	h7	h7	h7	h7	h7	h7	h7	h6	h6	h6	h6	h6	h5

Figure 7.1: A possible consideration of the interaction matrix for 18 slip systems

to each other is appeared. The collinear interaction is often assumed to be the strongest of the above three. The Coefficients g_4 and g_5 indicated the remaining interactions between the non-coplanar slip systems. The glissile type lock is represented by g_4 and the sessile or Lomer-Cottrell dislocation locks are produced by g_5. The strengths of different interactions are proposed as $g_5 > g_4 > g_3 > g_2 > g_1$ [228, 282]. These later dislocation lock types are argued as predominant during stage II hardening [234]. Some authors considered this matrix with 4 independent components where coplanar, collinear and Hirth types were united under one value. There are two and three parameter model for latent hardening representation as well, based on sessile junctions as the primary source and glissile plus Hirth lock as secondary [272]. It is also believed that the lower the stacking-fault energy of the crystal, the higher is the latent hardening [272, 282]. A seven value based hardening interaction matrix considering 18 slip systems can be given as shown in Fig. 7.1, where independent components are given by h_1 to h_7.

Self interactions (e.g. coplanar, collinear) and non-self-interactions (e.g. noncoplanar, non-collinear) based interaction matrix modeling is sometimes also observed [293]. It is to be noted that different latent hardening matrices lead to noticeable differences especially in the prediction of the flow stress anisotropy. In many cases, the most complex interaction matrix does not perform better than the more traditional simplified models. According to Palm et al. [40] latent hardening cannot effectively describe the hardening behavior of some solid solution strengthened alloys during multistep strains. Moreover, these conventional latent hardening effects cannot account for all sources of anisotropy. It is also believed that the latent hardening is the hardening of inactive slip systems, the effect that an active slip system influences the hardening of a neighboring inactive slip system [74]. Most latent hardening models have focused only on dislocation–dislocation interactions; which might be a reason of poor prediction [272]. Two more troubling points are: a) strong latent hardening will lead to a nonuniform pattern of slip (patchy slip) which will complicate the prediction of texture development, and b) higher latent hardening might lead to a loss of uniqueness in the slip mode [177]. Since the operative physical processes are considered in a dislocation density based CP modeling, the consideration of the self-latent based hardening phenomenology is not necessary. Rather some sort of interaction strengths among slip systems have been considered with different evolution equations for different locks and junctions [3].

7.3.5 Latent hardening consideration in this study

Since we have considered (i) separate internal variable for internal stress, (ii) explicit terms for climb assisted recovery, and (iii) all possible systems to be active at very high homologous temperature, we have tried to develop a constitutive model with minimum dependency on latent hardening. At the end, we see that even without latent hardening consideration a material with highly complex microstructure can be modeled for high-temperature deformation. Accommodating slip system level backstress makes latent hardening insignificant [272]. Regarding our phenomenological model, since there is a separate state variable for internal stress, we can say that the burden of LH thus become far less significant at high homologous temperature. If we consider recovery term in our evolution equation then the LH contribution (due to lack of mobile dislocations) would be less or insignificant at high-temperature. In our case, stage I or primary creep experiences hardening through changes in the dislocation substructure, and in the next stage, hardening is overturned by the dynamic recovery. Since it is high homologous temperature deformation and since we have distinctive terms and variables for internal stress and dynamic recovery, we can consider minimum or marginal contribution from latent hardening. We ignored both level of hardening interactions i.e. (a) individually in octahedral and/or cubic system and (b) interaction between octahedral and cubic systems.

Our results also support this finding that marginal or no latent hardening does not make a significant difference in the overall behavior, except in type-1 where the model was almost ideal. Similar approach and conclusion about insignificant contribution from LH can also be found in [174, 294–296]. More and more contribution of latent hardening would be necessary if fewer slip systems are taken to be active, operating temperature is low with slip only deformation process, and microstructures are highly complex. Similarly, higher contribution of LH would also be necessary when only one internal variable with standard evolution equation is introduced neglecting one or more mechanisms like micro-twinning, and grain boundary effect in polycrystals. Based on the large volume of experimental results and theoretical analyses so far one can conclude that the actual latent hardening matrix (or interaction matrix) for a given material and loading condition is still remains controversial and hence an open problem [234].

Chapter 8

Model prediction: Tension-compression asymmetry

8.1 Introduction

8.1.1 Preliminary remarks

Tension-compression asymmetry (TCA) of inelastic behavior, or in a more broad sense, the dependence of inelastic behavior on the kind of loading and the direction, is common for most high-temperature materials. In the last decades, there has been a huge attention from the research community regarding asymmetric phenomena including their strain rate and temperature dependencies. TCA or strength differential (SD) has a wide range of effects in mechanical properties. Strong asymmetric effects in alloys are often detrimental to mechanical properties like deformation, bending and failure of beams, sheets and tubes [297, 298]. For a particular level of stress, creep strains under tension and compression can vary from 2 to 10 times for metallic materials and this can be up to 289 times for crystalline ceramics [299]. Due to strength differential, the mechanical properties obtained from the tensile test cannot reflect the accurate mechanical behavior under the compressive stress state [300]. TCA of the soft substrate not only affects the critical strain of buckling but, more importantly, may also influence the wrinkling pattern that occurs in the film substrate system under specified loading conditions [301]. It is also observed that fracture modes (crack, kink etc.) can be different in tension and compression [302] and the plastic forming with pronounced asymmetry might pose tremendous challenges in the industry [298]. Proper understanding of TCA is useful for many engineering applications including the prediction of critical strain of buckling [301]. To explain and accurately predict the torsional response, it is necessary to account for the combined effects of anisotropy and tension–compression asymmetry at polycrystalline level [298]. Moreover, understanding of TCA is crucial for the structural analysis of power plant components under transient thermo-mechanical loading. Indeed, start-ups and shut-downs of components induce local alternating tensile and compressive loading [192]. As documented in Yaguchi and Takahashi [303], different inelastic behaviors under tension and compression lead to anomalous ratcheting phenomena under cyclic loading at high-temperature. Many results of thermo-mechanical fatigue tests show different stress responses under direct and reversed cyclic strain with the same strain amplitude [199]. Calibrating a constitutive model for asymmetry needs experimental data on creep and/or deformation behavior for tension and compression. In our case experimental data for brittle Al-rich TiAl single crystal are only available for compression as tensile test is often difficult and unsuitable for brittle materials [151]. Therefore an important point is to simulate the macroscopic behavior under tension along with compressive case anisotropy.

8.1.2 Origin of TCA

Microstructure and mechanism dependent various observations can be found when investigating the origin of asymmetry. Salehinia and Bahr described TCA according to the microstructures whether FCC or BCC, and reported that normally BCC structures show TCA due to the effect of non-Schmid stresses on the screw dislocation core [304]. Due to non Schmid effect (e.g. normal stress to the slip system [304]) and twinning, the material with HCP structure would exhibit higher asymmetry than that of BCC/FCC materials. However, pronounced asymmetry can be observed if the above two effects combine in materials with BCC and FCC structures [305]. This asymmetry originates from the differences in dominant deformation modes associated with tension and compression [302, 306, 307]. Besides, directional sensitivity of various kinds of microstructural phenomena (e.g. motion of dislocation, growth of micro-cavities interface, cracks), phase transformation, and non Schmid effect [308] etc. are some other sources of asymmetry. For instance, investigation on B2 Nb-15Al-20V alloy shows that the most active slip plane is different in tension and compression [309]. Due to morphological boundary, grain boundary, misorientation, etc., if the dislocation movement encounters one or more barriers in any of the tensile or compressive loading case then the corresponding loading type would result in higher resistance manifesting TCA. At high-temperature, preferred orientation of dynamic recrystallization might also be different in tension and compression resulting in pronounced SD. Barros et al. [298] mentioned that the hexagonal metals deform due to mechanical twinning or non-Schmid effects at single crystal level, where shear in one direction can produce twin while in the opposite direction cannot, which results in different CRSS with TCA. So strong asymmetry is mainly associated with twinning. Hence the terms hard and soft-mode of deformation came into picture [310]. This view is supported by [311] referring synergistic interplay between slip and twinning, for which CRSS differs based on the loading directions. Directionality of twinning, as the main factor of asymmetry in twin induced deformation, is also discussed in [311–314]. At the nanoscale, heterogeneous dislocation nucleation stress asymmetry exists resulting in SD [315]. In Mg-RE-Zn alloy, strengthened by long-period stacking ordered (LPSO) phase, the LPSO phase cracks during tensile deformation while it exhibits a kinking characteristic in the process of compression. It is concluded that the two different deformation modes of the LPSO phase are the cause of asymmetry [302]. Dominant different non-Schmid behaviors at high-temperature may cause asymmetry in MN11 Mg-alloy [307]. Normal stresses to the slip system and different Schmid stresses for compression and tensile loadings causes asymmetry as reported by Salehinia and Bahr [304]. According to Luo et al. [316], TCA originates from the dislocation-mediated plastic deformation mechanism and from its nanoscale grain microstructure in nanocrystalline Al93-Fe3-Cr2-Ti2 alloy.

8.1.3 General observations on TCA

There are various asymmetries observed in the literature depending on the material microstructure, morphology, strain rate and temperature. In general, a better overview of strength differential is expected when the asymmetry is tested from various loading directions e.g. from various microstructural and morphological orientations. The overall asymmetric behavior can roughly be divided into three broad categories. **Firstly**, one loading case (tensile or compressive) is more resistive in all tested directions for the whole range of deformation. For example, tensile cases are found to be stronger than compression in in high-strength Ti-3Al-2.5V alloys [305]. Some other similar works are Ti and Mg based alloys [297, 317]. The opposite trend (compressive condition is stronger) can be found in Ti-6Al-4V [113], and in various other Ti, Al, Ni and Cu based alloys [113, 318–325] etc. The later case shows a strong presence in various Mg-alloys [302, 311, 326–328]. **Secondly**, tensile case is stronger in some directions while compression is dominant in other directions. To mention few of such case materials are Nickel-based single-crystal superalloy [329], Molybdenum nano pillars [330], severely deformed pure copper [331], etc. **Finally**, either tension or compression is dominant in some directions, however in other directions, if tension is stronger up to some amount of strain then compression becomes dominant for the rest part and vice versa. In some cases only latter behavior is observed in all tested directions especially in Mg-alloys. Few examples of such cases can be found in this reference list [332–343], etc. For many Mg-alloys, there is a possibility that the harder prismatic glide becomes more favored relative to basal glide as the dislocation density rises, which means basal slip has been hardened and prismatic slip softened during the plastic deformation [248]. Apart from the above categories, some unique strain rate and temperature dependent anisotropic and asymmetric behaviors are observed in some Mg-alloys. A summary of these peculiar responses for different Mg-alloys at different strain rates, loading directions and temperatures is presented in Zachariah et al. [344]. For example, it is observed that responses under tension are rate-dependent, but under compression, some responses are rate-dependent some are not [306]. Such mixed behavior is also found in AZ80 Mg-alloy tested at high-temperature [345]. Temperatures dependent asymmetry shows strength differential responses are similar in all tested temperature [346, 347]. For Ti-6.6Al-3.3Mo-1.8Zr-0.29Si alloy, Zhang et al. [348] presented that tension is more rate sensitive than compression and TCA increases with strain rate. A novel tension-compression-tension and compression-tension-compression experimental data for Mg AZ31B show that the tensile stress is almost higher in both cases for all temperatures [349]. Different other unexpected responses can also be found in [307, 348, 350–352].

8.1.4 TCA reduction

To reduce TCA, there are various treatments discussed in the literature. Asymmetry is generally reduced with the grain size refinement by suppressing some twinning activation modes [327, 353, 354], texture modification [355–357], and with precipitations inside the grains and on the grain boundaries [332]. SD can also be reduced with the dominant nature of recovery [358]. Lv et al. [338] found that aging treatment was much more effective in reducing asymmetry of extruded AZ80 alloy. For nanocrystalline Cu, Dongare et al. [320] reported that initially SD decreased with grain size increasing, then again increased. It is revealed in a hot-rolled Mg-3Al-1Zn alloy that the SD is greatly decreased via multidirectional pre-compression [337]. To explain and accurately predict the room-temperature torsional response of a strongly textured material, [298] referred that it is necessary to account for the combined effects of anisotropy and tension-compression asymmetry at polycrystalline level. Sometimes, the plastic anisotropy tends to diminish at a higher strain rate [253].

8.1.5 Macroscopic modeling approach

There are various efforts to model anisotropy and asymmetry for different materials in different scales. In the macroscale, Cazacu et al. [359] proposed a model by developing asymmetric yield function as a continuous function of plastic strain. The asymmetric yield function accommodates twining induced asymmetry as well as in-plane anisotropy through a linear transformation of the deviatoric stress tensor. Plunkett et al. [360] proposed yield functions describing the anisotropic behavior of textured metals extending orthotropic yield function proposed by Cazacu et al. [361]. Later, others have adopted several linear transformations in order to capture in-plane anisotropy more accurately [298, 360]. Similar models with or without combined isotropic-kinematic hardening can be found in [323, 333, 361]. An evolving anisotropic/asymmetric continuum-based material model based on a Cazacu-Plunkett-Barlat-type yield function is proposed to fit the material behavior of AZ31B magnesium-alloy as a continuous function of plastic strain [333]. Another approach is based on the separation of the deformation modes into tension and compression and assuming two independent hardening laws for each case [333, 362]. By defining two or more internal variables e.g. backstress, softening stress, distortional hardening stress and misfit stress etc. [187, 193, 305, 363], is also a well known approach. Sometimes softening stress and misfit stress are combined in hardening-recovery based isotropic hardening [363]. Continuum-based plasticity model with distortional hardening is proposed to model the evolving asymmetric/anisotropic hardening response of Magnesium alloys for both monotonic and reverse loading paths [328]. Three potentials (creep, hardening and recovery) based asymmetric creep deformation has been proposed for initially isotropic materials with different properties in tension and compression within the thermodynamic formulation [299]. By introducing principal shear stress-based models and stress invariants-based models to capture the distorted shape of the yielding, Li et al. [305] adopted a subsequent interpolation approach to smoothly present the nonlinear evolution of the distorted plasticity in the full stress space. An anisotropic yield criterion to decouple the anisotropy and tension compression asymmetry characteristics has also been proposed for Ti-6Al-4V alloy in Khan et al. [112], as the coupling of anisotropy and tension compression asymmetry causes potential problems in the prediction of responses under different strain levels, strain rates and temperatures. The evolution of the yield surface is largely described using the combinations of isotropic and kinematic hardening laws [305] by which both anisotropy and asymmetry can be predicted. Besides, Verma et al. [323] proposed an asymmetric yield function which to be used with a combined isotropic-kinematic hardening model for ultra low-carbon high-strength steel. Another paper is devoted to the development of a macroscopic anisotropic yield criterion for a porous material when the matrix material is incompressible, anisotropic and displays tension–compression asymmetry [314]. The use of an anisotropic yield criterion that captures strength-differential effects and an anisotropic hardening rule that accounts for texture evolution associated to twinning is proposed by Nixon et al. [257]. An overview of phenomenological modeling approaches to consider tension-compression asymmetry can also be found in Naumenko and Altenbach [223].

8.1.6 Microscopic modeling approach

With a proper physical framework, it is expected that micro-mechanical models can capture a wide range of experimentally observed macroscopic deformation phenomenon including anisotropy and asymmetry. Analysing above approaches it can be said that, with a number of proper mechanism-driven slip-system-level necessary internal variables, crystal plasticity (CP) model is expected to be capable of a wide range of experimentally observed macroscopic deformation phenomenon including tension/compression asymmetry as CP is strongly orientation dependent [3]. For highly rate-dependent case, crystal viscoplasticity modeling is a good candidate to capture important deformation characteristics of different alloys including anisotropy as it is strongly orientation dependent [3, 364]. By introducing an isotropic degradation function, Leidermark et al. [365] proposed a crystal plasticity model for elastic anisotropy and tension-compression asymmetry by accounting both Schmid as well as non-Schmid stresses. Using this model, the constitutive behavior of both virgin and degraded material has been described with good agreement with the experimental results. A self-consistent model with physical description of internal stress and internal resistance at different length-scale has been developed by Hu et al. [76] to capture Bauschinger effect. Kim et al. [362] divided the deformation modes into tension and compression and assumed two independent hardening laws for each case [333]. An overview of phenomenological modeling approaches to consider tension-compression asymmetry is also presented in [366]. Three potentials (creep, hardening and recovery) based creep deformation theory with kinematic hardening is proposed for initially isotropic materials with different properties in tension and compression within the thermodynamic formulation [299]. A modified asymmetric yield function is proposed to be used with a combined isotropic–kinematic hardening model for ultra low-carbon high-strength steel [323]. The evolution of the yield surface is largely described using combinations of isotropic and kinematic hardening laws [305, 364, 365] by which both anisotropy and asymmetry can be predicted. Asymmetry occurs because tension and compression represent two different types of strain path changes [331]. One internal variable based CP model with Voce hardening for anisotropy-asymmetry and Swift effect has been applied, and it is shown that Swift effects in AZ31 Mg are due to the combined effects of anisotropy and tension–compression asymmetry [336]. This CP model (with different evolution equation of slip resistance rate) is able to capture important deformation characteristics of Ti-based alloys anisotropy and tension–compression asymmetry [364]. Hardening law implemented in a viscoplastic self-consistent polycrystal model demonstrate that the tension–compression asymmetry and its anisotropy arise not only from crystallographic texture but also from the directional substructure induced by the severe prestraining. Slip activity differs in each grain and in each axial test, depending on its crystallographic orientation, orientation relationship with the previously generated substructure and prestrain history. Asymmetry occurs because tension and compression represent two different types of strain path changes [331]. Apart from microscale, there are models for the plastic anisotropy and tension–compression asymmetry in the discrete dislocation and atomic scales as well [367], where it is shown that non-Schmid effects on screw dislocations of both 1/2<110] and <112] slip systems must be implemented in order to predict the strong plastic anisotropy and tension–compression asymmetry of single crystal Ta.

8.1.7 Modeling of Al-rich TiAl alloys

The generation of TiAl alloy system is well known for high-temperature structural applications. Even though the anisotropy and the asymmetry in Ti-rich side of this alloy system have been investigated reasonably for single-crystal and polycrystalline materials, the lamellar orientation dependence of the plastic anisotropy and the tension/compression asymmetry in Al-rich side, either theoretically or experimentally, is not well documented. In spite of being integral part of modern engineering problems, to the best of authors' knowledge, rate-dependent asymmetric phenomena for Al-rich alloy at high homologous temperature have not been investigated so far. The only work in Al-rich family is Zupan and Hemker [244] regarding Ti-55.5% Al, where asymmetry is investigated for different loading directions, temperatures and orientations which displayed anomalous yielding and a pronounced tension/compression asymmetry. This Al-rich family of alloys is specially important as the overall mechanical responses are resulted from the combined effect of lamellar morphology and long-period superstructure. We have some set of

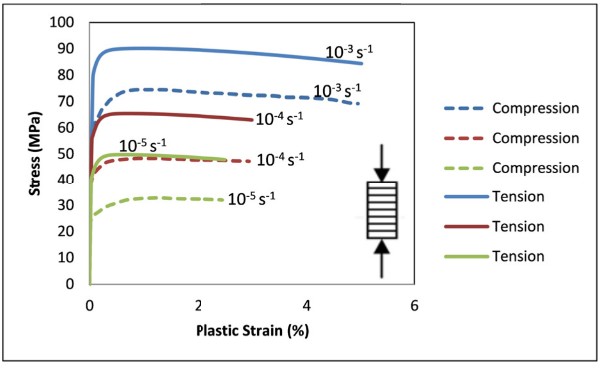

Figure 8.1: Tension-compression asymmetry at 1050°C for different strain rates when $\phi = 90°$

experimental compressive loading responses with no tensile test data. Since the tensile test is often difficult for brittle materials and expensive for single crystals [151], an important point, with a proper modeling approach, would be to simulate the macroscopic behavior under tension in order to get a qualitative understanding of TCA. The main assumption of the model used here is that the critical stresses of all slips systems are similar for tension and compression. Constitutive model has also been calibrated using two sets of rate-dependent experimental data in two different lamellar directions.

8.2 TCA prediction in two lamellar directions

Since the material is highly anisotropic, we can expect high asymmetry in tension and compression as well. We are limiting our asymmetry analysis for two lamellar orientation only as our model is calibrated for these two orientations i.e. for $\phi = 90°$ and $\phi = 0°$. In the flow-rule of the model, asymmetry has been accommodated in the term $|\tau - X|$. Predicted rate-dependent asymmetry has been summarized in Figs. 8.1 and 8.2. Like anisotropy, tension-compression asymmetry is also highly pronounced for responses at $\phi = 90°$. For this case, there is no sharp increase or decrease in asymmetry with increasing strain rates i.e. similar amount of asymmetry is maintained for all strain rates and for the whole range of deformation. This case partly belongs to the first category as described in the introduction, Sect. 8.1. Tensile state is stronger than that of compressive one.

On the other hand, we see a mixed asymmetric responses when $\phi = 0°$. Tensile response offers more resistance at higher strain rate and it decreases with decreasing strain rates with a reverse trend at lower strain rate. Softening effect is more visible in the tensile case than that in the compressive one. This case combinedly belongs to the second and the third category as discussed in the introduction. At $\phi = 90°$, it seems the most dominant slip system offers higher resistance in tension influenced mostly by the lamellar morphology. On the other hand, at $\phi = 0°$, dominant systems are highly rate sensitive and they are motivated by the long-period superstructures. Accuracy of prediction is largely dependent on the accuracy of CRSS both in tension and compression. Instead of directional dependent anisotropic CRSS, we considered a fixed CRSS for anisotropic responses in order to reduce the number of unknown parameters. Moreover, since there is no experimental study about the difference of CRSS in tension and compression,

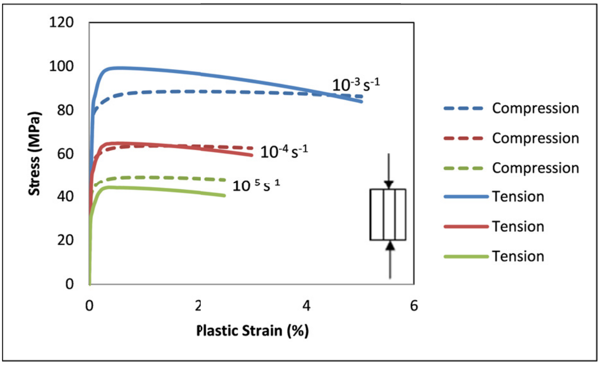

Figure 8.2: Tension-compression asymmetry at 1050°C for different strain rates when $\phi = 0°$

we used the same set of CRSS both for compression and tension and hence the overall asymmetric results remain as qualitative. In fact the evolution of CRSS is motivated by different dislocation mechanics like dislocation accumulation, rearrangement, substructure formation and annihilation etc. For an active slip system, this quantity is reasonably asymmetric for the whole range of deformation. This asymmetric effect has been accommodated in the phenomenological model, which can be realized by observing the asymmetry of operative stresses. To compare this asymmetric effect, one can look at Figs. 8.3-8.6. The asymmetry in operative stresses along SS12 can be seen from Figs. 8.3-8.4, similar asymmetry along SS8 can be observed from Figs. 8.5-8.6. However, at the onset of plastic deformation, the asymmetry in initial CRSS is expected to be very small because of lower or no dislocation activities. Since there is no solid experimental observation about the quantitative assessment of the asymmetric initial CRSS in tension and compression, we assumed it equal for both loading conditions i.e. compression and tension. At the end, the overall asymmetric results remain as qualitative. To the best of authors' knowledge, there is no recent studies investigating the origin of TCA in Al-rich TiAl alloys at high-temperature with long-period superstructures. Our results show that the number of contributing slip systems are different in tension and compression at both orientation of $\phi = 90°$ and $0°$. More importantly, the dominating system or major contributing slip systems are different in tension and compression. Three and two major contributing systems when $\phi = 90°$ and $\phi = 0°$, respectively, have been shown both in tension and compression in Figs. 8.3-8.6. Additionally, the asymmetric operative stresses on SS12 and SS8 have been included in Figs. 8.4 and 8.6 in order to have an idea about the asymmetry associated with the internal variables. Here *T* for tensile and *C* for compressive loading cases and *SS* for corresponding slip systems as numbered in Tables 6.1-6.3.

It is also evident that the compressive deformation is dictated by some ordinary slips, like slip system 12 and 8 for $\phi = 90°$ and $\phi = 0°$. On the other hand, tensile deformation is dominated by superdislocation slips like slip system 9 and 3. These findings are consistent with Ti-rich lamellar single crystals, for example, Inui et al. [159] mentioned that the CRSS of some slip systems are dependent on the direction of dislocation motions. However, in Ti-55.5at%Al single phase single crystal deformed at 700°C, investigation suggests that the same deformation mode was active in both tension and compression [368]. This is also quite possible considering simplicity of the single phase microstructure. Furthermore, the

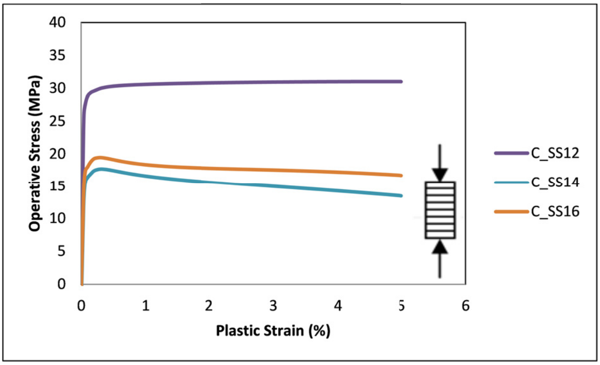

Figure 8.3: Operative stress on the three major contributing systems when $\phi = 90°$, C for compressive loading

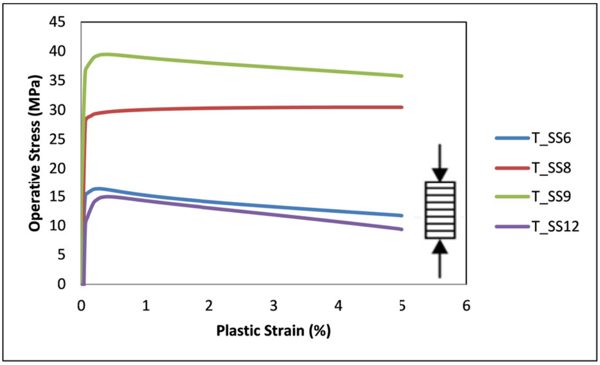

Figure 8.4: Operative stress on the three major contributing systems when $\phi = 90°$, T for tensile loading. The asymmetry in operative stresses along SS12 can be compared with Fig. 8.3

role of the octahedral slip family is more than that of the cubic systems as evident from the operative stresses. If the lamellar morphology were the sole cause of the asymmetry then we would have seen more or less similar slipping activities in tension and compression. Moreover lamellar morphology based CRSS approach have failed to reproduce experimental anisotropy. So we may conclude that the origin of asymmetry is associated more with long-period superstructures than lamellar morphology, and the dominating systems are different in tension and compression. From Nakano et al. [158], it is observed that the difference in CRSS of ordinary and superslips groups increases with the appearance of superstructures. Considering the issue we can expect the crystal lattice level or slip level origins of the anisotropy and asymmetry are also significant as compared to lamellar level origin. Our study also supports the view showing crystal structure or superstructure level origin. Otherwise, we would have seen a smaller value of the maximum to minimum CRSS ratio. Nevertheless, the morphological anisotropy is expected to be significant in all cases irrespective of Ti-rich or Al-rich side. From a number of reports, e.g. [140, 157–159]

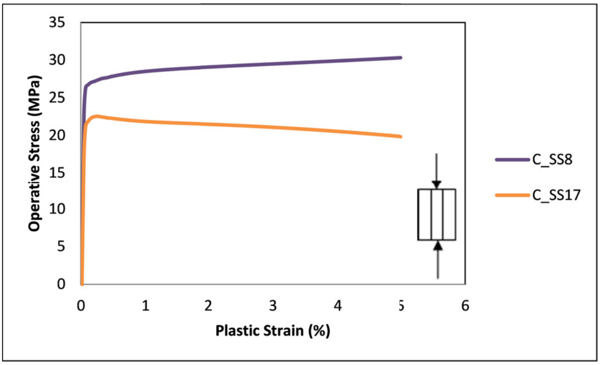

Figure 8.5: Operative stress on the two major contributing systems when $\phi = 0°$, C for compressive loading

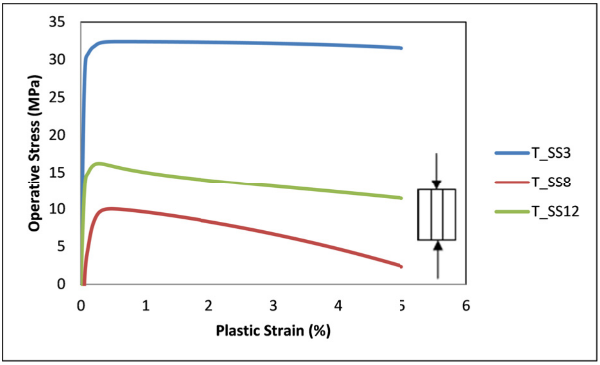

Figure 8.6: Operative stress on the two major contributing systems when $\phi = 0°$, T for tensile loading. The asymmetry in operative stresses along SS8 can be compared with Fig. 8.5

we know that the differences of CRSSs among different slip systems/families at around 1050°C with 62%Al contents are considerably lower as compared to the peak temperature. So the plastic anisotropy and asymmetry near the peak temperature conditions are expected to be very high. The severity of anisotropy and asymmetry is strongly influenced by the size and condition of the superstructural phase, morphology and working temperature. In short, the origin of anisotropy and asymmetry have been rooted in different length-scales.

Chapter 9

Summary and outlook

9.1 Summary

The family of Al-rich TiAl alloys has been studied in terms of phases, microstructures, morphology, deformation mechanisms, etc. With the increase of Al-concentration, Al-rich phases (e.g. Ti_3Al_5, h-$TiAl_2$, r-$TiAl_2$, etc.) start to grow. Heat treatment parameters, phase stability and the operating temperature etc. direct how many and which phases will exist at the end. Comparing with the Ti-rich side, the formation of one or more stable/metastable long-period superstructures is one of the most characteristic features of the Al-rich alloys, which considerably changes the deformation mechanisms and mechanical properties. Controlling hardness and brittleness with the increasing of Al concentration and annealing temperature is still a challenge for the Al-rich side. Within the mean filed homogenization approach a crystal viscoplasticity based phenomenological modeling has been applied for an important alloy from this family in order to analyze the plastic anisotropy and tension-compression asymmetry. Microstructure sensitivity and the presence of different length-scales that influence the mechanical properties have also been attempted to be understood. Crystal viscoplasticity based constitutive model has been implemented for that alloy in Abaqus Standard within its UMAT functionality. Hardening-recovery based phenomenological crystal viscoplasticity formulation with two internal variables has been applied to describe the overall plastic anisotropic response of a highly rate-dependent intermetallic alloy Ti-61.8at.%Al at high homologous temperature for three different strain rates, 10^{-3} s^{-1}, 10^{-4} s^{-1} and 10^{-5} s^{-1}. The proposed crystal viscoplasticity model can successfully reproduce the plastic anisotropy of Al-rich TiAl alloys with different complex superstructures when CRSS are chosen carefully. Then the model with identified parameters has been used to get a qualitative understanding of asymmetry in tension and compression for two loading directions and at the same temperature, as the model was a generalized one for the plastic anisotropy and asymmetry. The important feature of this proposed modeling approach is the rate-dependent anisotropy and asymmetry modeling, and the approach is largely general as it is expected to be successfully applied with a variety of loading conditions and material behaviors. The approach can be applied to other alloys especially from this family. The advances and current understanding about this family and the findings of this work can be summarized by the following points:

9.1.1 Regarding microstructural and morphological impact on the mechanical properties

In contrast to the Ti-rich side, we know from the experimental observation that the superlattice dislocation slips are more operative below the peak temperature than that of ordinary slips. In the approximate range of 700-1000°C, anomalous hardening of different slips is a characteristic feature of the Al-rich alloys. After 1000°C, a variety of slip systems is expected to be operative depending on the loading orientation. Hence both families of slip systems, octahedral and cubic, are important for the simulation process. A few experimental observations pointed out that the some slips from the cubic family are dominating even at that high-temperature range, although it is commonly believed that operative slip systems change from the $\{111\}$ octahedral to (001) cubic family. This study also supports the view indicating that the activity of the cubic family is vital and some systems from the octahedral family are also operative at high-temperature for some loading/lamellar orientations.

At lower temperature, some ordinary dislocations are suppressed to move, however, they can overcome the resistance at higher temperature by changing plane due to thermally active mechanisms like climb, so they become softer. Nevertheless, some ordinary systems would remain hard for certain loading orientations. All superlattice dislocation slips are harder at high-temperature, some ordinary slips are softer and the rest ordinary systems are in between hard and soft. This is another finding of the present study in contrast to the common believe that all ordinary slips are softer at high-temperature. Due to the presence of one or more superstructures, some ordinary systems are found to be little harder than others ordinary slips, which is consistent with conventional approaches and some observed experimental observations. Depending on the orientation and temperature, both microstructural and morphological features ensures alloy strengthening by suppressing dislocation movement resulting in higher CRSS of some slip systems.

When the applied load is parallel to the lamellar axis, responses show comparatively higher strength indicating the probable dominance of the long-period superstructures. Lamellar orientation of 0° with the loading direction has the highest strength and tensile state is stronger than that of compressive loading responses. On the other hand, for 90°case, anisotropy and asymmetry are influenced more by the long-period superstructure than that of lamellar morphology. In overall plastic deformation, the role of the octahedral family is more pronounced than the cubic one. The compressive deformation is dominated by ordinary slips while the tensile responses by superdislocation slips. The slip mechanisms and total number of active slip systems are found to be different in tension and compression. The major contributing slip systems and the most dominant one, are also different. It is also found that the most active slip system dictates the overall plastic deformation in reproducing experimental data. Instead of purely morphological as Ti-rich side, the plastic anisotropy in the Al-rich side is found to be dependent on the lamellar morphology and long-period superstructure. The family of Al-rich alloys are expected to be highly anisotropic and asymmetric. It is found that tension-compression-asymmetry evolution is anisotropic and highly pronounced throughout the deformation process influenced by the lamellar morphology and long-period superstructures.

The presence of difference length-scale, specially superstructure level scale is present for these alloy, which is another vital point of our study. So the origins the anisotropy and the asymmetry for polycrystalline Al-rich alloys can be considered to be associated with at least three different length-scales e.g. grain scale, lamellar (morphological) scale and superstructural scale. The size of the superstructures could be an independent scale of understanding, since we do not understand all aspects of long-range ordering on the behavior of the material.

9.1.2 Regarding CRSS estimation

CRSS estimation is very crucial for the modeling of anisotropy and asymmetry. The more accurate values of CRSS we can pick, the more reliable material parameters we can expect. A novel iterative scheme for CRSS estimation and slip system characterization consistent with experimental observations has been proposed and a simple version of this approach has been applied for two phase lamellar Al-rich TiAl alloys with long-period superstructures. The proposed approach of CRSS estimation has been compared with three other conventional approaches. The proposed modeling approach can successfully reproduce rate-dependent experimental data in both loading directions whereas other methods of slip classification and CRSS estimation, if successful for one experimental data set, eventually under or overestimate the other set.

9.1.3 Regarding material parameters

Related material parameters have also been identified. The most important parameter for the proposed model is the rate sensitivity, which is found to be very reasonable for the analyzed case considering lower stress and very high homologous temperature. It is revealed that, irrespective of the type of the flow-rules, two internal variables based flow-rules including slip-system-level kinematic hardening variable makes significant improvement in simulating high-temperature medium stress viscoplasticity with estimating reasonable material parameter set. The role of latent hardening decreases with the increase of operating temperature and with the addition of slip system level backstress variable. The viscous flow parameters in the power-law can vary not only depending on the material, microstructure and loading conditions but also on the choice of the flow-rule definition.

9.1.4 Regarding the model and power-law flow-rules

Commonly used power-law flow-rules of crystal plasticity have also been examined for this alloy with six strain rate controlled experimental data sets. In contrast to the popular approaches, it is revealed that the consideration of Schmid stress as the driving force, the sole cause for plastic deformation is not appropriate for highly heterogeneous and anisotropic materials even after with complex evolution equations, and particularly, such modeling cannot be applied at high-temperature moderate to lower moderate stress regimes. In other words, flow-rule with one internal variable is not a good choice for high-temperature recovery driven case. This type flow-rule suits best when the plasticity is glide driven only, or if the anisotropic behavior is not pronounced. If the stress is moderate to high and the operating temperature is relatively low, this simpler flow-rule can be used. Including slip system level backstress in effective stress definition gives significant improvement in these cases. Including internal stress as state variable in the effective stress definition facilitates to cover a range of heterogeneous material behaviors like anisotropy and tension-compression asymmetry, hardening-recovery driven softening, cyclic loading behavior and possibly some sort of damage as well. If temperature dependent drag K along a slip system is separated from the microscopic yield or slip resistance quantity, then it can be used more reliably for above cases with temperature dependent behavior as well up to a temperature range. Rearrangement of the internal variables or separating yield and drag in the flow-rule increases the prediction power of the model. According to our results, without considering a separate internal state variable for internal stress, it is not straightforward to simulate such a high-temperature viscoplasticity with such level of accuracy. Rate sensitivity exponent, slip activities, lattice rotation etc. might vary with the choice of the flow-rule. With slip-system-level necessary internal variables and glide-climb driven constitutive equations, we assume that crystal viscoplasticity model is well capable to capture experimentally observed macroscopic deformation phenomenon when critical stresses are designed properly.

9.2 Outlook

Generally the single crystals are studied in order to understand the microstructure-properties relationship of polycrystalline materials. Even though the material parameters and properties of single crystals are expected to be different than that of polycrystals up to certain degree, nevertheless, the information extracted from single crystals are of paramount importance for the analysis of polycrystals. Due to the unavailability of experimental data for polycrystals, this work has been stopped after analyzing single crystals only. So an important outlook for the future might be the analysis of the polycrystalline alloys belong to the same class of single crystals. In a lamellar Ti-rich TiAl single crystals, the origin of anisotropy is purely morphological, whereas in Al-rich side, it is found that the superstructure scale also contributes to the anisotropy. So for a lamellar polycrystalline Al-rich alloy, the sources of anisotropy are expected to be associated with three different length-scales, i.e. grain scale, lamellar scale and superstructure scale. An interesting point would be to understand the relative contributions at different scales for polycrystalline alloys.

Often a phenomenological model contains a number of fitting parameters that can be measured from the experimental procedures. A number of such parameters is also present in the proposed model. In the evolution equation of backstress, an additional coupling function has been considered where two fitting parameters, ϕ_0 and δ are involved. This coupling function is usually needed for more complex cases e.g. cyclic loading. So there is an option left for slight modification of the evolution equation and without that function and hence two fitting parameters can be escaped. Models with small number of fitting parameters usually ensures a better prediction capability.

In the constitutive modeling, the most well-known physical processes are considered only. However, there might have been more than one less contributing mechanisms are active. For developing an efficient model, understanding all underlying mechanisms are necessary to establish a physics based phenomenology. Such type of physical-phenomenological model is expected to be highly effective. So an important aspect for the future would be to perform more rigorous experimental investigations for understanding the detailed deformation mechanisms. Moreover, a dislocation density based modeling with knows physical processes can be establish to check the predictive power of the model and possibly comparing with physical-phenomenological one.

A simpler version of the proposed technique of estimating CRSS for all slip system has been implemented for two sets of anisotropic data. Since the original proposed technique is an iterative scheme for many sets of anisotropic data, an important point would be to test the algorithm for many data-sets.

There is growing interest in the research community to understand the interface mechanics. Lamellar boundary effect has not been explored in the presented modeling approach directly, where only the first order effect has been considered. So another interesting aspect would be to study the detailed interface effects along with lamellar width and spacing effects, for which gradient based higher order continuum theory might be necessary.

Bibliography

[1] F. Fritzen. *Microstructural modeling and computational homogenization of the physically linear and nonlinear constitutive behavior of micro-heterogeneous materials*. PhD thesis, Karlsruhe Institute of Technology, KIT Scientific Publishing, Karlsruhe, 2011.

[2] J. Kadkhodapour, S. Schmauder, D. Raabe, S. Ziaei-Rad, U. Weber, and M. Calcagnotto. Experimental and numerical study on geometrically necessary dislocations and non-homogeneous mechanical properties of the ferrite phase in dual phase steels. *Acta Materialia*, 59(11):4387 – 4394, 2011.

[3] F. Roters, P. Eisenlohr, L. Hantcherli, D.D. Tjahjanto, T.R. Bieler, and D. Raabe. Overview of constitutive laws, kinematics, homogenization and multiscale methods in crystal plasticity finite-element modeling: Theory, experiments, applications. *Acta Materialia*, 58(4):1152 – 1211, 2010.

[4] F. Roters, P. Eisenlohr, T.R. Bieler, and D. Raabe. *Crystal Plasticity Finite Element Methods: In Materials Science and Engineering*. Wiley-VCH Verlag, Weinheim, 2010.

[5] S. Bargmann. *Computational modeling of material behavior on different scales based on continuum mechanics*. habilitation, TU Dortmund, Dortmund, 2011.

[6] J. Ning and E.C. Aifantis. 7 - anisotropic and inhomogeneous plastic deformation of polycrystalline solids. In A.S. Krausz and K. Krausz, editors, *Unified Constitutive Laws of Plastic Deformation*, pages 319 – 341. Academic Press, San Diego, 1996.

[7] M.E. Kassner and M.T. Pérez-Prado. *Fundamentals of Creep in Metals and Alloys*. Elsevier Science Ltd, Oxford, 2004.

[8] P. Steinmann. *Geometrical Foundations of Continuum Mechanics*. Springer-Verlag, Berlin Heidelberg, 2015.

[9] J. Lubliner. *Plasticity Theory*. Dover Books on Engineering, 2008.

[10] K. Domkin. *Constitutive models based on dislocation density*. PhD thesis, Lulea University of Technology, Lulea, 2005.

[11] M. Fivel. Discrete dislocation dynamics: Principles and recent applications. In O. Cazacu, editor, *Multiscale Modeling of Heterogenous Materials: From Microstructure to Macro-scale Properties*. ISTE, London, 2008.

[12] D. Kuhlmann-Wilsdorf. The theory of dislocation-based crystal plasticity. *Philosophical Magazine A*, 79(4):955–1008, 1999.

[13] F. Appel and R. Wagner. Microstructure and deformation of two-phase γ-titanium aluminides. *Materials Science and Engineering R: Reports*, 22(5):187 – 268, 1998.

[14] Jan Kratochvíl. Formation of deformation substructures observed in ductile materials. In Jörg Schröder and Klaus Hackl, editors, *Plasticity and Beyond: Microstructures, Crystal-Plasticity and Phase Transitions*, pages 199–304. Springer, Vienna, 2014.

[15] H. Mughrabi. Dislocation wall and cell structures and long-range internal stresses in deformed metal crystals. *Acta Metallurgica*, 31(9):1367 – 1379, 1983.

[16] B. Chen, P.E.J. Flewitt, A.C.F. Cocks, and D. J. Smith. A review of the changes of internal state related to high temperature creep of polycrystalline metals and alloys. *International Materials Reviews*, 60(1):1 – 29, 2015.

[17] M. F. Ashby. The deformation of plastically non-homogeneous materials. *Philosophical Magazine*, 21(170):399–424, 1970.

[18] L.P. Evers, D.M. Parks, W.A.M. Brekelmans, and M.G.D. Geers. Crystal plasticity model with enhanced hardening by geometrically necessary dislocation accumulation. *Journal of the Mechanics and Physics of Solids*, 50(11):2403 – 2424, 2002.

[19] V. Levkovitch and B. Svendsen. On the large-deformation- and continuum-based formulation of models for extended crystal plasticity. *International Journal of Solids and Structures*, 43(24):7246 – 7267, 2006.

[20] S. Bargmann, M. Ekh, K. Runesson, and B. Svendsen. Modeling of polycrystals with gradient crystal plasticity: A comparison of strategies. *Philosophical Magazine*, 90(10):1263–1288, 2010.

[21] M.F. Ashby. A first report on deformation-mechanism maps. *Acta Metallurgica*, 20(7):887 – 897, 1972.

[22] Jr. W.D. Callister. *Materials Science and Engineering - An Introduction to Homogenization*. John Wiley & Sons, Inc., New York, 2007.

[23] Y.S. Chen. *Continuum theory of self-similar dislocation cellular structures*. PhD thesis, Cornell University, Ithaca, 2012.

[24] M.S. Pham and S.R. Holdsworth. Evolution of relationships between dislocation microstructures and internal stresses of aisi 316L during cyclic loading at 293 K and 573 K (20°C and 300°C). *Metallurgical and Materials Transactions A*, 45(2):738–751, 2014.

[25] M.S. Pham and S.R. Holdsworth. Dynamic strain ageing of aisi 316L during cyclic loading at 300°C: Mechanism, evolution, and its effects. *Materials Science and Engineering: A*, 556(Supplement C):122 – 133, 2012.

[26] Jr. J.W. Morris. Overview of dislocation plasticity. MSE-205 lecture notes, University of California Berkeley, 2001.

[27] T.M. Pollock and R.D. Field. Chapter 63 dislocations and high-temperature plastic deformation of superalloy single crystals. In F.R.N. Nabarro and M.S. Duesbery, editors, *Dislocations in Solids*, volume 11, pages 547 – 618. Elsevier, 2002.

[28] L. Meric, P. Poubanne, and G. Cailletaud. Single crystal modeling for structural calculations: Part 1 - Model presentation. *ASME Journal of Engineering Materials and Technology*, 113(1):162 – 170, 1991.

[29] G.A. Maugin. *The Thermomechanics of Plasticity and Fracture*. Cambridge University Press, UK, 1992.

[30] M.E. Kassner and M.T. Perez-Prado. Five-power-law creep in single phase metals and alloys. *Progress in Materials Science*, 45(1):1 – 102, 2000.

[31] E.C. Aifantis. The physics of plastic deformation. *International Journal of Plasticity*, 3(3):211 – 247, 1987.

[32] J. Huang, N.M. Ghoniem, and J. Kratochvíl. On the sweeping mechanism of dipolar dislocation loops under fatigue conditions. *Modelling and Simulation in Materials Science and Engineering*, 12(5):917, 2004.

[33] M.C. Miguel, A. Vespignani, S. Zapperi, J. Weiss, and J.R. Grasso. Intermittent dislocation flow in viscoplastic deformation. *Nature*, 410(6829):667–71, 2001.

[34] H. Zhang, X. Dong, D. Du, and Q. Wang. A unified physically based crystal plasticity model for fcc metals over a wide range of temperatures and strain rates. *Materials Science and Engineering: A*, 564(Supplement C):431 – 441, 2013.

[35] N. Ohno and J.-D. Wang. Kinematic hardening rules with critical state of dynamic recovery, part I: formulation and basic features for ratchetting behavior. *International Journal of Plasticity*, 9(3):375 – 390, 1993.

[36] H.J. McQueen and W.J.M. Tegart. The deformation of metals at high temperatures. Technical Report 4, Scientific American, 1975.

[37] U.F. Kocks and H. Mecking. Physics and phenomenology of strain hardening: the FCC case. *Progress in Materials Science*, 48(3):171 – 273, 2003.

[38] R.E. Stoller and S.J. Zinkle. On the relationship between uniaxial yield strength and resolved shear stress in polycrystalline materials. *Journal of Nuclear Materials*, 283(Part 1):349 – 352, 2000.

[39] K. Naumenko. *Modeling of High-Temperature Creep for Structural Analysis Applications*. habilitation, ML University of Halle-Wittenberg, Halle-Wittenberg, 2006.

[40] M.S. Pham, M. Iadicola, A. Creuziger, L. Hu, and A.D. Rollett. Thermally-activated constitutive model including dislocation interactions, aging and recovery for strain path dependence of solid solution strengthened alloys: Application to AA5754-O. *International Journal of Plasticity*, 75:226 – 243, 2015.

[41] G.B. Sarma, B. Radhakrishnan, and T. Zacharia. Finite element simulations of cold deformation at the mesoscale. *Computational Materials Science*, 12(2):105 – 123, 1998.

[42] B. Klusemann and T. Yalçinkaya. Plastic deformation induced microstructure evolution through gradient enhanced crystal plasticity based on a non-convex helmholtz energy. *International Journal of Plasticity*, 48(Supplement C):168 – 188, 2013.

[43] R.D. Doherty, D.A. Hughes, F.J. Humphreys, J.J. Jonas, D.Juul Jensen, M.E. Kassner, W.E. King, T.R. McNelley, H.J. McQueen, and A.D. Rollett. Current issues in recrystallization: a review. *Materials Science and Engineering: A*, 238(2):219 – 274, 1997.

[44] S.B. Brown, K.H. Kim, and L. Anand. An internal variable constitutive model for hot working of metals. *International Journal of Plasticity*, 5(2):95 – 130, 1989.

[45] K. Joechen. *Homogenization of the Linear and Non-linear Mechanical Behavior of Polycrystals*. PhD thesis, Karlsruhe Institute of Technology, KIT Scientific Publishing, Karlsruhe, 2013.

[46] J.R. Greer and J.T.M.D. Hosson. Plasticity in small-sized metallic systems: Intrinsic versus extrinsic size effect. *Progress in Materials Science*, 56(6):654–724, 2011.

[47] A. Javili, S. Saeb, and P. Steinmann. Aspects of implementing constant traction boundary conditions in computational homogenization via semi-dirichlet boundary conditions. *Computational Mechanics*, 59(1):21–35, 2017.

[48] H.J. Boehm. A short introduction to basic aspects of continuum micromechanics. ILSB Report 206, TU Wien, 2016.

[49] L.P. Evers. Strain gradient crystal plasticity based on dislocation densities. Technical report, TU Eindhoven, 2003.

[50] D. Cioranescu and P. Donato. *An Introduction to Homogenization*. Oxford University Press Inc., New York, 1999.

[51] M. Geers and J. Yvonnet. Multiscale modeling of microstructure–property relations. *MRS Bulletin*, 41(8):610–616, 2016.

[52] M.G.D. Geers, V.G. Kouznetsova, and W.A.M. Brekelmans. Multi-scale computational homogenization: Trends and challenges. *Journal of Computational and Applied Mathematics*, 234(7):2175 – 2182, 2010.

[53] D. Helm, A. Butz, D. Raabe, and P. Gumbsch. Microstructure-based description of the deformation of metals: Theory and application. *JOM*, 63(4):26–33, 2011.

[54] R. Corcolle. Comparison between different approaches in homogenization: Mean-field approach vs. full-field approaches. In *COMPUMAG 2013, Budapest, Hungary*, volume June, 2013.

[55] P. Eyckens, H. Mulder, J. Gawad, H. Vegter, D. Roose, T. van den Boogaard, A. Van Bael, and P. Van Houtte. The prediction of differential hardening behaviour of steels by multi-scale crystal plasticity modelling. *International Journal of Plasticity*, 73(Supplement C):119 – 141, 2015. Special Issue on Constitutive Modeling from Micro-Scale to Continuum in Honor of Prof. Frédéric Barlat.

[56] R.D. McGinty and D.L. McDowell. Multiscale polycrystal plasticity. *ASME Journal of Engineering Materials and Technology*, 121(2):203–209, 1999.

[57] H.F. Al-Harbi. *Crystal plasticity finite element simulations using discrete Fourier transforms*. PhD thesis, Georgia Institute of Technology, Georgia, 2013.

[58] R. Aghababaei and S.P. Joshi. A crystal plasticity analysis of length-scale dependent internal stresses with image effects. *Journal of the Mechanics and Physics of Solids*, 60(12):2019 – 2043, 2012.

[59] H. Wang, P.D. Wu, C.N. Tome, and Y. Huang. A finite strain elastic-viscoplastic self-consistent model for polycrystalline materials. *Journal of the Mechanics and Physics of Solids*, 58(4):594 – 612, 2010.

[60] S. Nemat-Nasser and M. Hori. *Micromechanics: Overall Properties of Heterogeneous Materials*. Elsevier, North Holland, 1998.

[61] L. Scheunemann, D. Balzani, D. Brands, and J. Schröder. Construction of statistically similar rves. In Sergio Conti and Klaus Hackl, editors, *Analysis and Computation of Microstructure in Finite Plasticity*, pages 219–256. Springer International Publishing, Cham, 2015.

[62] K. Terada, M. Hori, T. Kyoya, and N. Kikuchi. Simulation of the multi-scale convergence in computational homogenization approaches. *International Journal of Solids and Structures*, 37(16):2285 – 2311, 2000.

[63] Asaro RJ. Crystal plasticity. *ASME Journal of Applied Mechanics*, 50(4b):921–934, 1983.

[64] M. Kooiman, M. Hütter, and M.G.D. Geers. Viscoplastic flow rule for dislocation-mediated plasticity from systematic coarse-graining. *Journal of the Mechanics and Physics of Solids*, 90(Supplement C):77 – 90, 2016.

[65] J.A.W. van Dommelen, W.A.M. Brekelmans, and F.P.T. Baaijens. Computational visco-plasticity for kinematicallyconstrained crystals. *International Journal for Numerical Methods in Engineering*, 48:1311 – 1330, 2000.

[66] N. D. BATSOULAS. Mathematical description of the mechanical behaviour of metallic materials under creep conditions. *Journal of Materials Science*, 32(10):2511–2527, 1997.

[67] A. Bertram. An alternative approach to finite plasticity based on material isomorphisms. *International Journal of Plasticity*, 15(3):353 – 374, 1999.

[68] G.A. Maugin. The saga of internal variables of state in continuum thermo-mechanics (1893–2013). *Mechanics Research Communications*, 69(Supplement C):79 – 86, 2015.

[69] S. Schmitt, P. Gumbsch, and K. Schulz. Internal stresses in a homogenized representation of dislocation microstructures. *Journal of the Mechanics and Physics of Solids*, 84(Supplement C):528 – 544, 2015.

[70] F. Roters. *Advanced Material Models for the Crystal Plasticity Finite Element Method*. habilitation, RWTH Aachen, Aachen, 2011.

[71] R. A. Lebensohn, P. Ponte Castañeda, R. Brenner, and O. Castelnau. Full-field vs. homogenization methods to predict microstructure–property relations for polycrystalline materials. In S. Ghosh and D. Dimiduk, editors, *Computational Methods for Microstructure-Property Relationships*, pages 393–441. Springer US, Boston, MA, 2011.

[72] R. Hill and J.R. Rice. Constitutive analysis of elastic-plastic crystals at arbitrary strain. *Journal of the Mechanics and Physics of Solids*, 20(6):401 – 413, 1972.

[73] A. Bertram. *Elasticity and Plasticity of Large Deformations*. Springer Verlag, Berlin Heidelberg, 2012.

[74] S. Bargmann, B. Svendsen, and M. Ekh. An extended crystal plasticity model for latent hardening in polycrystals. *Computational Mechanics*, 48(6):631–645, 2011.

[75] B. Chen, J.N. Hu, P.E.J. Flewitt, D.J. Smith, A.C.F. Cocks, and S.Y. Zhang. Quantifying internal stress and internal resistance associated with thermal ageing and creep in a polycrystalline material. *Acta Materialia*, 67:207 – 219, 2014.

[76] J. Hu, B. Chen, D.J. Smith, P.E.J. Flewitt, and A.C.F. Cocks. On the evaluation of the bauschinger effect in an austenitic stainless steel - the role of multi-scale residual stresses. *International Journal of Plasticity*, 2016. In Press.

[77] Y. Estrin. 2 - dislocation-density–related constitutive modeling. In A.S. Krausz and K. Krausz, editors, *Unified Constitutive Laws of Plastic Deformation*, pages 69 – 106. Academic Press, San Diego, 1996.

[78] F. Roters, D. Raabe, and G. Gottstein. Work hardening in heterogeneous alloys—a microstructural approach based on three internal state variables. *Acta Materialia*, 48(17):4181 – 4189, 2000.

[79] G Cailletaud, S Forest, D Jeulin, F Feyel, I Galliet, V Mounoury, and S Quilici. Some elements of microstructural mechanics. *Computational Materials Science*, 27(3):351 – 374, 2003.

[80] A. McBride, S. Bargmann, and B.D. Reddy. A computational investigation of a model of single-crystal gradient thermoplasticity that accounts for the stored energy of cold work and thermal annealing. *Computational Mechanics*, 55:755–769, 2015.

[81] P. Steinmann. Views on multiplicative elastoplasticity and the continuum theory of dislocations. *International Journal of Engineering Science*, 34(15):1717 – 1735, 1996.

[82] A. Arsenlis and D.M Parks. Crystallographic aspects of geometrically-necessary and statistically-stored dislocation density. *Acta Materialia*, 47(5):1597 – 1611, 1999.

[83] A. Ma, F. Roters, and D. Raabe. A dislocation density based constitutive model for crystal plasticity fem including geometrically necessary dislocations. *Acta Materialia*, 54(8):2169 – 2179, 2006.

[84] M.S. Pham, S.R. Holdsworth, K.G.F. Janssens, and E. Mazza. Cyclic deformation response of aisi 316l at room temperature: Mechanical behaviour, microstructural evolution, physically-based evolutionary constitutive modelling. *International Journal of Plasticity*, 47(Supplement C):143 – 164, 2013.

[85] G.A. Henshall, D.E. Helling, and A.K. Miller. 4 - improvements in the {MATMOD} equations for modeling solute effects and yield-surface distortion. In A.S. Krausz and K. Krausz, editors, *Unified Constitutive Laws of Plastic Deformation*, pages 153 – 227. Academic Press, San Diego, 1996.

[86] A.B. Tanner, R.D. McGinty, and D.L. McDowell. Modeling temperature and strain rate history effects in OFHC Cu. *International Journal of Plasticity*, 15(6):575 – 603, 1999.

[87] B. Chen, J.N. Hu, P.E.J. Flewitt, D.J. Smith, A.C.F. Cocks, and S.Y. Zhang. Quantifying internal stress and internal resistance associated with thermal ageing and creep in a polycrystalline material. *Acta Materialia*, 67:207 – 219, 2014.

[88] R. Hoppe and F. Appel. Origin and magnitude of internal stresses in TiAl alloys. In Y.W. Kim, W. Smarsly, J. Lin, D. Dimiduk, and F. Appel, editors, *Gamma Titanium Aluminide Alloys 2014*, pages 159 – 168. John Wiley & Sons, Inc., 2014.

[89] K. Naumenko, H. Altenbach, and A. Kutschke. A combined model for hardening, softening and damage processes in advanced heat resistant steels at elevated temperature. *International Journal of Damage Mechanics*, 20:578 – 597, 2011.

[90] K. Naumenko and E. Gariboldi. A phase mixture model for anisotropic creep of forged Al-Cu-Mg-Si alloy. *Materials Science and Engineering: A*, 618:368 – 376, 2014.

[91] M. Kuroda. Interfacial microscopic boundary conditions associated with backstress-based higher-order gradient crystal plasticity theory. *Journal of Mechanics of Materials and Structures*, 12(2):193–218, 2017.

[92] M.E. Kassner, B.C. Larson, P. Geantil, and L.E. Levine. Backstress, the Bauschinger Effect and Cyclic Deformation. In *Recent Developments in the Processing and Applications of Structural Metals and Alloys*, volume 604 of *Materials Science Forum*, pages 39–51. Trans Tech Publications, 3 2009.

[93] I. Ertürk, J.A.W. van Dommelen, and M.G.D. Geers. Energetic dislocation interactions and thermodynamical aspects of strain gradient crystal plasticity theories. *Journal of the Mechanics and Physics of Solids*, 57(11):1801 – 1814, 2009.

[94] G.J. Weng. Anisotropic hardening in single crystals and the plasticity of polycrystals. *International Journal of Plasticity*, 3(4):315 – 339, 1987.

[95] M.E. Kassner, P. Geantil, and L.E. Levine. Long range internal stresses in single-phase crystalline materials. *International Journal of Plasticity*, 45:44 – 60, 2013.

[96] D.L. McDowell. Viscoplasticity of heterogeneous metallic materials. *Materials Science and Engineering: R: Reports*, 62(3):67 – 123, 2008.

[97] T.M. Holden, R.A. Holt, and A.P. Clarke. Intergranular strains in inconel-600 and the impact on interpreting stress fields in bent steam-generator tubing. *Materials Science and Engineering: A*, 246(1):180 – 198, 1998.

[98] E. Nakamachi, K. Hiraiwa, H. Morimoto, and M. Harimoto. Elastic/crystalline viscoplastic finite element analyses of single- and poly-crystal sheet deformations and their experimental verification. *International Journal of Plasticity*, 16(12):1419 – 1441, 2000.

[99] J.L. Chaboche. A review of some plasticity and viscoplasticity constitutive theories. *International Journal of Plasticity*, 24(10):1642 – 1693, 2008.

[100] M. Kuroda and V. Tvergaard. Studies of scale dependent crystal viscoplasticity models. *Journal of the Mechanics and Physics of Solids*, 54(9):1789 – 1810, 2006.

[101] Y. Estrin. Dislocation theory based constitutive modelling: foundations and applications. *Journal of Materials Processing Technology*, 80(Supplement C):33 – 39, 1998.

[102] R. Gluege, M. Weber, and A. Bertram. Comparison of spherical and cubical statistical volume elements with respect to convergence, anisotropy, and localization behavior. *Computational Materials Science*, 63(Supplement C):91 – 104, 2012.

[103] O. van der Sluis, P.J.G. Schreurs, W.A.M. Brekelmans, and H.E.H. Meijer. Overall behaviour of heterogeneous elastoviscoplastic materials: effect of microstructural modelling. *Mechanics of Materials*, 32(8):449 – 462, 2000.

[104] R. Gluege and M. Weber. Numerical properties of spherical and cubical representative volume elements with different boundary conditions. *Technische Mechanik*, 33(2):97 – 103, 2013.

[105] R.J.M. Smit, W.A.M. Brekelmans, and H.E.H. Meijer. Prediction of the mechanical behavior of nonlinear heterogeneous systems by multi-level finite element modeling. *Computer Methods in Applied Mechanics and Engineering*, 155(1):181 – 192, 1998.

[106] P. Suquet. *Homogenization techniques for composite media*, chapter Elements of homogenization for inelastic solid mechanics, pages 193–278. Springer-Verlag, 1987.

[107] C.M. Austin. Current status of gamma Ti aluminides for aerospace applications. *Current Opinion in Solid State and Materials Science*, 4(3):239 – 242, 1999.

[108] J. Lapin. TiAl-based alloys: present status and future perspectives. In *Proceedings of 18th International Mettalurgical and Materials Conference (METAL2009)*, 2009.

[109] F. Appel, H. Clemens, and F.D. Fischer. Modeling concepts for intermetallic titanium aluminides. *Progress in Materials Science*, 81:55 – 124, 2016.

[110] B. Bewlay, M. Weimer, T. Kelly, A. Suzuki, and P. Subramanian. The science, technology, and implementation of TiAl alloys in commercial aircraft engines. *MRS Proceedings*, 1516:49–58, 2013.

[111] G. Chen, Y. Peng, G. Zheng, Z. Qi, M. Wang, H. Yu, C. Dong, and C.T. Liu. Polysynthetic twinned TiAl single crystals for high-temperature applications. *Nature Materials*, 15:876–881, 2016.

[112] A.S. Khan, S. Yu, and H. Liu. Deformation induced anisotropic responses of Ti-6Al-4V alloy part II: A strain rate and temperature dependent anisotropic yield criterion. *International Journal of Plasticity*, 38:14 – 26, 2012.

[113] V. Tuninetti, G. Gilles, O. Milis, T. Pardoen, and A.M. Habraken. Anisotropy and tension compression asymmetry modeling of the room temperature plastic response of Ti-6Al-4V. *International Journal of Plasticity*, 67:53 – 68, 2015.

[114] C. Zambaldi. *Micromechanical modeling of γ-TiAl based alloys*. PhD thesis, RWTH Aachen, Aachen, 2010.

[115] D. Hautmann. Titanium Aluminides–A class all by itself. Report 1, MTU Aero Engines, 2013.

[116] S. Xu, X. Xu, Y. Xu, Y. Liang, and J. Lin. Phase transformations and phase equilibria of a Ti-46.5Al-16.5Nb alloy. *Materials & Design*, 101:88 – 94, 2016.

[117] W.T. Marketz, F.D. Fischer, and H. Clemens. Deformation mechanisms in TiAl intermetallics-experiments and modeling. *International Journal of Plasticity*, 19(3):281 – 321, 2003.

[118] F. Appel, J.D.H. Paul, and M. Oehring. *Gamma Titanium Aluminide Alloys: Science and Technology*. John Wiley & Sons, 2011.

[119] J.E. Benci, J.C. Ma, and T.P. Feist. Evaluation of the intermetallic compound Al_2Ti for elevated-temperature applications. *Materials Science and Engineering: A*, 192:38 – 44, 1995.

[120] M. Palm, L.C. Zhang, F. Stein, and G. Sauthoff. Phases and phase equilibria in the Al-rich part of the Al-Ti system above 900°C. *Intermetallics*, 10(6):523 – 540, 2002.

[121] D. Sturm, M. Heilmaier, H. Saage, M. Paninski, G.J. Schmitz, A. Drevermann, M. Palm, F. Stein, N. Engberding, K. Kelm, and S. Irsen. Creep strength of centrifugally cast Al-rich TiAl alloys. *Materials Science and Engineering: A*, 510–511:373 – 376, 2009.

[122] M. Palm, N. Engberding, F. Stein, K. Kelm, and S. Irsen. Phases and evolution of microstructures in Ti-60at.%Al. *Acta Materialia*, 60:3559 – 3569, 2012.

[123] R. Lebensohn, H. Uhlenhut, C. Hartig, and H. Mecking. Plastic flow of γ-TiAl-based polysynthetically twinned crystals: micromechanical modeling and experimental validation. *Acta Materialia*, 46(13):4701 – 4709, 1998.

[124] D. Batalu, G. Cosmeleata, and A. Aloman. Critical analysis of the Ti-Al phase diagrams. Series B 4, UPB Science Bulletin, 2006.

[125] L.C. Zhang, M. Palm, F. Stein, and G. Sauthoff. Formation of lamellar microstructures Al-rich TiAl alloys between 900 to 1100°C. *Intermetallics*, 9:229 – 238, 2001.

[126] B.K. Kad and H.L. Fraser. On the contribution of climb to high-temperature deformation in single phase γ-TiAl. *Philosophical Magazine A*, 69(4):689–699, 1994.

[127] Y. Umakoshi, T. Nakano, and K. Ashida. High-temperature deformation in Ti-62.5at.%Al single crystals containing small Al_2Ti-type precipitates. *Materials Science Forum*, 304-306:163–168, 1999.

[128] T. Fujiwara, A. Nakamuraa, M. Hosomia, S. R. Nishitania, Y. Shiraia, and M. Yamaguchia. Deformation of polysynthetically twinned crystals of TiAl with a nearly stoichiometric composition. *Philosophical Magazine A*, 61(4):591 – 606, 1990.

[129] V. Chakravadhanula, K. Kelm, L. Kienle, V. Duppel, A. Lotnyk, D. Sturm, M. Heilmaier, G.J. Schmitz, A. Drevermann, F. Stein, and M. Palm. TEM studies of the ternary $Ti_{36}Al_{62}Nb_2$ alloy. In *MRS Proceedings*, volume 1295, 2011.

[130] T. Nakano, A. Negishi, K. Hayashi, and Y. Umakoshi. Ordering process of Al_5Tl_3, h-Al_2Ti and r-Al_2Ti with f.c.c.-based long-period superstructures in rapidly solidified Al-rich TiAl alloys. *Acta Materialia*, 47(4):1091 – 1104, 1999.

[131] J. Braun and M. Ellner. Phase equilibria investigations on the aluminum-rich part of the binary system Ti-Al. *Metallurgical and Materials Transactions A*, 32(5):1037–1047, 2001.

[132] K. Hayashi, T. Nakano, and Y. Umakoshi. Metastable region of Al_5Tl_3 single-phase in time-temperature-transformation (TTT) diagram of Ti-62.5 at.% Al single crystal. *Intermetallics*, 10(8):771 – 781, 2002.

[133] F. Stein, L.C. Zhang, G. Sauthoff, and M. Palm. TEM and DTA study on the stability of Al_5Ti_3- and h-Al_2Ti-superstructures in aluminium-rich TiAl alloys. *Acta Materialia*, 49(15):2919 – 2932, 2001.

[134] S. Hata, K. Higuchi, M. Itakura, N. Kuwano, T. Nakano, K. Hayashi, and Y. Umakoshi. Short-range order in Al-rich γ-TiAl alloys studied by high-resolution transmission electron microscopy with image processing. *Philosophical Magazine Letters*, 82(7):363–372, 2002.

[135] T. Nakano, K. Hayashi, Y. Umakoshi, Y. Chiu, and P. Veyssiere. Effects of long-period superstructures on plastic properties in Al-rich TiAl single crystals. *MRS Proceedings*, 842, 2004.

[136] F. Gregori and P. Veyssiere. Planar debris in plastically deformed al-rich γ-TiAl. *Philosophical Magazine A*, 79(2):403–421, 1999.

[137] T. Nakano, K. Hayashi, and Y. Umakoshi. Formation and stability of transitional long-period superstructures in Al-rich TiAl single crystals. *Philosophical Magazine A*, 82:763 – 777, 2002.

[138] S. Hata, K. Higuchi, T. Mitate, M. Itakura, Y. Tomokiyo, N. Kuwano, T. Nakano, Y. Nagasawa, and Y. Umakoshi. HRTEM image contrast and atomistic microstructures of long-period ordered Al-rich TiAl alloys. *Journal of Electron Microscopy*, 53(1):1–9, 2004.

[139] T. Nakano, K. Hayashi, K. Ashida, and Y. Umakoshi. Effect of Al_2Ti phase on plastic behavior in Ti-62.5 At%Al single crystals. In E.P. George, M.J. Mills, and M. Yamaguchi, editors, *High-Temperature Ordered Intermetallic Alloys VIII*, volume 552 of *MRS Proceedings*, 1998.

[140] T. Nakano, K. Hayashi, Y. Nagasawa, and Y. Umakoshi. Plastic deformation behavior of Al_5Tl_3 single-phase single crystals. *MRS Proceedings*, 753, 2002.

[141] M. Doi, T. Koyama, T. Taniguchi, and S. Naito. Morphological changes of the Ti_3Al_5 phase formed by phase-decomposition of tial intermetallics. *Materials Science and Engineering: A*, 329:891 – 897, 2002.

[142] S. Hata, K. Higuchi, T. Mitate, N. Kuwano, M. Itakura, Y. Tomokiyo, T. Nakano, Y. Nagasawa, and Y. Umakoshi. HRTEM observation of partially ordered long-period superstructures in Al-rich TiAl alloys. *MRS Proceedings*, 753, 2002.

[143] S. Hata, T. Nakano, K. Higuchi, Y. Nagasawa, N. Kuwano, M. Itakura, Y. Tomokiyo, and Y. Umakoshi. Semi-quantitative HRTEM for partially ordered materials: Application to Al-rich TiAl alloys. *Materials Science Forum*, 426-432:1721–1726, 2003.

[144] S. Hata, K. Higuchi, M. Itakura, N. Kuwano, T. Nakano, K. Hayashi, and Y. Umakoshi. Short-range order in Al-rich γ-TiAl alloys studied by high-resolution transmission electron microscopy with image processing. *Philosophical Magazine Letters*, 82(7):363–372, 2002.

[145] T. Nakano, S. Hata, K. Hayashi, and Y. Umakoshi. *Some long-Period superstructures and the related motion of dislocations in Al-Rich TiAl single crystals*, volume 2, pages 797–804. John Wiley & Sons, Inc., 2012.

[146] S. Hata, T. Nakano, N. Kuwano, M. Itakura, S. Matsumura, and Y. Umakoshi. Microscopic properties of long-period ordering in Al-rich TiAl alloys. *Metallurgical and Materials Transactions A*, 39(7):1610–1617, 2008.

[147] T. Koyama, M. Doi, and S. Naito. Experimental and theoretical investigations of the phase transformation in Al-rich TiAl intermetallic compounds. *MRS Proceedings*, 646, 2000.

[148] S. Hata, K. Shiraishi, N. Kuwano, M. Itakura, Y. Tomokiyo, T. Nakano, and Y. Umakoshi. TEM analysis of long-period superstructures in TiAl single crystal with composition gradient. *MRS Proceedings*, 842, 2004.

[149] J. Li and G.J. Weng. Time-dependent creep of a dual-phase viscoplastic material with lamellar structure. *International Journal of Plasticity*, 14(8):755 – 770, 1998.

[150] M. Grujicic and S. Batchu. A crystal plasticity materials constitutive model for polysynthetically-twinned γ-TiAl+α_2-Ti_3Al single crystals. *Journal of Materials Science*, 36:2851 – 2863, 2001.

[151] D. Sturm. *Herstellung und Eigenschaften Al-reicher TiAl Legierungen*. PhD thesis, OvGU Magdeburg, Magdeburg, 2010.

[152] B. Kad, P. Hazzledine, and H. Fraser. Lamellar interfaces and their contribution to plastic flow anisotropy in TiAl-based alloys. *MRS Proceedings*, 288:495–500, 1992.

[153] T. Nakano, K. Matsumoto, T. Seno, K. Oma, and Y. Umakoshi. Effect of chemical ordering on the deformation mode of Al-rich Ti-Al single crystals. *Philosophical Magazine A*, 74(1):251–268, 1996.

[154] T. Kawabata, T. Kanai, and O. Izumi. Positive temperature dependence of the yield stress in TiAl $L1_0$ type superlattice intermetallic compound single crystals at 293-1273 K. *Acta Metallurgica*, 33(7):1355 – 1366, 1985.

[155] Q. Feng and S.H. Whang. Deformation of Ti-56at.%Al single crystals oriented for single slip by $\frac{1}{2} < 110]$ ordinary dislocations. *Acta Materialia*, 48(17):4307 – 4321, 2000.

[156] M. Werwer and A. Cornec. The role of superdislocations for modeling plastic deformation of lamellar TiAl. *International Journal of Plasticity*, 22(9):1683 – 1698, 2006.

[157] K. Hayashi, T. Nakano, and Y. Umakoshi. Plastic deformation behaviour and deformation substructure in Al-rich TiAl single crystals deformed at high temperatures. *Science and Technology of Advanced Materials*, 2:433 – 441, 2001.

[158] T. Nakano, K. Hayashi, Y. Umakoshi, Y.L. Chiu, and P. Veyssiere. Effects of Al concentration and resulting long-period superstructures on the plastic properties at room temperature of Al-rich TiAl single crystals. *Philosophical Magazine*, 85(22):2527–2548, 2005.

[159] H. Inui, M. Matsumuro, D.H. Wu, and M. Yamaguchi. Temperature dependence of yield stress, deformation mode and deformation structure in single crystals of TiAl (Ti-56 at.% Al). *Philosophical Magazine A*, 75(2):395–423, 1997.

[160] S. Jiao, N. Bird, P. B. Hirsch, and G. Taylor. Yield stress anomalies in single crystals of Ti-54.5 at.% Al: I. Overview and (011) superdislocation slip. *Philosophical Magazine A*, 78(3):777–802, 1998.

[161] T. Kawabata, T. Kanai, and O. Izumi. Dislocation microstructures of a tial single crystal with the [110] orientation deformed at 1073 k. *Philosophical Magazine A*, 70(1):43–51, 1994.

[162] B. Viguier, K.J. Hemker, J. Bonneville, F. Louchet, and J.L. Martin. Modelling the flow stress anomaly in γ-TiAl I. Experimental observations of dislocation mechanisms. *Philosophical Magazine A*, 71(6):1295–1312, 1995.

[163] T. Kawabata, T. Abumiya, T. Kanai, and O. Izumi. Mechanical properties and dislocation structures of TiAl single crystals deformed at 4.2–293 K. *Acta Metallurgica et Materialia*, 38(8):1381 – 1393, 1990.

[164] S. Jiao, N. Bird, P. B. Hirsch, and G. Taylor. Yield stress anomalies in single crystals of Ti–54.5 at.% Al III. Ordinary slip. *Philosophical Magazine A*, 81(1):213–244, 2001.

[165] C. Lei, Q. Xu, and Y.Q. Sun. Tem investigation of interfaces between Ti_3Al_5 and $TiAl_2$. *physica status solidi (a)*, 179(1):77–82, 2000.

[166] Q. Feng and S.H. Whang. Cross-slip and glide behavior of ordinary dislocations in single crystal γ-Ti-56Al. *Intermetallics*, 7(9):971 – 979, 1999.

[167] F. Gregori and Patrick Veyssiere. A microstructural analysis of Al-rich γ-TiAl deformed by $<$011] dislocations. *Materials Science and Engineering: A*, 309–310:87 – 91, 2001.

[168] S. Jiao, N. Bird, P. B. Hirsch, and G. Taylor. Yield stress anomalies in single crystals of Ti-54.5 at.% Al II. 1/2[112](111) slip. *Philosophical Magazine A*, 79(3):609–625, 1999.

[169] F. Gregori, P. Penhoud, and P. Veyssiere. Extrinsic factors influencing the yield stress anomaly of Al-rich γ-TiAl. *Philosophical Magazine A*, 81(3):529–542, 2001.

[170] C. Lei, Q. Xu, and Y. Sun. Phase orientation relationships in the TiAl-TiAl$_2$ region. *Materials Science and Engineering A*, 313:227 – 236, 2001.

[171] R.J. Asaro and A. Needleman. Overview no. 42 texture development and strain hardening in rate dependent polycrystals. *Acta Metallurgica*, 33(6):923 – 953, 1985.

[172] K.K. Mathur and P.R. Dawson. On modeling the development of crystallographic texture in bulk forming processes. *International Journal of Plasticity*, 5(1):67 – 94, 1989.

[173] M. Zhang, J. Zhang, and D.L. McDowell. Microstructure-based crystal plasticity modeling of cyclic deformation of Ti-6Al-4V. *International Journal of Plasticity*, 23(8):1328 – 1348, 2007.

[174] S. Groh, E.B. Marin, M.F. Horstemeyer, and H.M. Zbib. Multiscale modeling of the plasticity in an aluminum single crystal. *International Journal of Plasticity*, 25(8):1456 – 1473, 2009.

[175] S. Conti and K. Hackl. *Analysis and Computation of Microstructure in Finite Plasticity*. Springer International Publishing Switzerland, 2015.

[176] R.J. Asaro and J.R. Rice. Strain localization in ductile single crystals. *Journal of the Mechanics and Physics of Solids*, 25(5):309 – 338, 1977.

[177] R.J. Asaro. Micromechanics of crystals and polycrystals. *Advances in Applied Mechanics*, 23:1 – 115, 1983.

[178] C. Miehe and J. Schotte. *Crystal Plasticity and Evolution of Polycrystalline Microstructure*. John Wiley & Sons, Ltd, 2004.

[179] M. Kuroda. On scale-dependent crystal plasticity models. In J. Schroeder and K. Hackl, editors, *Plasticity and Beyond: Microstructures, Crystal-Plasticity and Phase Transitions*, pages 305–353. Springer Vienna, 2014.

[180] D. Peirce, R.J. Asaro, and A. Needleman. Material rate dependence and localized deformation in crystalline solids. *Acta Metallurgica*, 31(12):1951 – 1976, 1983.

[181] J. Lubliner. On the structure of the rate equations of materials with internal variables. *Acta Mechanica*, 17(1):109–119, 1973.

[182] C. Keller, E. Hug, A.M. Habraken, and L. Duchene. Finite element analysis of the free surface effects on the mechanical behavior of thin nickel polycrystals. *International Journal of Plasticity*, 29:155 – 172, 2012.

[183] Y. Cui, M. Sauzay, C. Caes, P. Bonnaillie, B. Arnal, C. Cabet, M. Blat-Yrieix, and S. Dubiez-Legoff. Modeling and experimental study of long term creep damage in austenitic stainless steels. *Engineering Failure Analysis*, 58, Part 2:452 – 464, 2015.

[184] B. Alfredsson, I. Linares Arregui, and J. Lai. Low temperature creep in a high strength roller bearing steel. *Mechanics of Materials*, 100:109 – 125, 2016.

[185] M. Vose, F. Otto, B. Fedelich, and G. Eggeler. Micromechanical investigations and modelling of a Copper–Antimony-Alloy under creep conditions. *Mechanics of Materials*, 69(1):41 – 62, 2014.

[186] X.S. Yang, Y.J. Wang, H.R. Zhai, G.Y. Wang, Y.J. Su, L.H. Dai, S. Ogata, and T.Y. Zhang. Time-, stress-, and temperature-dependent deformation in nanostructured copper: Creep tests and simulations. *Journal of the Mechanics and Physics of Solids*, 94:191 – 206, 2016.

[187] K. Naumenko and E. Gariboldi. A phase mixture model for anisotropic creep of forged Al–Cu–Mg–Si alloy. *Materials Science and Engineering: A*, 618:368–376, 2014.

[188] A. Staroselsky and B.N. Cassenti. Creep, plasticity, and fatigue of single crystal superalloy. *International Journal of Solids and Structures*, 48(13):2060 – 2075, 2011.

[189] H. Altenbach, Y. Gorash, and K. Naumenko. Steady-state creep of a pressurized thick cylinder in both the linear and the power law ranges. *Acta Mechanica*, 195(1):263–274, 2008.

[190] K. Naumenko, H. Altenbach, and Y. Gorash. Creep analysis with a stress range dependent constitutive model. *Archive of Applied Mechanics*, 79(6-7):619–630, 2009.

[191] B.F. Dyson and M. McLean. Micromechanism-quantification for creep constitutive equations. In S. Murakami and N. Ohno, editors, *IUTAM Symposium on Creep in Structures: Proceedings of the IUTAM Symposium held in Nagoya, Japan, 3–7 April 2000*, pages 3–16. Springer Netherlands, Dordrecht, 2001.

[192] K. Naumenko, A. Kutschke, Y. Kostenko, and T. Rudolf. Multi-axial thermo-mechanical analysis of power plant components from 9–12% Cr steels at high temperature. *Engineering Fracture Mechanics*, 78(8):1657–1668, 2011.

[193] K. Naumenko, H. Altenbach, and A. Kutschke. A combined model for hardening, softening, and damage processes in advanced heat resistant steels at elevated temperature. *International Journal of Damage Mechanics*, 20(4):578–597, 2011.

[194] F. Garofalo. An empirical relation defining stress dependence of minimum creep rate in metals. *Transactions of the Metallurgical Society of AIME*, 227(2):351, 1963.

[195] A.A. Miller. An inelastic constitutive model for monotonic, cyclic, and creep deformation: Part I - Equations development and analytical procedures. *ASME Journal of Engineering Materials and Technology*, 98(2):97–105, 1976.

[196] R. Becker. Analysis of texture evolution in channel die compression-I. effects of grain interaction. *Acta Metallurgica et Materialia*, 39(6):1211 – 1230, 1991.

[197] W. Chen and M. Feng. A study of a cyclic viscoplasticity model based on hyperbolic sine form for the inelastic strain rate. *International Journal of Mechanical Sciences*, 101–102:155 – 160, 2015.

[198] P. Zhang, C. Hu, Q. Zhu, C. Ding, and H. Qin. Hot compression deformation and constitutive modeling of GH4698 alloy. *Materials & Design (1980-2015)*, 65:1153 – 1160, 2015.

[199] F. Längler, K. Naumenko, H. Altenbach, and M. Ievdokymov. A constitutive model for inelastic behavior of casting materials under thermo-mechanical loading. *The Journal of Strain Analysis for Engineering Design*, 49(6):421–428, 2014.

[200] H. Farnoush, A. Momeni, K. Dehghani, J.A. Mohandesi, and H. Keshmiri. Hot deformation characteristics of 2205 duplex stainless steel based on the behavior of constituent phases. *Materials & Design*, 31(1):220 – 226, 2010.

[201] M. Cowan and K. Khandelwal. Modeling of high temperature creep in ASTM A999 structural steels. *Engineering Structures*, 80:426 – 434, 2014.

[202] N. Liu, Z. Li, W.Y. Xu, Y. Wang, G.Q. Zhang, and H. Yuan. Hot deformation behavior and microstructural evolution of powder metallurgical tial alloy. *Rare Metals*, 36(4):236–241, 2017.

[203] R.A. Barrett, T.P. Farragher, C.J. Hyde, N.P. O'Dowd, P.E. O'Donoghue, and S.B. Leen. A unified viscoplastic model for high temperature low cycle fatigue of service-aged P91 steel. *ASME Journal of Pressure Vessel Technology*, 136(2), 2014.

[204] R.A. Barrett, P.E. O'Donoghue, and S.B. Leen. An improved unified viscoplastic constitutive model for strain-rate sensitivity in high temperature fatigue. *International Journal of Fatigue*, 48(Supplement C):192 – 204, 2013.

[205] Z.L. Kowalewski, D.R. Hayhurst, and B.F. Dyson. Mechanisms-based creep constitutive equations for an aluminium alloy. *The Journal of Strain Analysis for Engineering Design*, 29(4):309–316, 1994.

[206] B. F. Dyson. Microstructure based creep constitutive model for precipitation strengthened alloys: theory and application. *Materials Science and Technology*, 25(2):213–220, 2009.

[207] B.F. Dyson. A new mechanism and constitutive law for creep of precipitation hardened engineering alloys. Report A102, NPL Report DMM, 1993.

[208] C.R Barrett and W.D Nix. A model for steady state creep based on the motion of jogged screw dislocations. *Acta Metallurgica*, 13(12):1247 – 1258, 1965.

[209] Shyam M. Keralavarma, T. Cagin, A. Arsenlis, and A. Amine Benzerga. Power-law creep from discrete dislocation dynamics. *Phys. Rev. Lett.*, 109:265504, 2012.

[210] S. Keshavarz, S. Ghosh, A.C.E. Reid, and S.A. Langer. A non-schmid crystal plasticity finite element approach to multi-scale modeling of nickel-based superalloys. *Acta Materialia*, 114:106 – 115, 2016.

[211] A.F. Bower. *Applied Mechanics of Solids*. CRC Press, 2009.

[212] J.W. Hutchinson. Bounds and self-consistent estimates for creep of polycrystalline materials. *Proceedings of the Royal Society of London A: Mathematical, Physical and Engineering Sciences*, 348(1652):101–127, 1976.

[213] J.B. le Graverend, J. Cormier, F. Gallerneau, P. Villechaise, S. Kruch, and J. Mendez. A microstructure-sensitive constitutive modeling of the inelastic behavior of single crystal nickel-based superalloys at very high temperature. *International Journal of Plasticity*, 59:55 – 83, 2014.

[214] A. Zubelewicz and W. Oliferuk. Mechanisms-based viscoplasticity: Theoretical approach and experimental validation for steel 304L. *Scientific Reports*, 6(Article Number 23681), 2016.

[215] K.A. Padmanabhan, J. Leuthold, G. Wilde, and S.S. Bhattacharya. On the power law description of low-stress uni-axial steady-state high-homologous-temperature deformation. *Mechanics of Materials*, 91, Part 1:177 – 193, 2015.

[216] J. Lu, W. Sun, and A. Becker. Material characterisation and finite element modelling of cyclic plasticity behaviour for 304 stainless steel using a crystal plasticity model. *International Journal of Mechanical Sciences*, 105:315 – 329, 2016.

[217] Q. Liu, A. Roy, S. Tamura, T. Matsumura, and V.V. Silberschmidt. Micro-cutting of single-crystal metal: Finite-element analysis of deformation and material removal. *International Journal of Mechanical Sciences*, 118:135 – 143, 2016.

[218] M. Knezevic, J. Crapps, I.J. Beyerlein, D.R. Coughlin, K.D. Clarke, and R.J. McCabe. Anisotropic modeling of structural components using embedded crystal plasticity constructive laws within finite elements. *International Journal of Mechanical Sciences*, 105:227 – 238, 2016.

[219] Y. Tadano, K. Yoshida, and M. Kuroda. Plastic flow localization analysis of heterogeneous materials using homogenization-based finite element method. *International Journal of Mechanical Sciences*, 72:63 – 74, 2013.

[220] J.L. Bassani. Plastic flow of crystals. *Advances in Applied Mechanics*, 30:191 – 258, 1993.

[221] T.Y. Wu, J.L. Bassani, and C. Laird. Latent hardening in single crystals I. theory and experiments. *Proceedings of the Royal Society of London A: Mathematical, Physical and Engineering Sciences*, 435(1893):1–19, 1991.

[222] M.F. Bartholomeusz, Q. Yang, and J.A. Wert. Creep deformation of a two-phase TiAl-Ti_3Al lamellar alloy and the individual TiAl and Ti_3Al constituent phases. *Scripta Metallurgica et Materialia*, 29(3):389 – 394, 1993.

[223] K. Naumenko and H. Altenbach. *Modeling High Temperature Materials Behavior for Structural Analysis Part I: Continuum Mechanics Foundations and Constitutive Models*, volume 28. Springer International Publishing Switzerland, 2016.

[224] G. I. Taylor and C. F. Elam. The plastic extension and fracture of aluminium crystals. *Proceedings of the Royal Society of London. Series A, Containing Papers of a Mathematical and Physical Character*, 108(745):28–51, 1925.

[225] J. W. Hutchinson. Elastic-plastic behaviour of polycrystalline metals and composites. *Proceedings of the Royal Society of London A: Mathematical, Physical and Engineering Sciences*, 319(1537):247–272, 1970.

[226] D. Peirce, R.J. Asaro, and A. Needleman. An analysis of nonuniform and localized deformation in ductile single crystals. *Acta Metallurgica*, 30(6):1087 – 1119, 1982.

[227] E. Voce. A practical strain hardening function. *Metallurgica*, 51:219–226, 1955.

[228] J.L. Bassani and T.Y. Wu. Latent hardening in single crystals II. analytical characterization and predictions. *Proceedings of the Royal Society of London A: Mathematical, Physical and Engineering Sciences*, 435(1893):21–41, 1991.

[229] Y. Nakada and A.S. Keh. Latent hardening in iron single crystals. *Acta Metallurgica*, 14(8):961 – 973, 1966.

[230] U.F. Kocks. Laws for work-hardening and low-temperature creep. *ASME Journal of Engineering Materials and Technology*, 98(1):76–85, 1976.

[231] Y. Huang. A user-material subroutine incorporating single crystal plasticity in the abaqus finite element program. Mech report 178, Harvard University, 1991.

[232] C.O. Frederick and P.J. Armstrong. A mathematical representation of the multiaxial bauschinger effect. *Materials at High Temperatures*, 24(1):1–26, 2007.

[233] W. Dettmer and S. Reese. On the theoretical and numerical modelling of Armstrong–Frederick kinematic hardening in the finite strain regime. *Computer Methods in Applied Mechanics and Engineering*, 193(1):87 – 116, 2004.

[234] M. Khadyko, S. Dumoulin, G. Cailletaud, and O.S. Hopperstad. Latent hardening and plastic anisotropy evolution in AA6060 aluminium alloy. *International Journal of Plasticity*, 76:51 – 74, 2016.

[235] R.D. McGinty and D.L. McDowell. Multiscale polycrystal plasticity. *ASME Journal of Engineering Materials and Technology*, 121(2):203–209, 1999.

[236] Y. Zhu, G. Kang, Q. Kan, O.T. Bruhns, and Y. Liu. Thermo-mechanically coupled cyclic elasto-viscoplastic constitutive model of metals: Theory and application. *International Journal of Plasticity*, 79:111 – 152, 2016.

[237] W. Truszkowski. *The Plastic Anisotropy in Single Crystals and Polycrystalline Metals*. Springer , Netherlands, 2001.

[238] J. Lemaitre. Thermodynamics and phenomenology. In G.A maugin, R. Drouot, and F. Sidoroff, editors, *Continuum Thermomechanics - The Art and Science of Modelling Material Behaviou*, pages 209–223. Springer Netherland, 2000.

[239] Q. Du, D. Wang, and L. Zhu. On mesh geometry and stiffness matrix conditioning for general finite element spaces. *SIAM Journal on Numerical Analysis*, 47(2):1421–1444, 2009.

[240] R. N. Rieben, D. A. White, and G. H. Rodrigue. Improved conditioning of finite element matrices using new high-order interpolatory bases. *IEEE Transactions on Antennas and Propagation*, 52(10):2675–2683, 2004.

[241] S.R. Agnew and O. Duygulu. Plastic anisotropy and the role of non-basal slip in magnesium alloy AZ31B. *International Journal of Plasticity*, 21(6):1161 – 1193, 2005.

[242] J. Jockweg and E. Nembach. Anisotropy of the critical resolved shear stress of a superalloy containing 6 vol.% L12-ordered γ'-precipitates. *Acta Metallurgica et Materialia*, 43(9):3295 – 3300, 1995.

[243] W. Oesterle, D. Bettge, B. Fedelich, and H. Klingelhoeffer. Modelling the orientation and direction dependence of the critical resolved shear stress of nickel-base superalloy single crystals. *Acta Materialia*, 48(3):689 – 700, 2000.

[244] M. Zupan and K.J. Hemker. Yielding behavior of aluminum-rich single crystalline γ-TiAl. *Acta Materialia*, 51(20):6277 – 6290, 2003.

[245] H. Li, D.E. Mason, T.R. Bieler, C.J. Boehlert, and M.A. Crimp. Methodology for estimating the critical resolved shear stress ratios of α-phase Ti using EBSD-based trace analysis. *Acta Materialia*, 61(20):7555 – 7567, 2013.

[246] R. Sanchez-Martin, M.T. Perez-Prado, J. Segurado, J. Bohlen, I. Gutierrez-Urrutia, J. Llorca, and J.M. Molina-Aldareguia. Measuring the critical resolved shear stresses in Mg alloys by instrumented nanoindentation. *Acta Materialia*, 71:283 – 292, 2014.

[247] V. Herrera-Solaz, P. Hidalgo-Manrique, M.T. Perez-Prado, D. Letzig, J. Llorca, and J. Segurado. Effect of rare earth additions on the critical resolved shear stresses of magnesium alloys. *Materials Letters*, 128:199 – 203, 2014.

[248] W.B. Hutchinson and M.R. Barnett. Effective values of critical resolved shear stress for slip in polycrystalline magnesium and other HCP metals. *Scripta Materialia*, 63(7):737 – 740, 2010.

[249] M. Uranagase and R. Matsumoto. Tension–compression asymmetry in uniaxial deformation of a magnesium bicrystal with symmetric tilt grain boundary. *Computational Materials Science*, 118:124 – 132, 2016.

[250] C.J. Hamelin, B.J. Diak, and A.K. Pilkey. Multiscale modelling of the induced plastic anisotropy in BCC metals. *International Journal of Plasticity*, 27(8):1185 – 1202, 2011.

[251] A. Nitz and E. Nembach. Critical resolved shear stress anomalies of the $L1_2$-long-range ordered γ'-phase of the superalloy NIMONIC 105. *Materials Science and Engineering: A*, 263(1):15 – 22, 1999.

[252] M. A. Kumar, I.J. Beyerlein, and C.N. Tome. Effect of local stress fields on twin characteristics in HCP metals. *Acta Materialia*, 116:143 – 154, 2016.

[253] J. Huh, H. Huh, and C.S. Lee. Effect of strain rate on plastic anisotropy of advanced high strength steel sheets. *International Journal of Plasticity*, 44:23 – 46, 2013.

[254] C.S. Meredith and A.S. Khan. Texture evolution and anisotropy in the thermo-mechanical response of UFG Ti processed via equal channel angular pressing. *International Journal of Plasticity*, 30–31:202 – 217, 2012.

[255] A.S. Khan and H. Liu. Strain rate and temperature dependent fracture criteria for isotropic and anisotropic metals. *International Journal of Plasticity*, 37:1 – 15, 2012.

[256] A.S. Khan and S. Yu. Deformation induced anisotropic responses of Ti-6Al-4V alloy. part I: Experiments. *International Journal of Plasticity*, 38:1 – 13, 2012.

[257] M.E. Nixon, O. Cazacu, and R.A. Lebensohn. Anisotropic response of high-purity α-titanium: Experimental characterization and constitutive modeling. *International Journal of Plasticity*, 26(4):516 – 532, 2015.

[258] E. Gariboldi, K. Naumenko, O. Ozhoga-Maslovskaja, and E. Zappa. Analysis of anisotropic damage in forged Al–Cu–Mg–Si alloy based on creep tests, micrographs of fractured specimen and digital image correlations. *Materials Science and Engineering: A*, 652:175–185, 2016.

[259] F. Gregori and P. Veyssiere. Properties of $\langle 011]\{111\}$ slip in Al-rich γ-TiAl I. Dissociation, locking and decomposition of $\langle 011]$ dislocations at room temperature. *Philosophical Magazine A*, 80(12):2913–2932, 2000.

[260] R.A. Brockman. Analysis of elastic-plastic deformation in TiAl polycrystals. *International Journal of Plasticity*, 19(10):1749 – 1772, 2003.

[261] C. Zambaldi and D. Raabe. Plastic anisotropy of γ-TiAl revealed by axisymmetric indentation. *Acta Materialia*, 58(9):3516 – 3530, 2010.

[262] G. Wegmann, T. Suda, and K. Maruyama. Deformation characteristics of polysynthetically twinned (PST) crystals during creep at 1150K. *Intermetallics*, 8(2):165 – 177, 2000.

[263] A.J. Palomares-Garcia, M.T. Perez-Prado, and J.M. Molina-Aldareguia. Effect of lamellar orientation on the strength and operating deformation mechanisms of fully lamellar TiAl alloys determined by micropillar compression. *Acta Materialia*, 123:102–114, 2017.

[264] B.K. Kad, M. Dao, and R.J. Asaro. Numerical simulations of plastic deformation and fracture effects in two phase γ-TiAl + α_2-Ti_3Al lamellar microstructures. *Philosophical Magazine A*, 71(3):567–604, 1995.

[265] H. Inui, K. Chikugo, K. Nomura, and M. Yamaguchi. Lattice defects and their influence on the deformation behavior of single crystals of TiAl. *Materials Science and Engineering: A*, 329-331:377 – 387, 2002.

[266] D. Shechtman, M. J. Blackburn, and H. A. Lipsitt. The plastic deformation of TiAl. *Metallurgical Transactions*, 5(6):1373–1381, 1974.

[267] K. Tanaka. Single-crystal elastic constants of gamma-TiAl. *Philosophical Magazine Letters*, 73(2):71 – 78, 1996.

[268] Y. He, R.B. Schwarz, T. Darling, M. Hundley, S.H. Whang, and Z.M. Wang. Elastic constants and thermal expansion of single crystal γ-TiAl from 300 to 750K. *Materials Science and Engineering: A*, 239-240:157 – 163, 1997.

[269] M.H. Yoo and C.L. Fu. Physical constants, deformation twinning, and microcracking of titanium aluminides. *Metallurgical and Materials Transactions A*, 29:49 – 63, 1998.

[270] P.Y. Tang, B.Y. Tang, and X.P. Su. First-principles studies of typical long-period superstructures Al_5Ti_3, h-Al_2Ti and r-Al_2Ti in Al-rich TiAl alloys. *Computational Materials Science*, 50(4):1467 – 1476, 2011.

[271] M.E. Kassner, P. Kumar, and W. Blum. Harper-dorn creep. *International Journal of Plasticity*, 23(6):980 – 1000, 2007.

[272] M.F. Horstemeyer, D.L. McDowell, and R.D. McGinty. Design of experiments for constitutive model selection: application to polycrystal elastoviscoplasticity. *Modelling and Simulation in Materials Science and Engineering*, 7(2):253–273, 1999.

[273] K.S. Havner. *Finite Plastic Deformation of Crystalline Solids*. Cambridge University Press, UK, 1992.

[274] A.M. Cuitino and M. Ortiz. Computational modelling of single crystals. *Modelling and Simulation in Materials Science and Engineering*, 1(3):225, 1993.

[275] K. Anguige and P.W. Dondl. Energy estimates, relaxation, and existence for strain-gradient plasticity with cross-hardening. In S. Conti and K. Hackl, editors, *Analysis and Computation of Microstructure in Finite Plasticity*, pages 157–173. Springer International Publishing, 2015.

[276] P. Franciosi. The concepts of latent hardening and strain hardening in metallic single crystals. *Acta Metallurgica*, 33(9):1601 – 1612, 1985.

[277] J. Hu and A.C.F. Cocks. A multi-scale self-consistent model describing the lattice deformation in austenitic stainless steels. *International Journal of Solids and Structures*, 78–79:21 – 37, 2016.

[278] U.F. Kocks. The relation between polycrystal deformation and single-crystal deformation. *Metallurgical and Materials Transactions*, 1(5):1121–1143, 1970.

[279] P. Franciosi, M. Berveiller, and A. Zaoui. Latent hardening in copper and aluminium single crystals. *Acta Metallurgica*, 28(3):273 – 283, 1980.

[280] F. Appel. An electron microscope study of the origin of latent hardening in NaCl. *Philosophical Magazine A*, 63(1):71–85, 1991.

[281] D. Cereceda, M. Diehl, F. Roters, D. Raabe, J.M. Perlado, and J. Marian. Unraveling the temperature dependence of the yield strength in single-crystal tungsten using atomistically-informed crystal plasticity calculations. *International Journal of Plasticity*, 78:242 – 265, 2016.

[282] Y. Zhou, K.W. Neale, and L.S. Tóth. A modified model for simulating latent hardening during the plastic deformation of rate-dependent FCC polycrystals. *International Journal of Plasticity*, 9(8):961 – 978, 1993.

[283] E.P. Busso and G. Cailletaud. On the selection of active slip systems in crystal plasticity. *International Journal of Plasticity*, 21(11):2212 – 2231, 2005.

[284] H. Chowdhury, K. Naumenko, H. Altenbach, and M. Krüger. Rate dependent tension-compression-asymmetry of Ti-61.8at%Al alloy with long period superstructures at 1050°C. *Materials Science and Engineering: A*, 700:503 – 511, 2017.

[285] H. Chowdhury, H. Altenbach, M. Krüger, and K. Naumenko. Reviewing the class of Al-rich Ti-Al alloys: Modeling high temperature plastic anisotropy and asymmetry. *Mechanics of Advanced Materials and Modern Processes*, 3(1):16, 2017.

[286] H. Chowdhury, K. Naumenko, and H. Altenbach. Aspects of power law flow rules in crystal plasticity with glide-climb driven hardening and recovery. *International Journal of Mechanical Sciences*, 2017. In press.

[287] H. Chowdhury, K. Naumenko, H. Altenbach, and M. Krüger. Critical stresses estimation by crystal viscoplasticity modeling of rate dependent anisotropy of Al-rich TiAl alloys at high temperature. *Archive of Applied Mechanics*, 2017. Accepted.

[288] H. Chowdhury, K. Naumenko, and H. Altenbach. On the choice of the power law flow rule and its consequences in crystal plasticity. *Key Engineering Materials*, 725:359 – 365, 2016.

[289] N. Bertin, C.N. Tomé, I.J. Beyerlein, M.R. Barnett, and L. Capolungo. On the strength of dislocation interactions and their effect on latent hardening in pure magnesium. *International Journal of Plasticity*, 62:72 – 92, 2014.

[290] M.S. Pham, A.D. Rollett, A. Creuziger, M.A. Iadicola, and T. Foecke. Constitutive modeling based on evolutionary multi-junctions of dislocations. *Key Engineering Materials*, 611-612:1771–1776, 2016.

[291] C. Gerard, G. Cailletaud, and B. Bacroix. Modeling of latent hardening produced by complex loading paths in FCC alloys. *International Journal of Plasticity*, 42:194 – 212, 2013.

[292] C. Gerard, B. Bacroix, M. Bornert, G. Cailletaud, J. Crepin, and S. Leclercq. Hardening description for FCC materials under complex loading paths. *Computational Materials Science*, 45(3):751 – 755, 2009.

[293] M.S. Pham, A. Creuziger, M. Iadicola, and A.D. Rollett. Roles of texture and latent hardening on plastic anisotropy of face-centered-cubic materials during multi-axial loading. *Journal of the Mechanics and Physics of Solids*, 99:50 – 69, 2017.

[294] C. Soyarslan, B. Klusemann, and S. Bargmann. A directional modification of the Levkovitch-Svendsen cross-hardening model based on the stress deviator. *Mechanics of Materials*, 86:21 – 30, 2015.

[295] H. Lim, Jay D. Carroll, Corbett C. Battaile, Brad L. Boyce, and Christopher R. Weinberger. Quantitative comparison between experimental measurements and CP-FEM predictions of plastic deformation in a tantalum oligocrystal. *International Journal of Mechanical Sciences*, 92:98 – 108, 2015.

[296] D. Juul Jensen and N. Hansen. Flow stress anisotropy in aluminium. *Acta Metallurgica et Materialia*, 38(8):1369 – 1380, 1990.

[297] Y. Jiang, Y. Chen, and G. Gao. Role of volume fraction of second phase particles, dislocation-twin and twin-twin interactions in the reduced tension-compression yield asymmetry. *Materials & Design*, 97:131 – 137, 2016.

[298] P.D. Barros, J.L. Alves, M.C. Oliveira, and L.F. Menezes. Modelling of tension-compression asymmetry and orthotropy on metallic materials: Numerical implementation and validation. *International Journal of Mechanical Sciences*, 2016. In Press.

[299] A. Zolochevsky and G. Z. Voyiadjis. Theory of creep deformation with kinematic hardening for materials with different properties in tension and compression. *International Journal of Plasticity*, 21(3):435 – 462, 2005.

[300] M.S.J. Hashmi. *Comprehensive Materials Processing*. Elsevier, 2014.

[301] X. Huang, B. Li, W. Hong, Y.P.g Cao, and X.Q. Feng. Effects of tension-compression asymmetry on the surface wrinkling of film-substrate systems. *Journal of the Mechanics and Physics of Solids*, 94:88 – 104, 2016.

[302] Z. Leng, H. Pan, C. Guo, Z. Wang, G. Zou, and F. Jiang. Asymmetry of tensile-compressive mechanical behaviors of Mg-RE-Zn alloy strengthened by long period stacking ordered phase. *Materials Science and Engineering: A*, 667:468 – 472, 2016.

[303] M. Yaguchi and Y. Takahashi. Ratchetting of viscoplastic material with cyclic softening, part 1: experiments on modified 9Cr-1Mo steel. *International Journal of Plasticity*, 21(1):43 – 65, 2005.

[304] I. Salehinia and D.F. Bahr. Crystal orientation effect on dislocation nucleation and multiplication in FCC single crystal under uniaxial loading. *International Journal of Plasticity*, 52:133 – 146, 2014.

[305] H. Li, X. Hu, H. Yang, and L. Li. Anisotropic and asymmetrical yielding and its distorted evolution: Modeling and applications. *International Journal of Plasticity*, 82:127 – 158, 2016.

[306] K. Liu, X. Dong, H. Xie, Y. Wu, F. Peng, and F. Chen. Asymmetry in the hot deformation behavior of AZ31B magnesium sheets. *Materials Science and Engineering: A*, 659:198 – 206, 2016.

[307] P. Hidalgo-Manrique, V. Herrera-Solaz, J. Segurado, J. Llorca, F. Gálvez, O.A. Ruano, S.B. Yi, and M.T. Pérez-Prado. Origin of the reversed yield asymmetry in Mg-rare earth alloys at high temperature. *Acta Materialia*, 92:265 – 277, 2015.

[308] R. F. Wang, J. Xu, R. T. Qu, Z. Q. Liu, and Z. F. Zhang. Intrinsic strength asymmetry between tension and compression of perfect face-centered-cubic crystals. *Acta Metallurgica Sinica (English Letters)*, 29(8):755–762, 2016.

[309] H. Jiao, F. Barradas, T. Rong, I.P. Jones, and M. Aindow. Observation of tension/compression asymmetry in an Nb-Al-V alloy. *Materials Science and Engineering: A*, 387–389:476 – 480, 2004.

[310] K. Gall and H. Sehitoglu. The role of texture in tension-compression asymmetry in polycrystalline NiTi. *International Journal of Plasticity*, 15(1):69 – 92, 1999.

[311] A. Vinogradov, D. Orlov, A. Danyuk, and Y. Estrin. Deformation mechanisms underlying tension-compression asymmetry in magnesium alloy ZK60 revealed by acoustic emission monitoring. *Materials Science and Engineering: A*, 621:243 – 251, 2015.

[312] F. Kabirian and A.S. Khan. Anisotropic yield criteria in $\sigma - \tau$ stress space for materials with yield asymmetry. *International Journal of Solids and Structures*, 67–68:116 – 126, 2015.

[313] J.W. Yoon, Y. Lou, J. Yoon, and M.V. Glazoff. Asymmetric yield function based on the stress invariants for pressure sensitive metals. *International Journal of Plasticity*, 56:184 – 202, 2014.

[314] J.B. Stewart and O. Cazacu. Analytical yield criterion for an anisotropic material containing spherical voids and exhibiting tension-compression asymmetry. *International Journal of Solids and Structures*, 48(2):357 – 373, 2011.

[315] H. Xie, T. Yu, and F. Yin. Tension-compression asymmetry in homogeneous dislocation nucleation stress of single crystals Cu, Au, Ni and Ni_3Al. *Materials Science and Engineering: A*, 604:142 – 147, 2014.

[316] H. Luo, L. Shaw, L.C. Zhang, and D. Miracle. On tension/compression asymmetry of an extruded nanocrystalline Al-Fe-Cr-Ti alloy. *Materials Science and Engineering: A*, 409(1–2):249 – 256, 2005.

[317] H.B. Chen, T.M. Liu, Y. Zhang, Y.B. Zhai, and J.J. He. Reducing tension-compression yield asymmetry by free end torsion in extruded Mg alloy. *Materials Science and Technology*, 32(2):111–118, 2016.

[318] B. Revil-Baudard, O. Cazacu, P. Flater, N. Chandola, and J.L. Alves. Unusual plastic deformation and damage features in titanium: Experimental tests and constitutive modeling. *Journal of the Mechanics and Physics of Solids*, 88:100 – 122, 2016.

[319] M.E. Nixon, R.A. Lebensohn, O. Cazacu, and C. Liu. Experimental and finite-element analysis of the anisotropic response of high-purity α-titanium in bending. *Acta Materialia*, 58(17):5759 – 5767, 2010.

[320] A.M. Dongare, A.M. Rajendran, B.L., M.A. Zikry, and D.W. Brenner. Tension-compression asymmetry in nanocrystalline Cu: High strain rate vs. quasi-static deformation. *Computational Materials Science*, 49(2):260 – 265, 2010.

[321] J. Zhai, T. Luo, X. Gao, S.M. Graham, M. Baral, Y.P. Korkolis, and E. Knudsen. Modeling the ductile damage process in commercially pure titanium. *International Journal of Solids and Structures*, 91:26 – 45, 2016.

[322] G.J. Kleiser, B. Revil-Baudard, O. Cazacu, and C.L. Pasiliao. Plastic deformation of polycrystalline molybdenum: Experimental data and macroscopic model accounting for its anisotropy and tension–compression asymmetry. *International Journal of Solids and Structures*, 75–76:287 – 298, 2015.

[323] R.K. Verma, T. Kuwabara, K. Chung, and A. Haldar. Experimental evaluation and constitutive modeling of non-proportional deformation for asymmetric steels. *International Journal of Plasticity*, 27(1):82 – 101, 2011.

[324] X. Zhou and F. Li. Simulations of nonlinear deformations in Ni–Ti shape memory alloys under tension/compression using an energy minimization model. *Computational Materials Science*, 81:530 – 537, 2014.

[325] J.W. Wang, Q.Q. Duan, C.X. Huang, S.D. Wu, and Z.F. Zhang. Tensile and compressive deformation behaviors of commercially pure al processed by equal-channel angular pressing with different dies. *Materials Science and Engineering: A*, 496(1–2):409 – 416, 2008.

[326] Y. Jia and Y. Bai. Experimental study on the mechanical properties of AZ31B-H24 magnesium alloy sheets under various loading conditions. *International Journal of Fracture*, 197(1):25–48, 2016.

[327] J. Jain, W.J. Poole, C.W. Sinclair, and M.A. Gharghouri. Reducing the tension–compression yield asymmetry in a Mg–8Al–0.5Zn alloy via precipitation. *Scripta Materialia*, 62(5):301 – 304, 2010.

[328] W. Muhammad, M. Mohammadi, J. Kang, R. K. Mishra, and K. Inal. An elasto-plastic constitutive model for evolving asymmetric/anisotropic hardening behavior of AZ31B and ZEK100 magnesium alloy sheets considering monotonic and reverse loading paths. *International Journal of Plasticity*, 70:30 – 59, 2015.

[329] Z. Wen, H. Pei, B. Wang, D. Zhang, and Z. Yue. The tension/compression asymmetry of a high γ volume fraction nickel-based single-crystal superalloy. *Materials at High Temperatures*, 33(1):68–74, 2016.

[330] J.Y. Kim, D. Jang, and J.R. Greer. Crystallographic orientation and size dependence of tension-compression asymmetry in molybdenum nano-pillars. *International Journal of Plasticity*, 28(1):46 – 52, 2012.

[331] G.G. Yapici, I.J. Beyerlein, I. Karaman, and C.N. Tomé. Tension-compression asymmetry in severely deformed pure copper. *Acta Materialia*, 55(14):4603 – 4613, 2007.

[332] S. Kamrani and C. Fleck. Effects of calcium and rare-earth elements on the microstructure and tension-compression yield asymmetry of ZEK100 alloy. *Materials Science and Engineering: A*, 618:238 – 243, 2014.

[333] D.G. Tari, M.J. Worswick, U. Ali, and M.A. Gharghouri. Mechanical response of AZ31B magnesium alloy: Experimental characterization and material modeling considering proportional loading at room temperature. *International Journal of Plasticity*, 55:247 – 267, 2014.

[334] S. Kurukuri, M.J. Worswick, T.D. Ghaffari, R.K. Mishra, and J.T. Carter. Rate sensitivity and tension-compression asymmetry in AZ31B magnesium alloy sheet. *Philosophical transactions Series A, Mathematical, physical, and engineering sciences*, 372, 2014.

[335] S.H. Park, J.H. Lee, B.G. Moon, and B.S. You. Tension-compression yield asymmetry in as-cast magnesium alloy. *Journal of Alloys and Compounds*, 617:277 – 280, 2014.

[336] N. Chandola, R.A. Lebensohn, O. Cazacu, B. Revil-Baudard, R.K. Mishra, and F. Barlat. Combined effects of anisotropy and tension–compression asymmetry on the torsional response of AZ31 Mg. *International Journal of Solids and Structures*, 58:190 – 200, 2015.

[337] S. Xu, T. Liu, H. Chen, Z. Miao, Z. Zhang, and W. Zeng. Reducing the tension-compression yield asymmetry in a hot-rolled Mg-3Al-1Zn alloy via multidirectional pre-compression. *Materials Science and Engineering: A*, 565:96 – 101, 2013.

[338] C. Lv, T. Liu, D. Liu, S. Jiang, and W. Zeng. Effect of heat treatment on tension-compression yield asymmetry of AZ80 magnesium alloy. *Materials & Design*, 33:529 – 533, 2012.

[339] T. Kuwabara, Y. Kumano, J. Ziegelheim, and I. Kurosaki. Tension-compression asymmetry of phosphor bronze for electronic parts and its effect on bending behavior. *International Journal of Plasticity*, 25(9):1759 – 1776, 2009.

[340] X.Y. Lou, M. Li, R.K. Boger, S.R. Agnew, and R.H. Wagoner. Hardening evolution of AZ31B Mg sheet. *International Journal of Plasticity*, 23(1):44 – 86, 2007.

[341] M. Hakamada, A. Watazu, N. Saito1, and H. Iwasaki. Tension/compression anisotropy in hot forged Mg-Al-Ca-RE alloy. *MATERIALS TRANSACTIONS*, 50(7):1898–1901, 2009.

[342] L.Y. Chen, B.Z. Li, X.D. Wang, F. Jiang, Y. Ren, P.K. Liaw, and J.Z. Jiang. Atomic-scale mechanisms of tension–compression asymmetry in a metallic glass. *Acta Materialia*, 61(6):1843 – 1850, 2013.

[343] J. Ma, B. Kockar, A. Evirgen, I. Karaman, Z.P. Luo, and Y.I. Chumlyakov. Shape memory behavior and tension–compression asymmetry of a FeNiCoAlTa single-crystalline shape memory alloy. *Acta Materialia*, 60(5):2186 – 2195, 2012.

[344] Z. Zachariah, Sankara Sarma V. Tatiparti, S.K. Mishra, N. Ramakrishnan, and U. Ramamurty. Tension-compression asymmetry in an extruded Mg alloy AM30: Temperature and strain rate effects. *Materials Science and Engineering: A*, 572:8 – 18, 2013.

[345] F. Fereshteh-Saniee, Kh. Fallah-Nejad, A.Sh. Beheshtiha, and H. Badnava. Investigation of tension and compression behavior of AZ80 magnesium alloy. *Materials & Design*, 50:702 – 712, 2013.

[346] Q. Zhang, W. Zhang, and Y. Liu. Evaluation and mathematical modeling of asymmetric tensile and compressive creep in aluminum alloy ZL109. *Materials Science and Engineering: A*, 628:340 – 349, 2015.

[347] A.S. Khan and M. Baig. Anisotropic responses, constitutive modeling and the effects of strain-rate and temperature on the formability of an aluminum alloy. *International Journal of Plasticity*, 27(4):522 – 538, 2011.

[348] Q. Zhang, J. Zhang, and Y. Wang. Effect of strain rate on the tension-compression asymmetric responses of Ti-6.6Al-3.3Mo-1.8Zr-0.29Si. *Materials & Design*, 61:281 – 285, 2014.

[349] K. Piao, J.K. Lee, J.H. Kim, H.Y. Kim, K. Chung, F. Barlat, and R.H. Wagoner. A sheet tension/compression test for elevated temperature. *International Journal of Plasticity*, 38:27 – 46, 2012.

[350] K. Piao, J.K. Lee, J.H. Kim, H.Y. Kim, K. Chung, F. Barlat, and R.H. Wagoner. A sheet tension/compression test for elevated temperature. *International Journal of Plasticity*, 38:27 – 46, 2012.

[351] L.P. Chi L.L. Chang. Tension-compression asymmetry in an extruded Mg alloy AZ31: Texture and strain rate effects. *Materials Science Forum*, 849:109–113, 2016.

[352] R.R. Adharapurapu, F.J., K.S. Vecchio, and G.T. Gray III. Response of NiTi shape memory alloy at high strain rate: A systematic investigation of temperature effects on tension–compression asymmetry. *Acta Materialia*, 54(17):4609 – 4620, 2006.

[353] L.B. Tong, M.Y. Zheng, S. Kamado, D.P. Zhang, J. Meng, L.R. Cheng, and H.J. Zhang. Reducing the tension-compression yield asymmetry of extruded Mg-Zn-Ca alloy via equal channel angular pressing. *Journal of Magnesium and Alloys*, 3(4):302 – 308, 2015.

[354] G. Garces, P. Perez, S. Cabeza, H.K. Lin, S. Kim, W. Gan, and P. Adeva. Reverse tension/compression asymmetry of a Mg-Y-Zn alloys containing LPSO phases. *Materials Science and Engineering: A*, 647:287 – 293, 2015.

[355] A. Saigal and M. Fonte. Solid shape recovered bulk nitinol, part I: Tension-compression asymmetry. *Materials Science and Engineering: A*, 528(16–17):5536 – 5550, 2011.

[356] Y. Xin, X. Zhou, and Q. Liu. Suppressing the tension-compression yield asymmetry of Mg alloy by hybrid extension twins structure. *Materials Science and Engineering: A*, 567:9 – 13, 2013.

[357] E. Dogan, I. Karaman, G. Ayoub, and G. Kridli. Reduction in tension-compression asymmetry via grain refinement and texture design in Mg-3Al-1Zn sheets. *Materials Science and Engineering: A*, 610:220 – 227, 2014.

[358] F. Jiao, D. Bettge, W. Osterle, and J. Ziebs. Tension-compression asymmetry of the (001) single crystal nickel base superalloy SC16 under cyclic loading at elevated temperatures. *Acta Materialia*, 44(10):3933 – 3942, 1996.

[359] O. Cazacu, I.R. Ionescu, and J.W. Yoon. Orthotropic strain rate potential for the description of anisotropy in tension and compression of metals. *International Journal of Plasticity*, 26(6):887 – 904, 2010.

[360] B. Plunkett, O. Cazacu, and F. Barlat. Orthotropic yield criteria for description of the anisotropy in tension and compression of sheet metals. *International Journal of Plasticity*, 24(5):847 – 866, 2008.

[361] O. Cazacu, B. Plunkett, and F. Barlat. Orthotropic yield criterion for hexagonal closed packed metals. *International Journal of Plasticity*, 22(7):1171 – 1194, 2006.

[362] J. Kim, H. Ryou, D. Kim, D. Kim, W. Lee, S.H. Hong, and K. Chung. Constitutive law for AZ31B mg alloy sheets and finite element simulation for three-point bending. *International Journal of Mechanical Sciences*, 50(10–11):1510 – 1518, 2008.

[363] B.Z. Wang, D.S. Liu, Z.X. Wen, and Z.F. Yue. Tension/compression asymmetry of [001] single-crystal nickel-based superalloy DD6 during low cycle fatigue. *Materials Science and Engineering: A*, 593:31 – 37, 2014.

[364] S. Ghosh and M. Anahid. Homogenized constitutive and fatigue nucleation models from crystal plasticity FE simulations of Ti alloys, part 1: Macroscopic anisotropic yield function. *International Journal of Plasticity*, 47:182 – 201, 2013.

[365] D. Leidermark, J.J. Moverare, K. Simonsson, S. Sjostrom, and S. Johansson. Room temperature yield behaviour of a single-crystal nickel-base superalloy with tension/compression asymmetry. *Computational Materials Science*, 47(2):366 – 372, 2009.

[366] M.G. Lee, R.H. Wagoner, J.K. Lee, K. Chung, and H.Y. Kim. Constitutive modeling for anisotropic/asymmetric hardening behavior of magnesium alloy sheets. *International Journal of Plasticity*, 24(4):545 – 582, 2008.

[367] Z.Q. Wang and I.J. Beyerlein. An atomistically-informed dislocation dynamics model for the plastic anisotropy and tension–compression asymmetry of BCC metals. *International Journal of Plasticity*, 27(10):1471 – 1484, 2011.

[368] M. Zupan and K. Hemker. Measurement of the tension/compression asymmetry exhibited by single crystalline γ-Ti-55.5at%Al. *MRS Proceedings*, 646, 2000.

Erklärung

Ich versichere hiermit, dass ich die vorliegende Arbeit ohne unzulässige Hilfe Dritter und ohne Benutzung anderer als der angegebenen Hilfsmittel angefertigt habe. Die Hilfe eines kommerziellen Promotionsberaters habe ich nicht in Anspruch genommen. Dritte haben von mir weder unmittelbar noch mittelbar geldwerte Leistungen für Arbeiten erhalten, die im Zusammenhang mit dem Inhalt der vorgelegten Dissertation stehen. Bilder und Ideen aus fremden Quellen werden ordnungsgemäß zitiert. Ich habe insbesondere nicht wissentlich:

- Ergebnisse erfunden oder widersprüchliche Ergebnisse verschwiegen,
- statistische Verfahren absichtlich missbraucht, um Daten in ungerechtfertigter Weise zu interpretieren,
- fremde Ergebnisse oder Veröffentlichungen plagiiert,
- fremde Forschungsergebnisse verzerrt wiedergegeben

Mir ist bekannt, dass Verstöße gegen das Urheberrecht Unterlassungs- und Schadensersatzansprüche des Urhebers sowie eine strafrechtliche Ahndung durch die Strafverfolgungsbehörden begründen kann.

Ich erkläre mich damit einverstanden, dass die Dissertation ggf. mit Mitteln der elektronischen Datenverarbeitung auf Plagiate überprüft werden kann.

Die Arbeit wurde bisher weder im Inland noch im Ausland in gleicher oder ähnlicher Form als Dissertation eingereicht und ist als Ganzes auch noch nicht veröffentlicht.

Magdeburg

Helal Chowdhury

Curriculum vitae

Personal data

Name: Helal Chowdhury
Date of birth: 01.03.1983
Place of birth: Feni
Marital status: Married
Nationality: Bangladeshi

Study and professional background

1989–1997	School, Feni
1997–2000	School, Chittagong Exam name: Higher Secondary Certificate
2000–2005	B.Sc. in Mechanical Engineering Bangladesh University of Engineering and Technology Dhaka, Bangladesh
2005–2010	Project coordinator Siemens Bangladesh Ltd., Nokia-Siemens Networks BD Ltd. Dhaka, Bangladesh
2010–2013	M.Sc. in Computational Engineering FAU Erlangen-Nürnberg Erlangen, Germany
2013–2017	Wissenschaftlicher Mitarbeiter at the Chair of Applied Mechanics Institute of Mechanics at Otto-von-Guericke University Magdeburg

Magdeburg Helal Chowdhury

List of publications

International peer-reviewed journals

[1] H. Chowdhury, K. Naumenko, H. Altenbach and M. Krüger. Rate-dependent tension-compression-asymmetry of Ti-61.8at%Al alloy with long-period superstructures at 1050°C. *Materials Science and Engineering: A*, 700:503-511, 2017.

[2] H. Chowdhury, K. Naumenko, H. Altenbach and M. Krüger. Critical stresses estimation by crystal viscoplasticity modeling of rate-dependent anisotropy of Al-rich TiAl alloys at high-temperature. *Archive of Applied Mechanics*, Accepted, 2017.

[3] H. Chowdhury, K. Naumenko, H. Altenbach. Aspects of power-law flow-rules in crystal plasticity with glide-climb driven hardening and recovery. *International Journal of Mechanical Sciences*, Article in press, 2017.

[4] H. Chowdhury, H. Altenbach, K. Naumenko and M. Krüger. Reviewing the class of Al-rich Ti-Al alloys: Modeling high-temperature plastic anisotropy and asymmetry. *Mechanics of Advanced Materials and Modern Processes*, 3(1):16, 2017.

[5] H. Chowdhury and K. Naumenko and H. Altenbach. On the Choice of the power-law flow-rule and its consequences in crystal plasticity. *Key Engineering Materials*, 725:359-365, 2016.